Icelandic Dust Entrainment, Emission & Deposition

A Dissertation Submitted to the Committee on Graduate Studies in Partial Fulfillment of the Requirements for the Degree of Doctor of Philosophy in the Faculty of Arts and Science.

TRENT UNIVERSITY

Peterborough, Ontario, Canada

Environmental & Life Sciences Ph.D. Graduate Program

January 2020

In memory of my mother, Dawn Richards

Abstract

Icelandic Dust Entrainment, Emission & Deposition
Tamar Richards - Thomas

Extremely active dust sources within selected areas of Iceland that are comprised of particles supplied from both glacio-fluvial outwash systems and volcanic eruptions (Bullard et al., 2016; Gassó et al., 2018). The supply of sediments, sparsity of vegetation, high frequency of surface winds, and lack of adequate gravel pavement to reduce sand drifting are believed to influence the duration, frequency, and magnitude of these dust events in Iceland. Apart from recent collaborative efforts to measure and model dust entrainment, emission and deposition (Prospero et al., 2012; Zwaaftink et al., 2017), several underlying physical mechanisms that are unique to cold, humid climates and the geology of Iceland are not well understood. This study specifically aims to assess and understand the physics of Icelandic dust entrainment and deposition with an emphasis on the influence of climate and the physical characteristics of the particles. A series of laboratory experiments of different configurations were carried out on several sediments collected from some of the most emissive sources in Iceland in order to understand these dust processes. The results from this study show that the increasing particle sphericity is associated with progressively smaller particle size; and an abundance of amorphous glass increases the surface area and roughness of the particles, which contributes to high porosity that alters the particle skeletal density. The particle features and climate are interlinked with the entrainment and deposition rates. For instance, coarse sediments emit higher PM concentrations than sediments containing more clay. The strong wind shear at the bed surface acts to disperse many of the tiny particle aggregates and coated liquid droplets contained within

a splash structure created by the impact of a single water droplet. The deposition of suspended dust particulates is dependent on the particle characteristics and relative humidity. The retreat of glaciers and ice-cap masses in Iceland are expected to expose new dust particulate sources as the global mean temperature continues to rise (Cannone et al., 2008; Radic and Hock, 2011). Therefore, the influence of the particle characteristics and climate on the dust entrainment, emission and deposition must be accounted for in the parameterization of dust dispersion models related to suspended volcaniclastic particles.

Keywords: Icelandic dust, dust emission and deposition, high latitude cold climate environments, particle characteristics, settling velocity, laser Doppler anemometer, rain droplet impact, wind tunnel

Acknowledgments

The completion of this Ph.D. thesis could not have been possible without the support of my supervisor, Cheryl McKenna-Neuman. Cheryl has offered guidance, constructive feedbacks, valuable criticisms, encouragement, motivation and financial support throughout my doctoral program. Cheryl has also provided the opportunity to travel around the world and present my research findings at some of the most prestigious international conferences and workshops. Cheryl allowed me to explore several research directions throughout the early stages of my program at Trent before settling down on what formed my thesis. Cheryl did not restrict my thoughts or even my proposal objectives but instead encouraged creativity, novelty and innovation, which resulted in the formation of this thesis. I would also like to acknowledge the financial assistance received for this research provided by NSERC discovery grant and CFI grant to Cheryl McKenna-Neuman. I received personal financial support through several awards and scholarships, such as the Ontario Graduate Scholarship, and the Air & Waste Management Association (Ontario and internationally), as well as several other travel and conference awards for early career scientist.

I would also like to thank Tom Mockford from Loughborough University, Throstur Thorsteinsson and Pavla Dagsson-Waldhauserová from the University of Iceland for their valuable time spent collecting samples in the field for this study. I would also like to acknowledge Throstur for shipping the sediments from Iceland to Trent University and providing constructive feedback about the geology of the sample selection sites and their locations for ArcGIS mapping.

I would also like to acknowledges the assistance provided by Ian Power and the rest of my supervisory and examining committee members. Ian Power pro-

vided suggestions and insights towards the characterization of my samples from a geochemical perspective throughout the development of Chapter 2 of my thesis. Power support will lead to the publication of the first paper, which forms Chapter 2 of this thesis. I want to say thanks to all the other members of my committee for reading this thesis and providing valuable feedback.

A special thank you to George Kretschmann, Mike Gorton and Yanan Liu from the Earth Sciences Centre at the University of Toronto. I want to acknowledge Kretschmann for allowing me to gain useful skills in scanning electron microscopic imaging. Gorton provided valuable insights and expertise in the analyses of the mineralogy of these complex Icelandic samples. Liu provided further characterization of the phase compositions of the samples, using the JEOL JXA8230 5-WDS electron microprobe and X-ray diffractometer. The author would also like to thank Sterling Vanderzee from the University of British Columbia for some of the particle density measurements.

I also wish to express gratitude to the Wind tunnel laboratory research group both past and present members (Patrick O'Brien, Colette Preston, Taylor Brooks, Christina Von Bulow, Dami Ogungbemide and Stacey Johnston) for all the support received throughout the various stages of my research.

Most importantly, to my family and friends who have prayed for me and helped me to get to this point. I extend a special thank you to my spouse, Recy Thomas, who offered endless support, suggestions, and a helping hand in the laboratory during the data collected of chapter 3 and parts of chapter 4. I would also like to express gratitude to my father and other members of the family for their continuous encouragement throughout my academic career. Thank you to my friends for occasionally editing the late drafts of my thesis and providing valuable feedback.

'Nil Sine Magno Labore'

Nothing is achieved without hardwork

Co-Authorship Statement

The core chapters (2-5) of this thesis are written as four manuscripts that will be submitted later for publication. Tamar Richards-Thomas, who led this research project, formulated the study design, collected and analyzed the results, completed the data analysis, interpreted the results and wrote the manuscripts, will be the primary author on each of the manuscripts. Dr. Cheryl McKenna-Neuman, who provided suggestions for the initial research objectives, contributed to the study design and analysis, and provided constructive editorial feedbacks on all writing aspects, will be co-authors on all manuscripts. Dr. Ian Power, who provided guidance and suggestion on the particle characteristics analysis is also a co-author of the manuscript presented as Chapter 2.

Table of Contents

List of Figures

List of Tables

List of Abbreviations and Symbols

a	Coefficient	75
A	Filled area [m^2]	36
A_b	Bulk area [m^2]	38
A_{geo}	Geometric area [μm^2]	35
A_{surf}	Particle surface area [$m^2 g^{-1}$]	35
A_s	Solid area [m^2]	38
A_{total}	Total area [m^2]	113
A_{upwind}	Cross-sectional area of upwind side [m^2]	108
$A_{downwind}$	Cross-sectional area of downwind side [m^2]	108
b	Exponent	75
c	Dust concentration [$\mu g m^{-3}$]	73
C_D	Drag coefficient	62
c_{dw}	Center-to-center distance of wooden dowel [cm]	76
$c.g.$	Centre of Gravity	10
c_i	Interparticle cohesive	76
c_{tz}	Time averaged peak concentration [$\mu g m^{-3}$]	75
F_c	Interparticle cohesive force [N]	8
F_D	Drag Force [N]	9
F_g	Gravitational Force [N]	8
d	Particle Diameter [μm]	46
$\overline{d}$	Mean particle diameter [μm]	46
d_a	Arithmetic diameter [μm]	35
d_{dw}	Diameter of wooden dowel [cm]	76
d_g	Geometric diameter [μm]	35

d_t	Depth of the tray [cm]	114
d_{50}	Median particle diameter [μm]	49
E	Dust emission rate [$\mu g/m^2s$]	71
E_k	Kinetic energy [J]	104
F	Vertical dust flux [$\mu g/m^2s$]	71
g	Gravitational acceleration [9.81 ms^{-2}]	62
H	Wind Tunnel vertical height [m]	182
h_d	Splash height [mm]	126
h_{dw}	Height of wooden dowel [cm]	76
$hlcc$	High latitude cold climate	2
I	Intermediate dimension [m]	36
K	Turbulent diffusion coefficient [m]	72
L	Wind Tunnel cross-sectional length [m]	182
L	Longest dimension [m]	36
l_t	Length of the tray [cm]	114
L_b	Length of the bed surface [m]	72
m_i	Mass transport rate of dust into [mgs^{-1}]	72
m_o	Mass transport rate of dust out [mgs^{-1}]	72
M	Moments [N]	10
PM	Particulate Matter μm	28
PM_1	Particulate Matter less than 1 μm	69
$PM_{2.5}$	Particulate Matter less than 2.5 μm	69
PM_4	Particulate Matter less than 4 μm	69
PM_{10}	Particulate Matter less than 10 μm	68
P	Perimeter of a particle [μm]	36
S	Shortest dimension [m]	36

Chapter 1

General Introduction

1.1 Introduction

High latitude cold climate (hlcc, $\geq 50°$N and $\geq 40°$S) dust source regions range from hyper-arid to extremely humid environments that are comprised of sediments supplied from glacio-fluvial outwash systems (Bullard et al., 2016; Bullard, 2013, Fig. 1.1) and catastrophic volcanic eruptions (e.g., Iceland: Thorsteinsson et al., 2012). The lack of vegetation and high wind speeds are believed to influence the frequency and magnitude of dust storm events. Hlcc environments emit a total of 80−100 million metric tons of dust per year or 5 % of the global total (Bullard et al., 2016); however, 3% is sourced within latitudes >60°N (Zwaaftink et al., 2016). The quantity of dust emitted from sub-arctic environments is much less than the total amount of dust emitted from extreme dust sources in hot, sub-tropical semi-arid and arid deserts (e.g., 160−760 million metric tons from North Africa, Goudie and Middleton, 2001).

The retreat of glaciers and ice-cap masses is expected to expose new dust particulate sources as the global mean temperature continues to rise (Cannone et al., 2008; Radic and Hock, 2011). Catastrophic volcanic eruptions eject up to $10^4\,\mathrm{m}^3$ of unique, ultrafine particles into the atmosphere (Butwin et al., 2019) that replenish depleted terrestrial landscapes with fresh supply of ash deposits. The sediments available for transport by wind are believed to influence the frequency and duration of the dust storm occurrences (Björnsson and Pálsson, 2008; Bullard et al., 2016; Bullard, 2013; Mahowald et al., 2005; Marshall et al., 2012; Solomon et al., 2007; Thorsteinsson et al., 2012).

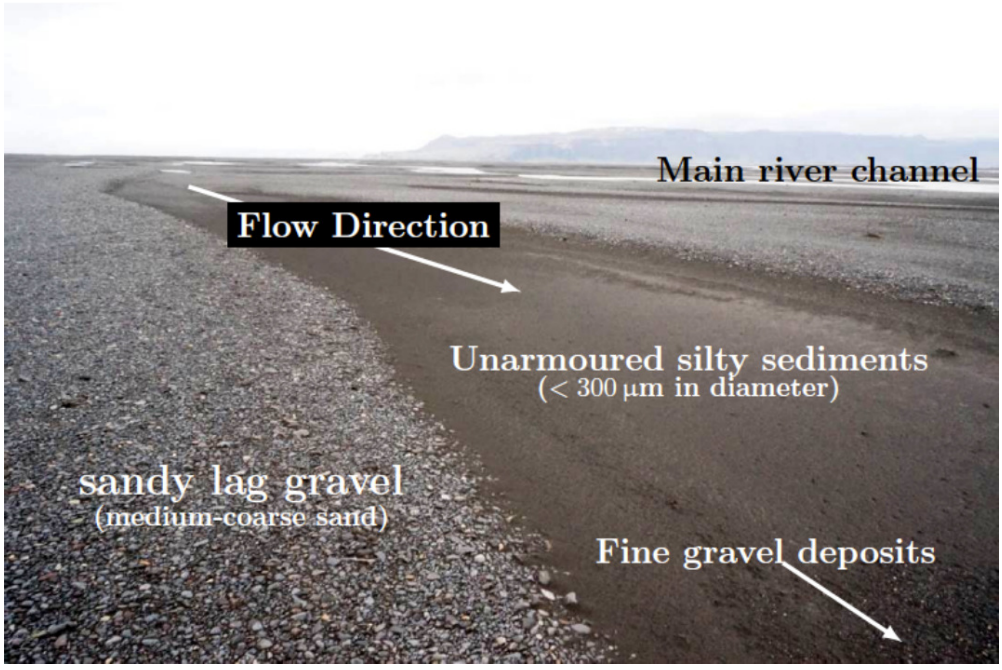

Figure 1.1: An ephemeral channel system created by the Markarfljót River, southern Iceland shows a barren region consisting of a silty sediment layer deposited between large strips of sandy gravel lags. The silt sediments remain unarmored, partially dried and poorly vegetated. Photo credit: Tom Mockford, May 2014.

Aeolian dust processes within humid, cold sub-arctic desert regions are not well studied as compared to those in dry, hot sub-tropical deserts because:

- Dust source regions within the sub-tropical dust belt ($\leq 50°$N) contribute up to 50 % of the global dust budget (Maher et al., 2010; Prospero et al., 2012) because they have the most extensive and emissive areas (e.g., Taklamakan desert in China: Xuan et al., 2004; e.g., Bodélé depression in North Africa: Todd et al., 2008). There are source regions of comparable size within humid, cold environments (e.g., Lake Eyre Basin in Australia: Bullard et al., 2008), but the total amount of dust contributed is up to 45 % less than that supplied

from the sub-tropics (Bullard et al., 2016).

- There are fewer meteorological stations located within emissive remote hlcc regions, as compared to those within emissive sub-tropical regions, and so, dust events within hlcc regions are often missed and not reported (Bullard et al., 2016). Whereas, meteorological instrumentations located within these regions miss dust storm events because of the changes in the landscape and topographical features caused by extreme climate and weather conditions that influence the dust transport pathways (Arnalds et al., 2001; Mockford, 2017).

- Winter darkness and cloud cover within sub-arctic regions strongly influence the detection of dust storms by satellite sensors, as compared to those within dust source regions located in the sub-tropics (Solomon et al., 2007), and so, poor dust visibility hinders data retrieval (e.g., wintertime in Iceland: NASA, 2014). For instance, images captured by the NASA Terra satellite show persistent cloud cover, as severe dust haze from Dyngjusandur spreads towards northern Iceland and the Arctic (Dagsson-Waldhauserová et al., 2017).

- Surface temperature intensity variations influence the ability of remote-sensing devices to distinguish between dust and the land surface. Where there is little to no vegetation cover (Bullard et al., 2016), the source regions naturally camouflage the suspended dust particulates over a region.

- Dust transport over the ocean can also reduce the ability of remote sensors to detect storm events because spectral variations over the water influence dust visibility. For instance, dust plumes are occasionally observed blowing off the northern and northeast coast of Iceland (Dagsson-Waldhauserová et al.,

2017), as well as the southern coast near Landeyjsandur (Thorsteinsson et al., 2011), but it is difficult to precisely estimate the suspended mass concentration over the Northern Atlantic Ocean.

Eight major hlcc dust source regions are well recognized by the high latitude dust network (`http://www.hlccd.org`); however, very little is known about the physics of aeolian dust processes within these environments (e.g., Iceland: Arnalds et al., 2013; Eurasia: Bullard et al., 2016; Greenland: Mockford et al., 2018; Alaska: Crusius et al., 2011; Canada: Nickling, 1978; Patagonia Gassó et al., 2010; New Zealand: McGowan and Sturman, 1996; Antarctica: Bhattachan et al., 2015). Among these eight sources, Icelandic dust regions are the most studied hlcc environments ($\geq$ 50N Bullard et al., 2016) because they provide an accessible and highly suitable analogue for similar present-day and historical settings (Arnalds et al., 2001; Bullard et al., 2016) as compared to other hlcc regions. Dust storms in hlcc environments pose a risk to human health when particulates are inhaled, particularly in the context of particulate matter $\leq 10\,\mu m$ in diameter (PM_{10}). High PM_{10} concentrations are often recorded in the capital city of Reykjavik, where over 80 % of the Icelandic population resides, and are believe to be linked to regional respiratory health problems (Bullard et al., 2016; Thorsteinsson et al., 2011).

Apart from recent collaborative efforts to measure and model Icelandic dust emission, transport and deposition (Dagsson-Waldhauserová et al., 2017; Gassó et al., 2018; Zwaaftink et al., 2017), a number of underlying physical mechanisms that are unique to the climate and geology of Iceland are not well understood. Indeed, much of the present work is based on studies carried out in dry, hot deserts. Direct measurements of dust processes within hlcc regions are needed to validate the theoretical assumptions used in parameterization schemes and to

minimize the uncertainties and limitations in model predictions of dust emission and deposition of future dust events and eruptions. For instance, dust transport models, as well as measurement algorithms, usually assume a constant density for ash particles from all types of volcanic eruptions (Grainger et al., 2013), and this leads to significant bias in calculation of the mass concentration within a volcanic dust cloud.

1.1.1 Conceptual Basis - A brief introduction

Suspended dust (PM_{10}) particulates in Iceland are influenced by the physical particle characteristics and regional weather and climate, which affect dust entrainment and deposition (Fig. 1.2). This section provides a brief introduction to the mechanics of dust entrainment, emission and deposition, and the associated literature. A more detailed description of these processes is provided in each of the four core chapters provided in manuscript format.

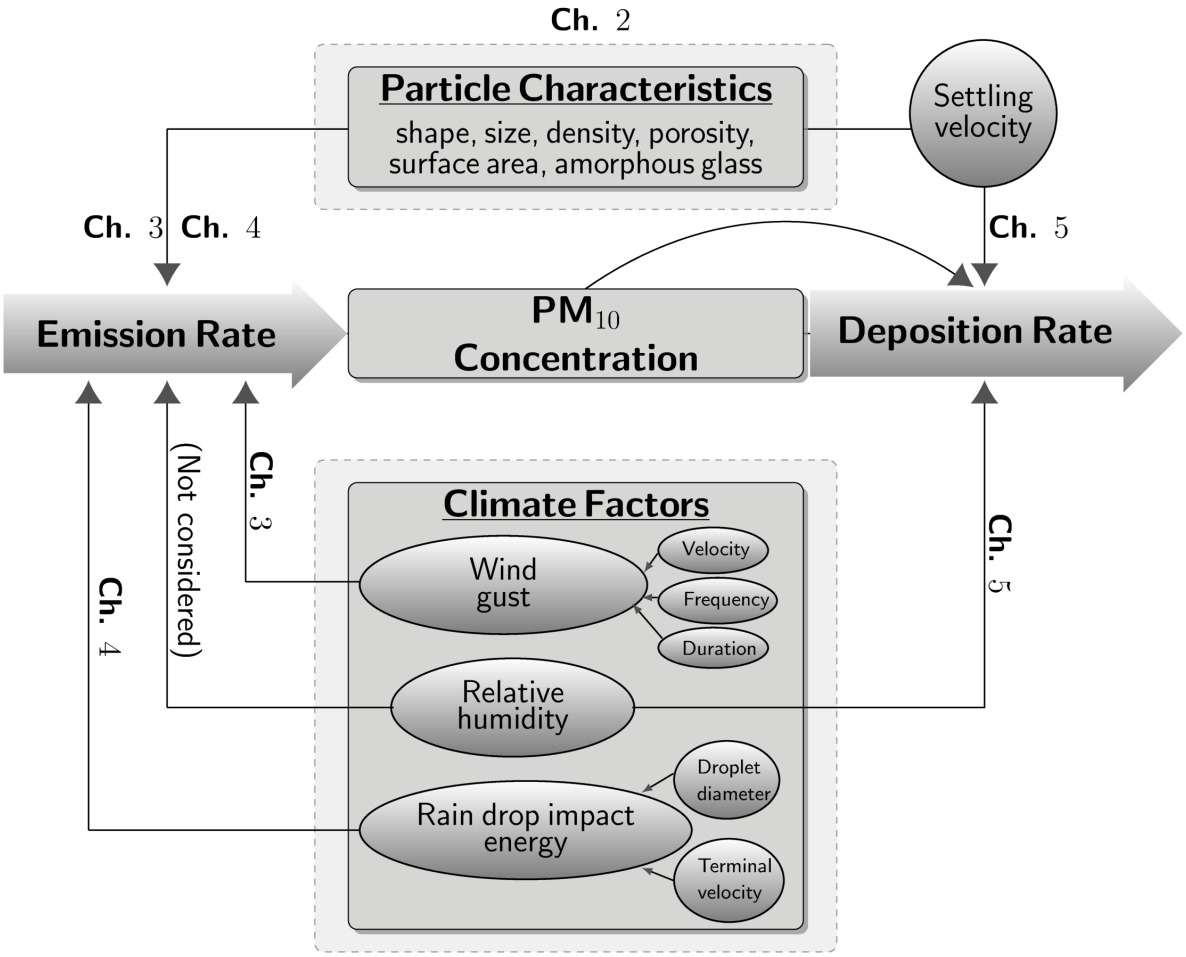

Figure 1.2: Dust transport system

1.1.1.1 Mechanism of dust entrainment

Three mechanisms that may initiate the motion of dust particles are aerodynamic entrainment, saltation bombardment and aggregate disintegration. Ideally, in pure dust environments, aerodynamic entrainment refers to the detachment of particles directly from the bed surface through the fluid drag of the turbulent wind motion, which arises from air pressure differences around discrete particles. The resistive forces (e.g., adhesion and cohesion) within and between particles are often dominant and hinder motion. Saltation bombardment refers to the ejection

of particles by the impact of individual saltators (sand particles with diameter 70−500 μm) that bounce along the surface in a projectile motion (Fig. 1.3; Shao, 2000). The strong, interparticle cohesive forces cause dust particles to attach to either other dust or sand particles to form aggregates. The breakdown of the aggregates to eject dust particulates during windblown aeolian processes is called disintegration. Natural environments contain a mixture of sediments, inclusive of particles ranging from clay to gravel, and so dust entrainment involves the removal of dust primarily by winds that initiate the motion of saltators, which collide into the surface and overcome the bonding forces (Shao, 2000, Fig. 1.3). A detailed description of the particle size classification system used in the present study is described in Appendix A.

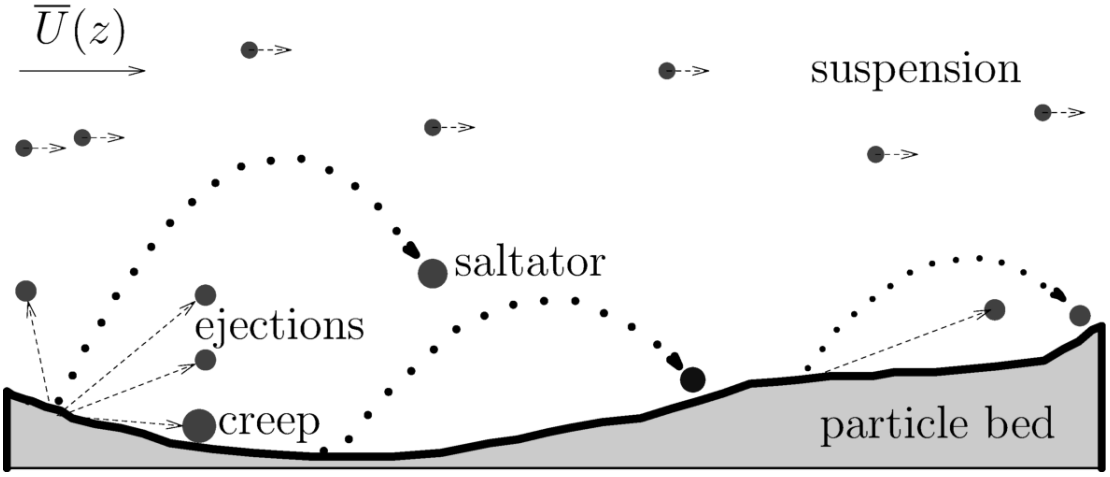

Figure 1.3: Aeolian particle transport processes

The primary forces that firmly hold particles at the surface are the gravitational (F_g) and cohesive (F_c) forces with magnitude dependent on the particle size. F_g is inherited from the particle weight (w_g) and becomes dominant for large particles (e.g., sand, Fig. 1.4); F_c is inherited from the interparticle cohesion and is dominant for clay-size particles $\leq 20\,\mu$m. The resisting forces are the interparticle cohesive force (F_c) acting between the particles at the surface, and the

gravitational force (F_g) acting vertically downwards in the direction of gravity (Fig. 1.4).

Dust entrainment by wind occurs when the aerodynamic forces (drag force, F_D and lift force, F_L; Fig. 1.4) overcome the resisting forces (F_c and F_G). When a combination of the drag force (F_D) acting horizontally in the wind direction and lift force (F_L) acting vertically upwards exceeds the resisting forces, motion will be initiated. F_L and F_D are components of the aerodynamic force. F_L arises from the near-surface velocity gradient. F_L is highest when the particles are resting on the bed surface, but decreases rapidly with increased height (Chepil, 1961). F_D is lowest near the bed and increases rapidly with increasing height above the surface layer of near zero velocity (also called the sub-viscous layer, Chepil, 1961). F_D is proportional to the square of the horizontal velocity ($F_D \propto \overline{u}(z)^2$). All of these forces are influenced by the size, shape and packing of the particles, and to some extent their mineralogy in the case of F_c.

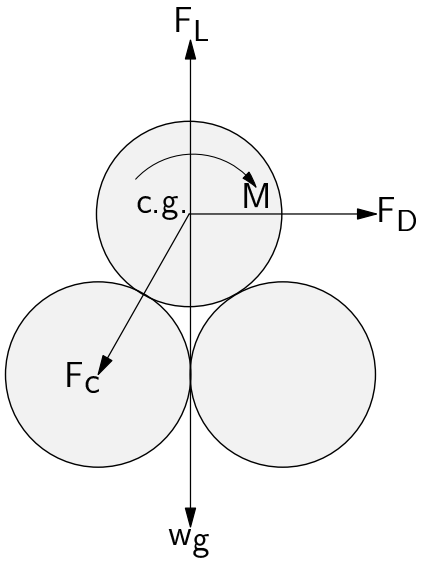

Figure 1.4: Forces acting on an erodible spherically-shaped particle in a wind stream, where F_L is the lift force, F_D is the drag force, F_c is the interparticle cohesive force, w_g is the particle weight, $c.g.$ is the center of gravity of a particle, and M is the moment (Modified from Pye, 1987).

1.1.1.2 Friction velocity

The friction velocity ($u_\star$) provides an indication of the shear stress ($\rho u_\star^2$) within the airflow near the surface. It is dependent upon the wind velocity and aerodynamic roughness (z_o). It is constant within the lowest $10-20\,\%$ of the atmospheric boundary layer (ABL, Tennekes, 1973; White, 1996) and within the lowest $10-15\,\%$ of the wind tunnel boundary layer (Li and McKenna-Neuman, 2012). The aerodynamic roughness refers to the height of the thin layer just above the sediment surface in which the velocity of the air motion is near zero. The thickness of z_o depends on the texture of the particles at the surface (e.g., size). If the value of (z_o) increases, then the value of ($u_\star$) also increases, thereby generating large eddies that sweep dust particles up into the turbulent airflow, increasing dust concentration levels. Above z_o, the wind velocity derived from the Prandtl-Von

Karman equation increases logarithmically with height in a turbulent boundary layer, as discussed in further detail in Chapter 3.

1.1.1.3 Threshold friction velocity

The threshold friction velocity ($u_{\star t}$) is the minimum friction velocity required to initiate the motion of particles at the bed surface (Bagnold, 1941; Greeley and Iverson, 1985). It represents a balance between the gravitational (resisting) forces and the lift forces acting on a particle at rest when subjected to an airflow. If $u_{\star t}$ is higher than the wind friction velocity, then larger particles will remain stationary on the surface. The value of $u_{\star t}$ is dependent on the particle characteristics, inclusive of shape, size and density, as well as the surface conditions, inclusive of sorting, arrangement and packing of particles on the bed surface (Chepil, 1959; Ravi et al., 2006).

The early work of Shield (1936) shows that at the threshold of entrainment, the shear stress is a unique function of the particle Reynolds number, as confirmed later by Bagnold (1941, Fig. 1.5). From a balance between F_D and F_g, Bagnold's (1941) pioneering work shows that $u_{\star t}$ is proportional to the square root of the particle diameter (d), $\left(u_{\star t}{=}\mathcal{A}\sqrt{\frac{\Delta\rho}{\rho_a}gd}\right)$, where $\mathcal{A} \cong 0.1$ is an empirical coefficient, g=9.8 ms^{-2} is the gravitational acceleration, $\Delta\rho{=}\rho_p - \rho_a$ is the density difference between the particle skeletal density (ρ_p) and air density (ρ_a).

Air density influences the threshold friction velocity required for dust entrainment, and decreases with rising air temperature (Davis, 1992; McKenna-Neuman, 1993), so that higher drag forces are exerted on particles at the surface in cold environments. A wind tunnel study of McKenna-Neuman (1993) suggests that up to 70 % more sand particles are transported during saltation at -40°C than at $+40$°C. The sediment transport rate within cold regions, such as Iceland, under

the same wind speed is expected to be higher than those in warm environments (McKenna-Neuman, 2003). This result has important implications for dust ejection through saltation under cold conditions (Gillette, 1978; Grini and Zender, 1977; Shao et al., 1993), although limited in-situ measurements exist to examine the effect of temperature on dust emission.

The threshold friction velocity required for the initiation of particle motion (e.g. fluid threshold: Bagnold, 1941) varies in high latitude regions, but the most commonly reported values vary from 4 to 10 ms^{-1} (Bullard and Austin, 2011; Gisladottir et al., 2005), similar to those reported for sub-tropical environments (e.g., Grini and Zender, 1977). One of the primary controls on hlcc dust storm events is wind speed (Mockford, 2017), but more studies are needed. The value of $u_{\star t}$ reaches a minimum when d=75 µm (Greeley and Iverson, 1985), but it then increases as d decreases for fine-textured particles $>$ 75 µm (Fig. 1.5) when the resisting forces become relatively important (Bagnold, 1941).

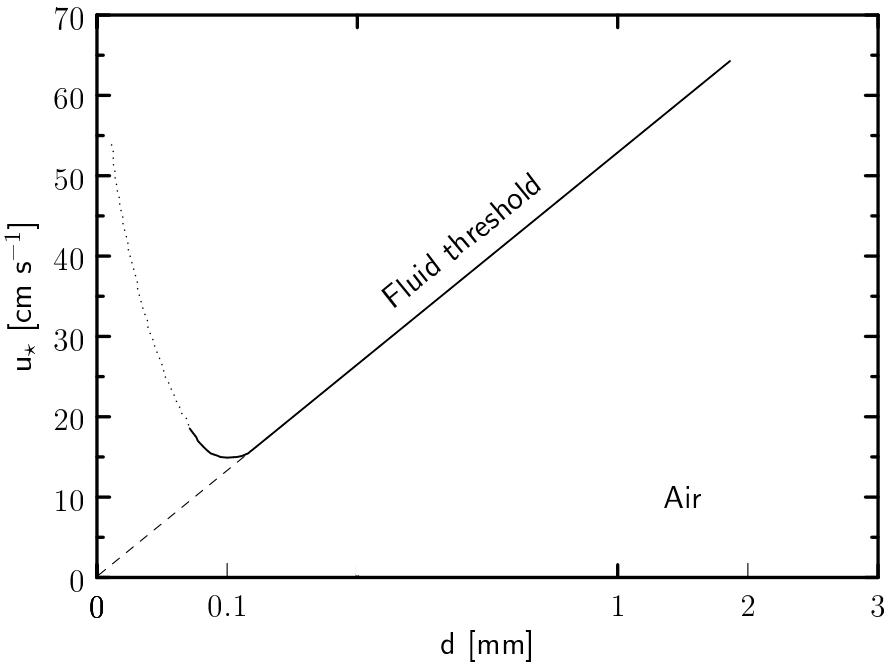

Figure 1.5: A distinction between the fluid and impact threshold variations for different particle diameters (Modified from Bagnold, 1941, pg 88).

1.1.2 Mechanism of dust emission

Dust particulates entrained and emitted by wind erosion mechanisms can be transported over thousands of kilometres from their sources (Joussaume, 1990; Tegen and Fung, 1994), and so adequate estimates of the emission rate are required to predict their contribution towards the global dust budget, so as to improve the assessment of its effects on the weather and climate systems. The following section reviews several approaches to measure the emissivity of a given surface.

1.1.3 Field versus wind tunnel studies

Many studies have been performed to examine dust entrainment and the emission rate of various natural and fugitive particulates, using the finite difference method

(e.g., field and laboratory wind tunnel studies) and to a lesser extent the control volume approach (e.g., wind tunnel).

It is generally accepted that a power-law relationship exists between the vertical dust flux (F) and surface friction velocity ($u_\star$), as $F \propto u_\star^b$, (Gillette, 1981; Gillette and Walker, 1977; Nickling and Gillies, 1989a, 1993, Table 1.1). Table 1.1 shows a list of published values for the exponent that vary widely. In many field settings, dust emission is driven by the impact of saltators, and so the magnitude of b is strongly linked to the sediment texture. While such studies have significantly contributed to the prediction of dust emission within dry, hot semiarid environments, very few studies have investigated this relationship ($F \propto u_\star^b$) for sediments within humid, cold climate regions (Nickling, 1978; Thorsteinsson et al., 2011). The wide variations of the value of b in the list of field studies are also dependent on fluctuations of the weather and climate, and the geology of a localized region. Wind tunnels can be used to overcome some of challenges associated with the lack of precise control in field experiments.

1.1.4 Dust entrainment and emission by rain splash

In aeolian studies, saltation bombardment and the lifting of particles from a rough surface layer are widely considered as the two primary mechanisms that drive dust emission (Gordon and McKenna-Neuman, 2009; Marticorena and Bergametti, 1995; Shao, 2008). However, in environments such as Iceland, where the geological origin of the particles, surface and climate conditions are unique, other mechanisms may enhance the dust entrainment process, such as the impact of rain droplets (Fig. 1.6). Rain droplet impact, from low to moderate rainfall, enhanced by strong winds can significantly contribute to soil particle mobilization that causes aerosol and bacteria suspension and their transport in the atmo-

Table 1.1: A summary of published models for the vertical dust flux.

Measurements	**Researchers**	**Surface Characteristics**	**Vertical Dust Flux** ($F \propto$)
PM_{10} wind tunnel (portable)	Houser and Nickling (2001)	Crusted playa, frequently disturbed	$u_*^{2.14}$
PM_{10} wind tunnel	Loosmore and Hunt (2000)	Arizona test dust, no saltation	u_*^3
TSP Field tower	Lopez et al. (1998)	Tilled field - mouldboard ploughing	$u_*^{5.67}$
TSP Field tower	Lopez et al. (1998)	Tilled field - chisel ploughing	$u_*^{5.98}$
TSP Field tower	Lopez (1998)	Tilled field (recalculated from original data)	$u_*^{6.57}$
PM_{10} Field tower	Nickling et al. (1999)	Australian rangeland	$u_*^{4.94}$
PM_{10} wind tunnel	McKenna-Neuman (2009)	Dry, pulverized tailings, no saltation	u_*^4
PM_{10} wind tunnel	McKenna-Neuman (2009)	Dry tailings, cracked crust, no saltation	$u_*^{1.3}$
PM_{10} wind tunnel	McKenna-Neuman (2009)	Dry tailings, cracked crust, saltation feed	$u_*^{3.3}$
PM_{10} wind tunnel	McKenna-Neuman (2009)	Damp tailings - 2−10% WC	$u_*^{3.3}$
PM_{10} wind tunnel	Nickling and Gillies (1989a)	Natural and disturbed desert sites	$u_*^{2.9}$
TSP - Portable wind tunnel	Nickling and Gillies (1989a)	Fluvial sites	$u_*^{3.32}$
TSP - Portable wind tunnel	Nickling and Gillies (1989a)	Construction sites	$u_*^{4.42}$
TSP-WT (portable)	Nickling and Gillies (1989b)	Sites $>$ 25% silt/clay	$u_*^{4.27}$
TSP-WT (portable)	Nickling and Gillies (1989b)	Sites $>$ 15% silt/clay	$u_*^{3.02}$
TSP Field tower	Nickling (1978)	Slims River delta	$u_*^{3.55}$
TSP Wind Tunnel	Gillette (1978)	Varying loamy soils	$u_*^{3.0}$
TSP Field tower	Gillette et al. (1997)	Owens (Dry) layer playa soils	$u_*(u_*^2 - u_{*t}^2)$
TSP Field tower	Gillette et al. (1997)	Owens (Dry) layer playa soils	$(u_*^3 - u_{*t}^3)$
TSP Field tower	Gillette (1974)	Moderate silt content	$(u_*/u_{*t})^{5.14}$
TSP Field tower	Gillette (1974)	High silt content	$(u_*/u_{*t})^{9.67}$
PM_{10} Tower	Nickling et al. (1999)	Australian Rangeland	$u_*^{4.94}$
TSP combined	Saxton et al. (2000)	Combined field/wind tunnel study	$u_*^3(u_* - u_{*t})$
TSP combined	Saxton et al. (2000)	Combined field/wind tunnel study	$u_*^2(u_* - u_{*t})$
$<$ PM_{20} combined results	Gillette and Passi (1988)	Deduced from communication with P.R. Owen	$u_*^4(1 - u_{*t}/u_*)$
TSP Wind tunnel	Gillette and Passi (1988)	Deduced from communication with P.R. Owen	$u_*^3(1 - u_{*t}^2/u_*^2)$
TSP Wind tunnel	Shao et al. (1993)	Kaolin clay (mean $d = 2\,\mu$m), heavy saltation	$u_*^3(1 - u_{*t}^2/u_*^2)$
PM_{10} WT	Roney and White (2006)	Owens (dry) lake playa soils	$(u_* - u_{*t})^2$

WT - Wind tunnel, TSP - Total suspended particulates

sphere, thereby having significant effects on the environment and human respiratory health. In Iceland, field workers report that dust emission often coincides with the onset of a precipitation event (Arnalds et al., 2001).

Figure 1.6: A dust storm in northern Iceland, where there is an extensive floodplain in a desert. Photo credit: Pavla Dagsson-Waldhauserova, September 2017.

1.1.5 Mechanism of particle deposition

The settling velocity (v) in still air is defined as the maximum vertical fall velocity that a given particle can attain, occurring when the sum of the forces acting on the particle and its acceleration decrease to zero. The settling velocity is dependent on the particle morphology (e.g., size, shape, density), and controls particle dispersal (e.g., volcanic ash), thereby affecting the particle residence time (Clift et al., 2005; Kylling et al., 2014; Loth, 2008; Riley, 2003). The dependency of v on climatic effects is not well understood.

Electron micrographs of Icelandic ash particles show that they are highly angular, porous and rough (Fig. 1.7); however, the effects of particle morphology on

the deposition rate are neither well understood nor quantified. Angular particles settling in still air drift horizontally, and so, they have lateral deflections (Wilson and Huang, 1979; Wu et al., 2008), which are not accounted for when Stoke's approximation is applied. The effects of neighboring particles within the particle cloud also remain unclear. Icelandic ash contains varied portions of dense minerals, which affect the skeletal density (Gislason et al., 2011; Olsson et al., 2013, ρ_s) and influence the particle transport rate in the atmosphere (Gislason et al., 2011; Olsson et al., 2013, and references within). The cold, moist atmospheric conditions typical of hlcc regions may also influence the particle morphology (Brown et al., 2012, e.g., shape and aggregation:), which may have significant implication in model parameterization schemes (Bagheri et al., 2016).

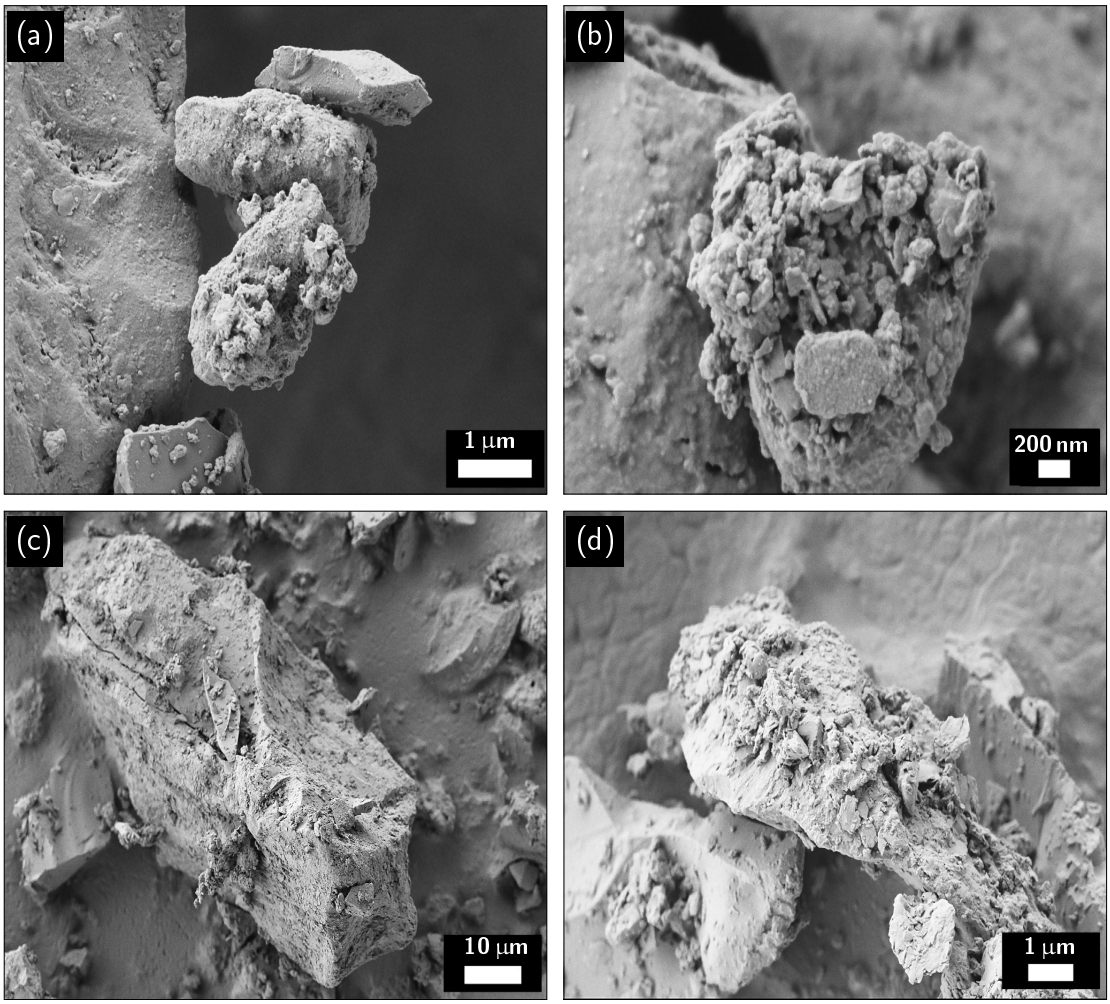

Figure 1.7: Scanning electron micrographs show the complex morphologies of Icelandic dust particles.

1.1.6 Problem Statements

Particle characterization

The morphology of Icelandic dust particulates is often not incorporated in atmospheric and climate models because it is poorly characterized (Bullard et al., 2016; Bullard, 2013; Mockford, 2017; Mockford et al., 2018). For instance, there were several missing particle morphologies in forecasts of the 2010 Eyjafjallajökull ash

cloud dispersion (Wiegner et al., 2012, and references therein), during and after the eruption. Particle shape and size are needed to derive statistically robust shape parameters so that the uncertainties within transport and mass concentration calculations for ash particulates can be minimized, yet very few direct measurements are available in the literature (Bagheri et al., 2015; Liu et al., 2015). Model parameterization schemes often assume that suspended volcaniclastic particles in the atmosphere are discrete, solid spheres with a constant density equivalent to either rhyolite glass (ρ=2.3 g cm^{-3}: Johnson et al., 2012; Leadbetter et al., 2012) or typical ash (ρ=2.6 g cm^{-3}: Wiegner et al., 2012). The particle density of 2010 Eyjafjallajökull ash is not well documented in the literature; although other particle morphologies, inclusive of the size, shape, surface area and mineralogy are reported (Alfano et al., 2011; Gislason et al., 2011; Olsson et al., 2013). While Icelandic dust particles are widely speculated to be highly porous (Bullard et al., 2016; Gislason et al., 2011), direct measurements of the complex particle porosity have never been reported in the literature because the technology is expensive and the technique is time-consuming.

Dust entrainment and emission

The key factors (e.g., particle morphology and climate) that distinguish aeolian dust processes in Iceland are not well understood, although saltation is believed to be the primary mechanism driving dust emission from surfaces subjected to boundary layer flows. In Iceland, extreme dust storm events are strongly linked to high-speed wind gusts (up to 50 ms^{-1}), which are initiated by strong density-driven katabatic flows ($>$ 10 ms^{-1}: Arnalds, 2010). The effects of the gust strength, frequency and duration on dust emission are not well understood because the surface and environmental factors are difficult to isolate in field studies, and so, wind tun-

nel laboratory studies are needed to overcome some of these challenges. While it is widely recognized that the particle morphology of Icelandic dust is different from those within dry, hot regions (Bullard et al., 2016; Rice et al., 1995), few wind tunnel studies have been carried out to address the influence of the variability in the surface properties and environmental conditions on the dust emission rate (Del Bello et al., 2018). Controlled wind tunnel studies are needed to understand the role of the particle morphology in Icelandic dust emission, as compared to particles with properties similar to those in hot, dry regions.

A special case of dust entrainment, emission and transport by rain droplet impact

In Iceland, field workers report that dust emission sometimes coincides with the onset of a precipitation event (Mockford, 2017; Prospero et al., 2012), although saltation is widely speculated to be the primary mechanism that drives Icelandic dust events (Cornelis and Gabriels, 2003; Ravi et al., 2006). The dust concentration within the plume generated by the impact of a rain droplet on a bed surface is not reported in the literature, and likely has never been measured. Laboratory studies are needed to understand the physics of dust entrainment and dispersion of the splash structure arising from the bed surface after the impact a rain droplet in still air and under wind-driven conditions. Icelandic dust particles are speculated to be hydrophobic (Meinander, 2016), which can influence the splash detachment of the dust particles ejected from a natural water-repellent soil surface (Hamlette et al., 2013). In general, the physics of particle hydrophobicity is not well understood.

Dust deposition

Many experimental studies have determined the drag coefficient (C_D) of volcaniclastic particles (Bagheri et al., 2015, 2013, 2016; Del Bello et al., 2017; Loth, 2008; Riley, 2003), as well as non-spherical ones of simple geometry (e.g., spheres, disks, cubes, cylinders, spheroids: McNown and Malaika, 1950; Pettyjohn and Christiansen, 1948), falling in still air. However, few studies evaluate C_D at low Reynolds numbers ($Re \ll 1$; Allen, 1984) for particles settling individually. Some have investigated the effect of the presence of neighbouring particles when $Re \gg 1$ (Del Bello et al., 2017; Wilson and Huang, 1979; Wu et al., 2008). Both the morphology and drag coefficient of volcaniclastic aggregates within large suspended volume fractions need to be studied at low Re (Bagheri et al., 2015), because they are most likely to be transported and persist in the atmosphere. No direct measurements of the settling velocity components in $2D$ ($x - horizontal$ and $z - vertical$) are reported in the literature, especially for large suspended volume fractions under varied climatic conditions. The horizontal and vertical velocities are quite challenging to measure, and so, only 1D model simulations currently exist. Direct measurement of the $x - horizontal$ component of the settling velocity could provide new insight into the dispersion of dust particles.

1.2 Objectives and thesis structure

The goal of this dissertation is to assess and understand the physics of Icelandic dust entrainment, emission, transport and deposition with an emphasis on the influence of climate and the physical characteristics of the particles. The primary objectives of each core chapter that address this overarching goal are listed as follows:

Chapter 2:

i) to evaluate the physiochemical properties of Icelandic dust

ii) to explore and compare the performance of several cutting-edge technologies in measuring the complex morphology of basaltic aerosols

iii) to provide a coarse approximation of the dynamical effects of this morphology, relative to a solid glass sphere.

The first objective of this study was to measure the micro-scale characteristics of the particles collected from some of the most emissive sources in Iceland, as identified in the study of Arnalds et al. (2016). Such measurements are required for the parameterization of dust dispersion models, as well as for evaluating their influence on the physics of dust emission, transport and deposition investigated in the remaining core chapters. Several state-of-the-art technologies and techniques are needed to quantify the particle shape, size, density, surface area, porosity and mineralogy. Calculation of the drag coefficient based on the morphology measured for an Icelandic dust particle is used to provide a coarse approximation of the particle residence time in the atmosphere relative to a solid sphere of the same size.

Chapter 3:

i) to quantify the response of the dust emission rate at varied wind speeds

ii) to identify the primary particle characteristics (e.g., size, surface area, density and mineral) that influence the dust emission rate of Icelandic basalts relative to a control

iii) to estimate the relative proportion of varied size fractions of airborne particulates (PM_1, $PM_{2.5}$, PM_4 and PM_{10})

A series of wind tunnel simulations was conducted to evaluate the influence of wind gust frequency and duration on the dust emission rate. The experiments were performed at a constant temperature and low relative humidity in order to eliminate the effects of climate and isolate the effects of the particle morphology. Suspended dust particulates generated from Icelandic sediments that are dominated by fine particles are compared to those emitted from relatively coarse sediments, inclusive of a control sample with different particle morphology. The dust emitted from Icelandic sediments with high surface area and amorphous glass content is compared with that for a control sample of low surface area and amorphous glass. The relative proportions of different size fractions of airborne particulates contained within the parent size distribution were also measured.

Chapter 4

i) to evaluate the particle, water droplet and crater characteristics, as well as the dimensions (e.g., base diameter, height and spread) of the splash structure emerging from the bed surface upon impact of a single water droplet

ii) to understand and quantify the factors influencing Icelandic dust emission with rain drop impact in still air and within a shearing flow

iii) to measure the PM concentration within a splash structure generated by the impact of a single water droplet

Three experimental configurations were used to gain an in-depth understanding of the consequent splash structure emerging from a bed surface upon the impact of a water droplet, in still air and within a shearing flow. Most of the experiments in still air were performed on top of a lab bench (*S1- low impact*) and within a stairwell (*S2 - high impact*), but all those within a shearing flow were carried out in a wind tunnel (*WT- high impact*). A constant-volume droplet was released at different heights to obtain low and high impact velocities in each of three experimental designs. The droplet and crater morphologies were obtained from image analysis, but the particle morphology was measured using several technologies, to explore their effects on dust entrainment and dispersion above the bed surface. Most existing studies on water droplet impact are very specific and narrow in scope (Behroozi, 2012; Ryan and Poduska, 2008). This study is one of the first to quantify the response of the splash structure arising from the bed surface in still air and at varying wind speeds (e.g., 2, 4, 6 and 8 ms^{-1}), which are similar to those observed in Iceland (Ashwell and Hannell, 1960). The dust fluxes sampled in this study are compared with those measured in Chapter 3 to examine the influence of conditions with and without rain droplet impact.

Chapter 5:

i) to evaluate the dependency of the particle settling velocity upon a) particle morphology (e.g., size, shape, porosity, density, surface area and minerals) and b) relative humidity (RH)

A settling chamber was designed to operate with a Laser Doppler Anemometer

(LDA) in order to measure the settling velocity of Icelandic dust particles relative to that for solid glass microspheres. The LDA is capable of measuring the settling velocity of particles that pass through its measurement volume in two dimensions (x - *horizontal* and z - *vertical*). This study is the first to provide direct measurements of the settling velocity of particles $\leq 50\,\mu m$ in diameter in $2D$ (x - *horizontal* and z - *vertical*), within large suspended volume fractions. The particles were recovered at the base of the chamber in order to perform several replicate measurements. An approximation of the drag coefficient was obtained, based on the measured particle settling velocity at low relative humidities ($20 - 30\,\%$).

1.3 Thesis structure

The objectives of this thesis, which involve a combination of conceptual, empirical and methodological contributions, are introduced above in the same order as the corresponding core Chapters, each written in manuscript format. Hence, some redundancy occurs in the contextual content.

A detailed analysis of the physical characteristics of Icelandic dust, using several state-of-the-art technologies and techniques, is presented in Chapter 2 and interlinked with the dust processes studied in the subsequent core chapters. Selected aspects of Chapter 2 were presented in an oral presentation at the Association of Canadian Universities of Northern Studies conference in 2018, as well as a poster at the International Conference on High-Latitude Dust in 2017 and the Northern Studies Colloquium in 2016.

A wind tunnel study of Icelandic dust emission at varying wind speeds was performed to satisfy the objectives of Chapter 3. A series of laboratory experiments designed to examine the impact of a rain droplet on Icelandic dust in still air and

within a shearing flow follows in Chapter 4. Selected aspects of Chapter 4 were presented orally at the Northern Studies Colloquium in 2019 (3rd place award) and as a poster at the Canadian Chapter of the International Erosion Control conference, Ontario, as well as the International Conference on Aeolian Research, and finally, as an AGU virtual poster in 2018.

An LDA was used to measure the settling rate of Icelandic dust particles released in a fall column to satisfy the objectives of Chapter 5. Portions of this Chapter were presented as a poster at the A&WMA's 112th Annual International Conference & Exhibition in 2019 (3rd place award), and orally at International Conference on Aeolian Research in 2018, the International Arctic Change Conference, the A&WMA Paul G. Complin Memorial Scholarship ceremony and the Trent Northern Studies Colloquium in 2017.

Chapter 6 presents the conclusion of this dissertation, which provides a summary of the major findings in the core Chapters, addresses several limitations associated with the cutting-edge technologies and techniques used, and provides a set of recommendations for study.

Chapter 2

Particle-Scale Characterization of Icelandic Dust Sources: Volcanic Ash & Glaciogenic Sediments

2.1 Background

Iceland is a major high latitude (63−67 °N) dust source located just below the Arctic Circle (Fig. 2.1). Outwash plains (sandurs) that make up more than 20 % (>20,000 km^2) of the surficial geology contain sediments from both glaciofluvial systems and volcanic eruptions (Arnalds et al., 2001, 2016). The source regions for particulate matter (PM) within Iceland are extremely windy, sparsely vegetated, and have little to no gravel pavement to reduce wind erosion, thereby creating favourable conditions for dust storm generation (Bullard et al., 2016). An estimated 30.5−40.1 Tg of ultrafine tephra and glaciogenic dust are released annually (Arnalds et al., 2016). The magnitude and frequency of Icelandic dust storms (Bullard et al., 2016; Thorsteinsson et al., 2011) are projected to increase with global warming, as glacial retreat exposes new particulate sources (Cannone et al., 2008). Re-suspension of ash from the 2010 Eyjafjallajökull eruption is reported to have increased the frequency of dust storms (Bullard, 2013; Prospero et al., 2012; Thorsteinsson et al., 2011), and is linked to poor air quality and respiratory health problems in Reykjavík, where more than 80 % of the population resides (Carlsen et al., 2012; Thorsteinsson et al., 2011, Fig. 2.2d) (Fig. 2.2d). The deposition of this dust onto glacial surfaces is observed to reduce the ice albedo (Wittmann et al., 2017), and through positive feedback, exacerbate glacial retreat.

Icelandic particles contain a large proportion of amorphous glass and are porous, with dust coats cemented in their pores. It is widely speculated that the geometry and porosity of these particles influence their susceptibility to aeolian entrainment, transport and deposition, yet few in-situ measurements exist to either test this hypothesis or support the parameterization of dust dispersion models. In theory, particle size, porosity and surface area should all be interlinked,

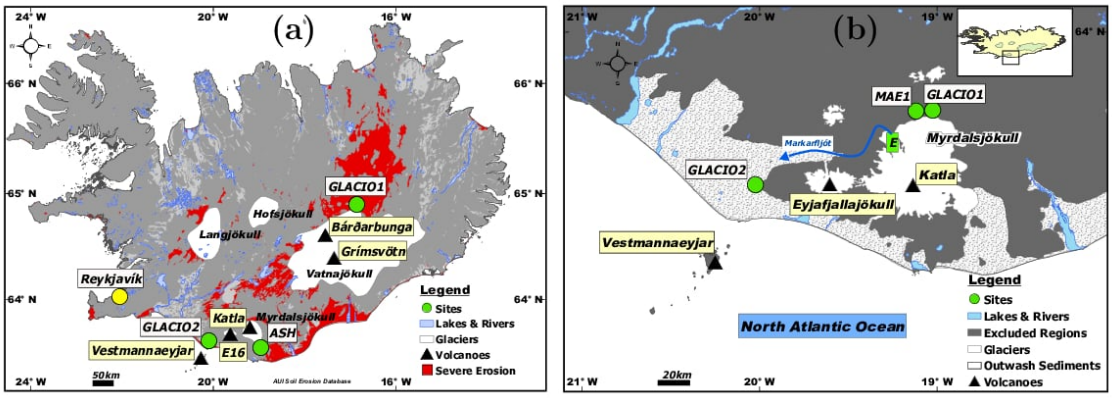

Figure 2.1: Sample collection sites located within severe dust regions in Iceland include (a) Álftaver (ash), Dyngjusandur (Glacio1), and Markarfljótsaurar (Glacio2) (Arnalds et al., 2001). (b) Glacio2 sediments are transported from Entujökull (E) located at the outlet of Katla glacier and Mýrdalsjökull to Markarfljótsaurar in southern Iceland. MAE1 sediments are fine particulate matter ($< 10\,\mu m$, MAE1) collected by Dagsson-Waldhauserova et al. (2014).

thereby affecting dust entrainment, dispersion and deposition rates (Riley, 2003; Robock, 2000) through variation in fluid drag and gravitational force. Indeed, Olsson et al. (2013) found that the specific surface areas of particles collected from ash plume fallout increase with growing distance from an eruption's caldera. Ash particles up to 70 µm in diameter from the Eyjafjallajökull eruption were detected by satellite over Europe, about 2000 km from their source (Stevenson et al., 2012), although Duce (1995) and Pye (1987) suggest that the largest expected diameter of a siliciclastic particle suspended in long range transport is much smaller at only 20 µm. However, Gislason et al. (2011, and references within) also associate such transport with high particle porosity, which no doubt is a key factor to consider when examining the transport of Icelandic dust particles.

Dust particles suspended in the atmospheric boundary layer (ABL) undergo

surface composition transformations that can lead to the formation of aggregates with altered geometries that further affect their aerodynamic behaviour and fall-out, by either dry or wet deposition. Relative humidity influences the amount of water adsorbed onto the surface of dust particles, thereby affecting hygroscopic growth that leads to aggregation, cloud condensation and wet deposition. Hence, modelling the fate of angular, porous particles in cold, humid environments presents numerous challenges that are not satisfied with the current model scheme parameterizations (Del Bello et al., 2018).

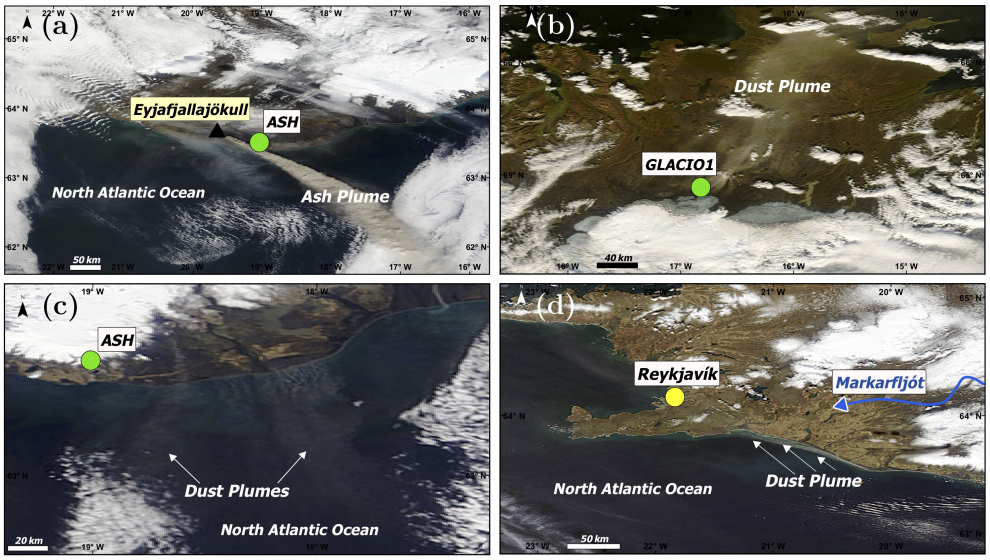

Figure 2.2: Satellite images show dust plumes from active regions in northeast and southern Iceland. (a) Dust plume from Eyjafjallajökull volcano blowing southeast towards the North Atlantic Ocean on May 8, 2010. (b) Large dust plume blowing ∼200 km from Dyngjusandur towards the Arctic on September 15, 2009. (c) Dust plume along the southern coast blowing from regions near Markarfljótsaurar towards the capital city of Reykjavík on April 28, 2007. (d) Multiple dust plumes blowing from the southern region towards the Northern Atlantic Ocean on April 23, 2017. All images are retrieved from NASA Goddard Space Flight Center, LANCE Rapid Response MODIS Terra satellite and labelled in ArcGIS.

A combination of analytical techniques is required to characterize the size, shape, density, porosity, surface area and mineralogy of dust particles. Laser diffraction techniques are commonly used to measure diameter, one of the most important particle properties affecting dust dynamics. However, they are suggested to be unreliable for aggregates and irregularly shaped particles $<10\,\mu m$ in diameter (Formenti et al., 2011; Horwell, 2007; Riley, 2003), as commonly found

in volcanic aerosols known to affect human health (Thorsteinsson et al., 2011). Scanning electron microscopy (SEM) can be used to obtain highly accurate, direct measurements down to nano-scale lengths, well below the lower limit for laser diffraction. However, the required image processing usually must be customized for the specific application, while the associated sample size is small relative to other techniques involving 'bulk' samples that are either suspended or circulated within a fluid.

Absorption of gas are widely used in material science, but have only recently been used to measure the density, porosity and surface area of volcanic particles (Alfano et al., 2011; Gislason et al., 2011; Olsson et al., 2013; Riley, 2003). These techniques generally are restricted to fine-grained powder, clay and porous rocks, while their reliability is dependent on the accessibility of pores within the material. Dust samples have pore diameters ranging from nano to micro scale with complex geometries, so that porosity is difficult to quantify. Specific surface area (m^2g^{-1}) can be measured using the Brunauer, Emmett, and Teller (BET) nitrogen absorption technique devised by Brunauer et al. (1938), which accommodates pore sizes ranging from 2 nm up to 300 nm. Mercury intrusion porosimetry is a widely practiced technique used to measure pore size distribution, inclusive of the pore spaces within (intraparticle) and voids between (interparticle) particles, at a resolution of 3−950 nm. In comparison, the narrowest of pores can be accessed using helium pycnometry, perhaps providing a more precise measurement of the true particle density. To distinguish between the intraparticle pores and interparticle voids within a size distribution poses a considerable challenge because the associated diameters can overlap significantly (Y. León, 1998). An SEM equipped with a focused ion beam (FIB-SEM) can be used to mill miniscule particles in order to obtain high-resolution micrographs of their internal pore structure (Chalmers

et al., 2012). However, this process is expensive and time-consuming with the milling of a single particle requiring up to hours, depending on the size of its cross-sectional area and speed of milling. Nonetheless without an accurate measure of porosity, the particle density associated with a given volcanic dust source will either be under- or overestimated, thereby introducing some degree of error in models of dust dispersion and deposition.

Hence, the three principal objectives of this study can be summarized as follows: (i) to evaluate the mineralogical properties of Icelandic dust, (ii) to explore and compare the performance of some cutting-edge technologies in measuring the complex morphology of basaltic aerosols, and (iii) to provide a coarse approximation of the dynamical effects of this morphology, relative to a solid glass sphere.

2.2 Sample Site

Samples were collected from three Icelandic source regions known to emit large amounts of dust, inclusive of Eyjafjallajökull Ash and Glaciogenic sediments (Fig. 2.1a).

The Ash deposits were obtained in Vík, approximately 5 years after the Eyjafjallajökull eruption in 2010 (Fig. 2.1a). Over the course of a 39-day event, approximately 10 million tonnes of fine particles ($2.8<d<28\,\mu m$) were ejected through the troposphere and into the stratosphere (Gislason, Hassenkam, Nedel, Bovet, Eiriksdottir, Alfredsson, and Sigfusson, 2011; Schumann et al., 2011; Stohl et al., 2011, and references within). The prevailing atmospheric conditions transported Eyjafjallajökull Ash directly toward Europe, causing the airspace to shut down for up to 7 consecutive days (Gislason et al., 2011; Horwell et al., 2013). During the eruption, dispersion model performance was undermined by a dearth of in-

formation concerning various particle parameters relating to size, shape, density, and mineralogy, as needed to attain suitable accuracy in calculating the dust deposition rate (Bagheri et al., 2015; Johnson et al., 2012; Leadbetter et al., 2012; Wiegner et al., 2012).

Glaciogenic sediments were collected from Dyngjusandur (Glacio1) located north of Vatnajökull glacier in northeast Iceland, and from Markarfljótsaurar (Glacio2) located west of Mýrdalsjökull and Eyjafjallajökull glaciers in southern Iceland (Fig. 2.1a). Dyngjusandur is the largest and most active dust region in Iceland (Arnalds et al., 2001; Baratoux et al., 2011), transporting particles toward the North Atlantic Ocean (Dagsson-Waldhauserova et al., 2014) and onto Greenland glaciers (Drab et al., 2002), where they may influence marine ecosystems and climate (Fig. 2.2b). The dust source at Markarfljótsaurar originates from frequent catastrophic meltwater floods (jökulhlaup) on the Markarfljöt river that are triggered by the interactions between the Mýrdalsjökull glacier and Katla volcano (Fig. 2.1b). Prevailing wind conditions occasionally direct the dust emitted from Markarfljótsaurar towards Reykjavík (Thorsteinsson et al., 2011, Fig. 2.1b) where the associated poor air quality has increased respiratory health problems among its residents (Carlsen et al., 2012; Thorsteinsson et al., 2011).

2.3 Methodology

Samples from each of the three sediments were individually (i) wet sieved in order to isolate the dust particles, (ii) dried for 24 hrs at 105 °C, (iii) mixed vigorously to homogenize the sample and reduce particle aggregation, and finally, (iv) stored inside a desiccator pending further analyses. The particle-size distribution of each sample was measured using a Horiba-Partica LA-950 V2 particle-size analyzer,

verifying that 90 % of the particles collected had a diameter $\leq$50 µm. Size distributions measured when calgon was added to the mixture as a dispersant were not found to be statistically different (when p<0.001) from those obtained using distilled water only.

Table 2.1: Overview of the different methods and techniques used to determine the physical and mineralogical characteristics of Icelandic dust particles. The methods used are optical (laser diffraction (LD)), electron (scanning electron microscopy (SEM)), gas absorption (helium (H), nitrogen (N_2) and mercury (Hg)) and analytical (X-ray diffraction (XRD), X-ray fluorescence (XRF), JEOL JXA8230 5-WDS electron microprobe (MProbe)).

Particle characteristics		Definition	Methodology							
			Optical	Electron	Gas adsorption			Analytical		
Morphology	Type		SEM	LD	N_2	He	Hg	XRF	XRD	EMPA
Diameter (m)	Arithmetic (d_a)	Table 2.2	✓	✓						
	Geometric (d_g)									
Shape	Sphericity (φ)									
Density (g/cm^3)	Bulk (ρ_b)	m/V_b		✓			✓			
	Skeletal (Mineral) (ρ_s)	m/V_s		✓		✓			✓	✓
Porosity (%)	Total (ϵ_t)	$100(1-(\rho_{Hg}/\rho_{He}))$					✓			
	Interparticle (ϵ_{inter})	$100(V_{inter}/V_{ps})$					✓			
	Intraparticle (ϵ_{intra})	$100(V_{tp}-V_{inter})/V_b$	✓				✓			
surface	Geometric (A_{geo})			✓						
	Specific (A_{surf})				✓					
Area (m^2/g)	Cross section (A_s)	Table 2.2	✓							
Hardness		see text							✓	✓
Geochemistry		see text						✓		
Mineralogy		see text							✓	✓

2.3.1 Particle imaging

In preparation for imaging with a Hitachi S4500 field emission scanning electron microscope operating at an accelerating voltage of 20 kV, sub-samples were first spread onto separate carbon conductive adhesive tabs mounted on aluminum stubs and then coated with 5 nm osmium to reduce charging effects. The SEM images (2351×595 pixels, $300 \times$ magnification) capture a wide range of particle size, down to very fine-grained Ash (d<0.1 μm), which cannot be measured reliably using laser diffraction. An unknown amount of bias may arise; however, from using only very small subsamples of particles to measure the particle size distribution.

A custom designed algorithm was written using Matlab image-processing software to analyze the particle image morphology. The image contrast was first adjusted to define clearly the boundary of each particle so that it could be traced (Fig. 2.3a and c). Particles either intersecting the edges of the camera frame or overlapping other particles were eliminated from the analysis to reduce error. A total of 2500 discrete (non-aggregated) particle images were analyzed for each of the three Icelandic samples, providing measurements of both 1D and 2D attributes. These included the particle perimeter (P), filled area (A_s), and the diameters of the smallest circumscribed and largest inscribed circles (Fig. 2.3c). The largest inscribed and smallest circumscribed circles correspond to the shortest (S) and longest (L) axes, respectively (Bagheri et al., 2015, Fig. 2.3c). The intermediate (I) axis is approximated by S because the SEM images were taken along a single projection of a particle. Other morphological indices were calculated from these fundamental measurements, as for example, the arithmetic $[(L + I + S)/3]$ and geometric $[\sqrt[3]{LIS}]$ means of the axis lengths, which are approximated as the arithmetic and geometric diameters, respectively. Sphericity ($\varphi = (4\pi A_s)/P^2$) is an index of the degree to which the shape of a given particle is approximated by that

of a true sphere, which by definition has a value of 1. Increasing particle angularity is represented by progressively smaller values for this index. Cox's index is used when working with non-vesicular particles (Cox, 1927) and Riley's index for vesicular ones (Riley, 1941). Finally, the surface areas of idealized particles having varied geometries (e.g., cylinder, cube, disk, ellipsoid and sphere) were calculated from the axis lengths measured in the particle images.

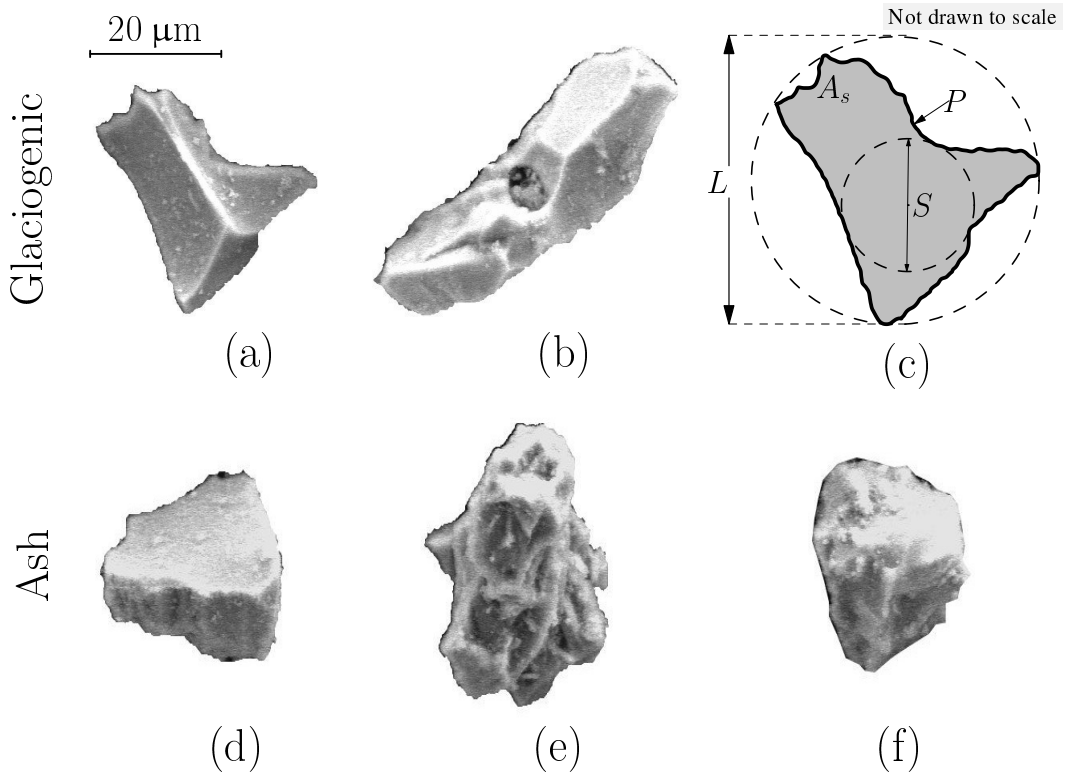

Figure 2.3: Representative SEM images of particles from the glaciogenic (a - c) and volcanic Ash (d - f) samples, only particles a) and d) are non-vesicular. A schematic of the 1 and 2D attributes defining a particle along a single projection is shown in (a), inclusive of the filled cross-sectional area (A_s) and perimeter (P). Also shown are the diameters of the smallest circumscribed circle and largest inscribed circle called the longest (L) and shortest (S) dimensions.

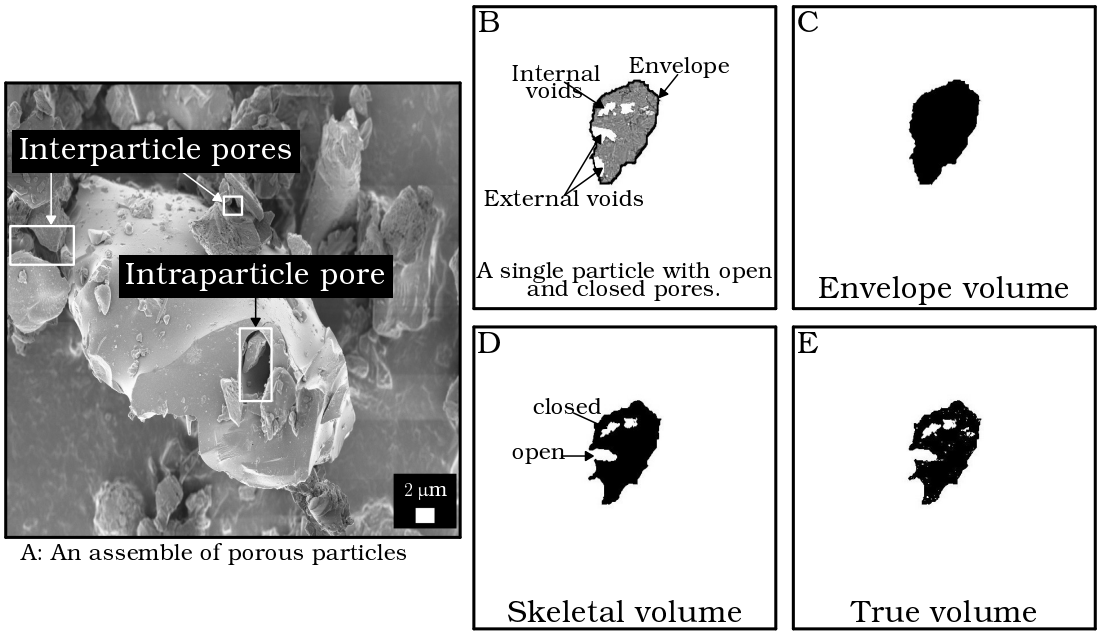

Figure 2.4: A description of the pores volume and voids that contributes to the porosity (ϵ).

Selected particles with an amorphous, porous surface were milled with nanometer-scale precision using a focused ion (gallium) beam (FIB) to reveal their internal structure. After milling, high-resolution images were collected using a LEO (Zeiss) 1540 XB field emission-scanning electron microscope (FE-SEM) equipped with a secondary electron detector set at an operating voltage of 1.0 kV. Matlab image-processing software then was used to measure the pore size distribution within one milled particle from each of the three Icelandic samples, as required to calculate the particle density (ρ_p) and porosity (ϵ). The particle density ($(A_s\rho_s)/A_b$) was calculated by multiplying the skeletal density (ρ_s) obtained using helium pycnometry by the ratio of the skeletal area (A_s) to the bulk area (A_b) within the cross section of the milled particle. The skeletal density calculation omits unexposed and subtle internal pore structures, which may underestimate the total pore volume. The solid area (A_s) of the milled particle was calculated from the

difference between the bulk area and total pore area (A_s=A_b−A_p), where A_p is estimated from the geometric diameter (d_g) of all the pore spaces identified along the cross-section of the milled particle. A_b is estimated from the geometric diameter of the milled particle cross section, which is inclusive of all pores and solid. A_p is calculated for either a sphere or an ellipsoid when φ is either >0.7 or <0.7, respectively.

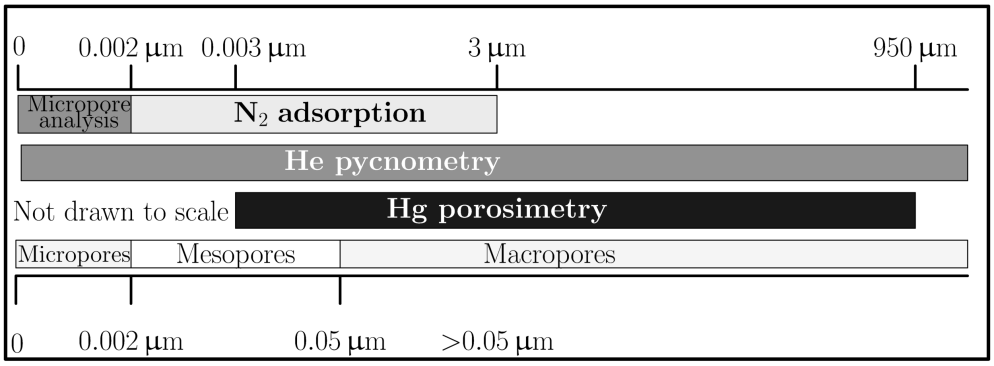

Figure 2.5: Pore-size ranges accessible by different analytical techniques used in the present study. The sizes are referred to as either the diameter of the pore spaces or width of slit shaped pores within and voids between the particles (IUPAC, 1994).

2.3.2 Density, surface area and porosity

Helium, nitrogen and mercury intrusion methods were used primarily to measure skeletal density (ρ_s), specific surface area (A_{surf}) and porosity (ϵ) for each of the three Icelandic samples, respectively (Table 2.1). Prior to performing each of these measurements, the Icelandic samples were outgassed for 24 hrs to remove any adsorbed gases, moisture, and volatile species. The pores within any given particle can be either open or closed (Fig. 2.4d), but together, they constitute the intraparticle pores (Fig. 2.5). Open pores are 3D spaces that have connections with

the external surface and are formed within and between the particles, whereas, closed pores are isolated from the outer surface and may not be accessible by gas absorption. Interparticle voids consist only of the void spaces between particles and are influenced by packing of the bulk sample (Fig. 2.5a). As summarized in Fig. 2.4, the intrusion techniques addressed herein vary considerably with regard to the detectable range in pore size.

The skeletal density (ρ_s) of a given sample of particles containing open micropores is best measured using a helium pycnometer. The technique is based on the principle that pressure decreases when a fixed volume of helium is allowed to expand into a confined space, inclusive of intraparticle pores and interparticle voids (Fig. 2.5). It can neither be used to measure pore size, nor distinguish between the proportionate amounts of intraparticle pores versus interparticle voids. It can only measure the total pore volume of the bulk sample; however, inert helium (He) gas is able to penetrate the smallest pore diameters down to 0.2 nm (Fig. 2.4) so that the measurement is highly accurate. When deducted from the bulk volume of the sample, the true skeletal volume (V_s) is obtained for the solid particles, excluding the volume of all intruded closed, open intraparticle pores and interparticle voids detected. Six replicate measurements of the skeletal density were obtained for each of the samples using two separate instruments on the helium gas absorption technique: (1) Micromeritics helium pycnometer and (2) helium picnometer. Three replicate measurements of the particle densities were also obtained using basic water pycnometry test.

In comparison, mercury porosimetry uses high-pressure intrusion to detect pore diameters ranging from 3 nm to 950 μm (IUPAC, 1994, and references within Fig. 2.5). Only one measurement of the distribution of pore size contained within and between the particles was obtained for each of the three wet-sieved samples:

Ash, Glacio1 and Glacio2. The minimal pore diameter limit of 3 nm is within the mesopore range (Fig. 2.5). Liquid mercury cannot intrude micropores unless the applied pressure is sufficient to rupture the pore wall, thereby increasing the pore size and access to the pore. Under high pressure, the mercury forced into small pores can cause the bulk sample to compress, especially when the sample contains closed pores, thereby resulting in the detection of too many large volumes of small to medium pores (Webb and Orr, 1997). From this method, the sample porosity (ϵ) can be determined as the percentage ratio of the total pore volume (V_p) to the bulk volume (V_b). Herein, V_p is represented as the total pore volume filled with mercury up to a maximum pressure of 61000 PSI, and includes the intraparticle (V_{intra}) and interparticle (V_{inter}) pore volumes (Table 2.1).

Using the nitrogen absorption technique (Brunauer, 1994), a BET Gemini VII 2390 analyzer was used to measure the surface area of six (replicate) 2 g subsamples of dust isolated from each Icelandic test sample. This technique is able to detect the pore spaces between 2 nm to 300 µm in diameter (mesopore to macropore; Fig. 2.5). Micropores are not detected. The specific surface area then is obtained by dividing the measurement by the sample mass. Sample preparation required the removal of any organic matter, achieved by placing a small portion of the subsamples inside a furnace at $400\,^{\circ}C$ for 24 hrs. Only trace amounts of organic matter were identified in some instances and none in the remainder (0.1 %). The remainder of the subsamples were then outgassed for another 24 hrs at $30\,^{\circ}C$ to remove any adsorbed gases, moisture and volatile species just before the nitrogen absorption measurements were made. The BET total surface area measurement, which accounts for both the external and internal void space, is based on measurement of the varied weight of absorbed nitrogen as determined by its relative pressure. While gas adsorption techniques are mainly used in material

science, they have recently been applied to the analysis of volcanic originated particles with good success (e.g., Alfano et al., 2011; Bagheri et al., 2016; Gislason et al., 2011; Olsson et al., 2013; Riley, 2003). The subsamples used to perform the BET surface area measurements were discarded after each experiment.

2.3.3 Mineral and phase compositions

Small samples (2 g) were mounted onto glass slides for X-ray diffraction (XRD) in order to determine their mineralogical composition. Fine dust particles were needed to achieve good signal-to-noise ratios and minimize preferred particle orientation. The device, a Philips PWR1830 X-ray diffractometer, was operated with copper (Cu) Kα radiation (1.54060 Å) at an accelerating voltage of 10 kV and beam current of 10 mA coupled with a nickel (Ni) filter between the X-ray source. For comparison with the helium and mercury intrusion methods, skeletal density was calculated from the sum of the weighted density based on the proportion by weight of the minerals detected and their known (ideal) density. The particle hardness was estimated in a similar way.

The mineral surface phase compositions of the particles were also quantified using a JEOL JXA-8230 electron probe micro-analyzer (EMPA) operated with a 5 wavelength dispersive spectroscopy (WDS). Prior to analysis, samples were first embedded in epoxy molds to create polished thin sections, following the standard procedure outlined in Hillier and Marshall (1988). A beam diameter of 1 µm with a current of 20 nA and accelerating voltage of 15 kV was used to examine polished sections of the particles without conductive coatings. The phase composition was determined from a combination of analyses, inclusive of phase mapping and SEM imaging of the thin sections. The EMPA (point analysis) and XRD (bulk analysis) methods were used to determine the homogeneity of the samples. The

weight percentage of each phase identified was determined based upon the total exposed surface (cross-sectional area) of each particle in the frame of reference of the microscope. The skeletal density for the samples was calculated from the weight percentages, similar to the XRD results.

Finally, the geochemical composition (major and minor elements) of the three Icelandic bulk samples was determined using a PW2404 PANalytical X-ray fluorescence (XRF) spectrometer. Sample preparation required the extraction of aliquots (∼6 g) of dried particles from each sample, which were then placed in an aluminum cap and compressed to form a pellet.

2.4 Results & Discussion

2.4.1 Geochemistry and mineralogy

The geochemical composition of the samples showed that the Ash is trachy-andesite while Glacio1 and Glacio2 are basalts with 53.3, 47.6 and 47.5 $wt.\%$ of SiO_2. The major oxides detected from the XRF analyses are compared in Fig. 2.6 to those identified for Ash samples collected from similar sites within Iceland. Although the Eyjafjallajökull Ash examined in this study was collected ∼5 years after the eruption, the relative abundance of oxides is essentially identical to that reported by Gislason et al. (2011) for samples collected during the event (Fig. 2.6a). Particle diameter and the location of the collection site within Dyngjusandur appear not to affect the phase composition, given the general similarity evident between the abundance values measured by Baratoux et al. (2011) for sand particles and those reported herein for dust particles isolated by wet sieving (Fig. 2.6b). However, the proportion of Al_2O_3 in the dust is marginally lower than for all five samples listed in the earlier publication. The similarity shown

in (Fig. 2.6c) between the major oxides detected in dust samples collected from Markarfljótsaurar (Glacio2) and Mælifellssandur (MAE1) is suggestive of similar source materials from Katla and Mýrdalsjökull (Fig. 2.1b), although Mælifellssandur is located near Dyngjusandur.

The EMPA and XRD results listed in Table 2.2 demonstrate good agreement with regard to the mineral compositions identified for the volcanic Ash and glacio-fluvial sediments. The Eyjafjallajökull Ash is mainly comprised of near equal proportions of plagioclase and amorphous glass ($\sim 40\, wt.\%$), pyroxene ($\sim 10\, wt.\%$), and minor amounts of sanidine and olivine. This composition is consistent with the phase materials reported for Eyjafjallajökull Ash in the study of Gislason et al. (2011). In contrast, the Glacio-fluvial sediments contain a great deal more glass, up to 75 % for Glacio2, and proportionately less plagioclase ($20 - 25\, wt.\%$).

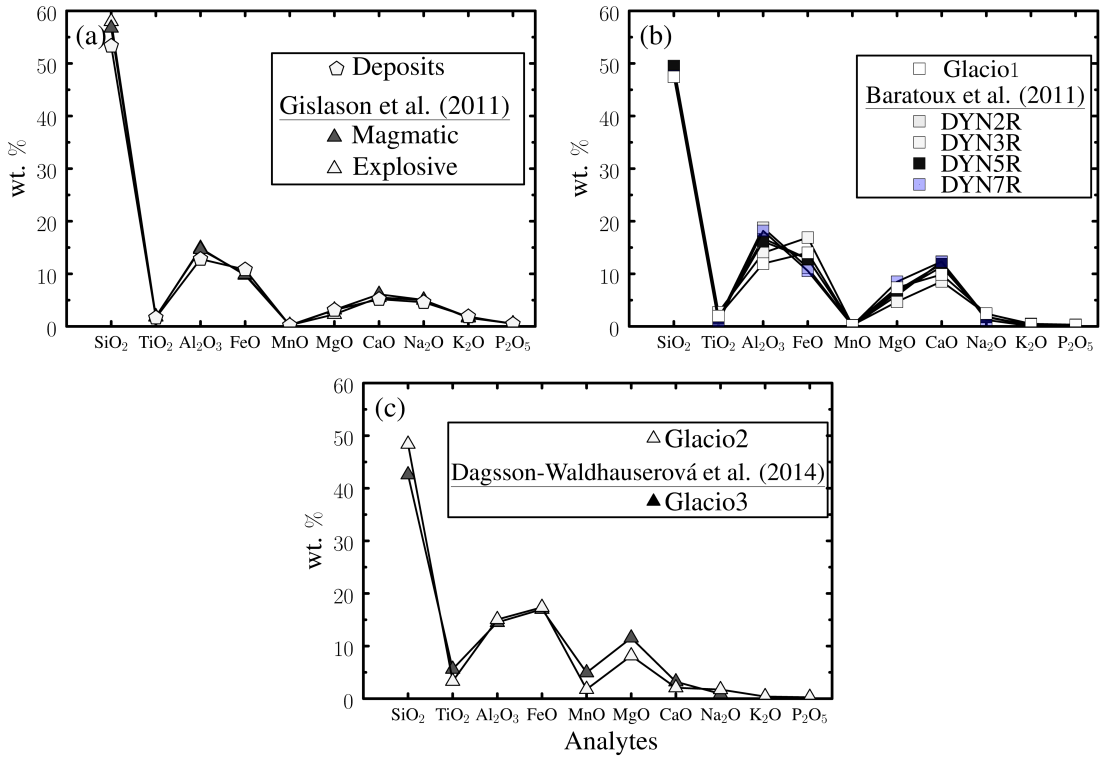

Figure 2.6: A comparison of major oxides revealed for the samples used in this study with similar samples used in other published studies. (a) Major oxides revealed for the 2010 Eyjafjallajökull ash deposits collected 5 years after the eruption ended while the other Ash samples were collected from explosive and magmatic sources during the same eruption (Gislason et al., 2011). (b) Major oxides revealed for Dyngjusandur samples from the study of Baratoux et al. (2011, DYN2R, DYN3R, DYN5R, DYN7R, average sand particles), and Glacio1 also collected in Dyngjusandur. (c) Major oxides revealed for Markarfljótsaurar (Glacio2) and Mælifellssandur (MAE1) samples collected from different outlets of Katla glacier and Mýrdalsjökull (Fig. 2.1b).

Baratoux et al. (2011) also identify glass, pyroxene, olivine and plagioclase within thin sections of rock and sand obtained from Dyngjusandur, the origin of the Glacio1 dust sample collected for this study. The comparatively high pro-

portion of glass ($80-90\,wt.\%$) reported by Baratoux et al. (2011) for particles ranging from $100-150\,\mu m$ could arise from the coarser mean diameter. The large abundance of calcite ($11\,wt.\%$) detected in Glacio1 appears to be unique to this particular sample.

Table 2.2 also includes a summary of the mineralogy of fine particulate matter ($<10\,\mu m$, MAE1) collected by Dagsson-Waldhauserova et al. (2014) from Mælifellssandur. The phase composition is notably similar to that for Glacio2, with particles from both Glaciogenic dust sources predominantly composed of amorphous glass ($>70\,wt.\%$) and plagioclase ($>10\,wt.\%$), while the remaining minor fractions are slightly different in proportion. The Markarfljótsaurar (Glacio2) and Mælifellssandur (MAE1) deposits are supplied with sediments from the same origin, Mýrdalsjökull glacier and Katla volcano (Fig. 2.1b), but transported by separate outwash systems.

To summarize, these findings are consistent with earlier work (Arnalds et al., 2016; Baratoux et al., 2011; Dagsson-Waldhauserová et al., 2015; Gislason et al., 2011), which demonstrates that the geochemical and mineralogical composition of Icelandic dust is dependent on the particulate source. Such connections may be useful for the reconstruction of dust transport pathways.

Table 2.2: Summary of the phase classes ($wt.\,\%$) for the dust particulates from Vík (Eyjafjallajökull Ash), Dyngjusandur (Glacio1) and Markarfljótsaurar (Glacio2) dust measured using JEOL JXA8230 5-WDS Electron Microprobe and XRD spectrometer. A summary of the estimated quantities of phase materials for Mælifellssandur (MAE1) was obtained from the study of Dagsson-Waldhauserova et al. (2014).

Methods	**EMPA**			**XRD**			
Phase	**Ash**	**Glacio1**	**Glacio2**	**Ash**	**Glacio1**	**Glacio2**	**MAE1**
Volcanic Glass	34.2	51.8	74.1	40.0	58.4	71.2	78.2
Plagioclase	45.5	17.0	24.5	36.5	15.8	19.9	12.2
Pyroxene	10.5	17.2		13.7	14.8	0.9	4.6
Sanidine	5.2		0.1	6.4		6.7	
Olivine	3.0	0.9	0.1		0.1	0.6	1.8
Pyrite	0.7		0.3				
Ilmenite	0.8	1.5	1.0				
Apatite	0.2						
Quartz (SiO_2)				3.3		1.1	0.8
Calcite		11.7			11.0		
Zeolite							1.1
Magnetite							0.7

2.4.2 Particle size (PSD) and shape distributions

Laser diffraction (Horiba) measurements of the three wet-sieved Icelandic samples show a range in particle diameter between 0.4 µm and 89 µm, with the medians of the distributions for each sub-sample varying from 12−25 µm (Fig. 2.7). The PSD for the Eyjafjallajökull Ash is negatively skewed with >80 % of the particles lying within the clay- and silt-size ranges (<20 µm; Fig. 2.7a). The distribution for Glacio1 is unimodal (Fig. 2.7b), whereas that for Glacio2 is bimodal with peaks at 2 µm and 30 µm (Fig. 2.7c) and a greater proportion of the sample lying within the silt-size range.

The Horiba provides an indirect measurement of a given PSD based on a population of particles that is many orders of magnitude larger in number than can be sampled via image analysis. However, SEM images do allow for direct and highly accurate measurement of the length, shape and surface texture characteristics of discrete particles down to nanometer scale, as identified by the closed boundary of each viewed in 2D. As a comparison, measurements of the distribution of geometric diameter (d_g), based on a sample size of 2500 particle images for each source of dust, are added to Fig. 2.7. Notably, the median particle diameters measured via SEM analysis are approximately $2-3\times$ smaller than those provided from laser diffraction, while the range also is narrower, reflective of better sorting. Glacio1 demonstrates the best agreement among the measurement approaches, with only a $2\,\mu$m difference in the median values. Few particles smaller than $3-4$ microns in diameter are represented in the SEM data, as these generally appear as *'dust coats'* on the surface of larger ones and are difficult to identify and isolate.

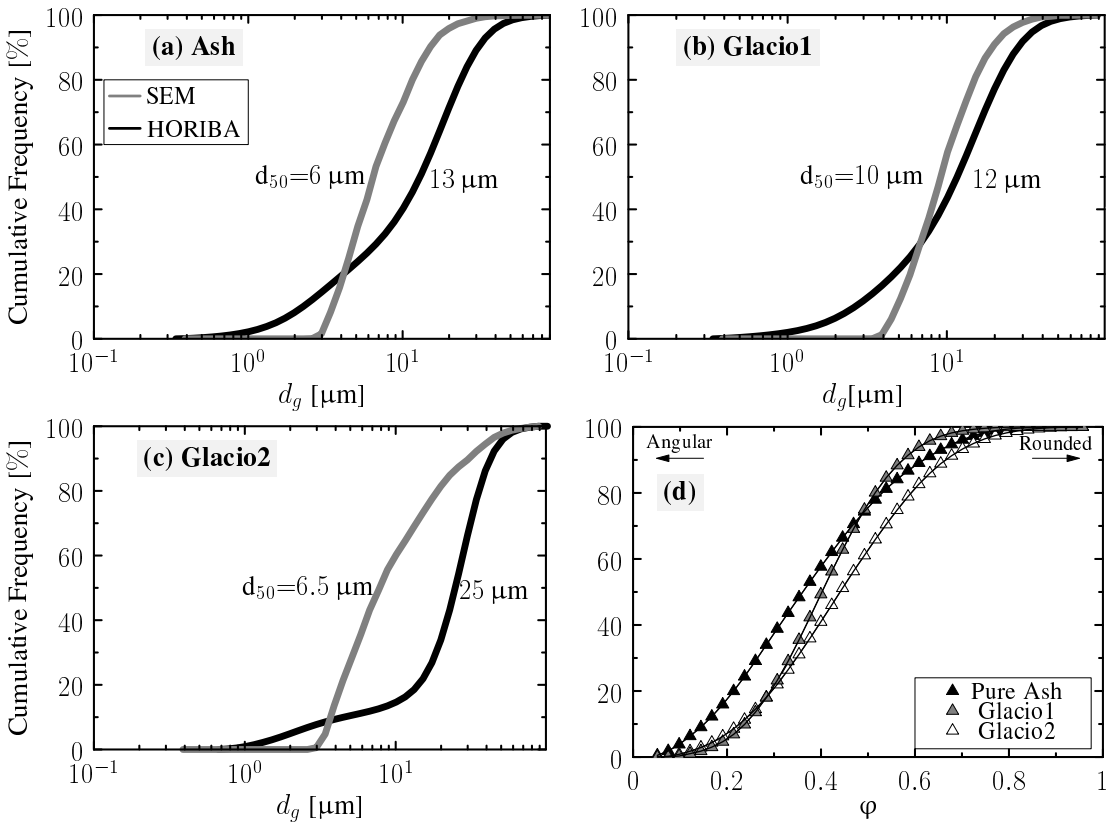

Figure 2.7: (a - c) Particle-size distribution of the wet-sieved portions of ash, Glacio1 and Glacio2 obtained from the Horiba (black) and SEM (gray) image analyses with median particle size, d_{50}. (d) The cumulative sphericity (φ) distributions derived from SEM for all samples.

The Horiba provides an indirect measurement of particle size based on a relatively large sample size in comparison to the analysis of SEM images. The analysis of SEM images provides a more accurate and direct measure that accounts for distinct particle shapes along a single projection, although the measurements are only based on a relatively small sample size. In this section, particle size and shape are defined by the geometric diameter (d_g) and sphericity (φ), respectively.

Fig. 2.7d provides a comparison of the distributions of particle sphericity (φ, dimensionless), confirming that these Icelandic fines have a non-ideal or highly

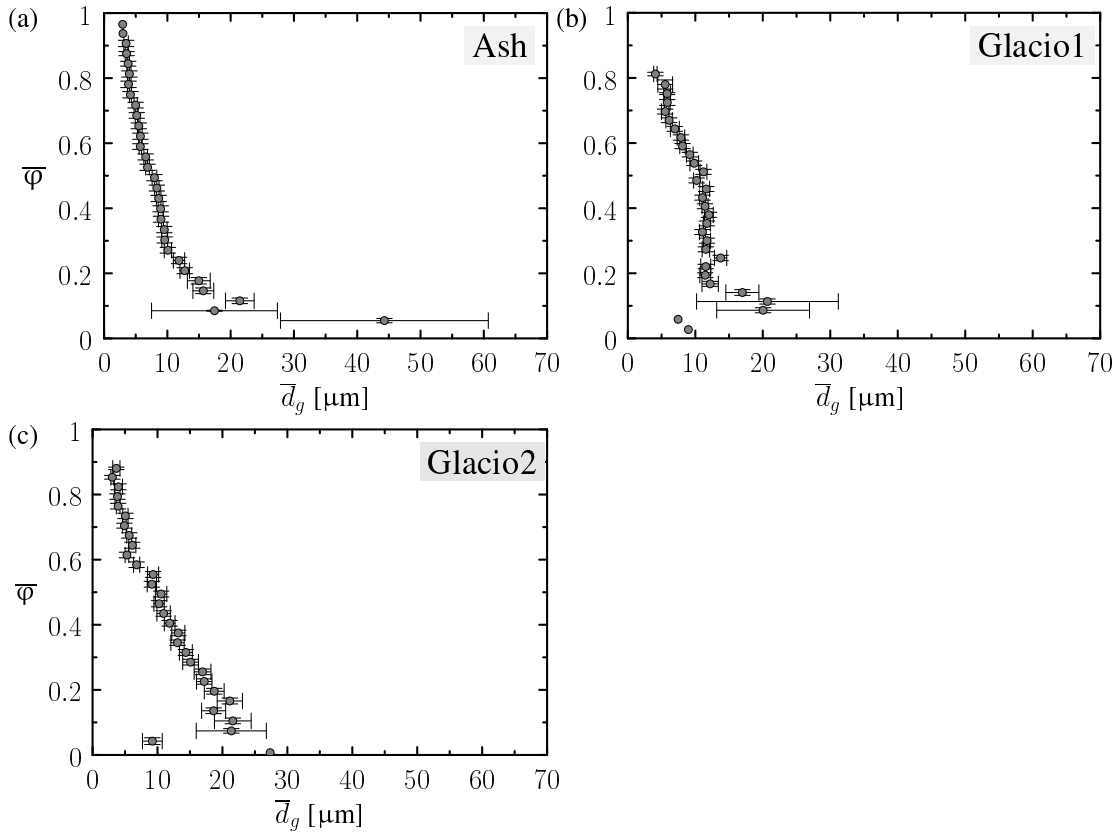

Figure 2.8: A relationship between the averaged sphericity ($\overline{\varphi}$) and particle diameter $\overline{d_g}$ for 2500 individual Icelandic particles with relatively low standard errors obtained from MATLAB image analysis.

irregular shape. The modal values for the Eyjafjallajökull Ash and glacial flour, Glacio1 and Glacio2, are given as 0.45, 0.38 and 0.36, respectively. On the whole, the Ash particles appear to be slightly more rounded than the Glaciogenic particles. Considerable overlap exists in the tails of the distributions, particularly between the Ash and Glacio1 for φ<0.3. Values of φ are binned in (Fig. 2.8) to determine whether or not particle diameter and shape are correlated. Indeed it would appear that in very general terms, increasing sphericity is associated with progressively smaller particle size, represented as $\overline{d_g}$. However, no relationship was found when all 2500 paired values were plotted for each sample.

2.4.3 Qualitative Observations of Morphology from Imaging

The morphometrics presented in the previous section provide a useful first approximation of the particle size and shape properties characterizing the Icelandic dust samples, as required for example, in dust entrainment and dispersion modelling. In many respects, however, these indices are inadequate representations of the complex but highly relevant particle structure observed in SEM images, like that shown in Fig. 2.9. Within the same particle, only 20 μm in diameter, both crystalline and amorphous glass is apparent. The planar facets of the crystalline phase are distinctively smooth and solid, as compared to the fine-scale roughness and high porosity of the amorphous portion. Nano-sized particles, and a $1-2$ μm fragment of high angularity and distinctively different mineralogy, adhere to the surface.

Other examples of particle images from each of the Icelandic sources are provided in Fig. 2.9, with each image repeated at two levels of increased magnification. For the most part, the particle surfaces of the Ash and both glacio-fluvial sediments can best be described as highly complex, with substantial variation in roughness and porosity that can significantly increase the surface area measured via gas adsorption techniques. The volcanic Ash particle (Fig. 2.9 a - c) bears a particularly intricate external structure that appears fragile and could be susceptible to spall. In comparison, a sparse coat of nano-scale flakes is apparent on the surface of the particle selected from Glacio1. Relative to the other examples in this figure, this particle appears smooth and crystalline in its general form (Fig. 2.9 d - f). SEM images of another Glaciogenic particle from Glacio2 show that it is dotted with a dense network of distinctive surface pores (Fig. 2.9 g -

i). These appear to be nested in form and possess particularly delicate sidewalls. Likewise, nanoscale shards of dust appear to be cemented to the walls of the pore sacks within the sand particle image captured for Glacio1 (Fig. 2.9 j - l). Field workers studying dust transport in Iceland speculate that these dust coats, as well as other frail surface structures, may be fractured and released with repeated inter-particle collisions that occur during active sand transport (saltation) over several kilometers of barren surface.

The Focus ion beam scanning electron microscopic (FIB-SEM) images of a milled volcanic Ash particle, 65 μm in diameter, capture the presence of three large internal macropores near the center of its cross-section, and fewer fine, irregular-shaped pores (Fig. 2.10a). Two of the three large macropores intersect, their diameters ranging from 8 μm to 10 μm. The macropores are relatively circular, have well-defined edges, and contain crystal structure formations (Fig. 2.10b-c). Fine pores can also be identified near the edge of the milled cross-section with diameters ranging from 0.6 μm to 1.8 μm (Fig. 2.10b). In comparison, the FIB-SEM images of a milled Glaciogenic silt-size particle, 35 μm in diameter, display finer internal macropores, as well as mesopores of irregular shape (Fig. 2.11). The pore diameters range from 0.02 μm to 1.25 μm, smaller than those identified for the milled Ash particle. The distribution of the internal pore diameters within the cross-section is positively skewed (Fig. 2.11c), though fine macropores clearly dominate. No micropores were detectable in the SEM images of the milled particles. Internal pores influence measurements of pore volume and surface area that rely on the adsorption of certain inert gases, as they are less accessible than surface pores, if not altogether unreachable in the case of closed pores.

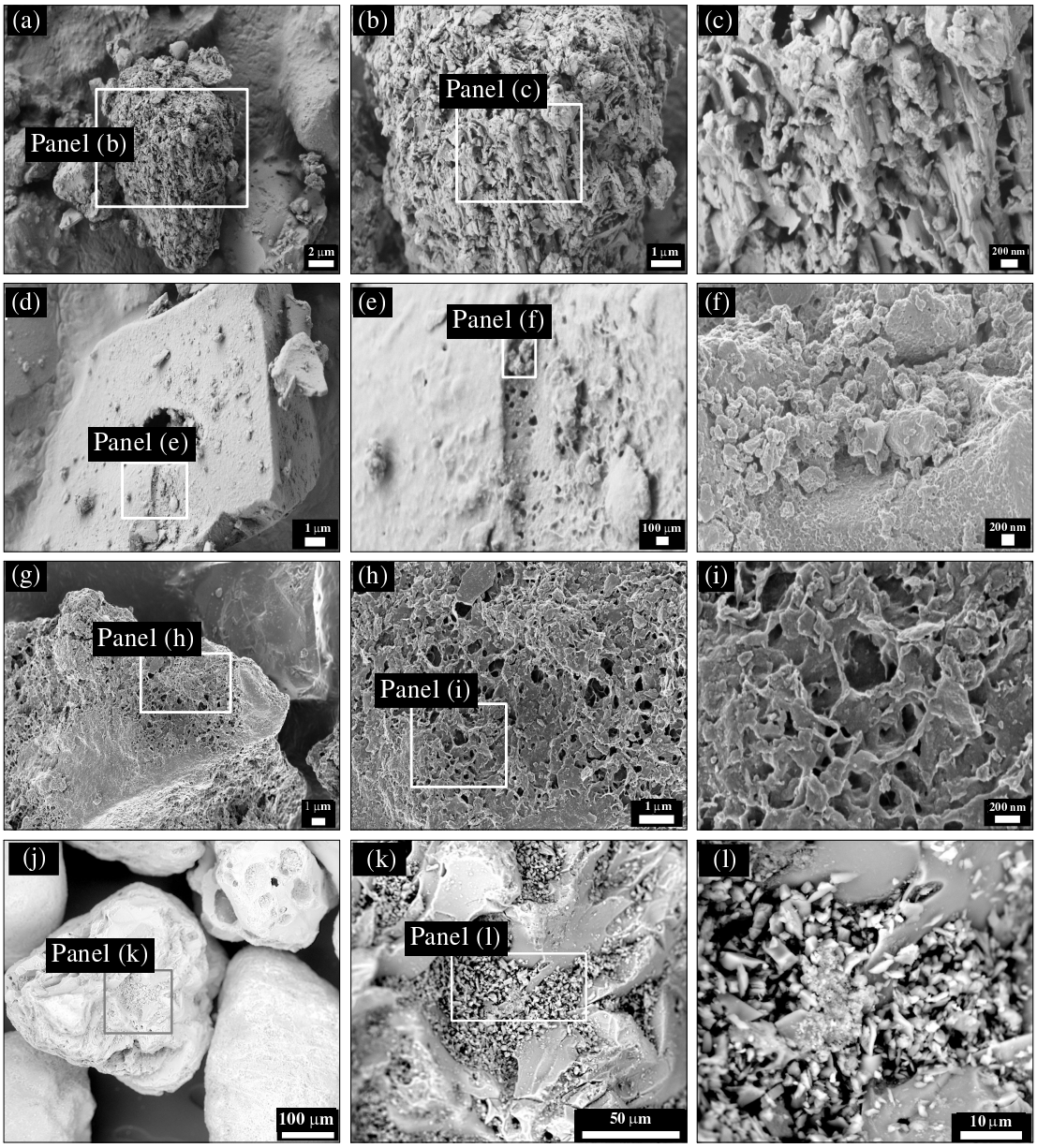

Figure 2.9: Scanning electron micrographs of external intrapores on selected particles within the Ash (a - c), Glacio1 (d - f) and Glacio2 (g - i) samples, as well as sand-size Glaciogenic particles, that reveal angular glass-like dust coats in the sacks of the pores (j - l).

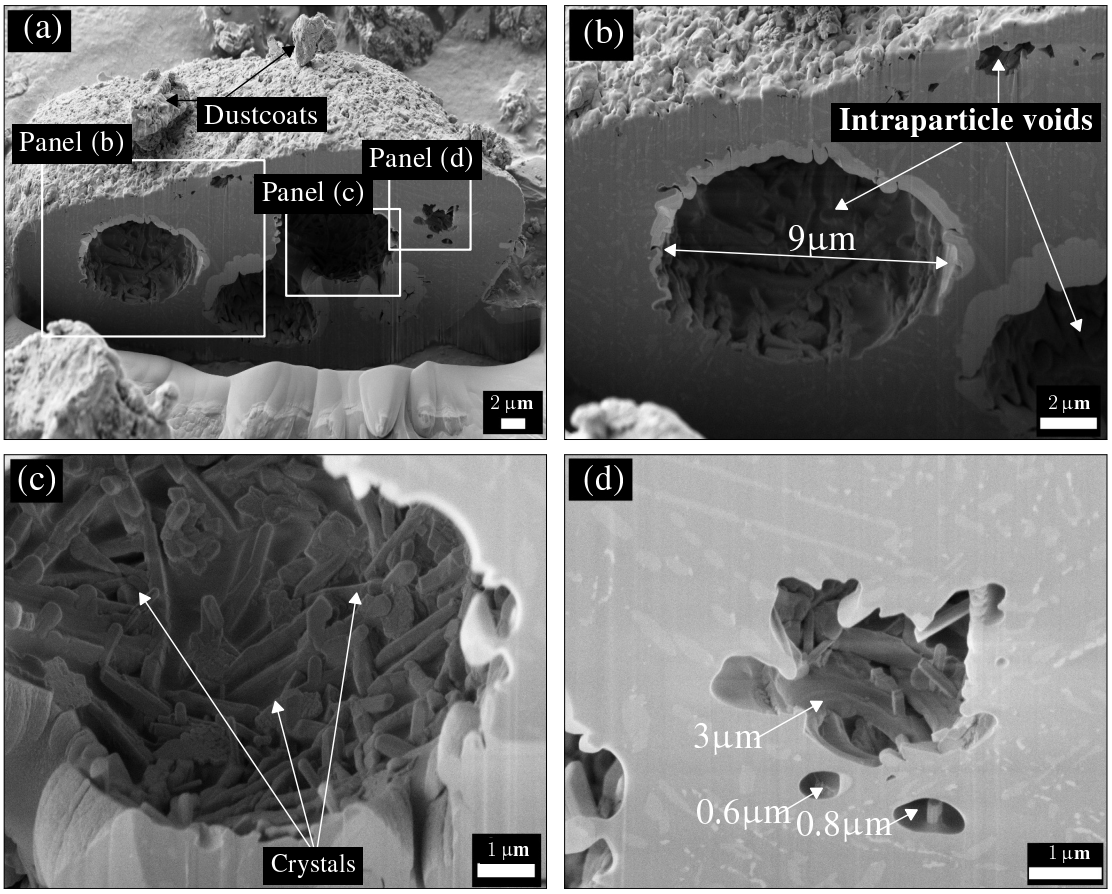

Figure 2.10: Focus ion beam scanning electron microscopic (FIB-SEM) images of the internal structure of a 65 µm Eyjafjallajökull Ash particle after focused ion beam milling. Macropores located within all panel boxes are further magnified in subsequent images (b - d).

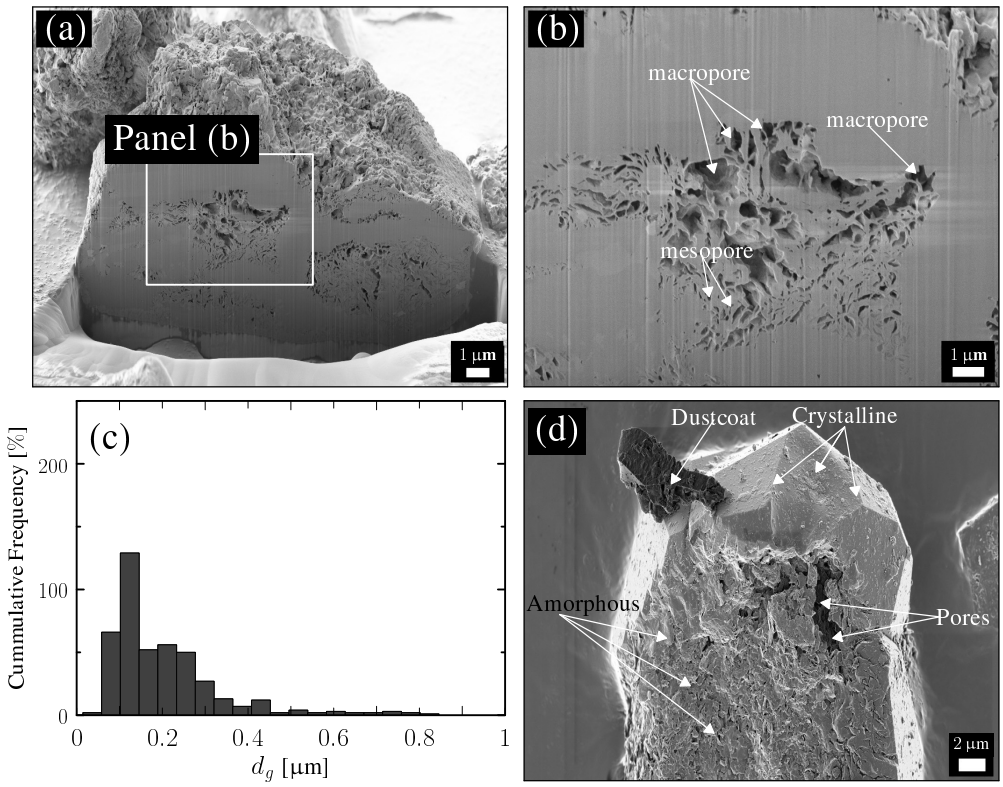

Figure 2.11: FIB-SEM images of a 35 µm Glaciogenic dust particle with panel box in (a) magnified in (b) to show examples of the meso- and marcopores. The pore-size distribution of the FIB-SEM image of the particle cross-section are shown in (c) while typical features of a Glaciogenic particle is shown in (d).

2.4.4 Porosity

The frequency distributions (Fig. 2.12a) for the inter- and intraparticle pores, obtained using mercury porosimetry, represent a wide range in pore diameter. Macropores (>0.05 µm) dominate each of the sample distributions, which are slightly negatively skewed. The modal pore diameter estimated from the measured pore volume (Fig. 2.12) appears to increase as the sample texture coarsens (Fig. 2.7).

The pore volume measurements allow for the calculation of porosity (Ta-

ble 2.1). The interparticle porosity (ϵ_{inter}) is the ratio of the interparticle (V_{inter}) and bulk (V_b) volumes of the sample, and is governed in part by its packing characteristics. Loose beds yield different interparticle pore volumes than compressed ones, with the latter yielding more reproducible results than the former ones (Y. León, 1998). The intraparticle porosity (ϵ_{intra}) is calculated by dividing the bulk (V_b) volume into the difference between the total intruded pore volume (V_p) and the interparticle volume (V_{inter}). The total intruded pore volume refers to the total pore volume, within and between the particles that is accessible to mercury.

The intra and interparticle volumes, as well as the distributions of pore diameter, are very similar for the Ash and Glacio1 samples (Table 2.3; Fig. 2.12). The median particle diameters obtained from laser diffraction (Fig. 2.7) and the frequency distributions of sphericity (below 40 %) obtained from SEM analysis (Fig. 2.7d) are near identical. This would suggest that Icelandic sediments of similar particle diameter may be assumed (as a first approximation) to have indistinguishable shape and porosity characteristics.

The values of V_{inter} and φ of Glacio2 are relatively higher and lower than the other samples, respectively (Table 2.3; Fig. 2.7d). This result indicates that a high quantity of concave and convex shards within Glacio2 may have increased the interparticle pore spaces, but in theory, the interparticle spaces should decrease with increased particle angularity. The intraparticle volume of Glacio2 is much lower than those for the other samples (Table 2.3), although its Horiba size and SEM angularity are higher than those for these samples. The intraparticle volumes are biased towards pore diameter $\leq$4 µm while the interparticle ones are biased towards those $\geq$4 µm; a criteria used to distinguish pore sizes obtained from mercury intrusion analysis (Y. León, 1998). The pore size distribution of

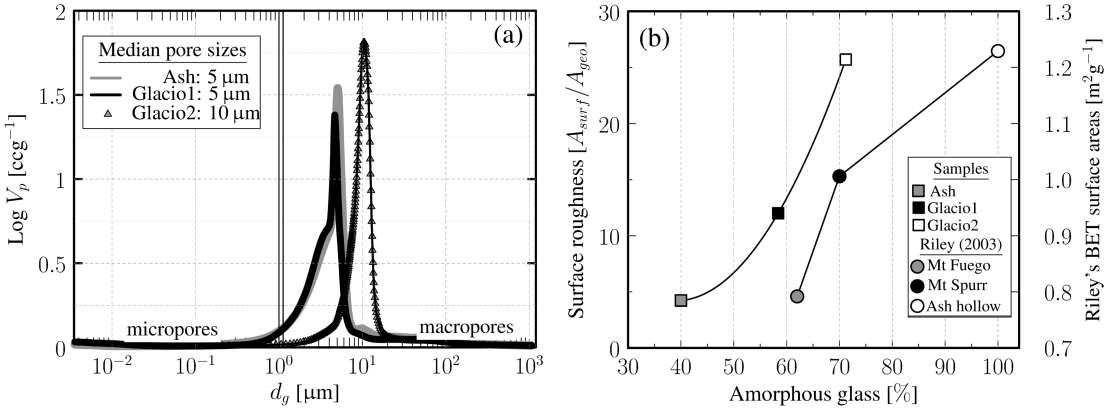

Figure 2.12: (a) Pore-size distribution for all samples with pore diameter ranging from 3 nm to 1 nm. The black vertical solid lines identify the boundaries for the micropores and macropores, with the mesopores lying within the narrow intermediate gap. (b) A relationship between the amorphous glass content obtained from XRD analysis (Table 2.2) and surface roughness factor (A_{surf}/A_{geo}, Table 2.3) for all Icelandic dust samples as well as A_{surf} for the Ash samples collected in Guatemala (Mt. Fuego), Alaska (Mt Spurr) and Nebraska (Ash hollow) in the study of Riley (2003).

the milled Glacio2 particle show that the internal pore diameters can be as small as 0.019 µm (Fig. 2.11c), suggesting that some particles may possess intra- and interparticle diameters of the same magnitude, in which case, making an indirect distinction between them is difficult.

2.4.5 Surface Area

The BET surface area (A_{surf}) determined for each the three Icelandic samples is listed in (Table 2.3). At 1.65 m^{2}g^{-1}, the surface area of the volcanic Ash is less than half that reported for either Glacio1 (4.19 m^{2}g^{-1}) or Glacio2 (5.14 m^{2}g^{-1}). Explosive and typical Ash collected at early and later times during the Eyjafjal-

lajökull volcanic eruption are reported to have BET surface areas of 4.3 m^2g^{-1} (Gislason et al., 2011; Olsson et al., 2013) and 0.45 m^2g^{-1} (Gislason et al., 2011), respectively, bracketing the values obtained for Ash in the present study. The surface area measurements for Glacio2 were replicated using two separate instruments based on the nitrogen gas adsorption technique: the Poremaster and Gemini VII 2390. The results obtained are relatively similar, differing by only 0.07 m^2g^{-1}. As expected, A_{surf} values obtained from mercury porosimetry (6.34 m^2g^{-1}−14.36 m^2g^{-1}) are 3−4 × higher than the corresponding BET measurements (Table 2.3). Mercury can penetrate large pore diameters up to 900 µm, whereas the upper limit for pore detection with nitrogen is 3 µm (Fig. 2.12). Mercury porosimetry is also affected by variation in particle alignment and pore wall collapse under high pressure.

The geometric diameter (D_g) determined for each of the samples was used to calculate the corresponding surface area for several idealized particle shapes (cylinders, cubes, ellipsoids, disks, spheres). All calculated values were found to be substantially smaller than the BET measurements by as much as 3 orders of magnitude (Table 2.3). This result clearly shows that image analysis along a single 2D projection does not adequately capture the complex surface structures that determine A_{surf}. Similarly, calculations of the surface area of the particles assumed spherical, based on the particle diameter measurements obtained by laser diffraction for each Icelandic sample, also grossly underestimate values of A_{surf} obtained by gas adsorption. In this case, surface areas estimated for the Ash (0.33 m^2g^{-1}) and Glacio1 (0.32 m^2g^{-1}) are nearly triple those for Glacio2 (0.1 m^2g^{-1}) as listed in Table 2.3, which again fails to represent the correct ranking identified by direct measurement. These findings are consistent with the earlier work of Riley (2003), who also found that the calculated surface areas of volcanic Ash particles are much

less than measured ones.

Fig. 2.12 suggests that the BET surface area scales positively with the abundance of amorphous glass. This outcome for the Icelandic samples is consistent with the results for three sources of Ash studied by Riley (2003), although in the latter case, the median grain size was somewhat coarser (25 μm to 77 μm) and the particles less porous (Fig. 2.12b). Indeed, Fig. 2.11d clearly shows that amorphous glass is rough and porous, so that the surface area of the particle increases, as compared to the crystalline form. Amorphous glass is most likely to form at early stages during the cooling process.

2.4.6 Density

As compared to Eyjafjallajökull Ash, the true skeletal density (ρ_s) of most Glaciogenic sediments in Iceland is not well documented. Although the measured surface areas were found to be substantially different, the density measured using helium pycnometry (Table 2.3) is similar for the three Icelandic samples: Ash (lowest at 2.66−2.72 $\mathrm{g\,cm^{-3}}$), Glacio1 (2.79−2.86 $\mathrm{g\,cm^{-3}}$) and Glacio2 (2.74−2.77 $\mathrm{g\,cm^{-3}}$), but greater than that of rhyolite glass (2.3 $\mathrm{g\,cm^{-3}}$: Johnson et al., 2012; Leadbetter et al., 2012). In comparison, the particle densities calculated from the proportional weight of solid minerals detected within the samples (i.e. using XRD phase and EMPA composition) are slightly lower: Ash (2.63−2.68 $\mathrm{g\,cm^{-3}}$), Glacio1 (2.59−2.67 $\mathrm{g\,cm^{-3}}$) and Glacio2 (2.45−2.46 $\mathrm{g\,cm^{-3}}$), with the Ash having the highest density. Likewise, the densities calculated from SEM images of the milled Ash and Glacio2 particles (shown in the cross-section in Figs. 2.10 and 2.11) are 1.73 and 2.02 $\mathrm{g\,cm^{-3}}$, respectively. Skeletal density measurement, based on the analysis of an SEM image of a given particle cross-section, excludes the volume of the internal pores observed. However, the sample size is usually unacceptably

small. The estimated skeletal density of the milled particle cross section is about 12 %, 26 % and 35 % less than that of the measured bulk density of the Glacio1, Glacio2 and Ash samples, respectively (Table 2.3). If such pores are inaccessible, though sufficiently large to decrease the particle density up to 35 %, then the true skeletal density (ρ_s) could be overestimated using a helium pycnometer. The bulk densities were all found to be extraordinarily low, $\sim$1.1$-$1.2 g cm^{-3} but near identical in magnitude (Table 2.3). The particle densities measured using the basic water penetration method are 2.72, 2.65 and 2.26 g cm^{-3} for the Ash, Glacio1 and Glacio2, respectively, as referenced against the particle density measured for four well-known minerals (e.g., Silica sand, Olivine, Wollastonite, Brucite). Although the minerals used were not pure, the particle density obtained using this basic water penetration method is well within the range of acceptable density in the literature. The value of ρ_p=2.32 g cm^{-3} for Glacio2 as calculated from the mercury intrusion measurement is similar to that of ρ_p=2.26 g cm^{-3} as measured from the water experiments, showing that the mercury may not have penetrated many of the pores within Glacio2 (Table 2.3) as compared with the Ash and Glacio1, and is consistent with rhyolite glass (2.3 g cm^{-3}: Johnson et al., 2012; Leadbetter et al., 2012).

Table 2.3: A summary of the measured and calculated particle characteristics, inclusive of surface area, density (bulk and skeletal), porosity and hardness details provided elsewhere.

Parameters		Analytical Technique	Sample Portions & Assumptions	Icelandic dust samples		
				Ash	Glacio1	Glacio2
Surface area (m^2/g)	Measured	BET Nitrogen absorption	(1−2 g)	1.65	4.20	5.14
		Mercury intrusion		6.34	11.58	14.36
	Calculated	Horiba (Geometric)	(1−2 g) Spherical assumption	0.39	0.35	0.20
		Horiba particle sizing		0.33	0.32	0.10
		SEM Image analysis	(2500 particles) Cylinder Cube Ellipsoid Disk Sphere	 0.34 0.62 0.26 0.1 0.41	 0.23 0.39 0.17 0.07 0.26	 0.33 0.59 0.26 0.09 0.2
Density (g/cm^3)	Measured	Mercury Mercury Helium$^{(1)}$ Helium$^{(2)}$	(1−2 g)	1.17* 1.77*** 2.66** 2.72**	1.26* 1.75*** 2.79** 2.86**	1.12* 2.32*** 2.74** 2.77**
		Water	(10−11 g)	2.72***	2.65***	2.26***
	Calculated	XRD	(1−2 g)	2.63**	2.59**	2.45**
		EMPA	Embedded particles	2.68**	2.67**	2.46**
		SEM Image analysis	milled particle	1.73** ($\rho_s^{(1)} \downarrow 35\%$)	2.46** ($\rho_s^{(1)} \downarrow 12\%$)	2.02** ($\rho_s^{(1)} \downarrow 26\%$)
Pore volume (cm^3)	Measured	Mercury intrusion	(2 g) Intraparticle Interparticle Total	 0.078 0.09 0.167	 0.082 0.068 0.149	 0.022 0.15 0.171
Porosity (%)			Intraparticle Interparticle Total	29.44 33.97 63.41	33.65 27.88 61.53	7.41 51.81 59.23
Moh's hardness	Calculated	XRD	(6 g)	5.8	5.19	5.5
		EMPA	Embedded particles	5.53	5.23	5.5

* ρ_b-bulk density, ** ρ_s-skeletal density, *** ρ_p-particle density

2.4.7 Dynamic Effects of the Particle Geometry

The micro-scale properties of Icelandic particles described above (e.g., angular morphology, high porosity, and nanoscale dust coats - shown in Figs. 2.9 and 2.10) influence rates of dust entrainment, emission and deposition. The magnitude of this influence is unaccounted for in dust models wherein an idealized geometric form, as for example, a solid sphere, is used to approximate natural particles.

A particle falling through a column of air reaches terminal velocity when its weight (F_G) is balanced by the opposing fluid drag (F_D), assuming all other forces acting on the particle are negligible. F_G is determined by mg, where the particle mass (m) is approximated by the product of its density (ρ) and volume (V), inclusive of its intraparticle pores (V_{intra}) and skeletal volume (V_s). The gravitational acceleration is constant in value (9.81 ms^{-2}) and represented by g.F_D can be calculated from the quadratic stress law:

$$F_D = \frac{1}{2}\rho_a w^2 A_p C_D, \tag{2.1}$$

requiring values for the air density (ρ_a), relative particle velocity (w), projected area of the sphere ($A_p = \frac{1}{4}\pi d_g^2$), and the drag coefficient (C_D). As a coarse approximation, the dependency of the settling rate of a given particle on its physical properties then can be expressed as $\sim\sqrt{\rho V/A_p}$, which for a sphere reduces to $\sqrt{\rho d_g}$.

In illustration of such effects, three particle images (Fig. 2.13) were selected for analysis, all having an identical geometric diameter (10 µm or PM_{10}), but varied shape and density and origin. A_p was measured to be 85.7 μm^2 for the solid glass sphere, with only a 3 % difference from the value calculated for a perfect sphere with a 10 µm diameter. The cross-sectional areas measured for the Ash

and Glaciogenic particles were up to 30 % larger at 111.6 μm^2 and 111.7 μm^2, respectively. As expected, particle densities measured for the porous Icelandic particles (e.g., 1.8, 1.7 and 2.3, $g\,cm^{-3}$ for the Ash, Glacio1 and Glacio2 particles, respectively), based on V obtained from mercury porosimetry, all fall below that for the solid glass sphere (2.5 $g\,cm^{-3}$ as provided by the manufacturer), although Glacio2 density is similar to that of rhyolite glass. Examination of the milled particles (Figs. 2.10 and 2.11) would suggest that if the inaccessible internal pores are accounted for, ρ drops further, by as much as 25 %. A comparison between calculations of $\sim\sqrt{\rho V/A_p}$ would therefore suggest that:

(i) the settling velocity of Icelandic dust may be as little as 30 % of that for a solid glass sphere of equivalent (geometric mean) diameter, and

(ii) the residence time of dust originating in Iceland is possibly longer (by as much as 5 ×) than projected by dust models based on idealized spherical particles.

The geometry of a solid sphere differs from that of the Icelandic particles with similar sizes so that when used in dust transport models to predict the residence time and settling rate, the outcome may vary significantly, although the effects of particle interactions were not considered in these calculations. Both of these estimates need to be tested in controlled laboratory experiments where both particle and fluid interactions are considered. Another factor not accounted for in this dynamical analysis concerns the effect of particle shape and roughness on the drag coefficient (C_D), where a change in the value of this parameter may either offset or enhance the influence of the enlarged silhouette area. Finally, the diminishing particle porosity (increasing density) observed with reduced diameter would suggest that the deposition rate of an idealized solid form of equivalent size may well approximate that for the finest aerosols of volcanic origin.

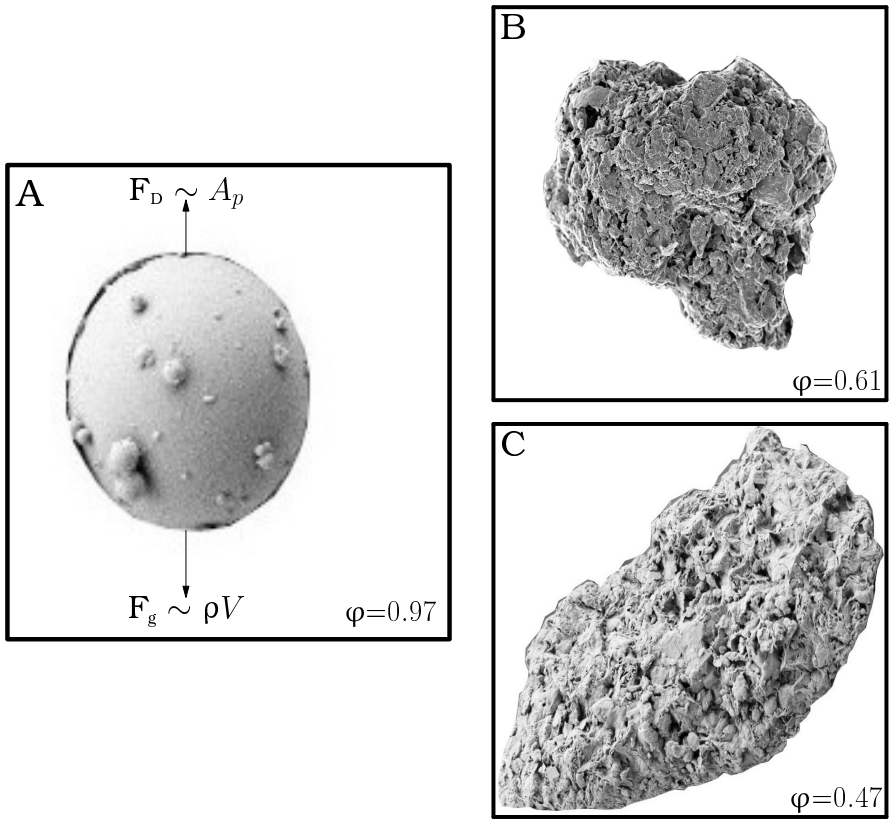

Figure 2.13: Selected PM_{10} particles with varied shape, density and origin used to estimate the geometries related to the gravitational ($F_G \sim \rho V$) and drag ($F_D \sim A_p$) forces as compared to a solid glass sphere of the same size.

2.5 Conclusions

Dust (PM_{10}) sources within Iceland include basaltic glaciogenic sediments and volcanic ash. The particles derived from these sites are characterized by unique physical properties that may affect rates of entrainment and deposition within the atmospheric boundary layer. The glass-like particles have a high degree of porosity that is shown in this study to increase with the proportion of amorphous glass. The high degree of porosity reduces the apparent density, and therefore the particle weight relative to a solid mineral particle of equivalent volume. In a

turbulent boundary-layer, this is expected to reduce the amount of lift required to maintain such particles in suspension and potentially increase their residence time. The low particle sphericity, rough surface texture and high porosity of the Icelandic particles investigated in this study are shown to contribute to very large surface areas, as measured via gas adsorption. The implications for dust transport are twofold:

(i) Abundant numbers of shard-like, nano-scale 'fragments' are observed in SEM images to adhere to the particle surfaces as 'flaky dust coats', while the highest concentrations appear within meso- to macro-scale pores. Some fraction of these dust coatings could be released as aerosols into the atmospheric boundary layer through abrasion that occurs with sand drifting during wind erosion events.

(ii) Water adsorption onto these capacious particle surfaces, and absorption within their pore spaces, may be sufficient to affect the rate of particle deposition through the growth of water films and lenses, and particle interactions that lead to aggregation, cloud condensation, precipitation and solar radiation.

Laboratory experiments, in which particle settling is measured with high accuracy under the cool, humid conditions, which are characteristics of Iceland's climate, are needed to test these possible effects.

Chapter 3

A wind tunnel investigation of Icelandic dust emission response to varied wind speed

3.1 Introduction

Icelandic dust particulates derive from sandur deposits within proglacial and paraglacial regions make up more than 20 % ($20,000$ km^2) of the total surface area of Iceland ($103,000$ km^2: Arnalds et al., 2001). These regions are sparsely vegetated with little to no gravel pavements and large near-surface winds that drive dust emission processes, thereby creating extremely large and frequent dust events (Arnalds et al., 2016). An average of about 135 dust days are reported annually in Iceland: 101 dust days in southern Iceland (Thorsteinsson et al., 2011, 2012) and 34 dust days in northern Iceland (Dagsson-Waldhauserova et al., 2013, 2014). A dust day is described as a 24 hr period when at least a weather station records at least one dust storm event (Dagsson-Waldhauserova et al., 2013, 2014). The frequent re-suspension of Icelandic dust contributes to the poor air quality within eastern Arctic and western Europe, but it also influences the global climate system when transported over long distances and the Earth's radiation balance when deposited on glaciers (e.g., Greenland glaciers: Drab et al., 2002) and Arctic sea ice (Arnalds et al., 2016). High exposure to respirable quantity of Icelandic dust is believed to affect human health (Carlsen et al., 2012; Thorsteinsson et al., 2012). Respirable quantity is defined as the fraction of inhaled airborne particulates capable of passing beyond the larynx and ciliated airways.

Most well-establish studies are focused on dust emission processes in dry, hot tropical and mid-latitude arid regions, which are the major contributors to the global dust budget (Bullard et al., 2016; Prospero et al., 2012, and references within). However, extreme dust sources in high latitude cold climate (hlcc) regions are supplied with sediments from melting glaciers (e.g., Alaska: Crusius et al., 2011; Hope et al., 1991; Greenland: Bullard and Austin, 2011; Iceland: Ar-

nalds, 2010; northern Canada: Nickling, 1978; New Zealand: Marx et al., 2005; southern Patagonia: Gassó and Stein, 2007) and explosive volcanic eruptions, which eject up to a volume of 10^4 m^3 of unique, fine particles into the atmosphere (e.g., Iceland: Arnalds et al., 2016; Butwin et al., 2019). The sediment transport rates associated with dust events in hlcc regions are comparable with those in low, mid-latitude regions (Bullard, 2013), yet little to no measurements of the dust emission rate are currently available in the literature. Sediment transport rates within hlcc regions (e.g., 4.5−52 $gmw^{-1}s^{-1}$ in Yukon: Nickling, 1978; 56 $gmw^{-1}s^{-1}$ in Iceland: Arnalds et al., 2001; 1600 $gmw^{-1}s^{-1}$ in Nunavut: Church, 1972; $>$ 7100 $gmw^{-1}s^{-1}$ in Greenland: Bullard and Austin, 2011) are generally higher than those within lower latitude regions, which typically range from $<$ 1 to 30 $gmw^{-1}s^{-1}$ (Bullard, 2013; Nickling and Gillies, 1993). While it is widely speculated that saltation bombardment is the principal mechanism that drives hlcc dust emission processes, variability in the surface and soil properties also play an important role (Marticorena and Bergametti, 1995; Shao, 2008), especially in the case of hlcc dust sources.

Icelandic desert regions are the most studied hlcc environments ($\geq$50 °N Bullard et al., 2016) because they provide an accessible and highly suitable analogue for similar present-day and historical settings. Measurements of particulate matter $\leq$10 µm in diameter (PM_{10}) have been obtained for some of the most emissive dust sources in Iceland (Dagsson-Waldhauserova et al., 2014; Thorsteinsson et al., 2011, 2012), but the aerodynamic mechanisms affecting dust entrainment and the subsequent rate of dust emission are not well understood. Icelandic field studies provide information on the temporal and spatial variability in PM_{10} concentration associated with sediments of varied texture (Baddock et al., 2017; Dagsson-Waldhauserova et al., 2014; Prospero et al., 2012), but very few have reported on

the scaling between the PM_{10} emission rates and friction velocity (Thorsteinsson et al., 2011). The effects of the complex surface and soil properties (e.g., sediment texture, roughness), as well as extreme atmospheric conditions (e.g., wind speed, temperature, relative humidity), are difficult to isolate and quantify during Icelandic dust events. Other factors, such as the large dust concentrations, extensive source areas and complications arising from dust advection, present many challenges for measuring and quantifying the vertical dust flux. Hence, large uncertainties exist within these datasets, which may hinder the understanding of the underlying physics. Wind tunnels allow for the strict control over some of these environmental factors (Neuman, 2004) and enable the precise study of the physics of particle entrainment, dispersion and emission (Shao et al., 1993; White, 1996).

This paper focuses on a wind tunnel investigation of Icelandic dust emission for varied sediment textures collected within some of the most active dust regions (Fig. 3.1). The specific objectives of the present study are as follows: i) to quantify the response of the dust emission rate at varied wind speeds, ii) to identify the primary particle characteristics (e.g., texture, surface area, density and mineral) that influence the emission of Icelandic basalts, relative to a control sample, and iii) to estimate the relative proportion of airborne particulates (PM_1, $PM_{2.5}$, PM_4 and PM_{10}) contained within and emitted by the Icelandic samples.

3.1.1 Icelandic sample sites

Samples were collected from five locations within regions known to emit large quantities of dust in Iceland (Fig. 3.1). The samples collected include: tephra from the 2010 Eyjafjallajökull eruption deposited in Alftaver (Ash), glaciogenic sediments from Dyngjusandur (Glacio1), Markarflótssandur (Glacio2), and Markarfljótsaurar (Glacio3), and a mixture of ash and glaciogenic sediments (Mixed) col-

lected in Vík (Fig. 3.1). The sediments obtained from Markarflótssandur and Markarfljótsaurar were both transported by the Markarfljót River. The Markarfljót River branches off into different ephemeral channels, one of which is located in each of these regions near the coast of southern Iceland. A detailed description of these site locations and their geology is provided in Chapter 2. The five Icelandic samples are identified as Ash, Mixed, Glacio1, Glacio2 and Glacio3 (Fig. 3.1). A control sample, containing coarse particles with low BET surface area (A_{surf}) and amorphous glass, was used as a reference comparison with the glaciogenic sediments of high BET surface area and amorphous glass but with varying texture. The control sample is Nepheline Syenite tailings (less than 1 mm size fraction) collected from a mine near Kasshabog Lake in the Township of Havelock within Peterborough County, Ontario. The particle characteristics, inclusive of the size, density and BET surface area, are believed to influence dust entrainment and emission, and so, using sediments with particles characteristics that differ from the Icelandic sediments will allow for a relative comparison, when the effects of climate are ignored.

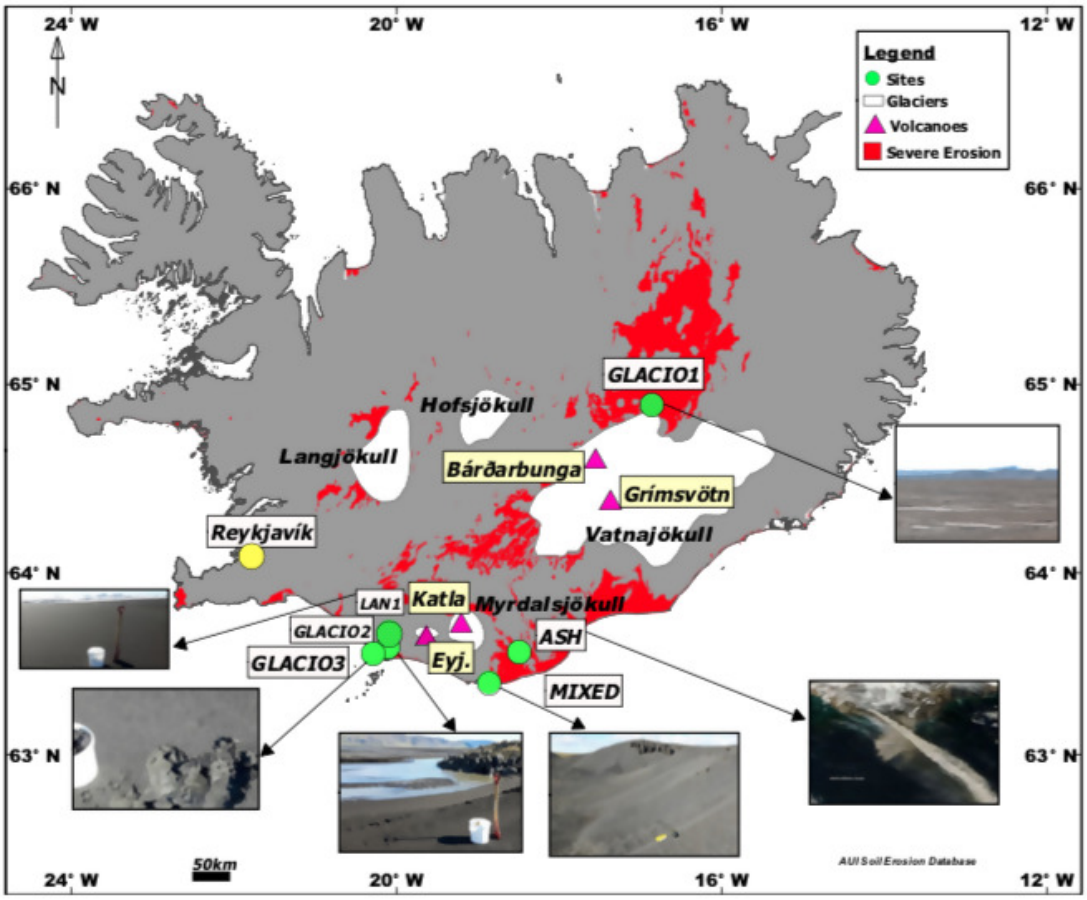

Figure 3.1: Map showing the location and images of the Icelandic sediment collection sites.

3.2 Quantifying the dust emission rate

The rate of entrainment of suspended particulate matter (PM) from a unit area of test surface into the atmospheric boundary layer (μgm^{-3}) is measured as either the vertical dust flux (F) or the emission rate (E).

The vertical dust flux is proportional to the vertical gradient of the dust con-

centration (Gillette, 1977; Gillette and Passi, 1988):

$$F = K(z)\frac{\partial c}{\partial z}, \tag{3.1}$$

where $K = \kappa u_\star z$ is the turbulent diffusion coefficient ($\mathrm{m^2 s^{-1}}$, also called eddy diffusivity), $\kappa \backsimeq 0.41$ is the von Kármán constant, $u_\star$ is the friction velocity, and z is the elevation.

Instrumentation does not exist to measure directly the flux of particles close to (and rising directly from) the surface. Therefore, F is determined indirectly from the difference in dust concentration between two (or more) elevations above the surface, as described in Eq. (3.1) (Gillette et al., 1972). The vertical dust flux from an eroding surface serves as an index of the surface's ability to emit dust for a given wind velocity:

$$F = -\kappa u_\star \frac{(c_2 - c_1)}{\ln\left(\frac{z_2}{z_1}\right)}, \tag{3.2}$$

where the gradient formed by c_1 and c_2 is obtained from the measured concentration at elevations of z_1 and z_2, respectively (Gillette, 1978), assuming that the dust emitted is dependent on the turbulent diffusion scaling with values of $u_\star$.

Alternatively, the dust emission rate can also be evaluated using a control-volume approach, as described by Roney and White (2006). This approach is most suitably applied in a controlled laboratory wind tunnel setting. Dust emission is calculated from the difference between the horizontal rate of dust transport in (m_i) and out (m_o) of a controlled volume ($W_b \times L_b \times H_t$) region from a test surface of known area, A_b (Roney and White, 2006, Fig. 3.2a):

$$E = \frac{1}{A_b}(m_o - m_i). \tag{3.3}$$

The mass of dust particles ascending into suspension is given by $m = \int_0^H c_z u_z W_b dz$. The horizontal rate of dust transport out of the control region requires measurement of both the wind velocity ($\overline{u}(z)$) and dust concentration (c_z, typically PM_{10}) in a vertical profile at the inlet and outlet of the control volume region (Fig. 3.2a). Therefore, using m_i and m_o of the control volume region, dust emission can also be given as:

$$E = \frac{1}{A_b} \int_0^H (c_{zo} u_{zo} - c_{zi} u_{zi}) dz. \tag{3.4}$$

Experiments with small and negligible dust advection recorded as the background dust entering the control region will flow into the control volume system as $m_i = 0$ (Roney and White, 2006). Deficient background PM_{10} concentration drawn into the control volume is assumed to be zero (Fig. 3.2).

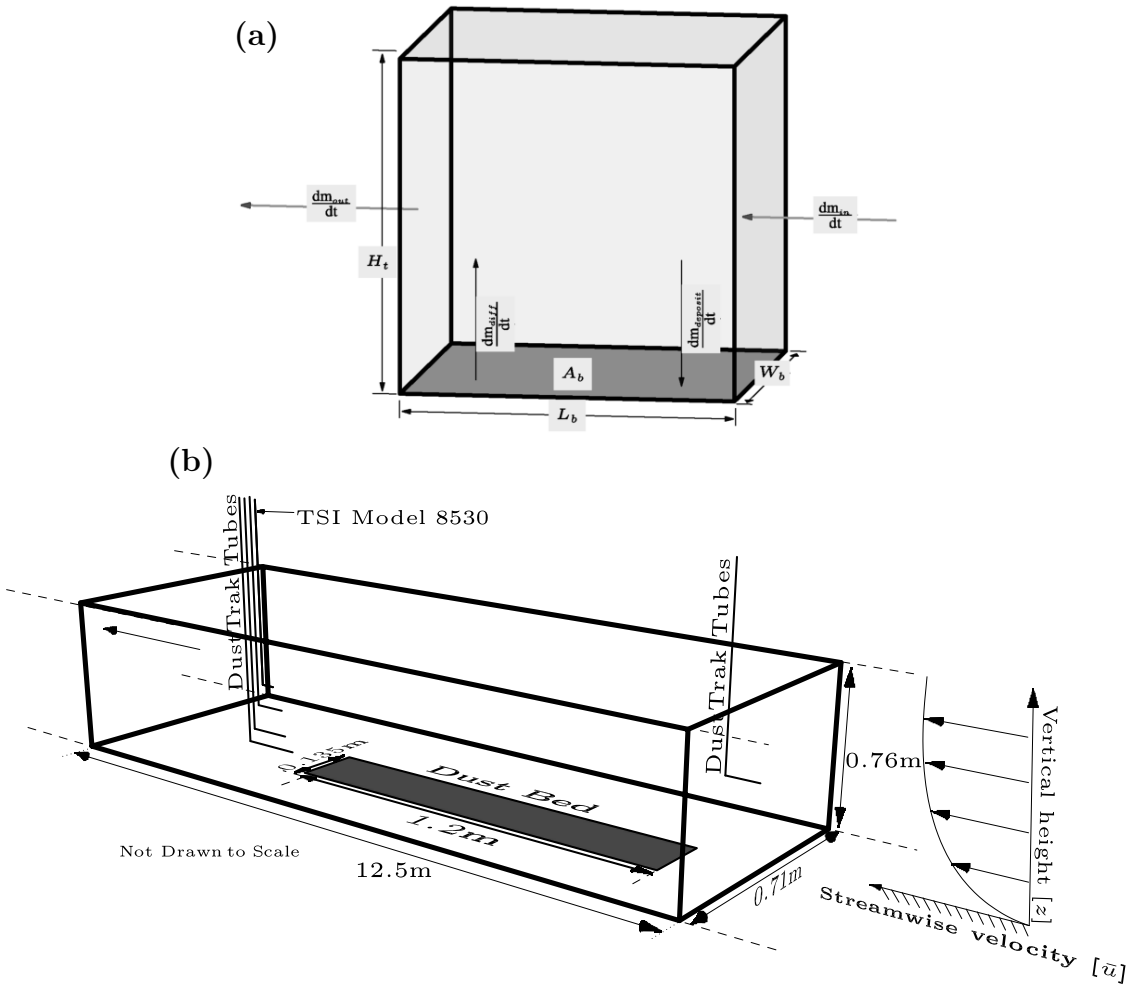

Figure 3.2: Schematic diagram of a) a control volume region showing the horizontal and vertical mass fluxes of dust in (m_i) and out (m_o) of the region with a dust surface area (A_b) and b) a wind tunnel showing the setup of dust tracks (*upwind* and *downwind*), test bed, and vertical wind profile through the working test section.

If the measured vertical dust and wind velocity profiles follow a logarithmic trend (Gillies and Berkofsky, 2004; McKenna-Neuman, 2009), then the dust concentration measured at the extreme top of the control volume region is assumed to be the same as that entering the region (Fig. 3.2a). In the present study, the wind velocity in and out of the region is assumed to be the same ($u_o = u_i$), and

the reference height of u_o is assumed to be the height ($z = 0.185$ m) at which the freestream velocity is measured (McKenna-Neuman, 2009, and references within). Using these assumptions, Eq. (3.4) allows for an estimation of the emission rate (based on the control volume approach) from the unit area of the test surface (A_b):

$$E = c_{tz}\overline{u}(z)\left(\frac{W_t\delta}{A}\right), \tag{3.5}$$

where $\overline{u}(z)$ is the freestream wind velocity measured at an elevation of 0.185 m above the surface; $\delta = 0.16$ m is the maximum elevation of the inlet copper tube used to measure dust concentration downwind above the bed. The values of c_{tz} represent the time-averaged peak PM_{10} concentration measured at each of the four elevations above the surface as

$$c_{tz} = \frac{c_1 + c_2 + ... + c_n}{t_1 + t_2 + ... + t_n}, \tag{3.6}$$

where c_n is the total PM_{10} concentration measured over n^{th} number of peaks at corresponding time, t_n over the duration of an experiment. The vertical PM_{10} profiles were extrapolated towards and away from the surface to obtain values of c_{tz} for 8 sublayers of thickness, Δz each corresponding to an elevation at which the values of $\overline{u}(z)$ were calculated from the measured wind velocity profile (Fig. 3.3a).

A wide range of wind tunnel studies have confirmed that dust emission increases as a power function of the friction velocity (Sanderson et al., 2014, and references within),

$$E = au_\star^b, \tag{3.7}$$

where the coefficient (a) and exponent (b) are dependent on the surface and soil properties. The value of b typically ranges between 3 (e.g., Shao et al., 1993) and 4 (e.g., Gillette and Passi, 1988), but it could be as high as 6 (e.g., Table 1.1: Lopez,

1998; Lopez et al., 1998). The various sources of resistance that influence near-surface dust entrainment by wind are taken into consideration when the threshold friction velocity ($u_{\star t}$) is incorporated into the dust emission model (e.g., Gillette and Passi, 1988),

$$F = a u_{\star}^{4} \left(1 - \frac{u_{\star t}}{u_{\star}}\right), \tag{3.8}$$

where dust emission occurs when $u_{\star} > u_{\star t}$, and a is the coefficient related to efficiency of saltation bombardment, which is the key mechanism for dust entrainment.

3.3 Methodology

3.3.1 Experimental Design

All experiments were performed in Trent Environmental Wind Tunnel (TEWT, Fig. 3.2b) of measured cross-sectional height ($H = 0.76$ m), width ($W = 0.71$ m), and working section length ($L = 12.5$ m) that create a vertical cross-sectional area of 0.54 m^2 (Neuman and Maljaars, 1997). TEWT is an open-looped straight-line suction system that first directs airflow through a compression bell followed by a honeycomb straightener. The honeycomb straightener consists of an array of cellular channels created from plastic straws stacked onto each other with their opening ends aligned in the same direction as the airflow. The primary function of the straightener is to reduce any external large-scale turbulence within the airflow before entering the working test section. The airflow is then directed over an array of evenly spaced staggered wooden dowels each has a diameter ($d_{dw} = 2.0$ cm), height ($h_{dw} = 2.5$ cm), and center-to-center distance ($c_{dw} = 4.5$ cm) used as roughness elements to create shear within the near-surface flow. Following this

region is the working test section, which rapidly develops the turbulent boundary layer flow, thereby producing a logarithmic wind profile. TEWT also has an in-house climate control system, which allows full control of temperature (T) and relative humidity (RH). All experiments in the present study were performed at $T = 19 \pm 1\,^{\circ}C$ and $RH = 20 \pm 2\,\%$ to exclude climatic effects. Further details about this facility and technology are described in other studies (McKenna-Neuman, 2003; Neuman, 2004).

The glaciogenic samples were dry sieved to remove all particles exceeding 2 mm in diameter thereby isolating the fine particles. All samples were also Mixed vigorously to distribute particles and break up aggregates. The particle-size distributions of the samples were measured using the Partica LA-950 V2 laser particle-size analyzer (PSA). The size distributions were used to classify the samples using a sediment texture triangle based on the United States Department of Agriculture specifications. The Brunauer, Emmett, and Teller (BET) surface areas were measured for Glacio3 and the Control sediments, and those for all other samples were extracted from Chapter 2, as well as for the X-ray fluorescence (XRF) spectrometry measurements, where specific details regarding this technology are also described in Chapter 2.

The Icelandic sediments were used to create a 0.31 m$\times$1.2 m test bed (Fig. 3.2b) layered flush with the tunnel floor (Fig. 3.2b) to improve measurement accuracy, create a safe working environment within respirable limits and maintain the full functionality of all TSI DustTraks$^{\text{TM}}$ (Appendix A.5), and prevent the device from clogging where measurements are near the surface ($z = 0.04$ m). The length of test bed slightly exceeded 1 m to ensure that its fetch length exceeds the minimum length required to eliminate its effects on the quantification of the dust emission rate (Sanderson et al., 2014). The wind tunnel was cleaned before the

start of each experiment to reduce the dust recirculation from the background airflow ($PM_{10} < 20\,\mu\,gm^{-3}$).

The wind tunnel fan was set to predetermined wind speeds and ran for 5 min long, depending on the emissivity of the samples while c_z and u_z were measured. Dust concentration in the airstream was measured using 5 non-isokinetic TSI DustTrak^{TM} II aerosol monitors: 1 of model 8530 and 4 of model 8532 with precision of about $\pm 2\,\mu\,gm^{-3}$. Four of the five TSI DustTrak^{TM} II aerosol monitors were connected to inlet copper tubes arranged in a vertical array, forming a logarithmic progression at four elevations (0.04, 0.08, 0.12 and 0.16 m) above the tunnel surface at 5 m downwind of the leading edge of the bed to prevent clogging (Fig. 3.2b). The TSI model 8530 was connected to a copper tube positioned at a fixed height of 0.16 m above the tunnel floor to simultaneously measure PM_1, $PM_{2.5}$, PM_4 and PM_{10} for all experiments (Fig. 3.2b). The 5th TSI DustTrak^{TM} II aerosol monitor was connected to a copper tube with inlet positioned at the entrance of the tunnel at $z = 0.08$ m to measure the background concentration (c_b) of the incoming airstream (Fig. 3.2b) to improve estimates of the dust concentration profile. Dust recirculation through the tunnel from the lab is assumed to be the measured background; therefore, as the tunnel's fan speed increases, the background concentration measured by the inlet tubes also increased. The values of c_b are subtracted from all measured values of c_z downwind of the bed to eliminate dust advection and to find c_z emitted from the test surface as required by Eq. (3.5). This subtraction was only performed for the PM_{10} concentrations used to calculate the emission fluxes because c_b for PM_1, $PM_{2.5}$ and PM_4 were not sampled.

Six vertical profiles of the steady-state streamwise velocity ($\overline{u}(z)$) were measured using a stainless steel micro-pitot tube that traversed vertically upwards

from a minimum (z_{min} = 0.05 m) to a maximum (z_{max} = 0.4 m) height as $\overline{u}(z)$ was computed from the pressure gradient developed around the inlet of the tube. The values of $\overline{u}(z)$ were averaged to eliminate the effects of unsteady air turbulence (Fig. 3.3a) and to create a single profile from which the friction velocity ($u_\star$, ms^{-1}) and aerodynamic surface roughness height (z_o, m) were obtained by fitting the Prandtl von Kármán equation to the data series. The friction velocity ($u_\star$) describes the shear stress near the surface and depends on the freestream velocity and aerodynamic surface roughness height:

$$u_\star = \frac{\kappa \overline{u}(z)}{\ln\left(\frac{z}{z_o}\right)}, \tag{3.9}$$

which is assumed constant within the lowest 10 % of the wind tunnel boundary layer (Tennekes, 1973; White, 1996, Fig. 3.3a). The thickness of the thin boundary layer just above the test bed with zero velocity is called the aerodynamic roughness height (z_o), which depends on the characteristics of the sediments (e.g., texture). The aerodynamic surface roughness ($z_o \backsimeq 10^{-5}$ m) of the working test section (Fig. 3.3a) is up to 3 orders of magnitude lower than those measured in field studies (Thorsteinsson et al., 2011; Zwaaftink et al., 2017), suggesting that the wind tunnel is smoother and has fewer complex roughness features than those within Icelandic dust source regions.

In the present study, wind gusting is defined as a constant mean velocity observed at time intervals of 1 min, 30 s and 15 s over the entire duration of an experiment; whereas, wind ramping is a changing mean velocity, which gradually increases over the duration of an experiment (Fig. 3.3b). Wind gust and ramp velocities were performed for Glacio2 and the control samples at time intervals of 1 min, 30 s and 15 s over a 5-min duration of an experiment.

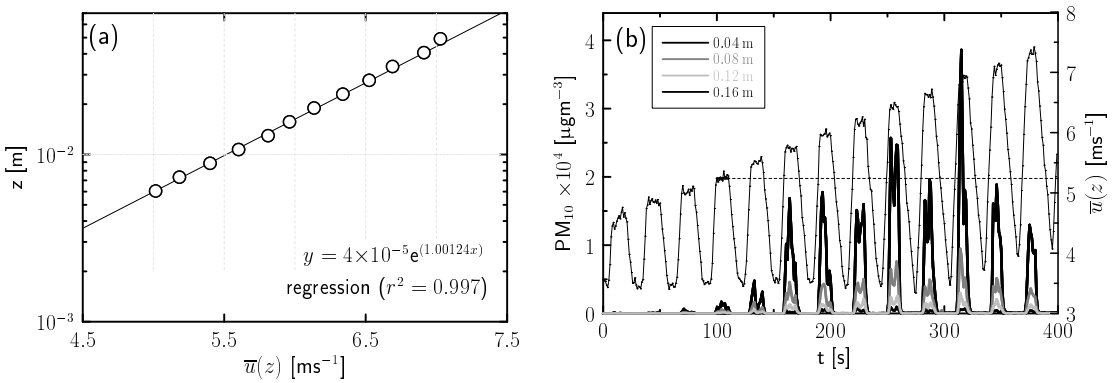

Figure 3.3: a) A semi-logarithmic freestream velocity profile of the clean airflow in the lower boundary layer measured at a requested fan speed of 7.5 ms^{-1} that correspond to friction velocity ($u_\star = 0.39$ ms^{-1}) and aerodynamic roughness height ($z_0 = 3.73{\times}10^{-5}$ m). b) An example of the time-dependence plot for Glacio3 of a requested wind ramp velocity (thin solid line) and measured PM$_{10}$ concentration response over a time period of 5 min.

Wind ramping runs were used to evaluate the PM$_{10}$ emission response of a test surface, when subjected to successively higher speeds (e.g., Fig. 3.3b). The freestream velocity was sampled at a fixed height ($z_f = 0.185$ m) while the fan speed increased from a minimum of $u_{cf} = 3.5$ ms^{-1} to $u_f = 4.75$ ms^{-1}, back to $u_{cf} = 3.5$ ms^{-1} and then to the previous u_f plus an increment of $\Delta u = 0.25$ ms^{-1} over a time interval of 10 s for a 5 min duration of each experiment (e.g., Fig. 3.3b). A threshold friction velocity of 5.15 ms^{-1} is observed at the fourth peak in wind velocity (dashed line, Fig. 3.3b). As a result, these experiments consisted of up to 13 incremental increases ($\Delta u = 0.25$ ms^{-1}) of the peak velocity at an interval of 10 s, which corresponds to the peak concentrations measured at each of the four elevations above the surface. Selected fan speeds were relatively low, as compared to those within Icelandic dust regions (Dagsson-Waldhauserova et al., 2013, $\overline{u}(z) > 8$ ms^{-1}), but are typical for wind tunnel laboratory studies of dust

emission events.

3.4 Results & Discussion

3.4.1 Particle morphology: size, shape, density, specific BET surface area and mineralogy

The particle-size distributions of the Icelandic samples, as well as the Control sample, range from 0.1 µm to 450 µm in diameter (Fig. 3.4a). Glacio1 peaks at about 20 µm, and up to 80 % of the particles are within the dust size range (< 63 µm in diameter). The Ash deposits are bimodal with peaks at 20 and 102 µm. The Mixed sample is bimodal with peaks at 17 and 200 µm, and it and contains a significant portion of dust (Fig. 3.4a). Glacio2, Glacio3 and the Control samples are negatively skewed towards the fines and appear to be poorly sorted. A combination of the size distributions of these three samples shows that they have and contain relatively coarse particles (Fig. 3.4a; Table 3.1) as compared to the dominantly fine samples (e.g., Ash, Mixed and Glacio1).

Following the study of Horwell (2007), the particle size distributions (Fig. 3.4a) were further analyzed to precisely determine the size fractions (Table 3.1: particle diameter ≤1, ≤2.5, ≤4 and ≤10) that are relevant to human respiratory health problems. They were later compared with the size fractions measured as concentrations by the model 8530 TSI DustTrak^{TM} positioned at an elevation of 16 cm downwind of the bed. As expected, the samples with median sizes ($d_{50} < 30$ µm, Ash, Mixed, Glacio1) contain higher portions of PM_{10} (< 30 vol. %) than those with $d_{50} > 40$ µm (Table 3.1). Notably, the quantity of $PM_{2.5}$ for the Mixed sample with $d_{50} < 30$ µm is comparable with Glacio3 ($d_{50} \sim 44$ µm), which contains

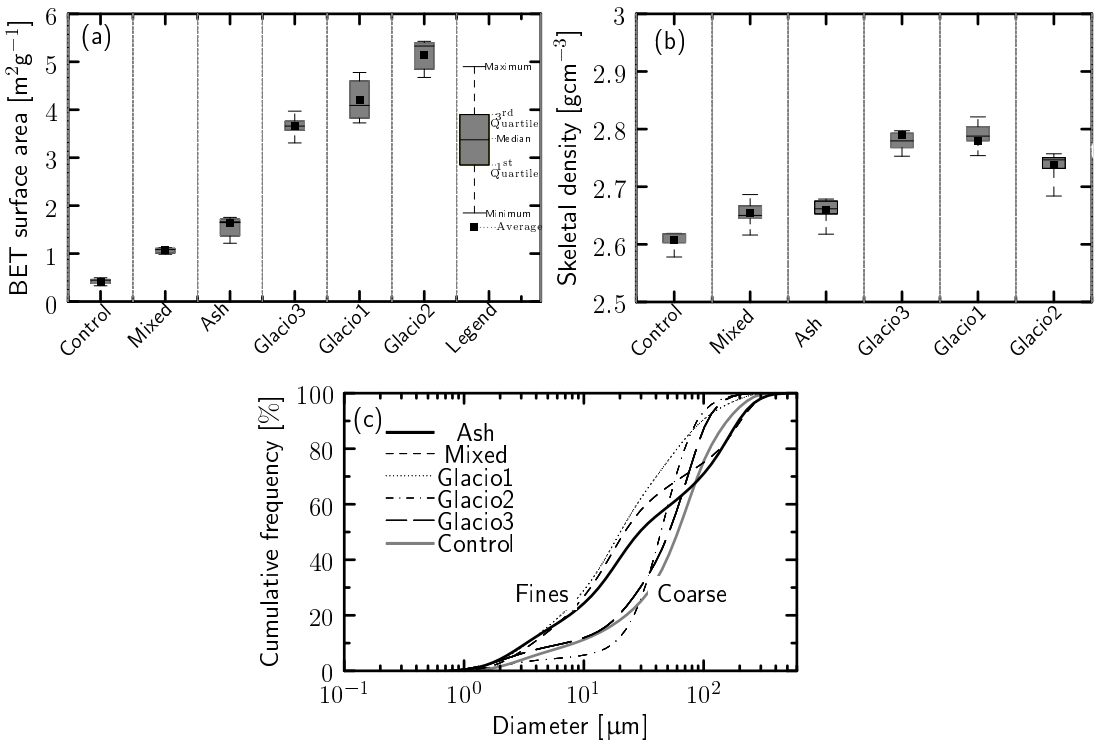

Figure 3.4: A summary of the various factors affecting near-surface dust entrainment and dispersion. a) Particle-size distribution of the samples analyzed using a Horiba Partica LA-950 V2 laser particle-size analyser (LPSA). b) The BET surface area measured using nitrogen gas absorption and c) skeletal density measured using a helium pycnometer for all samples (Chapter 2) used in the present study.

more coarse particles than the samples dominated by fines. This quantity of $PM_{2.5}$ in Glacio3 may be derived from detached dust coats on the surface and within the pores of the particles as established in Chapter 2. Glacio2 appears to contain the least respirable quantity of dust particulates, and no PM_1 was found in the Control sample. Glacio1 contains the most significant respirable dust particles in comparison to all other samples, inclusive of the Control, although the PM_{10} quantity is comparable to the Ash and Mixed samples. A breakdown of the aerosol size classes provides insight into the respirable quantity that could be generated

during dust entrainment in the wind tunnel laboratory experiments, which will be discussed in Subsection 3.4.3 below.

Table 3.1: Quantity of dust size fractions, relevant to human respiratory health, is expressed as a cumulative volume percent [vol. %]: airborne particulates (PM_1, $PM_{2.5}$, PM_4 and PM_{10}), clay ($d \leq 20\,\mu m$), silt ($20\,\mu m \leq d \geq 63\,\mu m$) and sand ($63\,\mu m \leq d \leq 2$ mm; Appendix A).

Texture classification (predominantly)		**Samples**	**Airborne particulates**				**Median**	**Size classes**		
			≤1 μm	**≤2.5 μm**	**≤4 μm**	**≤10 μm**	d_{50}	**Clay**	**Silt**	**Sand**
			[vol. %]				**[μm]**	**[vol. %]**		
Clay	**(Fines)**	Ash	0.4	7.0	11.8	23.9	29	40.5	23.2	36.3
Clay		Mixed	0.1	5.3	10.5	27.0	22	47.1	23	29.9
Clay		Glacio1	0.4	6.5	12.1	29.2	20	49.6	32.9	17.5
Silt loam	**(Coarse)**	Glacio2	0.1	2.7	3.7	5.7	44	12	57.6	30.4
Loam		Glacio3	0.1	5.3	7.6	12.0	52	20.4	36.6	43
Sandy loam		Control	0	3.0	5.6	11.3	61	18.2	30.2	51.6

The glaciogenic samples (Glacio1, Glacio2, Glacio3) have larger specific BET surface areas as compared to all other samples, inclusive of the Control. For instance, Glacio2 and the Control have the highest and lowest BET A_{surf}, respectively (Fig. 3.4a). The surface areas for all Icelandic samples (> 1 m^2g^{-1}) are more extensive than for the Control sample (< 0.5 m^2g^{-1}), which is comparable to a solid glass sphere (< 0.2 m^2g^{-1}) as measured in Chapter 2. The Control sediments are not as porous (2.5 wt.% glass) as compared to the Icelandic sediments (> 40 wt.% glass), and undoubtedly not as rough as the surface of the Icelandic particles because its BET A_{surf} is extremely low, although the particle appears to be sharp-edged after the milling process (Fig. 3.5).

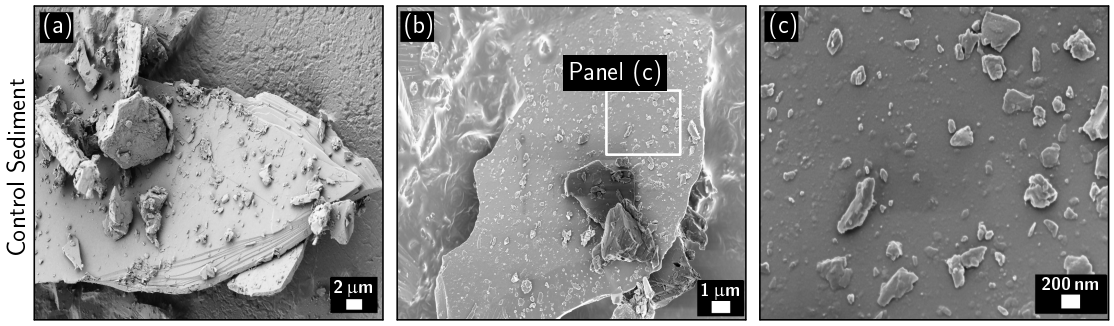

Figure 3.5: Scanning electron micrographs (sem) of selected particles from the control sediments, showing (a) diagonal striated particle, (b) flat sharp-edged particle with large surface area and inset panel box magnified in (c) to show the nanosize dust coats adhering to the surface.

All samples are predominantly composed of SiO_2 followed by the analyte, Al_2O_3, but the Control sample contains up to 2× more Al_2O_3 than all the Icelandic samples, which are dominantly iron-rich minerals (Table 3.2). The Control sample also contains very little iron but has a substantial amount of sodium and potassium (Table 3.2). The major oxides that were detected from the bulk chemistry analysis of the control sediments are also consistent with those identified in the literature on Canadian Syenite tailings (Chao et al., 1967; Gittins, 1961; Mitchell and Platt, 1982), as well as those from international sources (Burat et al., 2006; Jena et al., 2014).

Table 3.2: The chemical characteristics of the major oxides detected from the dust particles of the Control sediments in comparison to typical glaciogenic sediments and volcanic ash particles in mass percentage (wt. %).

Major Oxides [mass %]	Analytes	Samples		
		Ash	Control	Glaciogenic
		[wt %]		
	SiO_2	53.3	58.6	47.5
	Al_2O_3	12.8	23	11.5
	Fe_2O_3	10.8	1.9	13.8
	CaO	5.2	0.58	8.3
	Na_2O	4.597	9.81	2.5
	MgO	3.114	0.07	5.7
	K_2O	1.9	5.36	0.9
	TiO_2	1.651	< 0.01	2.6
	P_2O_5	0.45	0.02	0.4
	MnO	0.197	0.04	0.2
	SO_3	0.22	ND	0.15

*ND, not detected

3.4.2 Dust Profile: Temporal response of PM_{10} to varied wind frequency and duration

Wind gust and ramp runs were performed to understand the influence of the duration and frequency of the wind speed on dust entrainment and dispersion above the bed surface of two dissimilar sediments (Figs. 3.6 and 3.7): Glacio2 ($> 50\,\%$ Silt with high BET A_{surf}) and Control ($> 50\,\%$ Sand with low BET A_{surf}). Distinct peak PM_{10} concentrations emitted from Glacio2 and the control are observed at the start of a velocity stage (Figs. 3.6 and 3.7). The duration of the peak PM_{10} concentration appears to be dependent on the time interval of a velocity stage, and so the peak decays rapidly with the duration of the wind speed (Figs. 3.6 and 3.7). The maximum peak PM_{10} concentration is observed at the early and late stages of an experiment were performed at wind speeds of constant

(a, c and e) and varying (b, d and f) means, respectively. At an early stage after a peak in PM_{10} (a, c, and e), the bed surface becomes exhausted as the velocity exceeds threshold so that the subsequent peak PM_{10} concentrations are relatively much lower than the first peak of an experiment. A gradual increase in the PM_{10} concentration was observed for velocity stages at 15 s intervals (f).

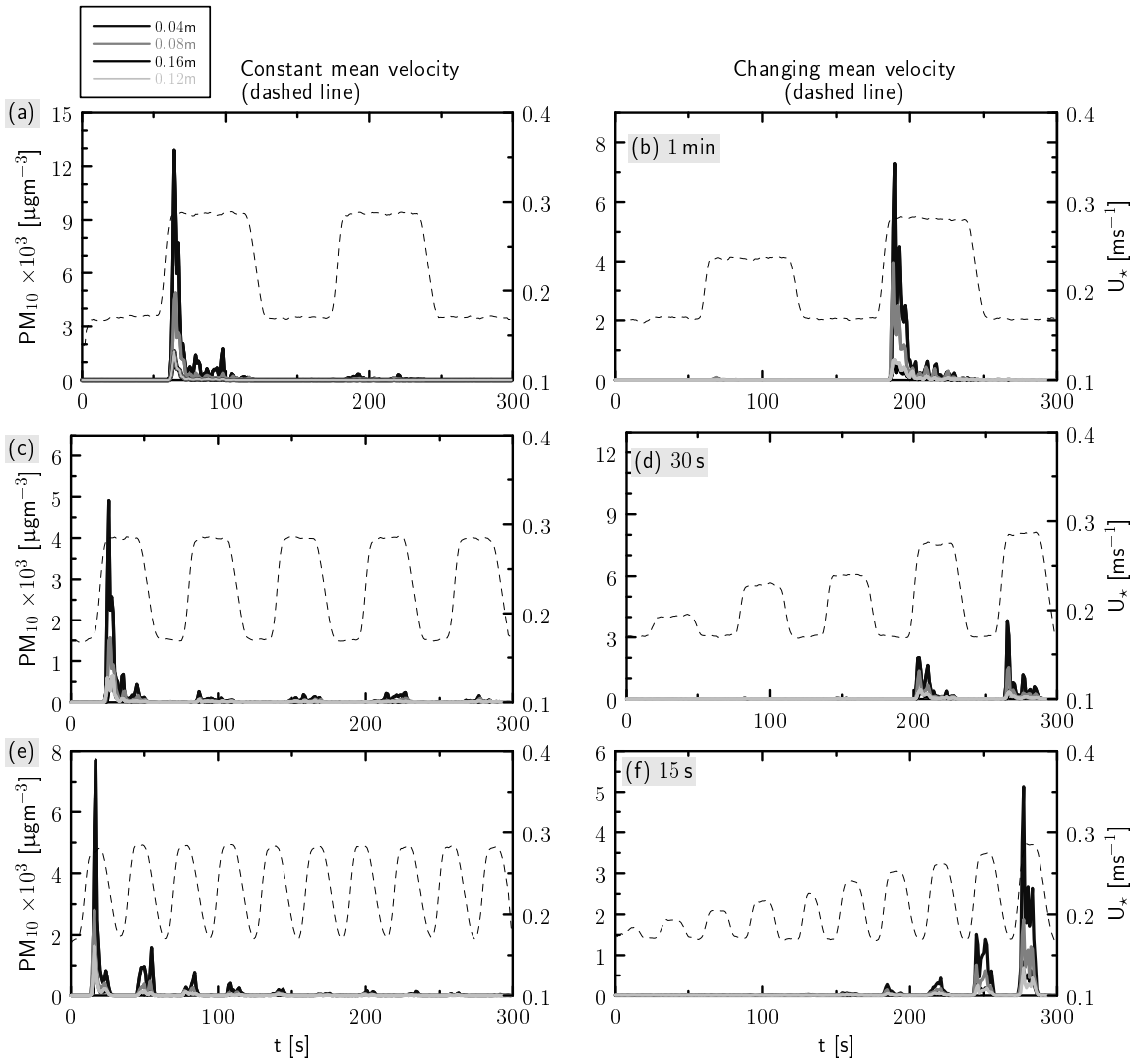

Figure 3.6: Temporal response of the PM_{10} concentration at varied wind speed (gust (a, c and e) and velocity ramp (b, d and f) up to 6 ms^{-1}) as measured at four elevations above the surface (0.04, 0.08, 0.12 and 0.16 m) for the Control sample. The dashed line represents the measured wind speeds at time intervals of 1 min (a - b), 30 s (c - d) and 15 s (e - f) over a duration of 5 min (300 s).

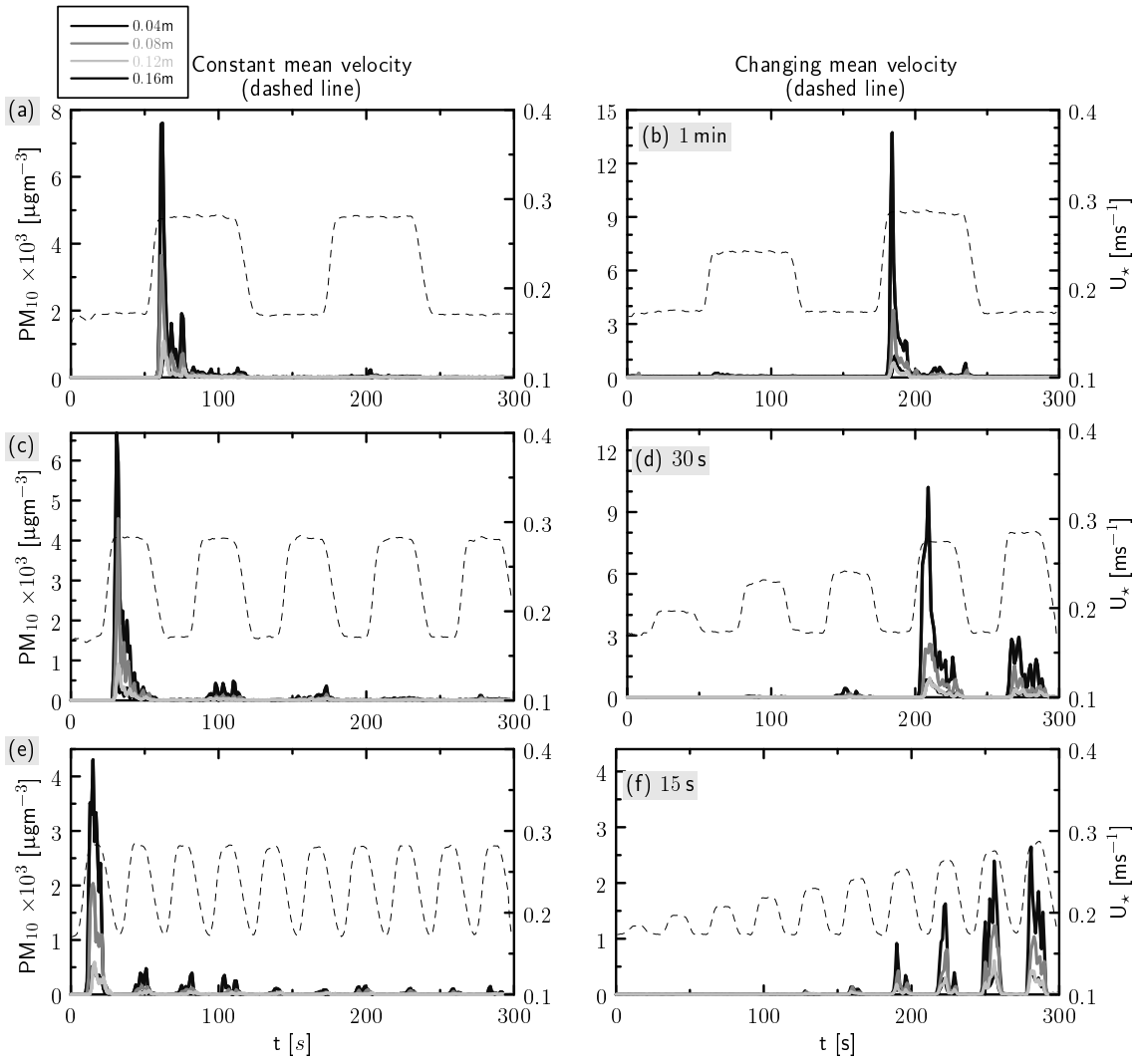

Figure 3.7: Temporal response of the PM_{10} concentration at varied wind speed (gust (a, c and e) and velocity ramp (b, d and f) up to 6 ms^{-1}) was measured at four elevations above the surface (0.04, 0.08, 0.12 and 0.16 m) for Glacio2. The dashed line represents the measured wind speeds at time intervals of 1 min (a - b), 30 s (c - d) and 15 s (e - f) over a duration of 5 min (300 s).

The PM_{10} concentration emitted from an active test surface is expected to decrease exponentially with elevation (e.g., Fig. 3.8), and so the vertical PM_{10}

profile follows an exponential function as:

$$c_{tz} = ae^{-(bz)}. \tag{3.10}$$

The time-averaged peak PM_{10} concentrations (c_{tz}) evaluated at each of the four elevations for varied frequency and duration of wind speeds were used to obtain the vertical dust profiles shown in Fig. 3.8. Although Glacio2 (silty) and the control (sandy) samples have the highest and lowest BET A_{surf}, respectively, as compared with all the other samples (Fig. 3.4), the vertical dust profiles are similar with absolute values of b ranging from 0.16 to 0.18 (Fig. 3.8), suggesting that the vertical diffusion of dust above the surface is also similar. This result also suggests that the effects of the particle texture are more significant than the particle A_{surf}.

The wind ramp runs of Glacio2 at varied time intervals, particularly at 15 s, show that the time-averaged PM_{10} concentration is an order of magnitude higher than those for all other experiments. The wind velocity ramp cycle at intervals of 15 s was also used for other experiments as more distinct peak concentrations were obtained, as compared to the other velocity cycles, to assess F and E, which will be discussed later in Subsection 3.4.3 below.

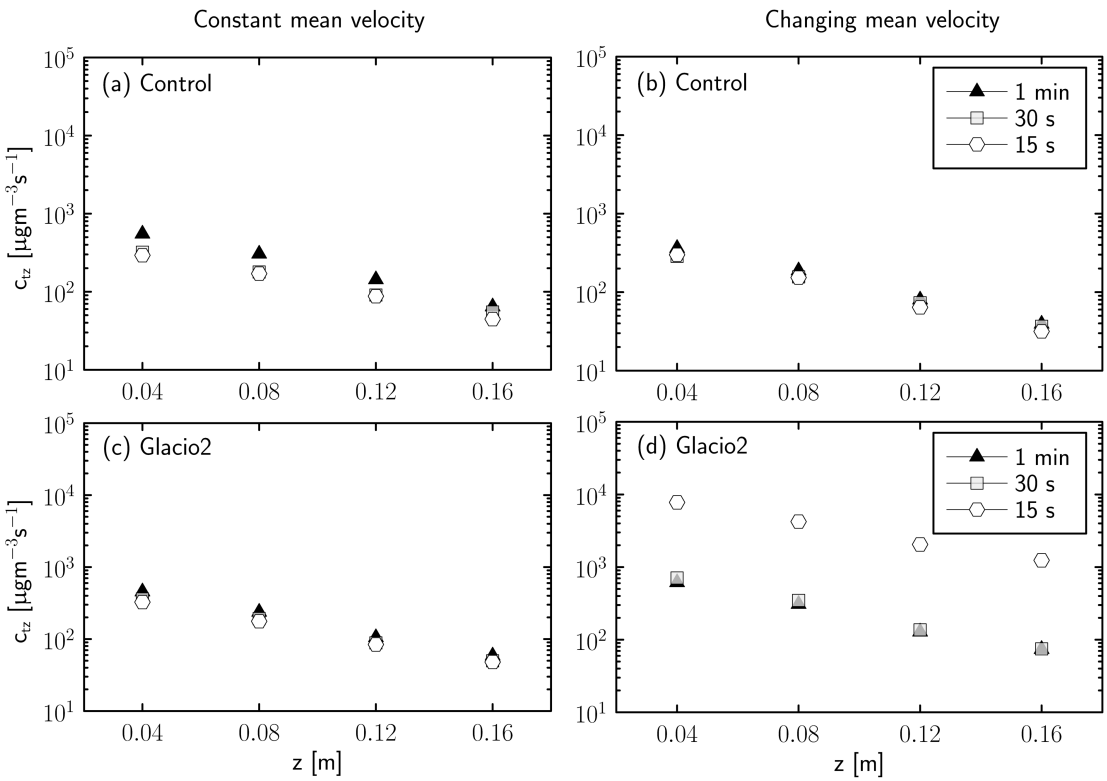

Figure 3.8: The vertical dust profiles show the time-averaged peak PM_{10} concentration at elevations of 0.04, 0.08, 0.12 and 0.16 m above the surface over 6 replicates of wind gust (a and c) and velocity ramp(b and d).

3.4.3 Dust cloud: temporal variation, vertical profile and airborne particulates

The temporal response of the PM_{10} concentration shows that discrete emission events are associated with the frequency of the wind speed (Fig. 3.9). The PM_{10} concentration emitted at a very early time represents the removal of extremely loose dust created from the preparation of the bed, which becomes stabilize ($1-2$: Fig. 3.9d). An increase in wind speed results in a new emission peak typically lower than subsequent peaks, showing a gradual increase of the PM_{10} concentration

Table 3.3: Quantity of dust fractions relevant to respiratory health, expressed as cumulative volume % for the three dustiest samples following the results in Fig. 3.4.

Samples	***Vertical PM_{10} Profile***		
	Coefficient (a)	**Exponent** (b)	**R squared** (r^2)
Ash	3136	0.14	0.97
Mixed	787	0.16	0.93
Glacio1	1320	0.14	0.92
Glacio2	13516	0.18	0.94
Glacio3	60178	0.19	0.94
Control	11966	0.16	0.96

at varied mean wind velocities (Ash, Mixed and Control). This observation is consistent with the outcome of Macpherson et al. (2008), who describe the episodes of dust concentration as an "*active emission behaviour*". While a new emission peak is observed at the start of each velocity stage (Fig. 3.9), the peak PM_{10} concentration for some of the samples did not show a gradual increase (Glacio1, Glacio2 and Glacio3). This observation is also consistent with other findings of Macpherson et al. (2008) and is described as a "*suppressed emission behaviour*".

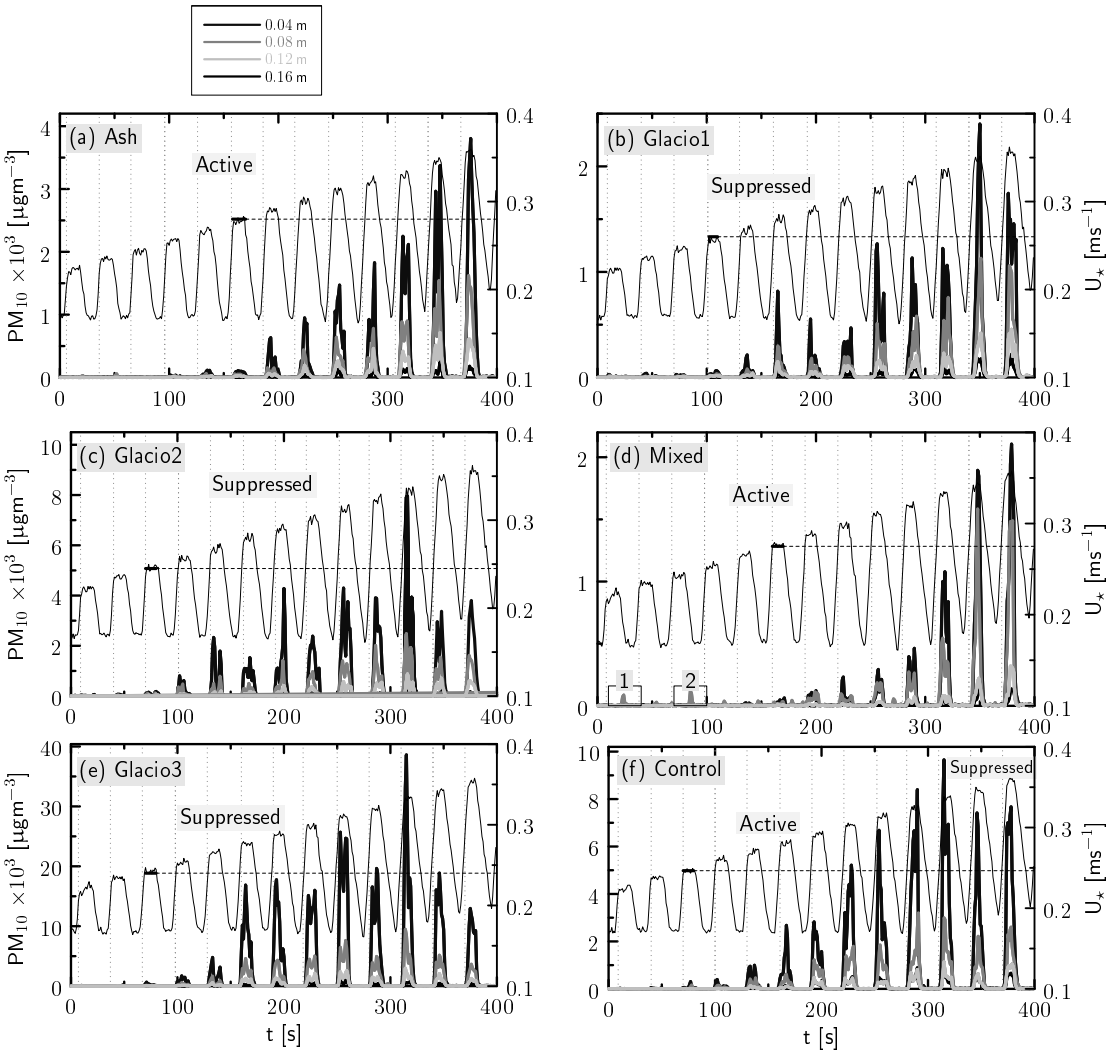

Figure 3.9: The temporal response of the PM_{10} (μgm^{-3}) concentration measured at four elevations above the surface shows examples of an active (a, d and f) and suppressed (b, c and e) emission behaviours (Macpherson et al., 2008). The vertical dotted lines correspond to the start of a new velocity stage, which ranges from 4.5 up to 7.5 ms^{-1}. d) The insets labeled as 1 and 2 show early peak PM_{10} of loose dust associated with the bed preparation. The horizontal dashed line corresponds to the value of $u_{\star t}$.

The glaciogenic samples demonstrate a "*suppressed emission behaviour*", but only those containing mostly coarse silt and sand particles with large BET A_{surf}

emit large PM_{10} concentrations comparable to the Control sediments, which contain predominantly sand. Active surfaces containing fine particles with varied BET A_{surf} emit low PM_{10} concentrations. However, of the three samples that contain $> 40\,\%$ clay (Ash, Mixed, Glacio1), Glacio1 contains the most fines with the largest BET A_{surf} emitted the most particulates. This result would appear to suggest that the BET A_{surf} may influence dust dispersion above the bed surface when the samples are predominantly fine.

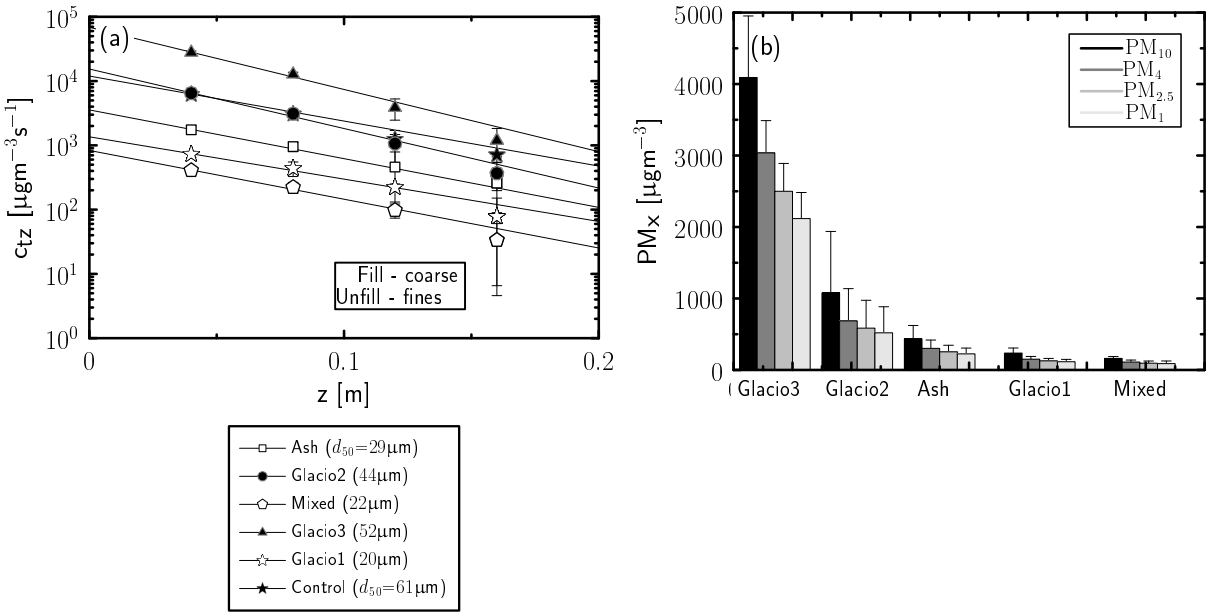

Figure 3.10: a) The vertical profile of the time-averaged PM_{10} concentration (c_{tz}) measured at four elevations above the surface at $u_\star = 0.31$ ms^{-1}. The values of d_{50} for each sample are shown in the brackets within the legend. b) Average airborne particulates (PM_1, $PM_{2.5}$, PM_4 and PM_{10}) measured at an elevation of $z = 0.16$ m and $u_\star = 0.31$ ms^{-1} with the error bars showing the standard deviations.

Only the control sediments comprised of $> 50\,\%$ sand (Table 3.1) with low BET A_{surf} demonstrate an "*active emission behaviour*" while releasing large PM_{10} concentration as compared to those with high BET A_{surf} (Glacio2, Glacio3) that show

a "*suppressed emission behaviour*" (Fig. 3.9 c and e). These samples (Glacio2, Glacio3, Control) containing predominantly coarse sediments also emitted the largest PM_{10} concentrations as compared to those with more clay and fine silt (Ash, Mixed and Glacio1). It would appear that saltation is the driving mechanism for dust ejection from a test surface, as suggested in the work of Del Bello et al. (2018) and Mockford (2017).

The peak PM_{10} concentration decreases with the frequency of the wind speed (Fig. 3.9: b, e and f), as the sediments are exhausted and the test surface becomes "*supply limited*". The active surface of the control sediments becomes slightly suppressed at time > 300 s (Glacio2, Glacio3 and Control) because the supply of dust particles has become exhausted (Fig. 3.9f). The samples with predominantly finer materials ($> 40\,\%$ clay) require higher wind speeds to overcome bonding forces and eject particles from the test surface. An Icelandic sand particle has low interparticle cohesion relative to its mass as compared to a fine dust particle that is angular, porous and has high interparticle bonds. Therefore, sand particles are easier to be ejected from the surface at low wind speeds than fine dust particles (Chapter 1).

A sand trap centered downwind of the test surface on the tunnel floor measured a maximum of $2\,\mathrm{gs}^{-1}$ of sand for the entire duration of several pilot runs. The portion of sand was considered to be negligible, and the trap was removed from these experiments. As expected, the values of $u_{\star t}$ range from 5.07 to 5.28 ms^{-1} for Glacio2, Glacio3 and the Control, which are lower than those ($u_{\star t} = 5.96 - 6.04\ \mathrm{ms}^{-1}$) observed for the Ash, Mixed and Glacio1 containing finer materials (Fig. 3.9).

Table 3.4: The values of the coefficient (a), absolute exponent (b) and regression (r^2), describing the vertical profile of the time-averaged PM_{10} concentration (c_{tz}) measured for all samples at $u_\star = 0.31$ ms^{-1} (Fig. 3.10a).

Samples	***Vertical*** PM_{10} ***Profile***		
	Coefficient (a)	**Exponent** (b)	**Regression** (r^2, %)
Ash	3136	0.14	0.97
Mixed	787	0.16	0.93
Glacio1	1320	0.14	0.92
Glacio2	13516	0.18	0.94
Glacio3	60178	0.19	0.94
Control	11966	−0.16	0.96

The vertical dust profiles are determined from the time-averaged peak PM_{10} concentration (Eq. (3.6)) for 6 replicate measurements at a maximum value of $u_\star = 0.31$ ms^{-1} (Fig. 3.10a). The vertical profiles scale in the same order as the median diameter (d_{50}) of the Icelandic samples, except for Glacio1 (Fig. 3.10a), suggesting that sandblasting is a key mechanism for dust entrainment.

The absolute values of b ($0.14 - 0.16$) for the Icelandic samples dominated by fine dust with low BET A_{surf} are slightly lower than those ($0.18 - 0.19$) dominated by coarse silt and sand with high BET A_{surf}, except for the Control sediments with low BET A_{surf} (Table 3.4). This result suggests that there may be better dust diffusion within the boundary layer when the samples contain more coarse particles with high BET A_{surf}. The slopes of the vertical profiles for the Control and Glacio2 sediments (Fig. 3.8) are similar to those obtained in Fig. 3.9, showing consistency with the outcome of the experiments in Subsection 3.4.2. The values

of the coefficient (a) for all the samples, inclusive of the Control sediments, containing more coarse particles are up to 2 orders of magnitude higher than those containing more fines (Table 3.4), showing that a is strongly dependent on the sediment texture consistent with the findings of several field studies in the literature (Baddock et al., 2017; Dagsson-Waldhauserova et al., 2014; Prospero et al., 2012; Thorsteinsson et al., 2011).

The airborne particulates (PM_1, $PM_{2.5}$, PM_4 and PM_{10}) were measured simultaneously by a model 8530 TSI DustTrak^{TM} positioned downwind of the test surface at an elevation of 0.16 m shows that up to 50 % of the measured PM_{10} are PM_1 concentrations (Fig. 3.10b). This result would suggest that the impact of saltators may have ejected dust coats adhering to the external surface, within the pores and fractured edges of the particles, supporting the findings of Mockford (2017), who showed that mechanical abrasion of coarse Icelandic particles creates dust particulates.

3.4.3.1 Measured PM_{10} emission rate

The average peak PM_{10} for values of $u_\star$ ranging from $0.22 - 0.31$ ms^{-1} (Fig. 3.11 c - d) was used to determine the PM_{10} emissions: E (Eq. (3.7)) and F (Eq. (3.2); $z_1 = 0.04$ m and z_2 equals either 0.12 m or 0.16 m). An example of the variation in E and F for a range of $u_\star$ values and a total of six replicate measurements obtained from Glacio2 is shown in Fig. 3.11 a - b. The values of E and F show a good agreement, and a gradual increase with $u_\star$ (Fig. 3.11 c - d) for all samples, which show an *active* and *suppress emission behaviour*. In an experiment, where the PM_{10} peak concentrations appear to be suppressed (Fig. 3.9 b, c and e), multiple peaks are formed during each episode of emission that results in relatively higher PM_{10} emission rates as compared to those that show an *active emission behaviour*

(Fig. 3.9).

Despite the similar range of $u_\star$ values, the PM_{10} fluxes are distinct for all Icelandic samples, but those for Glacio2 are similar to those for the Control sediments. Glacio2 has a slightly lower threshold friction velocity ($u_{\star t}$) than the Control, although the Control sediments contain coarser sand fractions (d_{50} up to 18 % higher), suggesting that the particle size characteristics influence dust entrainment. The values of E and F vary as a power law function of $u_\star$ and are larger for samples with more coarse particles (fill; Fig. 3.11c) as compared to those with more fine particles (unfill; Fig. 3.11c). The most emissive sample is Glacio3 with values of E up to an order of magnitude higher than all other samples, inclusive of the Control.

A linear plot of the values of E against F for all samples, inclusive of the Control, shows a strong agreement with a 1 : 1 ratio and a high correlation (Fig. 3.11d; $r^2 = 0.99$). At extremely low values of $u_\star$, the values of F slightly underestimate those for E, consistent with the outcome of Sanderson et al. (2014), although the experimental conditions in the present study differ significantly from those in the study of Sanderson et al. (2014). There is a slight deviation of the PM_{10} fluxes from the 1 : 1 ratio at low magnitudes (Fig. 3.11b), which does not appear to be as large as that in the study of Sanderson et al. (2014). This slight variation is caused by the high degree of resolution of E, which is more sensitive to small fluxes.

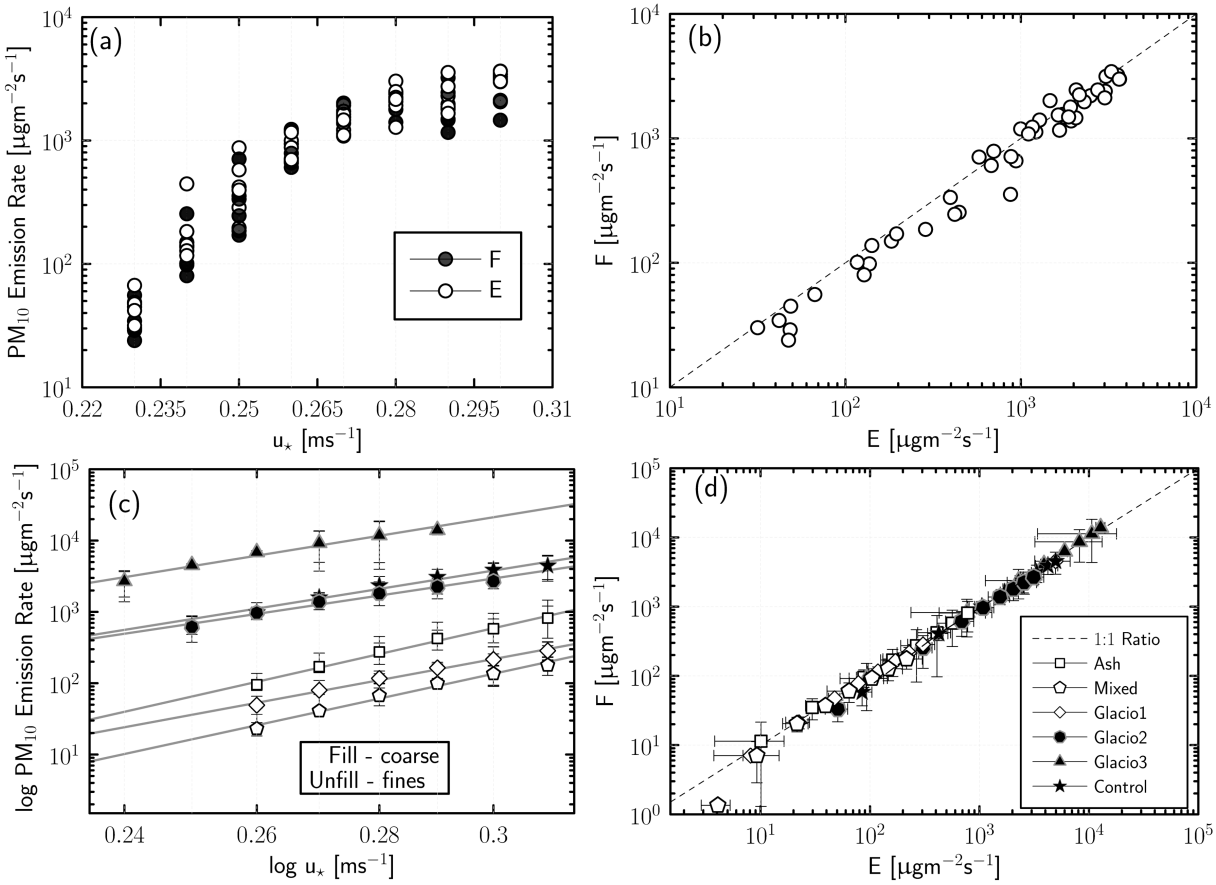

Figure 3.11: PM_{10} emission rates at varied friction velocity: a) as for example, those obtained for 6 replicate measurements of Glacio2. b) A linear plot of the PM_{10} emission rates showing a 1:1 ratio of F to E with a high correlation (r^2>0.95): b) Glacio2 and d) all samples. c) A comparison of the logged PM_{10} emission rate for all Icelandic samples, as well as the Control.

3.4.4 Comparing the vertical dust fluxes (field and laboratory studies)

The vertical dust fluxes for eroding soils in several well-established field studies and the present laboratory study (e.g., Ash and Glacio1 to 3) show a significant degree of variation within the datasets for the given samples (Fig. 3.12). The

variations between the sediment sources are caused by the differences between the surface characteristics, soil erodibility and saltation fluid threshold (Zobeck and Pelt, 2006), which differ within each study.

Vertical mass fluxes (F) were measured at Landeyjsandur (LAN1; Fig. 3.1), an active dust source in southern Iceland (Thorsteinsson et al., 2011, Fig. 3.11). The values of $u_\star$ were calculated from Eq. (3.9), using the wind velocity measured at an elevation of 2 m above the surface of $z_0 = 0.7$ mm (Arnalds et al., 2001; Thorsteinsson et al., 2011). For a grain diameter of 0.41 mm for medium sand within the source region (LAN1), Thorsteinsson et al. (2011) calculated $u_{\star t}$ to be 0.42 ms^{-1} based on the work of Liu et al. (2006). Landeyjsandur (LAN1), Markarflótssandur (Glacio2), and Markarfljótsaurar (Glacio3) are supplied with sediments from the same origin, Mýrdalsjökull glacier and Katla volcano (Fig. 3.1) as described in Chapter 2. The dust sources within these regions originate from frequent catastrophic meltwater floods (jökulhlaup) on the Markarfljöt river, which are triggered by the interactions between the Mýrdalsjökull glacier and Katla volcano (Fig. 3.1). The orders of magnitude of the measured PM_{10} fluxes for Landeyjsandur are comparable with those for Glacio2, as well as those from the Delta of the Slims River Valley, Yukon (Nickling, 1978), which has similar climate and sediment texture. However, they are up to an order of magnitude less than those measured for Glacio3. The measured PM_{10} fluxes for the Ash and Glacio1 are also comparable to those measured in lower latitude regions for varied surface texture and soil types (Fig. 3.11), although they contained $> 40\,\%$ clay.

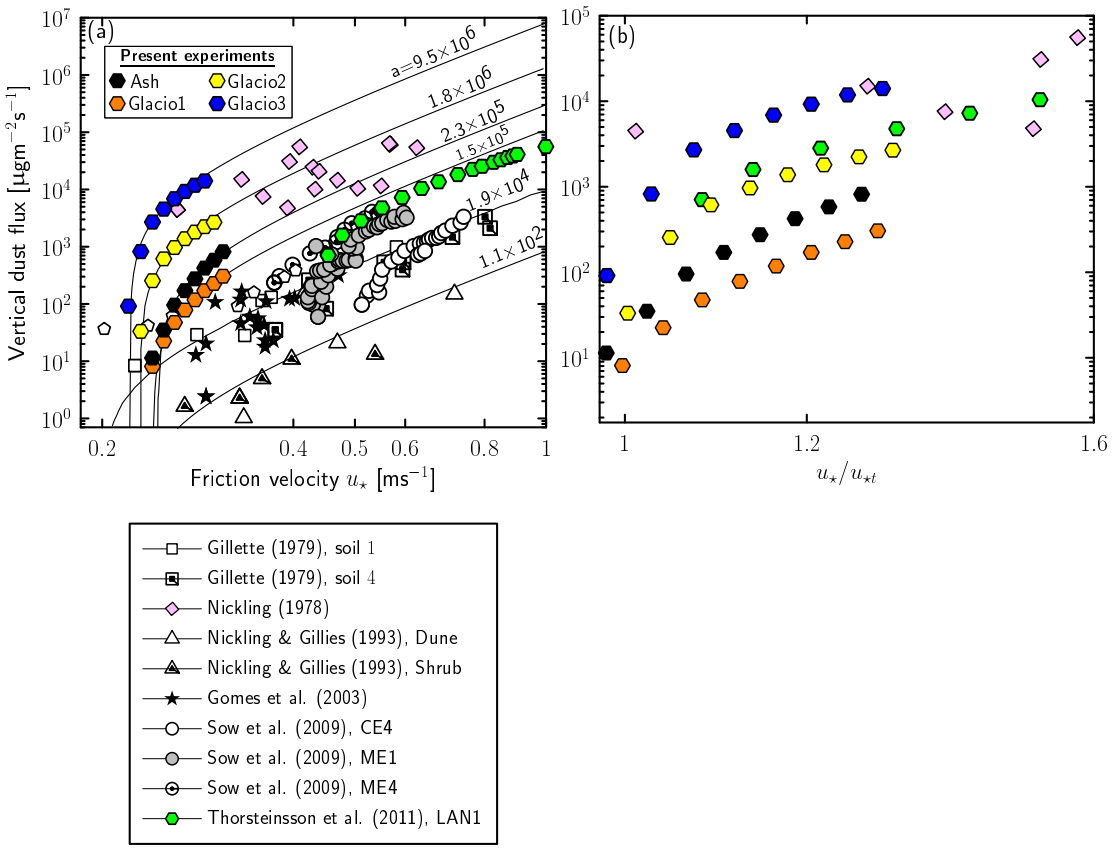

Figure 3.12: A comparison of the vertical dust flux (μgm^{-3}) measured for eroding soils in various field studies with those for the Icelandic samples. The solid lines represent the dust emission model of Gillette and Passi (1988) fitted in a least square regression to each of these datasets along with respective values for the coefficient (a).

The dust emission model of Gillette and Passi (1988, Fig. 3.9) was used to fit the measured PM_{10} fluxes at varied friction velocity along with the respective values of the coefficient (a, Fig. 3.11), which show a good agreement as compared to those from the model of Shao et al. (1993). As expected, the order of magnitude of the coefficient (a) in Eq. (3.7) increases for more emissive surfaces (Fig. 3.11). The values of F from the present laboratory study show a rapid increase over a short range of values for $u_\star$, as compared to those from the field studies (Fig. 3.11),

where the aerodynamic surface roughness and turbulence length scales are indeed larger than in the wind tunnel. However, the scaling effects are reduced when the flux datasets are re-plotted in Fig. 3.11b as a function of the normalized friction velocity, $(u_\star/u_{\star t})$. The dust fluxes measured in the study of Thorsteinsson et al. (2011) now appear to overlap directly with those for Glacio2, although the aerodynamic surface roughness and elevation of PM sampling at Landeyjsandur are up to 2 orders of magnitude higher than in those in the present study.

3.5 Conclusions

Dust emission processes within high latitude cold climate environments, such as Iceland, which is primarily associated with glaciofluvial processes and occasional volcanic eruptions, are becoming increasingly important, as new source regions are exposed with glacier retreat and depleted dust sources are replenished with ash deposits. The present study identifies the physical characteristics that strongly influence the entrainment, dispersion, and emission of Icelandic volcaniclastic particles at low relative humidity. The results show that:

(i) The sediments containing a higher portion of coarse silt and sand appear to be the most emissive, as compared to the finer sediments with more PM_{10} but less sand.

(ii) The sediments predominantly containing coarse particles generate the most airborne particulates during the wind tunnel experiments as compared to those directly measured by the Horiba PSA before these experiments were performed, as well as those emitted from the samples containing $> 40\,\%$ clay.

(iii) The sample containing the largest portion of fine particles with the largest

BET surface area emitted the largest quantity of particulates as compared to the other fines (e.g., Ash and Mixed).

(iv) The Icelandic dust emission rates measured in the wind tunnel experiments for the coarse glaciogenic samples are similar in magnitude to those measured in field studies within other high latitude regions with similar geomorphology and climate (e.g., Landeyjasandur: Thorsteinsson et al., 2011).

Chapter 4

Icelandic dust ejection by a water droplet impact in still air and winds

4.1 Introduction

Icelandic desert regions are one of the most studied high latitude cold climate (hlcc) environments ($\geq 50°$N, Bullard et al., 2016) because they provide an accessible and highly suitable analogue for similar present day and historical settings. Iceland is an active dust region in which glaciofluvial channel systems and volcanic eruption plumes supply sediments that create large extensive outwash plains (sandurs) and replenish exhausted dust surfaces, respectively. These regions are rapidly expanding with glacial retreat and the exposure of new dust sources. Given the sparsity of vegetation in Iceland and the high frequency of surface winds, up to 500 Mg of particulate matter (PM) is injected into the atmosphere each year (Arnalds, 2005; Duce et al., 1991; Gislason, 2008).

Saltation bombardment is considered the primary mechanism for the entrainment of wind-blown dust (Bagnold, 1941; Gordon and McKenna-Neuman, 2009). In Iceland, the climate and consequent weathering of the particles are different from hot deserts, and so other mechanisms, such as rain droplet impact, enhance dust entrainment and emission. The city of Reykjavík experiences poor air quality and high suspended particulate matter (PM) concentrations during periods of low-to-moderate rainfall and windy conditions (e.g., up to 6 ms^{-1}: Ashwell and Hannell, 1960; Prospero et al., 2012). Field workers report that dust emission often coincides with the onset of a precipitation event in several source regions outside the city of Reykjavík (Ashwell and Hannell, 1960; Prospero et al., 2012).

When a rain droplet with sufficient kinetic energy (E_k) strikes a bare soil surface, it ruptures and collapses to form a thin disk of fluid that spreads radially outwards from its central point of contact with the surface (Ellison, 1944; Rose, 1960). The high pressures associated with the water droplet impact, im-

part vertical stresses within the soil, thereby creating a compression crater with a compensatory bulge around the perimeter of the rim of the crater (Huang et al., 1983; Terry, 1998). As the fluid thins, the vertical stresses are transformed into horizontal shear forces that act radially outwards away from the original impact position to detach soil particles (resting along the side and bottom) away from the landing position of the droplet.

The outward radial spread of the droplet leads to the formation of several daughter ejection droplets that jet away from the impact origin in parabolic trajectories (Erpul et al., 2009; Terry, 1998; Worthington, 1908). The motion of the ejectors is controlled by gravity, friction, and wind drag (Terry, 1992). The formation of the crater is dependent on the vertical compression and lateral shear stress exerted by the water droplet on the soil surface. The morphology of the crater (e.g., wide and shallow, or deep and narrow) is dependent on the shear strength of the soil (Al-Durrah and Bradford, 1982), but the size of the crater appears to be dependent on the diameter and impact velocity of the water droplet (Mihara, 1952). The ejection of soil particles and water away from the impact zone is called "*splash detachment*".

There are two main factors that control the splash detachment (Terry, 1992) in a 2 dimensional (*x-horizontal* and *z-vertical*) space: the soil erodibility (e.g., particle size, interparticle cohesion: Legout et al., 2005) and droplet erosivity (e.g., size, shape, density, velocity: Epema and Riezebos, 1983). For instance, the study of Legout et al. (2005) shows that particles 50 µm to 2000 µm in diameter are typically ejected as discrete particles while fine dust particles $\leq$ 50 µm in diameter are transported within the daughter ejections, although some of the ejected particles are wet. The droplet erosivity is the ability of the droplet to exert vertical compression and lateral shear stress that can detach particles from

the test bed (Epema and Riezebos, 1983).

Dust detachment by the impact of a rain droplet under wind-driven conditions differs from that in still air. Rain splash erosion in still air creates a transport-limited system because the aggregates and liquid marbles are not ejected to a considerable distance away from the source but rather fall back to the surface (Kinnell, 2005; Kinnell and Risse, 1998). In comparison, winds during rain splash erosion can break up a portion of ejected aggregates, desiccate liquid marbles coated with particles, disperse non-wetted particulates, and initiate saltation that leads to the transport of particulates (Erpul et al., 2009). The morphology of the droplet also deforms under varied wind conditions, thereby affecting dust detachment. Alteration of the shape and size of the droplet (Boxel, 1998; Disrud and L. Lyles, 1969; Riezebos and Epema, 1985), as well as its impact angle, velocity and kinetic energy (Erpul et al., 2009, Fig. 4.1), influences the counterbalance effects of the gravitational (F_G) and drag (F_D) forces. An obliquely distorted rain droplet will displace more soil particles downwind of its impact position in the direction of the winds (Vieira et al., 2004), as compared to still air.

Raindrop impact is, therefore, an important process that may initiate soil erosion (Ellison, 1947; Morgan, 1978; Young and Wiersma, 1973). The influence of wind drag upon raindrop impact is widely documented in the literature (Ellison, 1947; Morgan, 1978; Terry, 1998; Young and Wiersma, 1973), but its effects on near-surface dust entrainment and dispersion are not well understood, as compared to sand transport processes (Erpul et al., 2003, 2008). This study aimed i) to quantify the response of dust emission within a splash structure arising from the surface upon the impact of a water droplet, and ii) to evaluate the particle (e.g., size, BET surface area), water droplet (e.g., size, shape, velocity and kinetic energy) and crater (e.g., size) morphologies, as well as the splash dimensions (e.g.,

base diameter, height and spread), in order to understand the factors influencing Icelandic dust dispersion in still air and within a shearing flow.

4.2 Methodology

This section provides a detailed outline of the experimental design and materials used to observe and quantify the effects of a water droplet impact on sediments that are representative of a range of Icelandic dust sources. The experiments were performed in still air and under wind-driven conditions at droplet release heights of 0.36 m, 1.52 m and 3.54 m (Table 4.1). Most of the experiments in still air were performed on top of a lab bench ($S1$), as well as within a stairwell ($S2$), but all those in a shearing flow were carried out in the Trent Environmental Wind Tunnel (WT; Table 4.1). An overview of the water droplet splash process in this study is also provided in Fig. 4.1. All experiments in the present study were performed at $T = 19 \pm 1°\text{C}$ and $RH = 30(\pm 2)\,\%$ to remove the effects of climate.

The methods involve the use of several technologies: an Horiba Partica LA-950 V2 particle size analyzer (PSA) to measure the size distributions of the samples, pitot tube to measure the steady-state streamwise velocity ($\overline{u}(z)$), dustTrak$^{\text{TM}}$ to quantify the dust concentration, and a high-speed PCO.Dimax™ camera to record images of the particle splash structure, which are further analyzed using Matlab image processing software (Table 4.1).

4.2.1 Sample site and characterization

Sediments collected at four different site locations in northeast and southern Iceland were used to perform this study. The samples included 2010 Eyjafjallajökull volcanic ash deposits (ash), a mixture of ash and glaciogenic dust (mixed), glacio-

Table 4.1: An overview of the methodology used to investigate a water droplet impact upon test beds containing Icelandic dust, under still air and windy conditions.

Parameters			**Methodology** (Technology)	**Experiment setup**		
	Characteristics	**Definition**		($S1$) **Bench**	($S2$) **Staircase**	(WT) **Wind Tunnel**
Samples	Particle size (median)	d_{50}	Horiba Partica	(Wet-sieved) Ash Mixed Glacio1 Glacio2	Wet-sieved Ash	original Ash
Boundary layer	Streamwise velocity	$\overline{u}(z)$	Pitot Tube	still air	still air	still air and winds
	Aerodynamic roughness	z_o				✓
	Friction velocity	$u_\star = \frac{k\overline{u}(z)}{\ln \frac{z}{z_o}}$				✓
Water droplet	Height	z	(see text)	0.36 m	3.65 m	1.52 m
	Shape (sphericity)	$\varphi = 4\pi A/P^2$	Matlab image processing	✓	✓	✓
	Angle	$\theta = \tan^{-1}(v_y/v_x)$	PCO.dimax™ camera			✓
	Velocity	$v = \sqrt{v_x^2 + v_y^2}$		✓	✓	✓
	Kinetic energy	$E_k = \frac{1}{2}mv^2$		✓	✓	✓
Dust plume	Dust Concentration	PM_{10}	DustTrak™ Aerosol monitor			✓
	Drag Force	$F_D = C_D \rho A v^2$	PCO.dimax™ digital camera			✓
	Cross-sectional area	A_{upwind}	Matlab image processing			
		A_{downwind}				
		$A_{\text{total}=}$ $(A_{\text{upwind}} + A_{\text{downwind}})$				

genic dust 1 (Glacio1), and glaciogenic dust 2 (Glacio2). A detailed description of the sample site location is provided in Chapter 2, which addresses the particle characterization. All samples were wet-sieved to isolate the dust-size fractions ($\leq 50\,\mu m$), which then were used to perform the bench top ($S1$) and staircase ($S2$) experiments, but the original ash was not sieved for the wind tunnel (WT) experiments. The wet-sieved samples were oven-dried at 110°C for 24 hrs and then mixed vigorously before their particle-size distributions were measured using an Horiba Partica LA-950 V2 PSA. A field emission-scanning electron microscope (SEM) was used to image particles from all samples (Ash, Mixed and glaciogenic dust) to obtain information concerning their complex structures. The BET surface area (A_{surf}) of the Ash, Mixed and Glacio1 samples is reported in Figure 2.12 while A_{surf} for Glacio2 was measured in the same way as the other samples.

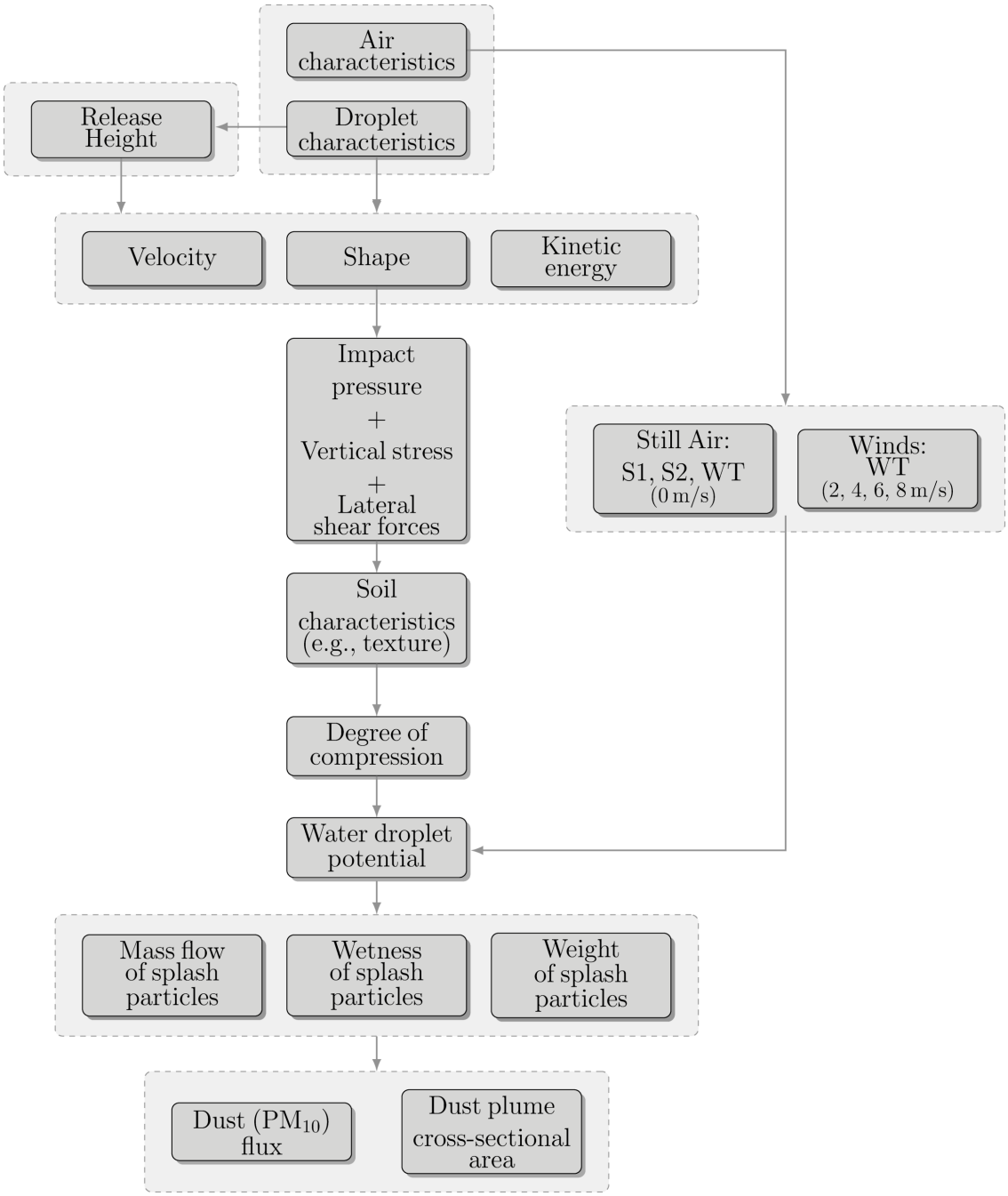

Figure 4.1: A summary of the water splash process as performed on top of bench ($S1$), within a stairwell ($S2$) and in a wind tunnel (WT).

4.2.2 $S1$ and $S2$ experiments

An 18 gauge, flat-end, syringe needle filled with distilled water was used to create a water droplet with a constant volume and diameter of about 9.2 µl and 2.6 mm, respectively. The water droplet was released from a vertical height of 0.36 m as measured from the tip of the needle to the point of impact upon the bed surface ($S1$), with an impact velocity of about 2.4 ms^{-1}. The low impact velocity experiments (2.4 ms^{-1}) were performed inside an enclosed room to minimize the ambient airflow to less than about 0.05 ms^{-1}, as measured by a portable hotwire anemometer. This velocity is less than those of typical rain droplets impacting a soil surface at a terminal velocity ranging from 9 to 13 ms^{-1} (Beard, 1976). In a second set of experiments, a droplet height of about 3.65 m was used to attain a higher impact velocity of $\sim$ 7.34 ms^{-1} ($S2$), which is comparable to a rain droplet, 2.7 mm in diameter, falling with a terminal velocity of about 7.7 ms^{-1} (Gunn and Kinzer, 1949), which is more representative of nature. Six replicates of each experiment were performed. The terminal fall velocity and kinetic energy of the water droplet were calculated as defined in Table 4.1, assuming a spherical droplet (Erpul et al., 2009).

To form a dust bed, selected samples were poured into a frame with inner dimensions 2 cm $\times$ 5 cm $\times$ 1.5 cm, and then tapped down with a glass microscope slide. The frame was slowly removed to maintain a fixed, smooth, pressed block of particles with the dimensions of the frame. Each test block was created on top of a transparent cellulose acetate sheet in order to recover all the dust particles after the $S1$ experiments (Fig. 4.2a).

Following the release of a water droplet, the splash (liquid water coated with particles) structure arising from the surface was recorded from side view using a high-speed PCO.Dimax^{TM} digital camera at a frame rate of 1.548 mHz (Fig. 4.2a).

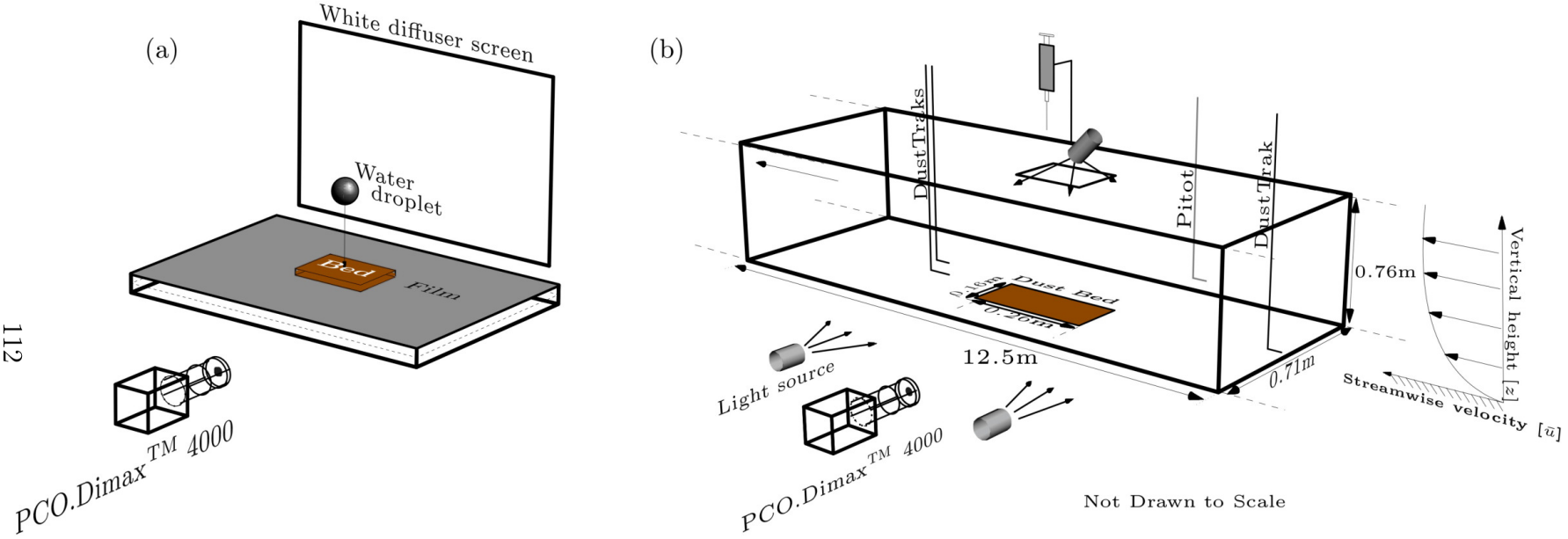

Figure 4.2: A schematic diagram of the experimental design performed on top of a bench ($S1$, $S2$; a) and in the working test section of Trent Environmental Wind Tunnel (WT, b).

The field of view of the digital camera was illuminated with 30 and 60 W bulb floodlights before recording the experiments. The dimensions (e.g., height, spread and base diameter; Fig. 4.3) were analyzed from the images of $S1$; details about the analysis are provided in Subsection 4.3.4 below.

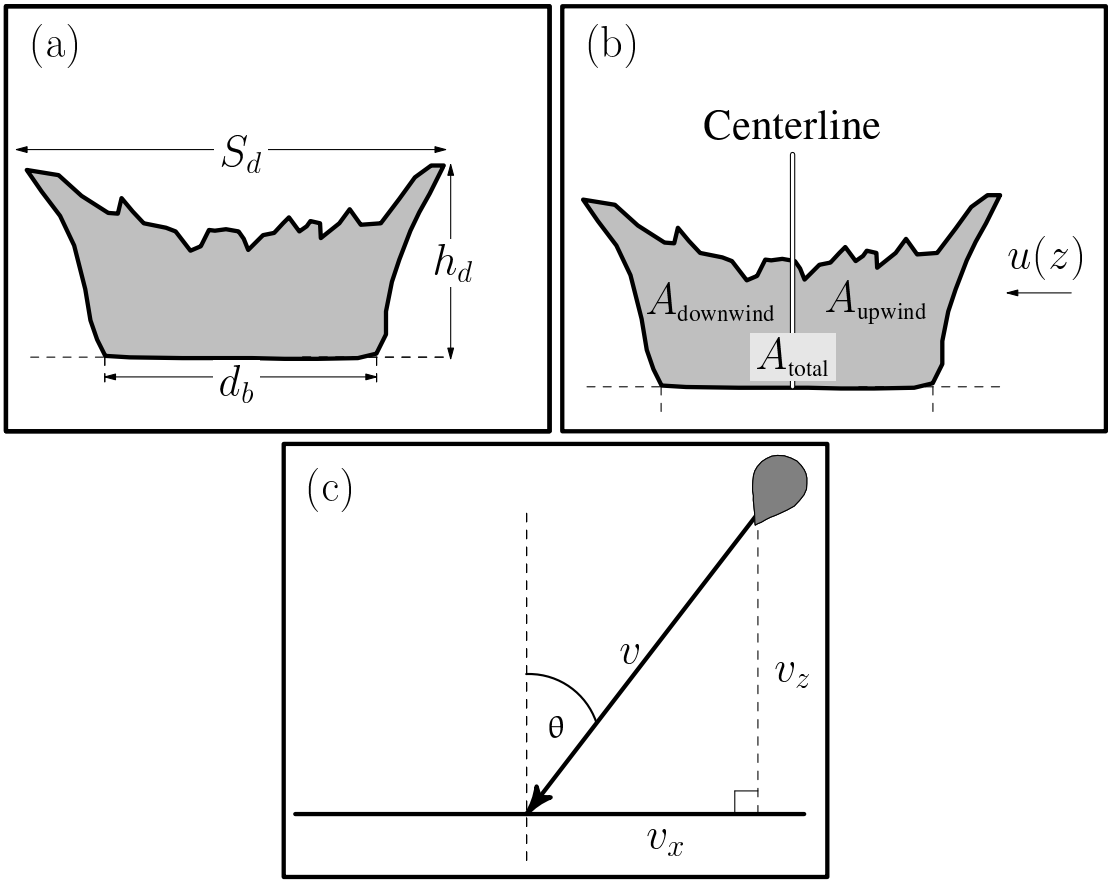

Figure 4.3: A schematic diagram showing the dimensions of the cross-sectional region of a dust structure a - b) arising from the surface: Spread (S_d), height (h_d), base diameter (d_b), and the total cross-sectional area (A_{total}), as well as the dimensions of the droplet impact c), where θ is the impact angle, v_x and v_z are the horizontal and vertical impact velocity components of the water droplet with resultant, v (Table 4.1).

4.2.3 WT experiments

A dry, loose plane bed created from the unsieved ash was used to perform water droplet impact experiments within a boundary layer flow (Table 4.1 and Fig. 4.2b) to simulate the initiation of some Icelandic dust storms. All experiments were performed in the working section of the Trent Environmental Wind Tunnel (WT, Fig. 4.2b) with a cross-sectional height ($H = 0.76$ m), width ($W = 0.71$ m), and length ($L = 12.5$ m, Chapter 3). TEWT is an open-looped, straight-line suction system that can be operated remotely from a control room. When TEWT is in operation, the airflow that enters the tunnel is directed through a compression bell with a honeycomb straightener. The airflow then is directed over an array of evenly spaced staggered wooden dowels, which hasten shearing within the turbulent boundary layer flow before entering the working test section. Further information about the TEWT facility and related instrumentation can be found in previous publications (McKenna-Neuman, 2003; Neuman, 2004) and online at `https://sites.google.com/view/tewt-at-trent/home`. Videos of the water droplet impact experiments can also be accessed through this website link.

The Eyjafjallajökull ash sample was loaded into a small tray of width ($w_t = 16.5$ cm), length ($l_t = 26.5$ cm), and depth ($d_t = 1.5$ cm, Fig. 4.2b), which is similar to the depth of the dust bed created in the $S1$ experiments. The sample tray was lowered into a cut-out section in the tunnel floor so that the dust surface lay flush with the floor and the boundary layer flow was not perturbed. White diffuser sheets were used to cover the walls and floor areas surrounding the test bed in order to illuminate the water droplet and dust structure for imaging. The sheets were laid flat and fixed to the surface to reduce disturbance of the airflow. The flat-end needle and syringe used to perform the $S1$ and $S2$ experiments were also used to perform the WT experiments to maintain a consistent volume of

water within each droplet. The water droplet was released from a vertical height of 1.52 m, up to 2× the height of the tunnel's roof (Fig. 4.2b, $H = 0.76$ m) to ensure that the droplet ejected sufficient PM for imaging. The water droplet was released through an opening of about 0.15 m in the tunnel roof with negligible effects on its properties.

Six vertical profiles of the steady-state streamwise velocity ($\overline{u}(z)$) were measured using a stainless steel micro-pitot tube, where the boundary layer flow is fully developed. The data were used to obtain the friction velocity ($u_\star$) and aerodynamic roughness length (z_o) from

$$u_\star = \frac{\kappa \overline{u}(z)}{\ln\left(\frac{z}{z_o}\right)}, \tag{4.1}$$

where $\kappa = 0.41$ is the von Kármán constant, and z is the elevation. The wind tunnel fan was then set to a predetermined rpm to obtain a constant freestream velocity of either 2, 4, 6 or 8 ms^{-1} for a given experiment. A micro-pitot tube was positioned at a fixed vertical height of 18.5 cm to sample the freestream wind velocity continuously.

The PM_{10} (particulate matter $\leq 10\,\mu$m in diameter) concentration was sampled while the particle splash evolution was recorded using the high-speed digital camera. The dust concentration profile was sampled each second using 3 non-isokinetic model 8532 TSI DustTrak$^{\mathrm{TM}}$ II aerosol monitors of precision, $\pm 2\,\mu\,\mathrm{gm}^{-3}$ (Appendix A). Two instruments were positioned in a vertical array at elevations of 20 mm and 50 mm, 2.2 m downwind of the leading edge of the tray and 2.4 m downwind of the droplet impact site. Another was positioned 4 cm above the tunnel floor at the entrance to the working section in order to sample the background dust concentration (c_b) of the airflow entering the tunnel. Before the droplet re-

lease, the tunnel fan ran at a requested freestream velocity over a 5-min duration to measure the background concentration (c_b). The values of c_b represent the particulate matter generated from air recirculation and extremely loose dust created from the bed preparation before the surface becomes stabilize. When a steady background was established, the water droplet was released. The values of c_b were subtracted from all PM_{10} concentration values to eliminate and compensate for dust advection. Extremely low PM_{10} concentrations were assumed to be zero in all experiments (e.g., Fig. 4.4).

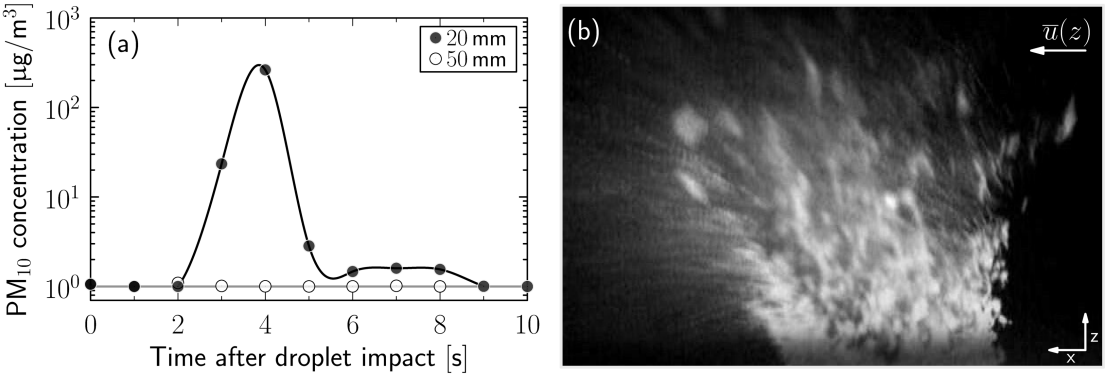

Figure 4.4: a) Temporal response of the PM_{10} concentrations sampled downwind of the impact site at 20 and 50 mm above the surface and at a wind speed of 8 ms^{-1} after the values of c_b are subtracted. The concentration measured at 50 mm is similar to the background levels. b) A sample image of the splash structure (developing plume of water and particulate matter, PM) after the average background image is subtracted at $\overline{u}(z)$=4 ms^{-1}.

4.3 Results & Discussion

4.3.1 Particle morphology: size and BET surface area

The scanning electron microscopic (SEM) images show examples of dust particles up to 20 μm in diameter that appear to be angular, rough, porous and contain fine dust aerosol aggregates cemented onto the exterior surface and within the pores (Fig. 4.4a - d). The cemented aggregates also appear to be irregularly shaped, up to 2 μm in diameter. The size distributions of the wet-sieved Icelandic samples ($S1$ and $S2$), as well as the Eyjafjallajökull ash (WT), are shown in Fig. 4.4f. The median particle diameters for the sieved Ash, Mixed and Glacio1 samples are similar ($d_{50} \sim 12\,\mu m$, Fig. 4.4f) but slightly finer than Glacio2 ($d_{50} = 18\,\mu m$). The Eyjafjallajökull ash used to perform the WT experiments has a substantial portion of coarse sand particles, with an approximate median of 27 μm (Fig. 4.4f). The values of BET A_{surf} are > 1 m^2g^{-1} for all Icelandic samples, suggesting that the particles are angular and porous (Fig. 4.4e) as described in Chapter 2. The glaciogenic dust samples have higher BET A_{surf} than those containing varied portions of volcanic ash.

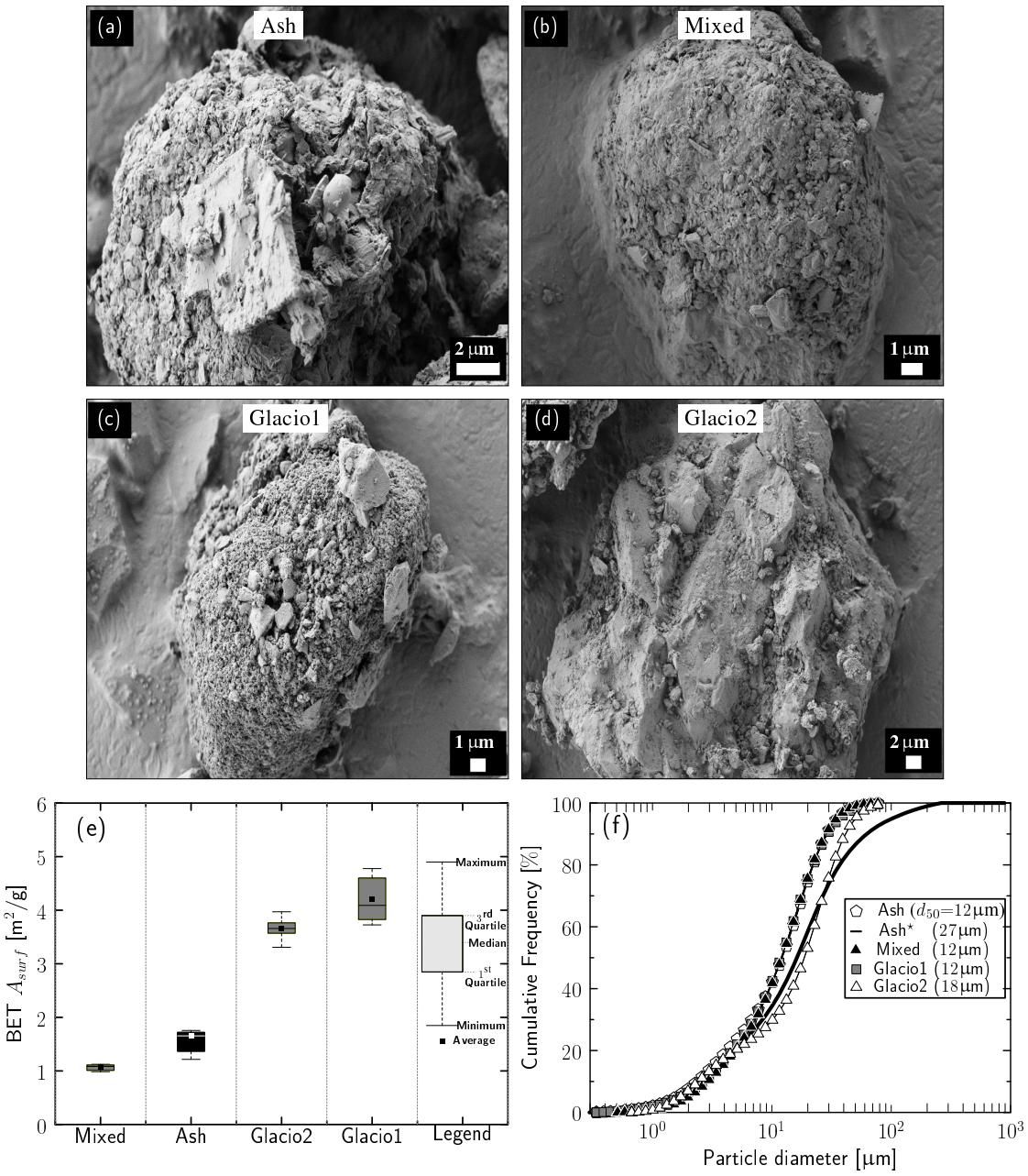

Figure 4.5: (a - d) Selected micrographs of angular, rough, porous Icelandic dust particles from each wet-sieved sample. (e) The size distributions for all Icelandic samples used in this study, where Ash* represents the unsieved Eyjafjallajökull ash used to perform the WT experiments.

4.3.2 Droplet morphology and dynamics

The physical properties (e.g., size, shape, velocity and kinetic energy) of each water droplet were quantified using Matlab image processing software according to an algorithm derived from the definitions provided in Table 4.1. The fundamental physics of these properties are well described in the literature (Ahn et al., 2012; Halliday et al., 2006; Yarin, 1984).

Boxel (1998) suggests that a water droplet > 2 mm in diameter becomes distorted as it falls through the air to attain terminal speed. To examine the effects of wind speed on the droplet shape, the sphericity (φ) of the droplet was assessed in the WT experiments. As described in Chapter 2, the sphericity ($\varphi = (4\pi A_s)/P^2$) is an index of the degree to which the droplet shape approximates that of a true sphere on a scale of 0 to 1, where P is the perimeter, and A_s is the cross-sectional area of the droplet. The values of φ decrease linearly with increasing wind speed ($\overline{u}(z)$) for all experiments (Fig. 4.6a, inset schematic). A net difference of up to 30 % in the droplet shape is observed for $0 \leq \overline{u}(z) \leq 8$ ms^{-1} (Fig. 4.6a), showing that wind drag strongly influences the shape of the droplet. The pressure differences surrounding the droplet contribute to the distortion of its shape; particularly in the case of the pressure reduction in the separated wake flow. The results from this study are consistent with the findings of Disrud and L. Lyles (1969), Riezebos and Epema (1985), and Boxel (1998).

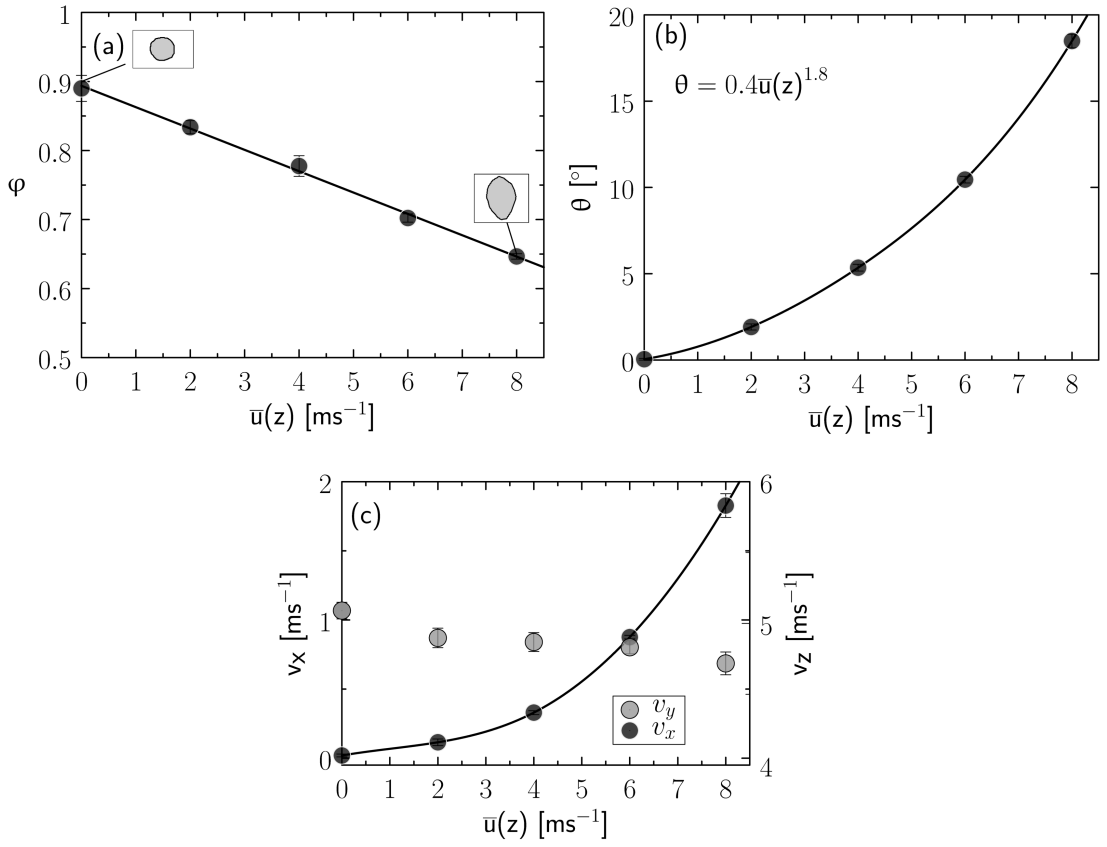

Figure 4.6: The physical properties of the water droplet inclusive of a) sphericity (shape), b) impact angle from the vertical, and c) impact velocity. The inset schematics show examples of the droplet shapes at 0 ms^{-1} and 8 ms^{-1} (not drawn to scale).

In the *WT* experiments, the impact angle (θ) increasingly deviates from the vertical (Fig. 4.2b) by up to 20° with increased streamwise wind velocity up to $\overline{u}(z) = 8$ ms^{-1}, with a high degree of correlation ($r^2 = 0.96$, Fig. 4.6b), which is consistent with the work of Heerden (1964), Umback and Lembke (1966), and De Lima (1989). As the droplet impact angle (θ) increases, the velocity component (u_x) acting horizontal to the soil surface increases while the vertical velocity component (u_z) decreases but remains larger than the values of u_x (Fig. 4.6c). This result shows that the gravitational effects are dominant over the wind drag effects,

although the lateral drifting of the droplet could potentially eject more dust from the bed surface upon impact (Fig. 4.6d).

The impact velocity (v) and kinetic energy (E_k) of each water droplet released from a height of 0.36, 1.52 and 3.54 m in $S1$, $S2$ and WT experiments (Table 4.1), respectively, were analyzed using Matlab image-processing software. The impact velocity (v) increases as a power function of the droplet release height with a high correlation factor ($v \propto h^{2.3}$; $r^2 = 1$) for all experiments performed in still air. This power function relationship shows a 5 % difference from those obtained in the study of (Hamlette et al., 2013, Fig. 4.7), who used a 6 µl water droplet released from a height of about 0.3 m, as compared to an approximate 9 µl droplet released from $z = 0.36$ m in the present study. The impact kinetic energy (E_k) of the water droplet is calculated from the square of the impact velocity, as the mass of the droplet is assumed to be constant with volume similar to a solid sphere (Table 4.1). The values of E_k vary almost linearly with the three release heights ($E_k \propto h^{0.9}$; Fig. 4.7). The impact angle (θ) of the water droplet shows little displacement from the vertical in still air ($S1$).

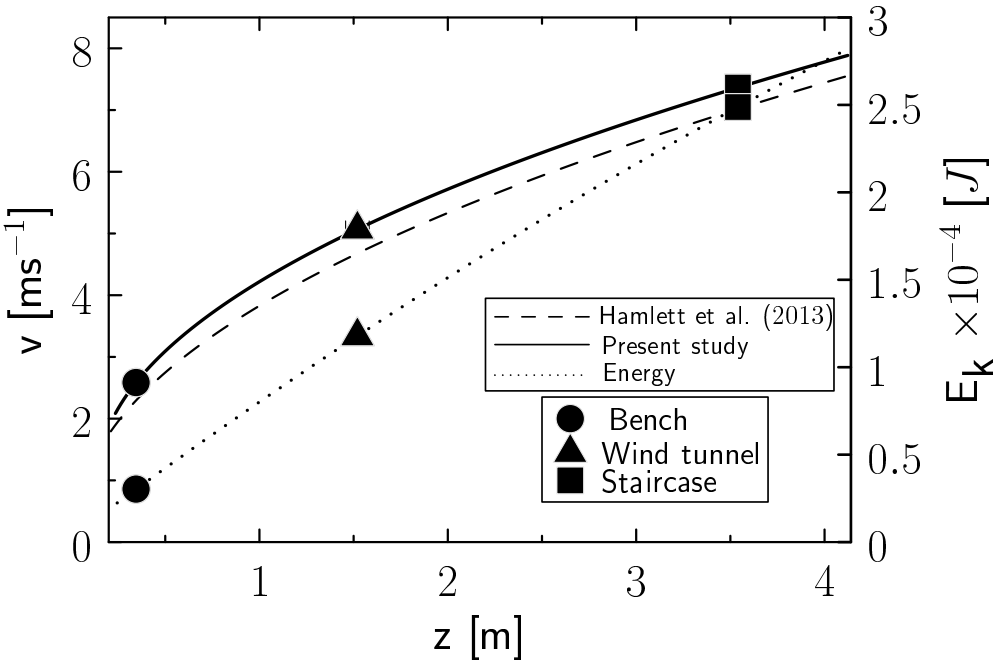

Figure 4.7: Relationship between the impact velocity (ms^{-1}) and release height (m) of a 9 µl water droplet released in still air as compared to those in the study of Hamlette et al. (2013) for a 20G needle dispensing 6 µl of distilled water in each droplet. The secondary axis shows the kinetic energy as a function of the release height.

In the $S1$ experiments, the water droplet generally rebounded at about 18 ms after impact upon the test bed (e.g., wet-sieved ash, Fig. 4.8), but it becomes coated with particles. The rebounding droplet remained above the surface for up to 20 ms, but in some cases the droplet rebound was slightly slower for Glacio2 than those for the other samples, which appears to be an effect of the particle diameter. This stage is further described in the work of Reyssat et al. (2006) and more recently Hamlette et al. (2013) in the case of hydrophobic particles. The water droplet experiences a radial inward pull after forming a thin disk upon impact, and so the water emerges at the top of the droplet at the central region of the crater. Observation of the drop rebound above the test bed reveals that the

rebounding column reaches a maximum height, remains poised for a short instant, and then descends back to the surface as the top of the water droplet collapses upon itself, and absorbs into the bed (Fig. 4.8f).

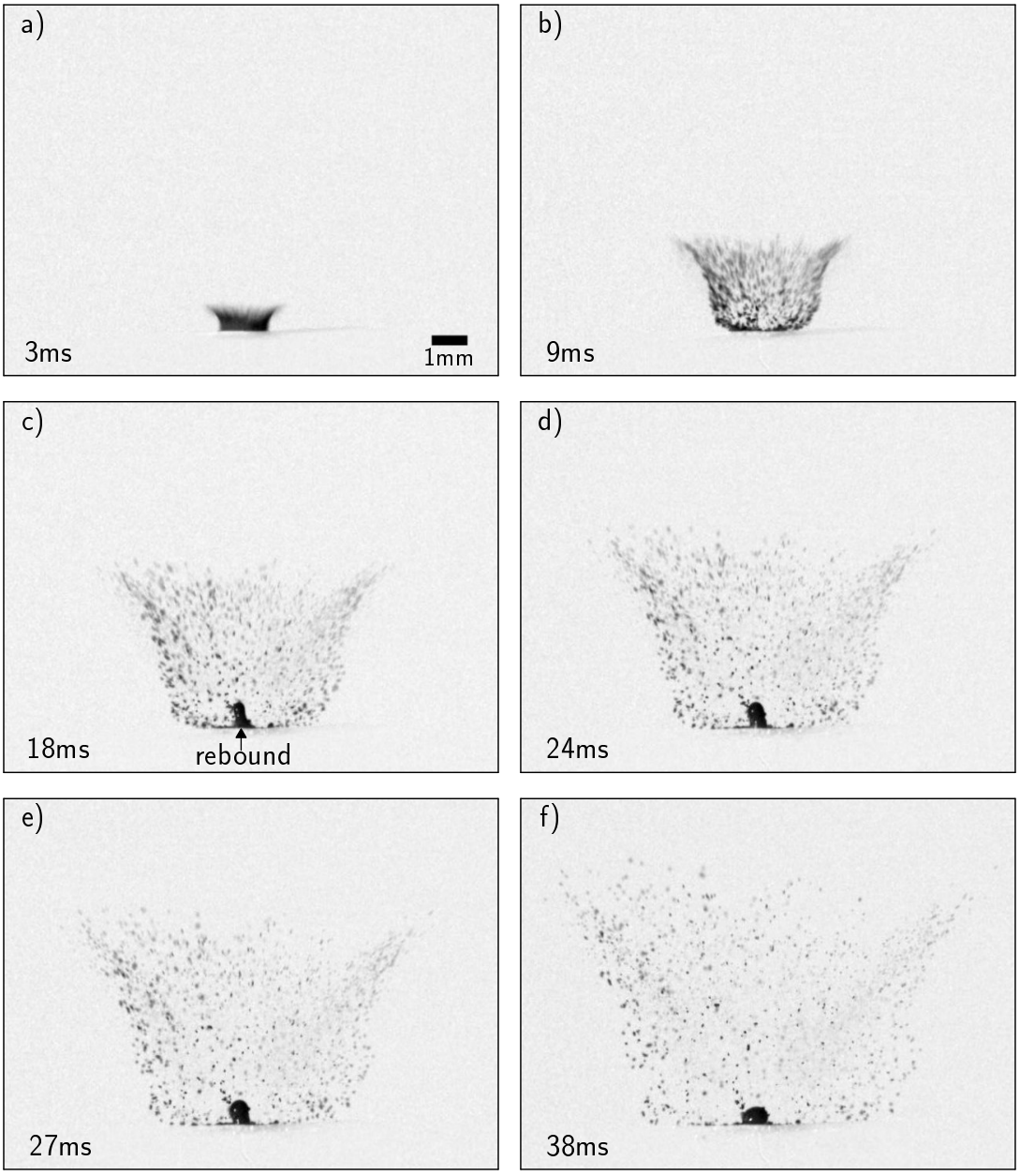

Figure 4.8: An example of the drop rebound within the splash structure.

4.3.3 Crater Morphology: Size

A costumed algorithm designed in Matlab was used to analyze photographs of each crater created by the droplet impact in order to determine its geometric diameter $\left(d_g = \sqrt{LIS}\right)$, where L, I and S are the longest, intermediate and shortest dimensions, respectively ($I = S$, Chapter 2). The rim is used to define the boundary of the crater for analysis (Fig. 4.9), although a marble (dry encapsulated particle) was formed inside the crater in all $S1$ experiments (Fig. 4.9a).

The surface layer of the water droplet is elastic so that it mimics the behaviour of a stretchable membrane when it impacts the surface. As the water droplet forms a thin disk, its surface becomes coated by the particles into which it falls; after which, its surface tension exerts an inward pull such that some of its energetic daughter ejections break away from the edges of the original droplet and splash. The remaining parts of the droplet in contact with the surface rebound and then reclaim its rounded shape as the surrounding particles absorb the water to leave a dried, small-encapsulated particle inside the crater (Fig. 4.9a). These observations are consistent with those from the work of Hamlette et al. (2013) and Katsuragi (2011) for loose hydrophobic particles. The rim of the crater in the WT experiments appears to be thicker than those in the $S1$ experiments (Fig. 4.9), indicating that as the droplet thins to form a disk upon impact, the crater grows wider and its walls get thicker as a consequence of the increased impact energy used to dislodge the particles from the surface. At the end of the droplet impact in $S1$ experiments, the water droplet is absorbed and evaporated into the surface and air, respectively. The ejected dust coats are apparent in all directions around the crater in still air (Fig. 4.9a) but are mostly spread in the direction of the winds as indicated by the arrow near the rim of the crater in winds at 4 ms^{-1} (Fig. 4.9b). This observation is consistent with the work of Vieira et al. (2004).

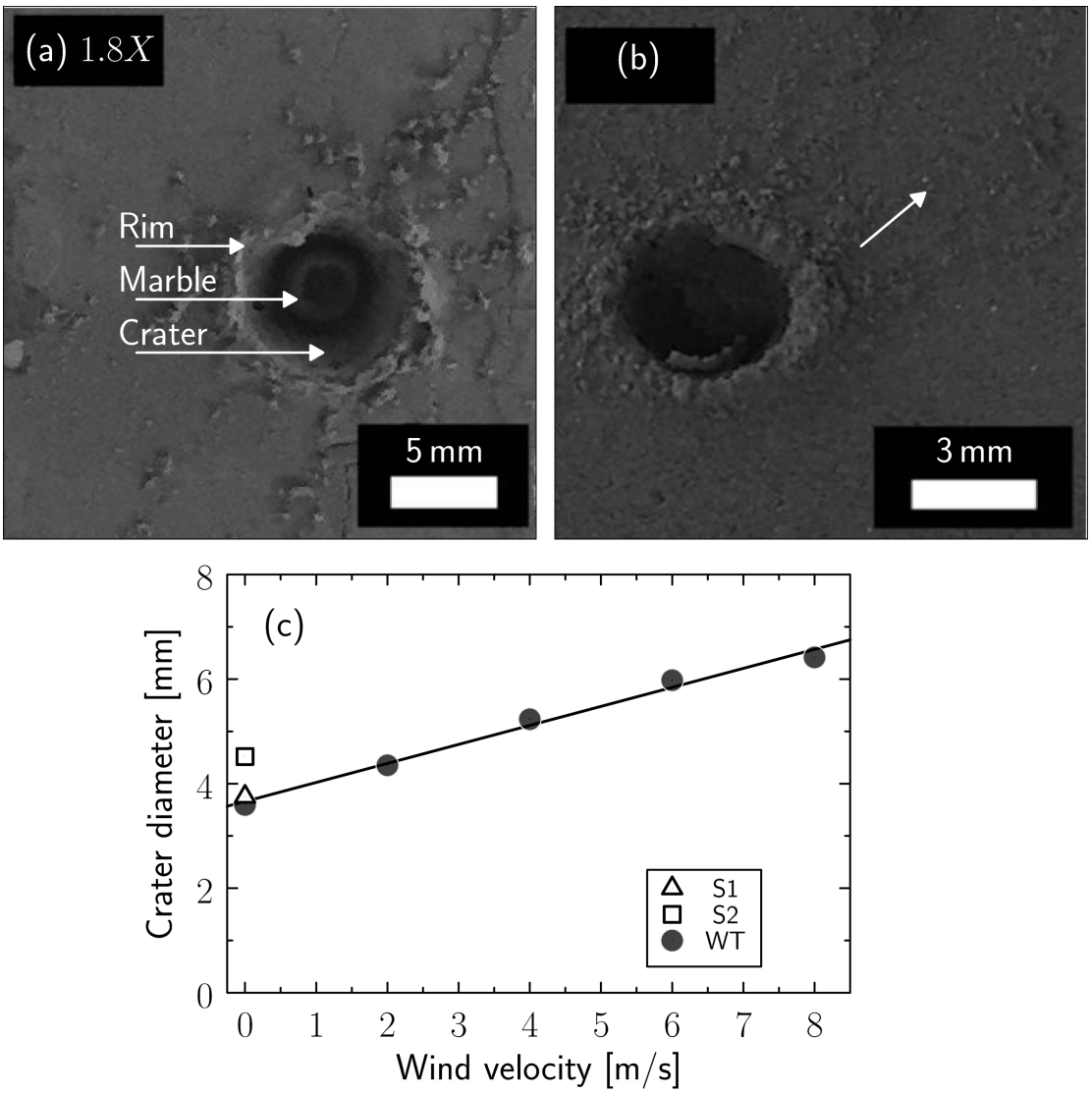

Figure 4.9: Image of the test bed surface illustrating crater formation in a) $S1$ and b) the wind tunnel at 4 ms^{-1}, as well as the c) crater diameter as a function of the streamwise velocity for all experiments. a) $S1$ shows the formation of a small drier marble trapped in the center of the original crater with a well-defined rim. b) WT shows the original crater formation with no secondary crater formed inside; the arrow shows the wind direction. Several dried dustcoats are also aligned with the wind direction.

The diameter of the crater increases linearly with the streamwise wind velocity

(Fig. 4.9c), suggesting that more wetted particles and aggregates are dislodged from the surface. It also appears that the droplet morphology influences the depth of the crater. The diameter of the crater in $S2$ is larger than those for $S1$ and WT in still air, showing that the droplet has high kinetic energy at impact (Fig. 4.7), which result in the displacement of more sediments.

4.3.4 Splash dimensions in still air

The temporal variation of the dimensions (e.g., height (h_d), spread (S_d), base diameter (d_b)) of the splash structure arising from the surface in the $S1$ experiments is shown in Fig. 4.10. The values of h_d and S_d increase as a power function of time, while the values of d_b increase linearly with time, consistent with the findings of other well-established studies in the literature (Ahn et al., 2012; Beczek et al., 2017). The maximum height of the splash structure ranged from about $2 - 5$ mm (Fig. 4.10a), with visible particles from Glacio1 ejected to the greatest extent, followed closely by the 2010 Eyjafjallajökull Ash. The values of h_d and S_d for Glacio2 are lower than those for the other samples. Glacio2 contains coarser particles than the other samples (Fig. 4.10), and so, the gravitational effects would appear to be dominant over the drag effects for ejected coarse semi-wetted particles and aggregates. It also is notable that this height lies well within and above the range ($0.7 - 2.8$ mm) of aerodynamic surface roughness length (z_o) cited for most Icelandic surfaces (Arnalds et al., 2001). These results also confirm that a single water droplet can eject dust into the air, but the majority of the ejected particles and wetted aggregates fall back to the surface, owing to fluid drag and gravity. Therefore, the values of h_d decrease as the values of d_{50} increase (Fig. 4.10a), showing that the particle weight influences the splash height. There are no apparent effects of the BET surface area on the dimensions of the splash

structure.

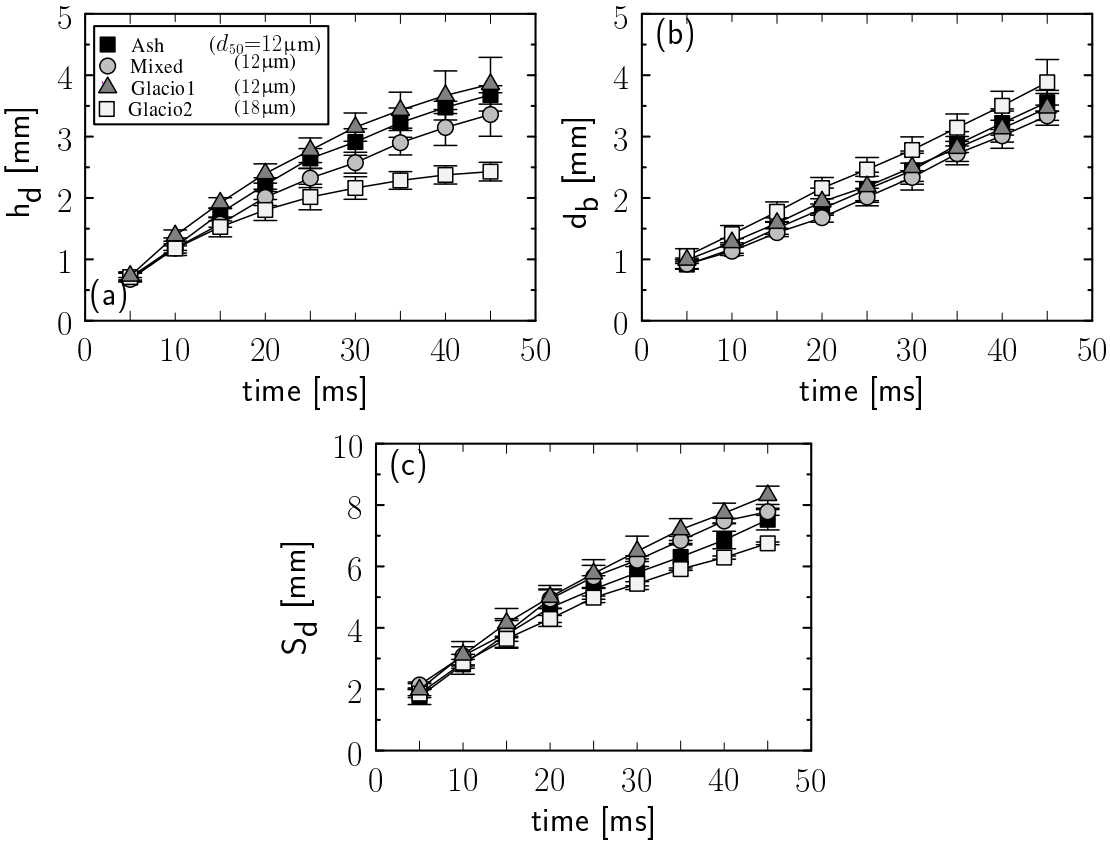

Figure 4.10: The rate of change in a) height (h_d), b) spread (S_d), and c) base diameter (d_b) of the crown per millisecond of time.

4.3.5 Splash, plume evolution and dust emission rate in a BL flow

A customized algorithm designed using Matlab^{TM} image-processing software was used to process the image frames from the PCO.Dimax^{TM} camera. The noise within the images was significantly reduced when an average of five background images was subtracted pixel by pixel from an average of multiples of five images recorded over the entire duration of an experiment (Fig. 4.11b). The algorithm was further developed to divide each resultant image into 10×10 pixel square grids.

The pixel values after the background subtraction within each grid box were used to create contour plots of varying intensity that represent the brightness of a pixel within a grayscale image. The intensity levels represent the light reflected from the mixture of ejected water and sediment within the cross-section of the emerging splash structure; however, the relative proportion of each ejection is unknown. The light reflected from the water contained within the droplet does not significantly affects the pixel brightness within an image after background subtraction.

Images of the splash evolution in still air were used to determine the effect of wind drag on the ejected particles using the quadratic stress equation,

$$\frac{F_D}{C_D} = \rho_a A_{total} \overline{u}(z)^2, \tag{4.2}$$

where ρ_a is the air density, A_{total} is the cross-sectional area of the splash structure, and $\overline{u}(z)$ is the streamwise wind velocity measured at the height of the centroid of the structure.

The splash structure spreads symmetrically as it rises above the surface in still air (Fig. 4.11), and so, its cross-sectional area viewed from sideways is assumed to be identical in a complete rotation around the structure as it spreads radially outwards. The streamwise wind velocity ($\overline{u}(z)$) at the height of the splash's centroid as it rises in time was calculated from the vertical velocity profile (Table 4.1). The centroid is the geometric center of the bounded cross-sectional region of the splash structure evolving in time (Fig. 4.3a). The resultant images were further analyzed to determine the total cross-sectional area of the bounded splash structure, as well as the upwind and downwind areas as defined by Fig. 4.3b. In Fig. 4.3b, the bounded cross-sectional region of the splash structure is divided into two parts by a fixed vertical or centerline to isolate an upwind area and a downwind area. The position of the centreline is defined by the initial water droplet

impact position, which varied with the conditions of a given experiment.

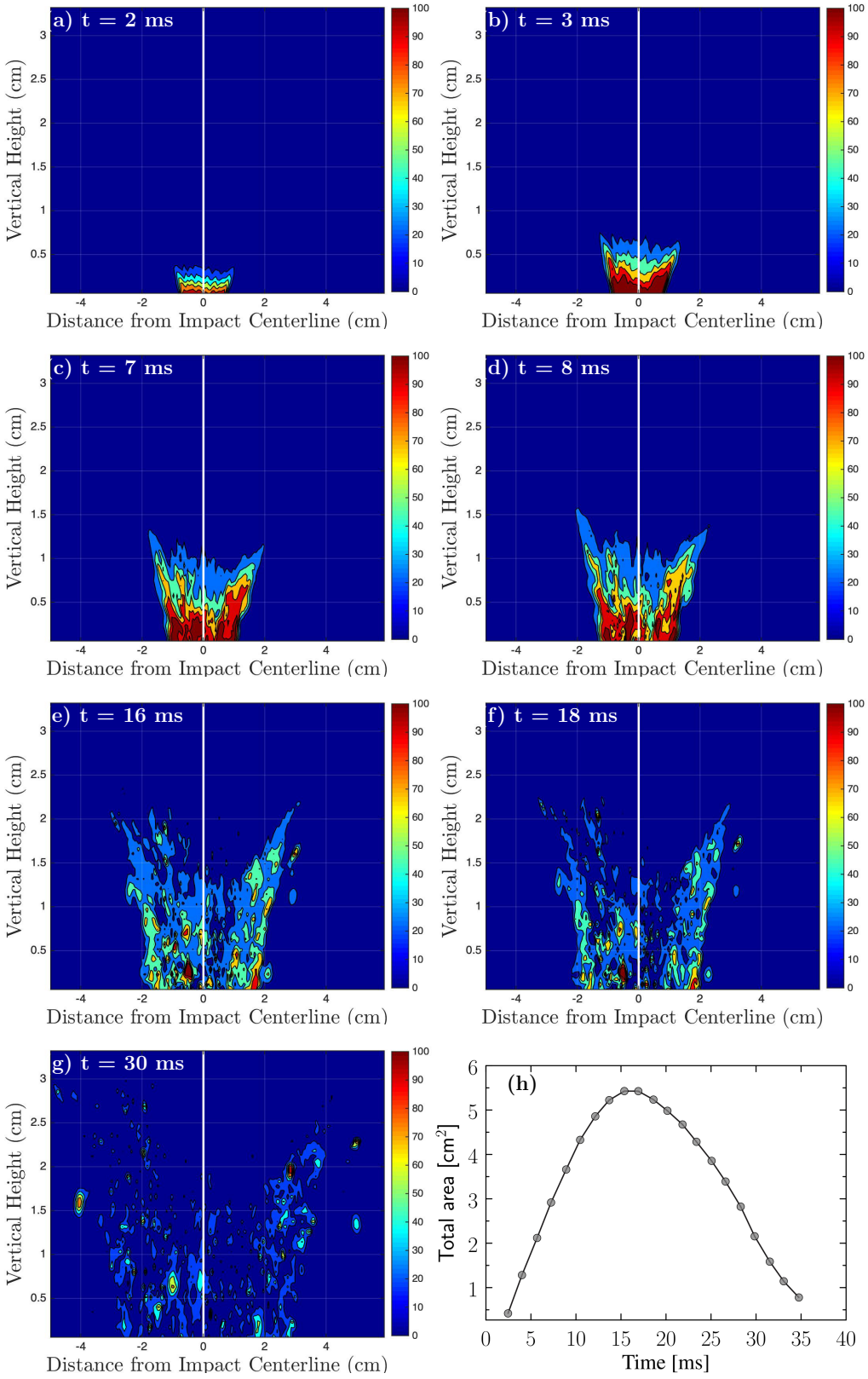

Figure 4.11: a - g) Images of the splash structure arising from the test bed upon the impact of a water droplet in still air. The white solid vertical line shows the centreline of the splash structure as determined by the droplet impact position. f) Temporal variation in the total cross-sectional area (cm^2) of the splash structure as it spreads away from the surface.

Within the first 3 ms of the experiment, the vertical cross-section of the spreading splash structure appears to be distinctly stratified with a well-defined shape as shown by the coherent intensity levels, which provide an indication of the concentration within the structure emerging from the surface in still air (Fig. 4.11a - b) and within a shearing flow (Fig. 4.12a - b). The velocity of the dust structure rising from the surface appears to exceed the effects of the near-surface wind drag beyond the sub-viscous layer ($z_o = 0.04$ mm), and so the dust structure remains mostly undisturbed at an early time (< 3 ms). This observation is also consistent with those in the $S1$ and $S2$ experiments. During the later stages (> 3 ms) of the splash development, the structure begins to disintegrate, as shown by the discontinuous intensity level, owing to the fluid drag, which overcomes the motion of the ejection. The vertical cross-section of the splash structure appears to spread symmetric about its centerline in the experiments performed in still air (Fig. 4.11a - d), but it disintegrates at a later time (Fig. 4.11e - g). As a result, most of the ejected wetted aggregates and particles fall back to the surface consistent with the results in $S1$ and $S2$ experiments.

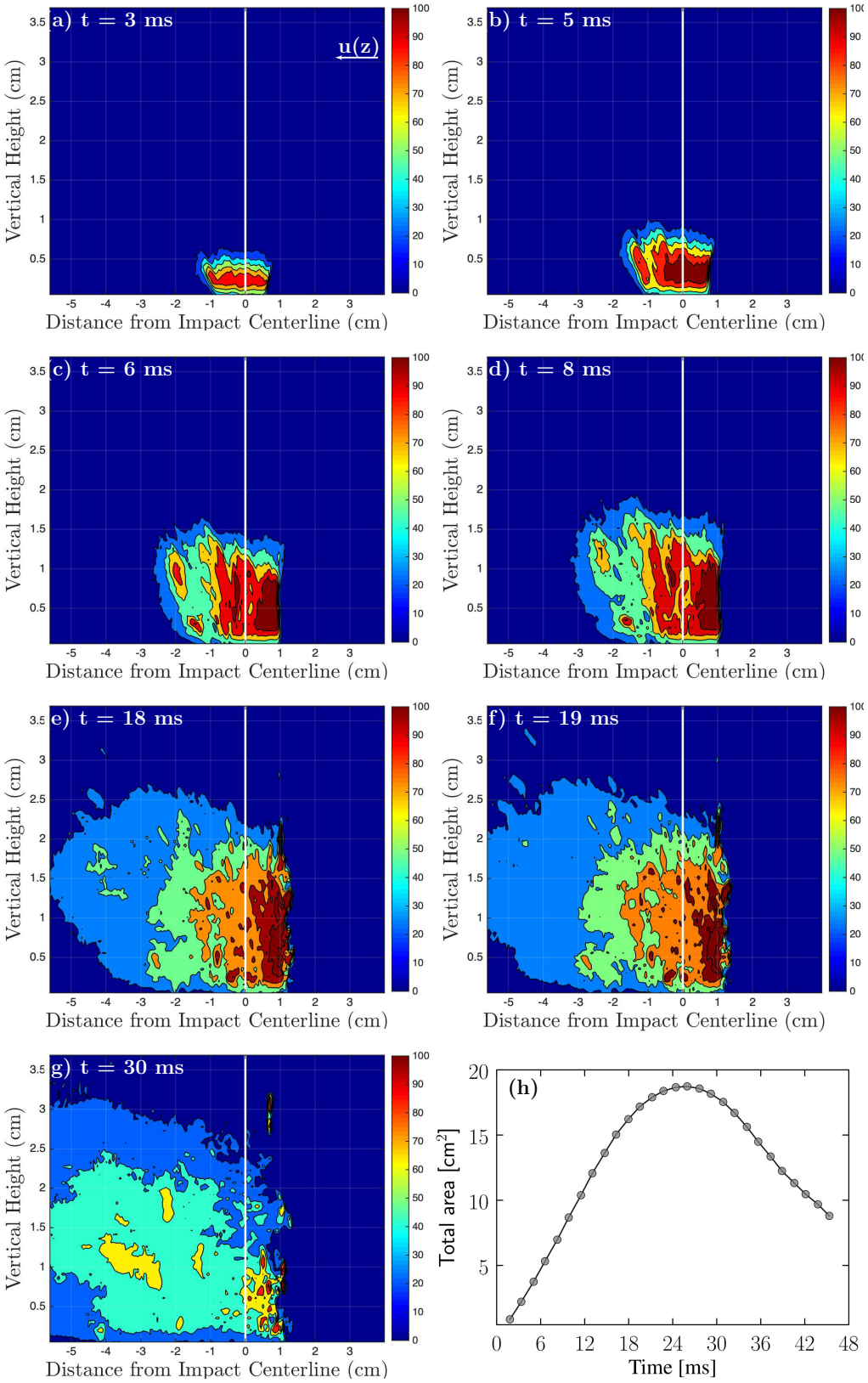
a) t = 3 ms
u(z)
b) t = 5 ms
c) t = 6 ms
d) t = 8 ms
e) t = 18 ms
f) t = 19 ms
g) t = 30 ms
Vertical Height (cm)
Distance from Impact Centerline (cm)
(h)
Total area [cm²]
Time [ms]

Figure 4.12: a - g) Images of the splash structure emerging from the test bed upon the impact of a water droplet in winds of 4 ms^{-1}. The white solid vertical line shows the centreline of the splash structure as determined by the droplet impact position. f) Temporal variation in the total cross-sectional area (cm^2) of the splash structure as it rises from the surface.

Strong near-surface winds disperse particle-coated droplets (daughter ejections) that rise above the sub-viscous layer and enter the near-surface turbulent flow (Fig. 4.12), causing the cross-sectional area of the dust structure to become asymmetric. As the splash structure rises from the surface, its upwind side becomes vertically aligned with the centerline (white line) as it adjusts to the cross-sectional flow, while its downwind side appears to be slightly tilted in the direction of the winds as wetted particulates are transported away from the bed surface (Fig. 4.12). The total cross-sectional area of the dust structure increases linearly in time up to a maximum of 5.5 cm^2 in still air (Fig. 4.11f) and to 18.5 cm^2 in winds up to 4 ms^{-1} (Fig. 4.12f), showing that the wetted dust particles are dispersed over a larger area within a boundary layer flow. In winds as low as 4 ms^{-1}, large aggregates that fall back to the surface and saltate may eject dust particles, which were difficult to quantify during image analysis.

The ratio of the downwind to upwind cross-sectional area shows only slight variation over time in still air (about a 1 : 1 ratio; Fig. 4.13c), confirming that the splash structure spreads symmetrically. However, this ratio increases by as much as 2 orders of magnitude in winds up to 8 ms^{-1} (Fig. 4.13c), substantiating the suggestion that wind drag strongly affects the dispersion rate of the splash structure arising from the surface (Fig. 4.13e -f). The wind drag above the surface disperses the dust particles downwind of the bed surface (Fig. 4.13d), such that the downwind area occupied by the cross-sectional flow increases significantly as

the contributing area upwind shrinks (Fig. 4.13b).

The growth and decay rates of the splash structure were obtained from the temporal variation in the total cross-sectional area as the structure expanded and then shrinks (Figs. 4.11 to 4.13) during the early and late stages of each experiment, respectively. The growth rate increases exponentially with increased streamwise wind velocity ($\overline{u}(z)$; Fig. 4.13e), suggesting that the expanding cross-sectional area influences turbulent dispersion within a shearing flow. Likewise, the decay rate decreases (negative) exponentially with increased values of $\overline{u}(z)$, showing that as the wind velocity increases dust particles are rapidly transported from the upwind to downwind side of the structure. The rate of decay is slightly faster than the rate of growth of the cross-sectional region of the splash structure (Fig. 4.13e - f), showing that the effects of wind drag become dominant as the structure loses its energy.

As expected, the growth rate in $S2$ is less than the respective values obtained for all wind-driven experiments, confirming that the wetted dust particulates are ejected and transported downwind of the bed surface by wind drag. Notably, the growth rate for $S2$ is also less than those for WT in still air, suggesting that the energy transferred from the droplet to the surface in $S2$ may have been used to overcome the compression within the bed to eject particles as compared to the loose bed created in WT. As mentioned earlier, a frame was used to create a fixed, pressed bed surface of particles in $S2$ runs. The decay rate obtained in $S2$ is slightly higher than the respective value obtained (Fig. 4.13f) in the WT experiments in still air, showing that the particles fall back to the surface owing to fluid drag, thereby creating a transport-limited system.

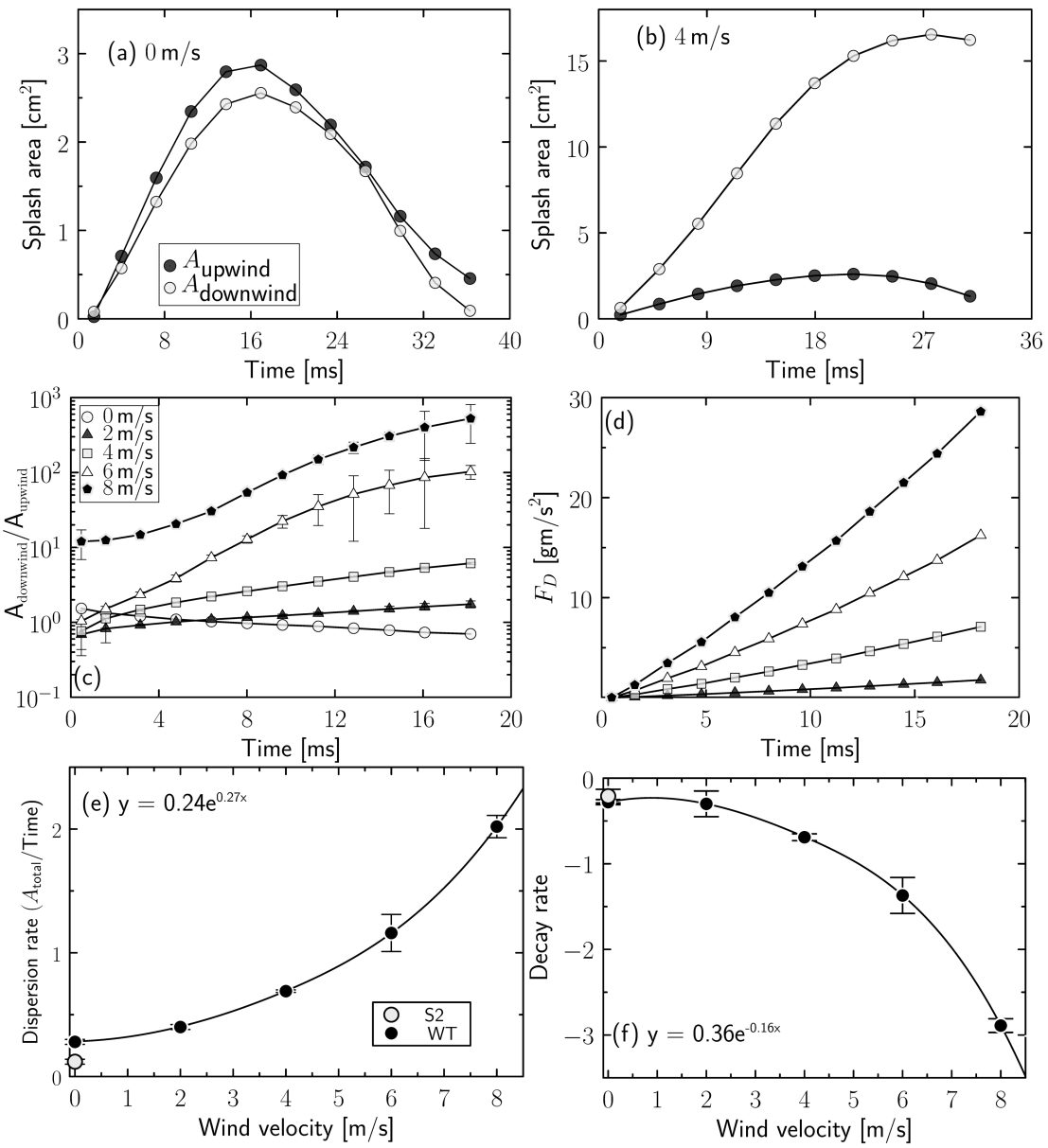

Figure 4.13: Examples showing the rate of change of the upwind to downwind cross-sectional areas in a) still air and b) winds of 4 ms^{-1}. c) The rate of change of the ratio of the upwind to downwind cross-sectional areas and d) wind drag (F_D) at varied fan speed. e) The dispersion/growth rate and f) decay rate of the cross-sectional area of the dust structure with varied wind velocity.

Reliable estimates of the suspended PM_{10} particulates obtained from the dust

concentration sampled at 20 mm downwind of the bed surface were used to calculate the mean concentrations over 10 sec immediately after the droplet impact over ten seconds (Fig. 4.14). The peak concentration were also identified over the same time period after the droplet impact. The results show that the peak and mean PM_{10} concentrations increase with increased wind speeds.

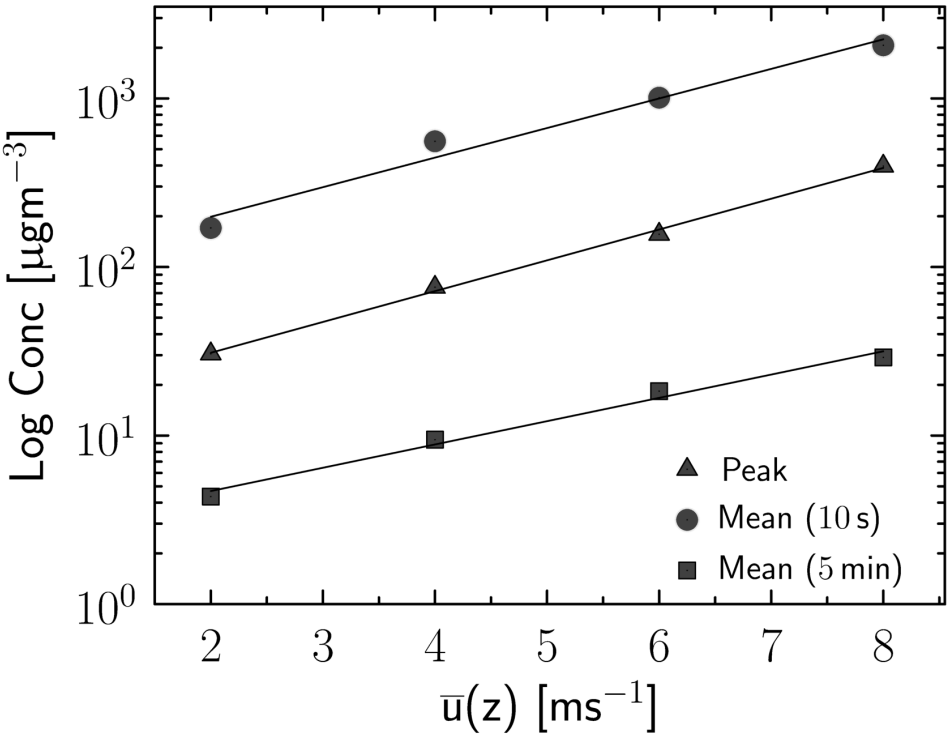

Figure 4.14: Peak and mean PM_{10} concentrations measured at varied wind speeds at an elevation of 20 mm above the surface over 10 sec and 5 min immediately after the droplet collides into the surface.

4.4 Conclusions

The detachment of dust particles by raindrop impact is an important mechanism for aerosol generation and the initiation of dust emission events in Iceland because it is essential in erosion models to describe the effect of rain droplet on bare

Icelandic soil surfaces in still air and wind-driven conditions. This experimental study was designed i) to investigate the particle, droplet and crater morphologies, as well as the splash dimensions to understand the factors influencing Icelandic dust entrainment and dispersion upon the impact of a water droplet, and ii) to quantify the dust emission rate. The results show that:

(i) The height of the splash structure decreases as the median particle diameter increases, suggesting that the particle weight influences the height of the splash structure rising from the bed surface.

(ii) The sphericity of the water droplet increases with increased wind speeds, which thereby increase the horizontal velocity component and decrease the vertical velocity component of the water droplet as it falls through the air to eject and dislodge more dust particulates from the surface.

(iii) The PM_{10} concentration sampled downwind of the impact site (up to 10^3 μgm^{-3}) is positively correlated with the water droplet velocity, impact angle and wind speed.

(iv) The dust structure is most likely to be dispersed by winds because the cross-sectional area occupied by the wetted dust particles increases at a faster rate than in still air, and so increased wind speeds suggest that more dust particulates are transported away from the source region, although the transport processes are not well understood in this study.

(v) The maximum height of the splash structure lies either well within ($S1$) or above ($S2$ and WT) the range ($0.07 - 0.28$ cm) in aerodynamic surface roughness length cited for most Icelandic surfaces (Arnalds et al., 2001) so that dust dispersion within the turbulent shearing flow is favoured.

(vi) The droplet rebound and dry encapsulated marble of sediments in the central region of the crater suggest some degree of hydrophobicity.

Icelandic dust emission coincides with the onset of a precipitation event within active dust regions (Prospero et al., 2012), which are sparsely vegetated and experience high frequency wind speeds. This understanding is fundamental to the development of soil-erosion models, as well as enhanced dust dispersion. Although the present study was not tested in the field, it may be a good step towards understanding the quantity of dust particulates ejected from the surface during wind-driven rain splash, although a single water droplet was used.

Chapter 5

Laboratory Investigation of Particle-Scale Factors Affecting the Deposition Rate of Icelandic Dust

5.1 Introduction

Atmospheric aerosols have a strong influence on climate, directly by interacting with sunlight and indirectly by serving as condensation nuclei to initiate cloud formation, thereby perturbing Earth's radiation balance (Harrison and Aplin, 2001; Haywood and Boucher, 2000; Tegen and Lacis, 1996). These effects depend on several microphysical properties such as particle size, composition, morphology, hygroscopic behaviour, and the concentration and vertical distribution of these aerosols within the atmospheric column. For instance, smaller particles effectively scatter more radiation energy than larger ones (Tegen and Lacis, 1996; Waggoner et al., 1981). Aerosols deposited on snow packs and glaciers in high latitude regions may alter the surface albedo and rate of melt (Bullard et al., 2016; Patterson, 1998; Tedesco et al., 2008). In the lowest portions of the atmospheric boundary layer (ABL) aerosols influence air quality, and indirectly, human health.

Iceland contains some of the largest and most active dust sources within the Arctic. Extreme emission events are associated with strong winds up to 30 ms^{-1} blowing over vast unsheltered glacio-fluvial outwash systems and tephra deposits that provide an abundant supply of particles (Bullard et al., 2016; Thorsteinsson et al., 2011). The annual emissions from Iceland are suggested to amount to as much as $30.5-40.1$ million tons (Arnalds et al., 2016) and may constitute $0.6-7.2\,\%$ of the total global estimate of $500-5000$ million tons (Engelstaedter et al., 2006). The average number of dust events recorded annually is 135 over a span of 34 dust days, and up to $300,000$ tons may be emitted in a single event (Arnalds et al., 2015). Major dust storms are more frequent in the wake of explosive catastrophic volcanic eruptions, such as the well-known Eyjafjallajökull 2010 eruption (Arnalds et al., 2016). Dust emissions from high latitude, cold climate

regions, inclusive of Iceland are, expected to increase with global warming, glacier retreat, and the consequent exposure of new dust sources (Gassó et al., 2018).

Unlike well-studied siliciclastic dust particles that are well rounded and smooth due to long-term weathering processes (Chuvochina et al., 2011; Goudie and Middleton, 2006), relatively juvenile Icelandic volcaniclastic dust particles are highly angular, porous, and enveloped with ultrafine dustcoats. The associated internal void space contributes to low particle density (Chapter 2), which may affect dust emission and deposition rates in the atmospheric boundary layer (ABL). For instance, siliciclastic dust particles transported over long distances in the atmosphere range from 0.1 to 20 μm in diameter (Duce, 1995; Pye, 1987), with the median typically between 1.5 to 3 μm (Bergametti, 1998). In comparison, Gislason et al. (2011) suggest that volcaniclastic dust particles up to 50 μm in diameter may be engaged in long distance transport. Substantial amounts of water may be adsorbed onto the expansive surface area of these highly irregular, porous particles, thereby affecting nucleation, aggregation, and settling. Only a few field studies have attempted to relate the unique physiochemical characteristics of Icelandic dust to its behaviour in the ABL (Arnalds et al., 2003, 2014; Dagsson-Waldhauserova et al., 2014; Dagsson-Waldhauserová et al., 2015), but no high precision experiments have been carried out to address the particle-scale physics.

Using a $2D$ Laser Doppler anemometer (LDA), the present paper reports on a set of highly controlled fall column experiments designed to evaluate the dependency of the settling velocity upon particle morphology (e.g., size, shape, porosity, surface area) and relative humidity (RH). The measurements are compared to those obtained for an idealized reference particle in the form of a solid glass sphere of similar diameter. Such work is relevant to the global deposition of volcanic ash

and suspended glaciogenic particles originating from basalts.

5.1.1 Regional context and sample collection sites

Located just south of the Arctic Circle, Iceland contains sandy deserts that comprise more than 20 % (22,000 km^2) of its area and are extremely active sites of dust emission, with little to no vegetation cover and gravel pavement to reduce sand drifting (Arnalds, 2010). These regions are currently expanding in area with the provision of new dust sources arising from glacier retreat and catastrophic volcanic eruptions (Swindles et al., 2017). Dust storms in Iceland are frequent and can transport large amounts of particulate matter less than 10 μm in diameter (PM_{10}). For instance, Dagsson-Waldhauserová et al. (2015) recorded a 24 hr mean PM_{10} concentration of 1281 $\mu g m^{-3}$ during a dust storm in southern Iceland. During a re-suspension event involving volcanic ash (Arnalds et al., 2013), an average PM_{10} transport rate of 1440 $kgmh^{-1}$ was recorded over 6.5 hrs. Dust emission events in northeast Iceland affect Arctic regions during the warm summertime (May - September), while those in southern Iceland affect sub-Arctic regions during the cool wintertime (March -May: Dagsson-Waldhauserova et al., 2014). The average spring/summer time relative humidity in southern and northern Iceland typically ranges from 50−70 % but can be as high as 90 % (Einarsson, 1984). The annual mean temperature in southern and northeast Iceland ranges from 4−5°C and up to 4 °C, respectively, but could be as high as 13 °C in the summer time (Einarsson, 1984). Dust emission events affect the air quality in Reykjavík (Thorsteinsson et al., 2011), the rate of glacial melt in the Arctic (Wittmann et al., 2017), and the rate of dust deposition within, and transport to the North Atlantic Ocean (Prospero et al., 2012). Hence, knowledge of the unique particle-scale factors affecting either the settling velocity or residence time is important to these cold,

humid regions. Four Icelandic field sites served as particle sources for the present study. As summarized in Table 5.1, three were collected in southern Iceland (Vík, Álftaver and Markarfljótsaurar), and the remaining one from the northeast (Dyngjusandur). All sites are associated with regions of severe erosion (Arnalds et al., 2001). Hereafter, these samples will be referred to as Ash (from the 2010 Eyjafjallajökull eruption, collected at Álftaver), Mixed (ash and glaciogenic dust from Vík), Glacio1 (glaciogenic dust from Dyngjusandur, northeast of Vatnajökull glacier), and finally, Glacio2 (glaciogenic dust from Markarflótsaurar).

5.2 Methodology

5.2.1 Fall column measurements of the settling velocity

Fall columns are widely used for measuring the settling velocity (v) and drag coefficient (C_D) of particles in laboratory settings (Chow and Adams, 2011; Christiansen and Barker, 1965; Willmarth et al., 1964). Using this apparatus, the settling velocity of particles released in still air from the top of the column is measured at some vertical distance from the drop point, where the acceleration of particles becomes negligible. For instance, Bagnold (1935, 1941) found that sand particles with diameters ranging from 0.13 mm to 1.23 mm reached terminal velocity within 1.09 m.

Table 5.1: Summary information for samples collected at four locations in Iceland.

Labels	Sediments	Collection Details			
		Sites	**Quantity (kg)**	**Source**	**Date**
Ash	Eyjafjallajökull ash	Álftaver	1.3	Tom Mockford Loughborough University	May 2015
Mixed	Glaciogenic dust and ash	Vík	3	Throstur Thorsteinsson University of Iceland	May 2015
Glacio1	Glaciogenic dust 1	Dyngjusandur	2	Pavla Dagsson-Waldhauserová University of Iceland	May 2017
Glacio2	Glaciogenic dust 2	Markarflótsaurar	15	Throstur Thorsteinsson University of Iceland	Sept. 2016

In the current study, test particles were released inside a 0.14 m × 0.09 m × 1.28 m fall column (Fig. 5.1) situated within an environmental chamber. The temperature was set to a constant value of $14\pm1\,^{\circ}C$, which is typical of summer weather in Iceland. The relative humidity was varied over three established ranges ($20-30\,\%$, $50-60\,\%$ and $70-80\,\%$), also taking into consideration respective summer, annual, and winter conditions in Iceland (Einarsson, 1984). The fall column and samples were both left overnight to equilibrate under the pre-set climatic conditions in preparation for the settling velocity experiments to be carried out the following day.

Present-day measurement of particle settling velocities within a fall column usually involves the use of some form of a digital imaging system based on high speed/high-resolution cameras (Bagheri et al., 2015, 2016). However, discrete dust particles with diameters less than 20 µm are very difficult to assess using this approach, due to: i) inter-overlapping particle images that commonly arise with large suspended volume fractions, and ii) insufficient light reflection so that these tiny particles seem invisible within the camera frame of view. In the present set of experiments, a $2D$ Dantec$^{\mathrm{TM}}$ Laser Doppler anemometer (LDA), which can detect

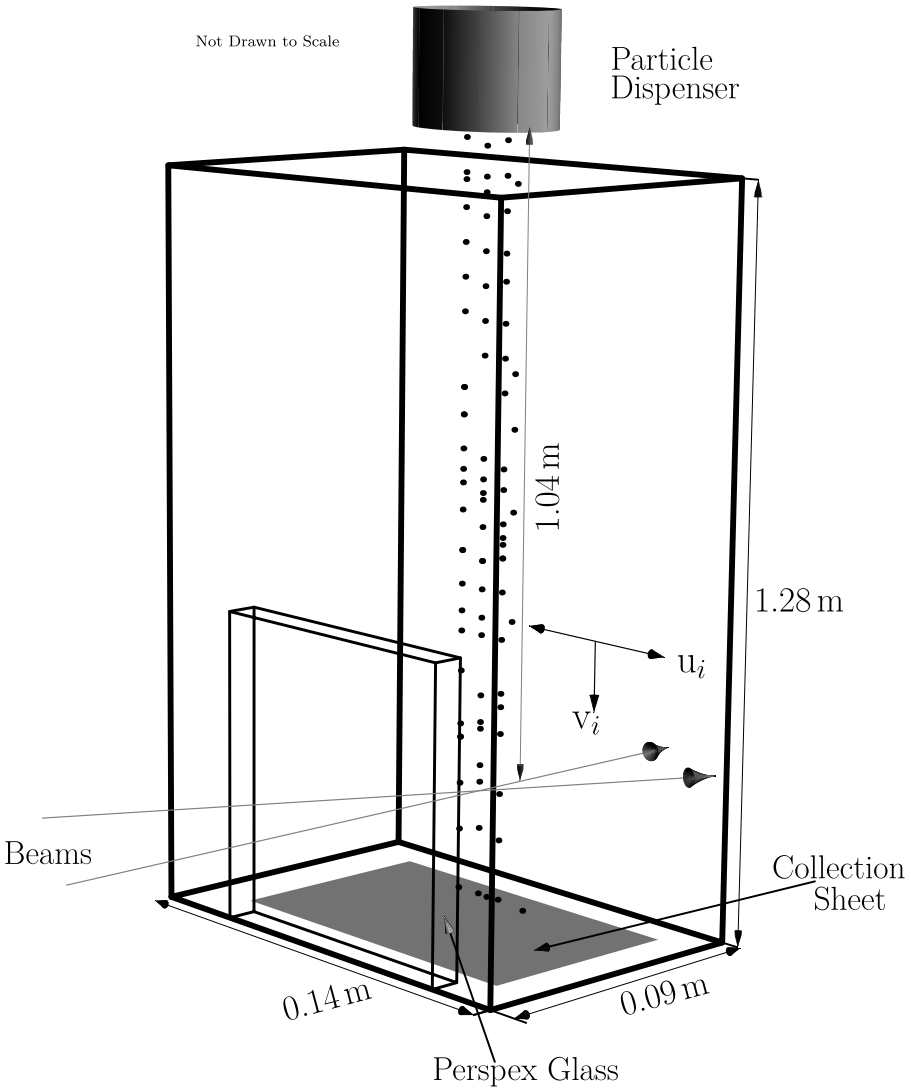

Figure 5.1: Schematic diagram of the fall column apparatus used for measuring the particle settling velocity. Intersection of the LDA laser beams denotes the position of the optical measurement volume. Particles are released from a dispenser (40 mm in diameter) with bottom screen (62 μm aperture). A collection sheet inserted into the base of the column may be used to solate and recover particles for subsequent runs.

with high accuracy sub-micron size particles down to 0.4 μm in diameter, was used to sample the distribution of fall velocity associated with each test sample (Li and

McKenna-Neuman, 2012). The LDA measures the Doppler shift of light scattered from particles passing through the intersection point of two visible monochromatic laser light beams of wavelength, λ=0.660 μm. The amount of scattering the beams undergo is dependent on the size, shape and concentration of the falling particles (Drain, 1980; Durst et al., 1976). Further details about the settings of the LDA are provided in Li and McKenna-Neuman (2012).

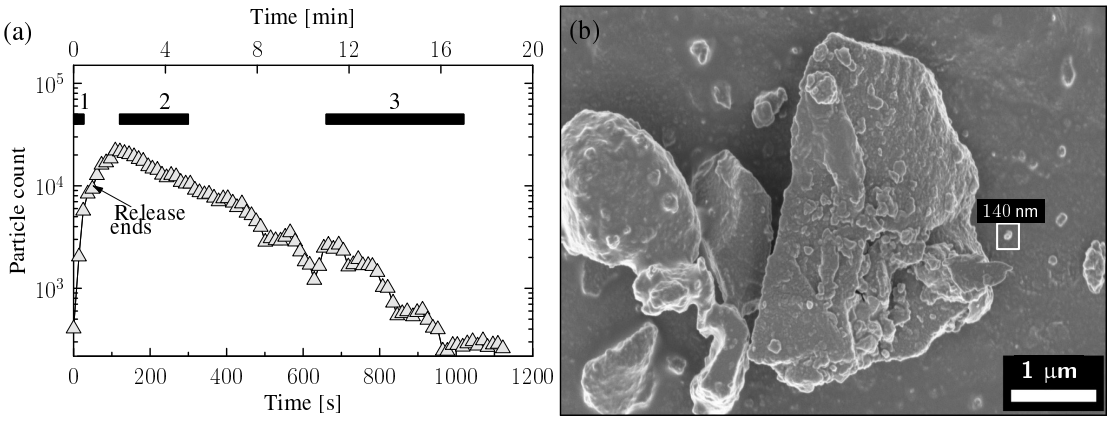

Figure 5.2: a) Example of a typical time-series plot of the particle count (20 %<RH<30 %, Mixed sample), showing that the peak occurs after the particle release period ends. The solid bars indicate the sampling periods 1 (45 sec), 2 (3 min), and 3 (6 min), during which particles were collected on carbon conductive adhesive tab mounted on an aluminum stub. b) Sample scanning electron microscopic (SEM) image of clumps of particles collected 22 min after the start of a given experiment.

Evaluation of the velocity components in two dimensions, *x-horizontal* and *z-vertical* (Drain, 1980; Durst et al., 1976), requires two additional beams of different wavelength, in this case, λ=0.785 μm. While the LDA can make high-resolution measurements without perturbing the airflow within the fall column, the velocity components sampled are restricted to particles that pass through the 0.04 m^2 optical measurement volume. In this study, the LDA was positioned directly in

front and outside of the fall column, with its four beams focused through the perspex glass window (Fig. 5.1) to intersect near the center of the chamber at a fixed position, 1.04 m below the point of particle release. The instrument will not operate when the ambient air temperature falls below or near $10 \pm 2\,^{\circ}C$, placing some constraint on the environmental conditions targeted for the experiments.

When an i^{th} particle passes through the optical volume, the fringe interferes to give the velocity in two dimensions with an horizontal, u_i, and a vertical, v_i, component (Li and McKenna-Neuman, 2012). Only velocity measurements that met the following criteria were analyzed in the present study: i) LDA data validation rate must exceed 80 % for a minimum sample size of 1000 particles, and ii) v_i must be positive and exceed u_i, indicating that the given particle was indeed falling and not strongly affected by particle-to-particle interactions and collisions. Less than 5 % of all particle velocities measured failed to meet the second criteria. The median value of v_i measured at the range of low humidity ($20-30\,\%$) was used to calculate the drag coefficient (C_D) and Reynolds number (Re), which will be discussed later.

Discrete particles were dispensed over a 45 s period by gently tapping a sieve (mesh grid opening 62 μm in diameter), which contained the selected test sample and was held over an opening in the top of the fall column. During each experiment, the falling particles were captured on a collection sheet (Fig. 5.1) inserted at the bottom of the column so that the sample could be recovered. A typical run lasted between 18 min to 22 min, after which, the fall column was cleaned to prevent the cross-contamination of samples. A total of nine replicates were carried out for each experimental condition.

Once the particles were released into the fall column, the particle count rate rose sharply to a peak value when the suspended volume fraction and validation

rate were high, before decreasing near exponentially through time as the number of remaining particles in the column diminished (Fig. 5.2a). Particles suspended beyond 22 min, as indicated by visibly red laser beams, were confirmed in SEM images to be dominated by nanometer-scale diameters that the LDA could not detect. Unfortunately, laser Doppler anemometers cannot independently measure particle diameter.

5.2.2 Particle characteristics: size, shape, density, and surface area

The original Icelandic samples were repeatedly wet sieved to remove the sand fraction, and thereby isolate the fines. Eventually, 88 % to 98 % of the particles retained in the test samples were $\leq 60\,\mu m$. These were subsequently dried for 24 hrs at $105°C$, Mixed vigorously to offset the tendency of particles to segregate by size, and then stored in a desiccator until further tests were performed. As a reference standard, manufactured solid glass microspheres, with diameters ranging from 0.4 to 60 μm and a particle density of 2.55 $g\,cm^{-3}$ (Cospheric Innovations) were also wet sieved for the fall column experiments.

Three replicates of the particle-size distribution within each sample were measured using a Horiba Partica LA−950 V2 particle size analyzer (PSA), which is based on laser diffraction. A tiny sub-sample was placed inside the mixing chamber containing distilled water, which was then stirred and agitated to break up any aggregates. Size distributions measured when calgon was added to the mixture as a dispersant were not found to be statistically different (when $p<0.001$) from those obtained using distilled water only. Sub-samples recovered after each experiment from the collection sheet inserted at the base of the fall column (Fig. 5.1) also were routinely sized in the Horiba to evaluate the consistency between runs.

The BET surface area (A_{surf}) were measured for the solid glass spheres and those for the Ash, Mixed, Glacio1 and Glacio2 samples were extracted from Chapters 2 and 3, where specific details regarding this technology are described in Subsection 2.3.2. The skeletal densities were measured using a helium pycnometry, which is described in Chapter 2 of this study.

For selected fall column runs carried out at $20\,\%<RH<30\,\%$, dust particles were collected on carbon conductive adhesive tab in order to analyze their size and shape characteristics in detail, and to search for evidence of particle aggregation. The adhesive tab was secured to an aluminium stub and then positioned 2 cm above the base of the fall column, perpendicular to and near the center of the stream of descending particles. Particle collection was carried out over four consecutive intervals during each run, beginning at 0, 3 and 6 (Fig. 5.2a; solid bars). The length of each sampling interval increased as the concentration of particles decreased through time, in order to ensure that a sufficient amount was collected on the adhesive tab. Although the air column was slightly perturbed during insertion and removal of the stubs throughout the run, the disturbance was very brief relative to the length of the sampling period, which lasted several minutes ($\sim$102$\times$ longer). Scanning electron microscopic (SEM) imaging and Matlab image-processing software were subsequently used to measure the primary dimensions and geometric diameter of each discrete particle isolated on the adhesive tab (Chapter 2).

5.2.3 Moisture adsorption measurements

To further verify that Icelandic dust particles are capable of adsorbing moisture while suspended in boundary layer flows of varied relative humidity, $\sim$1.2 g subsamples were dried at $105\,^{\circ}C$ for 24 hrs before spreading them onto a watch glass

surface. The median particle diameters for the Ash, Mixed, Glacio1 and Glacio2 samples were 13, 14, 14 and 25 μm, respectively measured in the Horiba. The samples were stored inside a sealed environmental chamber with various salt solutions, which allowed for precise variation in the relative humidity. As prescribed by Greenspan (1977), RH values of 39, 57, 68, 75, 85 and 95 % can be attained at T=24 °C (the lab temperature) with saturated salt solutions of sodium iodide, sodium bromide, potassium iodide, sodium chloride, potassium chloride and potassium nitrate, respectively. The salt solutions were placed in a glass petri dish and positioned in the bottom of the environmental chamber, below the watch glass containing the dust particles. A T-RH sensor was also placed inside the chamber to confirm the desired RH. The dust samples were allowed to equilibrate over a 24 hr period, during which measurements of the relative humidity and temperature of the air in the chamber were confirmed to match the targeted values from the study of Greenspan (1977). The water uptake by the test samples was determined from their changing weight, which was measured using a high precision (±0.0001 g) analytical balance. The equilibrium gravimetric moisture content (W_c) was calculated from:

$$W_c = \frac{W_{wet} - W_{dry}}{W_{wet}} \times 100 \tag{5.1}$$

The corresponding tension (Ψ_m) at which water molecules are adsorbed onto particle surfaces with varied T (K) and RH (%) can be estimated from the Kelvin equation:

$$\Psi_m = -\frac{RT}{V_m} \ln\left(\frac{RH}{100}\right), \tag{5.2}$$

where R=8.314 J($mol^{-1}K^{-1}$) is the ideal gas constant, and $V_m = 18{\times}10^{-6}$ m^3mol^{-1} is the partial molar volume of water, giving the $|\Psi_m|$ in pascals (Pa).

5.3 Results & Discussion

5.3.1 Scanning electron microscopy (SEM) imaging

Scanning electron microscope (SEM) images show that Icelandic dust is indeed highly complex in shape, varying from sharp-edged, highly angular shards to well-rounded but highly porous particles with flaky, rough surface structures (Fig. 5.3). The pores of the particles may contain a substantial amount of ultrafine dustcoats (Chapter 2). As expected, the glass spheres appear round, solid and smooth, with a trace amount of nano-scale fragments that would indicate a minor amount of contamination.

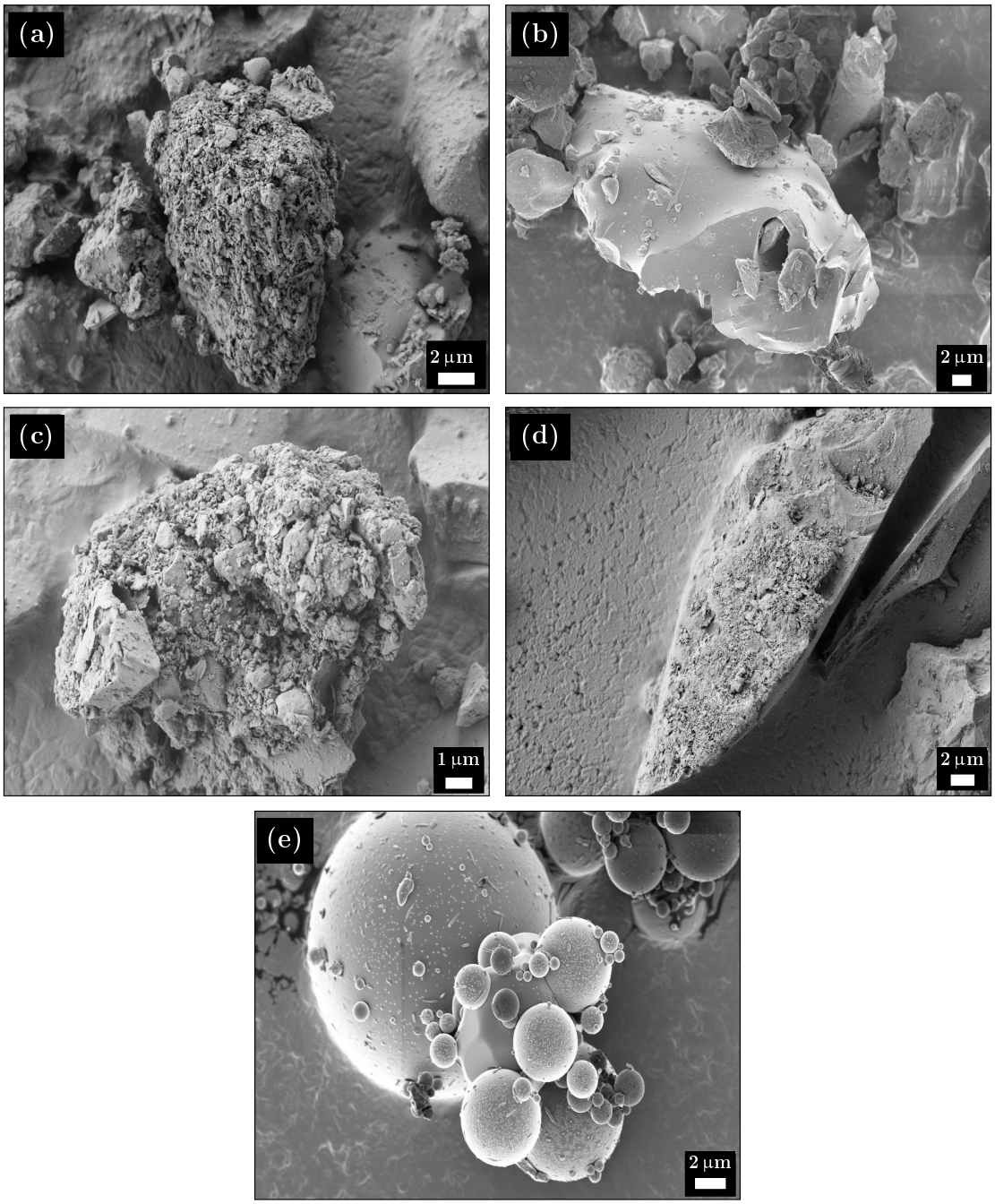

Figure 5.3: SEM images of selected particles from the (a) Ash, (b) Mixed, (c) Glacio1, (d) Glacio2, and (e) Glass Microsphere samples. All particles are under 10 µm in diameter and near the lower limit of detection by the LDA.

5.3.2 Particle size, specific surface area, and water adsorption

Particle size distributions for all Icelandic samples, inclusive of the reference glass spheres, are provided in Fig. 5.4 and summary statistics in Table 5.2. The samples are dominated in general by silt particles, constituting 88 %−94 % of the total weight, with only slight variations in their median diameters (d_{50}) as mentioned earlier. The only exception is Glacio2, which is considerably coarser (by a factor of ∼2 for the median diameter), and has peak frequencies at 1 and 30 µm. Notably, the grain-size distributions measured before the first fall column experiment was performed (Fig. 5.4e) show little (1−2 µm) to no variation from those measured for fines recovered from the sheet inserted at the base of the fall column after the final experiment (Fig. 5.4f).

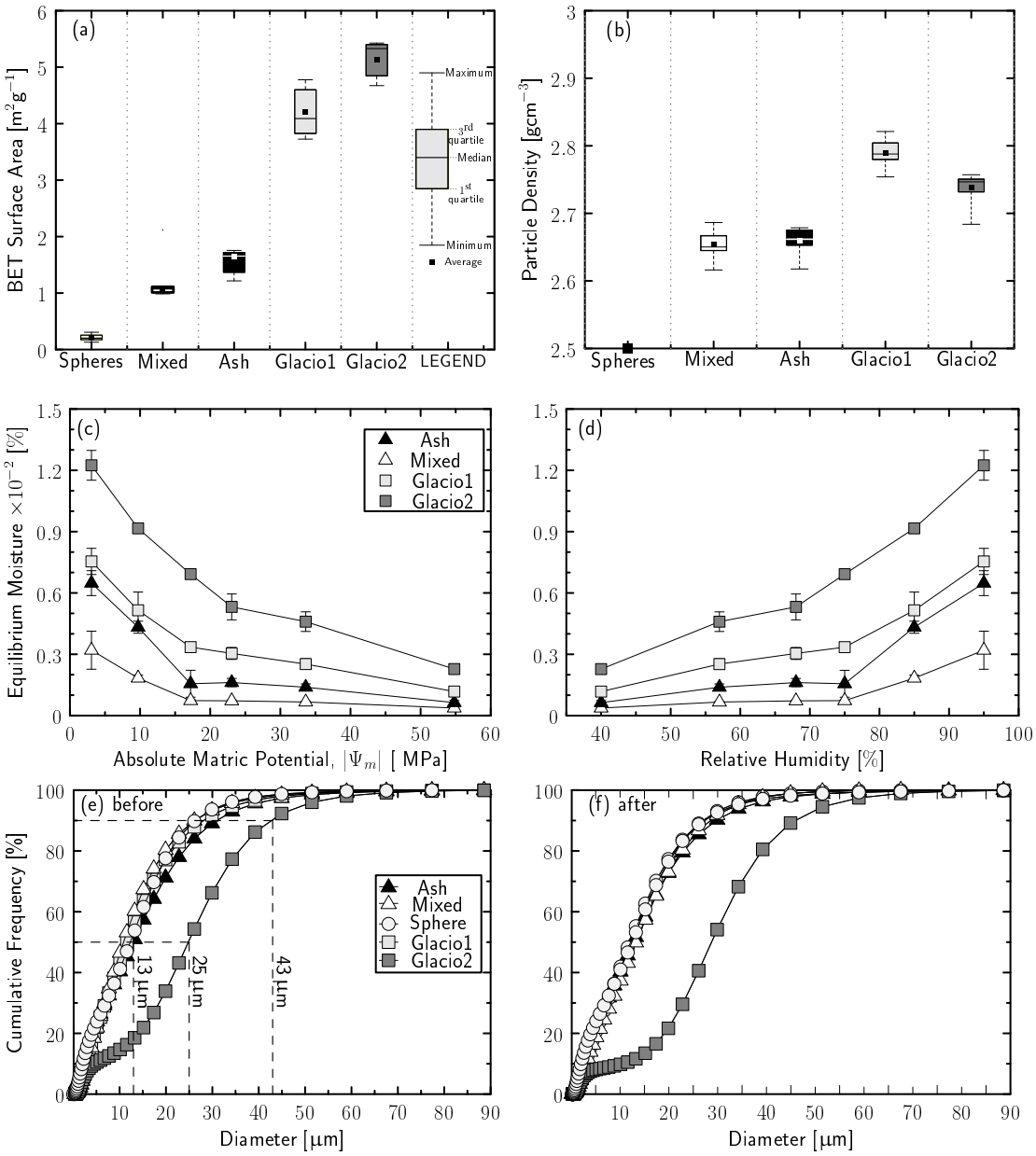
(a)
BET Surface Area [m²g⁻¹]
Spheres
Mixed
Ash
Glacio1
Glacio2
LEGEND
Maximum
3rd quartile
Median
1st quartile
Minimum
Average
(b)
Particle Density [gcm⁻³]
(c)
Equilibrium Moisture ×10⁻² [%]
Absolute Matric Potential, |Ψm| [MPa]
(d)
Relative Humidity [%]
(e) before
Cumulative Frequency [%]
13 µm
25 µm
43 µm
Diameter [µm]
(f) after

Figure 5.4: Summary plots of the various factors affecting water adsorption. Boxplots show the a) specific surface area and b) the skeletal density of the particle subsamples (Chapter 2), inclusive of the glass microspheres. Plots c) and d) respectively show the median gravimetric moisture content plotted against the water tension and relative humidity at T=24 °C, where the ends of the bars represent the lowest and highest values measured over six replicates. Particle size distributions are provided for the fall column experiments in plots e) before the first run, and f) after the final one.

Although the particle size distributions are similar, a one-way analysis of variance suggests that the corresponding BET surface areas (Fig. 5.4) are significantly different (P<0.001; Table 5.3) and, thereby, vary systematically with the sample origin. Specific surface area values for the Icelandic samples appear to be two orders of magnitude higher than that for solid glass spheres, which demonstrates the pivotal influence of the large porosity and intricate shape of these natural particles (Chapter 2). This result is consistent with the findings of Riley (2003) for volcanic ash collected in Guatemala, Alaska and Nebraska (Chapter 2). Direct calculation of the specific area ($\sim$0.2 m^2g^{-1}) for the reference spheres, based on their simple geometry and an ideal packing arrangement, is in excellent agreement with the BET measurements, affirming the instrument's calibration. The Mixed and Glacio2 samples have the lowest (1.07 m^2g^{-1}) and highest (5.14 m^2g^{-1}) specific surface areas, respectively. Measurements for the Ash ranged from 1.22$-$1.7 m^2g^{-1} with an average of 1.65 m^2g^{-1}. While much lower than the value (4.3 m^2g^{-1}) obtained by Gislason et al. (2011) for freshly deposited ash from the eruption of Eyjafjallajökull, the ash measurements from this study fall within the range of surface areas (1$-$2 m^2g^{-1}) reported for five

ash samples (particle diameters $\leq$100 µm) derived from other explosive eruptions (Delimelle et al., 2005, and references within).

Table 5.2: Summary of particle size statistics for subsamples obtained prior to fall column testing.

Samples	**Clay** % (<2 µm)	**Silt** % (2−50 µm)	**Sand** % (50−200 µm)
Ash	8	91	1
Mixed	5	94	1
Glacio1	5	94	1
Glacio2	5	88	7
Spheres	10	88	2

The effects of the high specific surface area on dust deposition are not well understood, particularly under the cool, humid conditions characteristic of Iceland. At a constant temperature of 24 °C, the adsorption (watch glass) experiments in the environmental chamber clearly demonstrate a systematic increase in the equilibrium gravimetric water content of the dust samples with rising relative humidity (Fig. 5.4b) and declining matric potential (water tension, Fig. 5.4c). Although the values of W_c are extremely low, they do suggest that each of the Icelandic samples is hygroscopic. Glacio2 adsorbs the highest quantity of water in comparison to the Ash, Mixed and Glacio1 samples. Likewise, the Mixed sample adsorbs the least. Notably, the order of moisture adsorption for all Icelandic samples is consistent with the ranking of their BET values; that is, the larger the specific surface area, the more moisture these particles adsorb. Finally, the rate of adsorption varies within two linear regimes, slow for RH below ~75 % and moisture tensions above ~20 MPa, and vice versa (e.g., rapid at higher humidities). The texture of the sample is associated with a slight shift in the inflection point near the median (e.g., dropping to 68 % for Glacio2). At 70 %<RH<75 %, prior studies have established that an additional layer of adsorbed water is formed at the particle surface (Yilbas

et al., 2018, and references within).

5.3.3 Settling velocity

To control for the effects of moisture on the settling rates of Icelandic dust particles and solid glass spheres, the initial fall column experiments were performed at a constant low humidity, $20\,\%<RH<30\,\%$. Cumulative frequency distributions of the horizontal and vertical velocity components sampled are provided in Fig. 5.5. The velocities used to create these distributions are not time dependent, but rather, represent the lumped data for each run. For the samples with similar particle-size distributions, inclusive of the solid glass spheres, the vertical velocity components are not significantly different with median values of 0.0051, 0.0053, 0.0056, and 0.0061 ms^{-1} for the Glacio1, Mixed, Ash, and Spheres, respectively (Fig. 5.5; Table 5.3). This result suggests that particle shape does not have a strong influence on the magnitude of the vertical velocity, as compared to the particle diameter. For example, the larger particles in the Glacio2 sample had the highest vertical velocities with a median of 0.0075 ms^{-1}. It has been suggested that the rotation of angular particles may interfere with the LDA diffraction patterns, causing slight variations in scattering that can introduce error in the velocity measurements (Drain, 1980). While the effect of particle rotation on the LDA fringe interference pattern is beyond the scope of this study, the absence of a clear influence of shape within the vertical velocity data would appear to indicate that this source of error is negligible relative to the magnitude of these measurements. For instance, the slowest particle horizontal velocities are similar in the lower tails, indicating that fewer lateral deflections are obtained within the fines. The vertical velocities of the Icelandic dust particles behave similar to those of the solid spheres (e.g., median vertical velocity: Stokes, 1951), and so the effects

of instrumentation artifacts would be negligible in vertical.

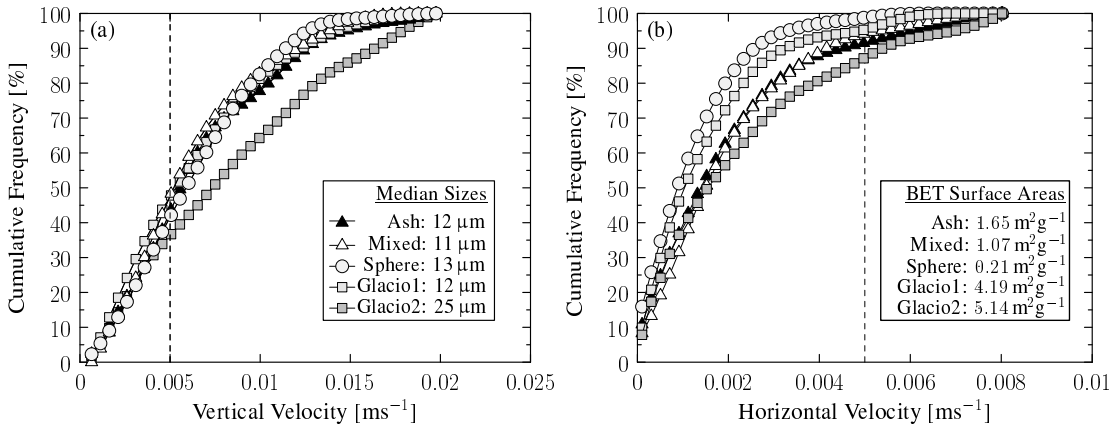

Figure 5.5: a) Vertical (v_i) and b) horizontal (u_i) velocity distributions measured at T=14±1 °C and 20 %<RH<30 %.

The magnitude of the median horizontal velocity is in general only 20−25 % of that for the corresponding vertical velocity (Fig. 5.5). Although infrequent, the magnitude of u_i can be similar in value to v_i (vertical dashed lines: Fig. 5.5). While not apparent in the vertical velocity dataset, the horizontal velocity distributions do appear to be influenced by both particle size and geometry. The glass spheres clearly stand apart in demonstrating the least horizontal diffusion, and the Glacio2 particles the most. Among all samples, there also appears to be a strong convergence of the vertical velocity component below 0.005 ms^{-1}, and the horizontal below 0.001 ms^{-1} (Fig. 5.5), presumably corresponding to particles lying within the fine tail of each of the size distributions (Fig. 5.4).

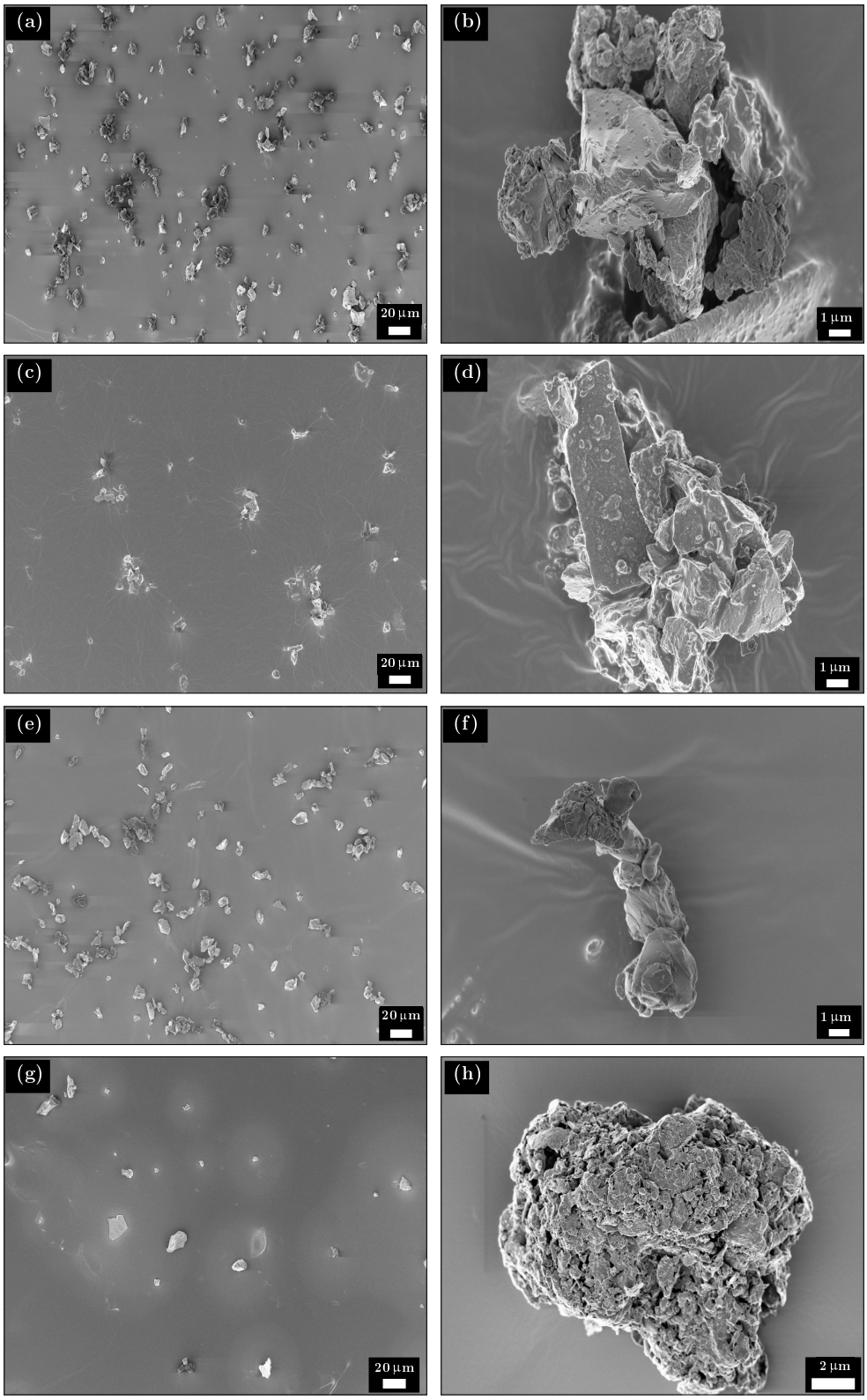
(a)
20 µm
(b)
1 µm
(c)
20 µm
(d)
1 µm
(e)
20 µm
(f)
1 µm
(g)
20 µm
(h)
2 µm

Figure 5.6: SEM images of particles collected on adhesive tape during the first three minutes of settling: Ash (a - b), Mixed (c - d), Glacio1 (e - f) and Glacio2 (g - h). Selected examples include both loose particle clusters (b and f) and well-cemented pellets (d and h).

The presence of a horizontal component in the settling velocities (u_i) measured in the fall column experiments is presumed to arise from complex interactions between the particles during their descent, inclusive of collisions that lead to drift. These observations are indeed consistent with the conclusions of Del Bello et al. (2017) who examined the effects of the volume fraction on the settling velocity of volcanic ash particles.

SEM images of particles deposited onto adhesive tabs near the bottom of the fall column within the first three minutes of the low humidity experiments include the aggregates shown in Fig. 5.6. These morphological structures range from loose particle clusters (b and f) to well-cemented pellets (d and h). The particle clusters appear fragile, and as suggested by Bagheri et al. (2016), can fracture during collision. Indeed, many of the particles on the adhesive tabs shown in Fig. 5.7(a, c, e and g) occur in clusters that appear to have been disrupted upon impact with the surface, clearly illustrating that some particles are not falling discretely. This phenomenon is commonly observed for fragile aggregates formed from highly porous particles, falling in dry conditions (Gilbert et al., 1991; Sorem, 1982). Conversely, the pellets most likely were not formed within the fall column but rather were present in the original samples. These results are also consistent with the SEM image observations of ash deposits collected in other studies, particularly during field measurements of volcanic ash fallout (Bagheri et al., 2016; Brown et al., 2012, and references within).

Time-dependence plots (Fig. 5.7) of the number and geometric diameter of aggregates observed in the SEM images indicate a general decline over a 6 min period, beginning with the release of the particles. The values of d_{50} of the grain-size distributions at each collection time are summarized in Table 5.3. For reference, the PSA curves obtained for the original wet-sieved samples are overlain on the plots for sampling performed at the start of the experiments. Although the aggregate distributions are number based and those for the PSA are volume based, both sets of distributions are skewed towards coarser diameters, particularly the glaciogenic particles. The large degree of overlap would seem to indicate that most aggregates derive from the original samples.

While the clusters and pellets observed on the adhesive tabs represent only a small fraction of all descending particles, their numbers are similar between the varied sources (Fig. 5.7), with one exception. The aggregates of Ash are distinctively finer in diameter and greater in number at the start of the experiment, as compared to the Glaciogenic and Mixed samples. Interestingly, aggregates with diameters $\leq$20 μm were collected on the adhesive tabs, both at the start of an experiment and near the end. This result would suggest that, in addition to the effect of their weight, complex particle interactions within the column (involving both aggregate growth and fracture/decay) play a key role in determining the deposition rate. For example, the potential for accretion of discrete particles to form aggregates within the air column is likely buffered over time by reduced particle interactions as the suspended volume fraction of dust decreases. Johnson et al. (1996) further suggest that the proportionate amount of pore space formed between the particles within aggregates may also alter their fall rate.

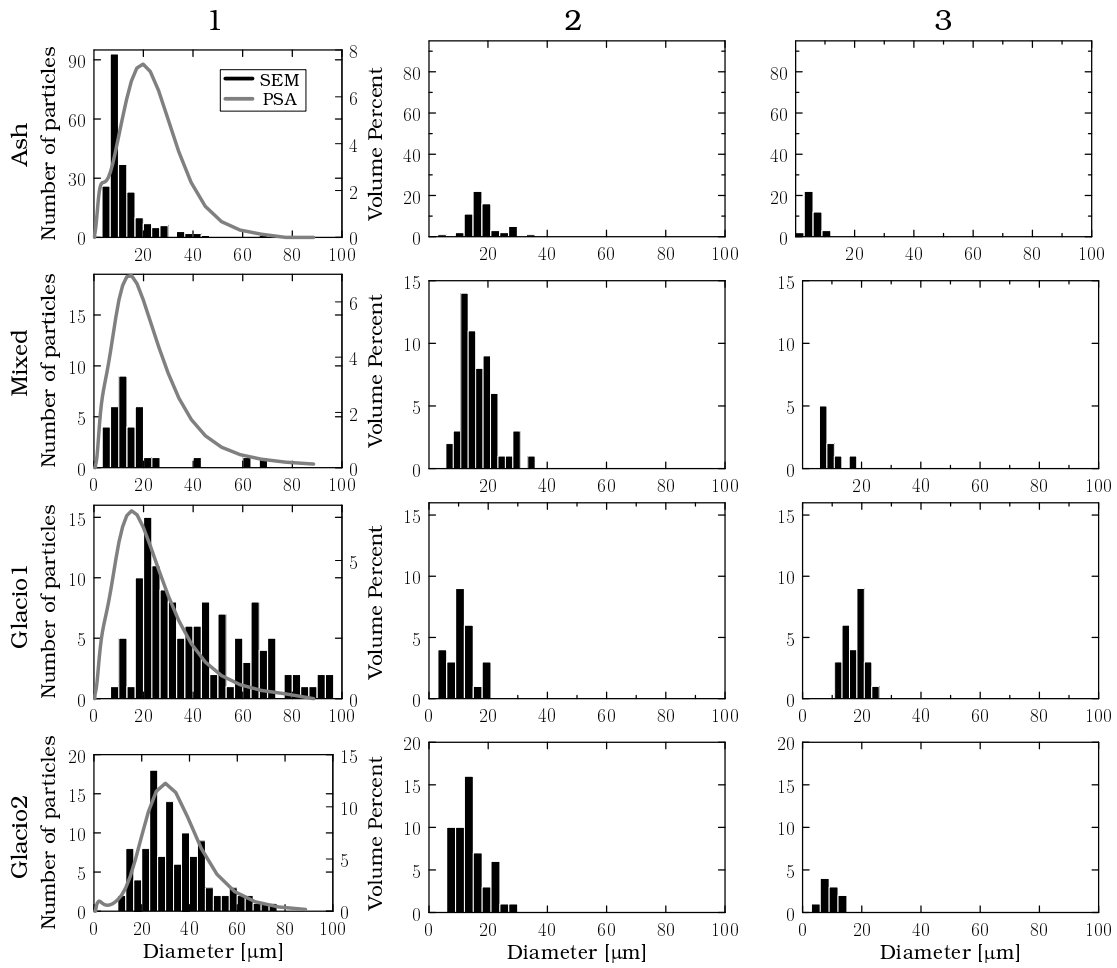

Figure 5.7: Time-dependence of the number and diameter of aggregates collected on SEM stubs at sampling periods of 1 (45 sec), 2 (3 min) and 3 (6 min) at the base of the fall column as described in Fig. 5.2. At the start of the experiment (period 1, start), the distributions of diameter obtained from image analysis are compared with those of the original wet-sieved samples measured with the Horiba PSA (solid line).

For each particle source, Fig. 5.8 compares the cumulative frequency distribution of the normalized fall velocity (v_i/v_{50}) with that for the normalized particle diameter (d_i/d_{50}). While it was not possible to measure synchronously the fall velocity and diameter of each particle sampled, the four plots attempt to corre-

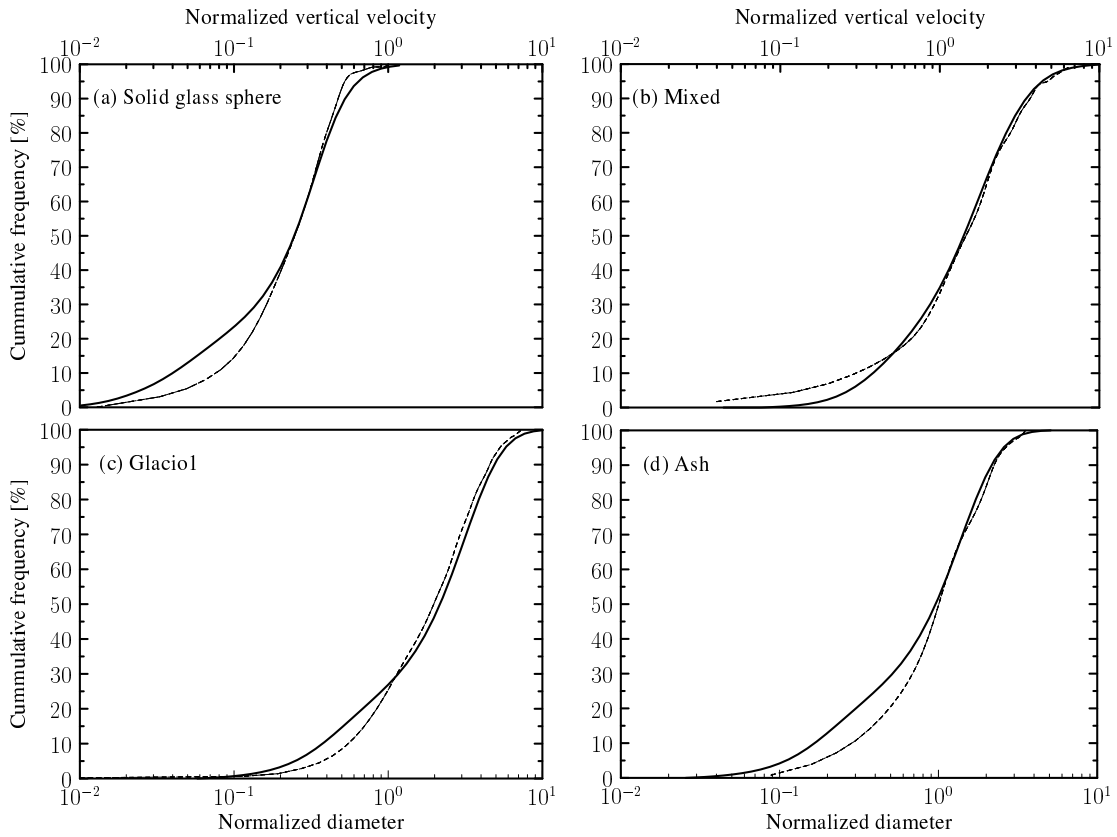

Figure 5.8: Log-linear distribution curves for particle diameter (solid line) and settling velocity (dashed line), normalized by the median values.

late the independently sampled distributions in matching the median fall velocity (v_{50}) with the median particle diameter (d_{50}). Indeed, for each particle type, inclusive of the glass spheres, the form of the normalized distributions demonstrates near-perfect overlap diameters exceeding $\sim 10\mu$m. However, there is some degree of departure in the fine tail with the distribution of particle diameter appearing slightly less skewed than for the fall velocity. Given their geometric complexity, a number of researchers acknowledge the high degree of uncertainty associated with diameter measurements obtained for particles of volcanic origin, especially for the finest fraction (Formenti et al., 2011; Horwell, 2007; Riley, 2003).

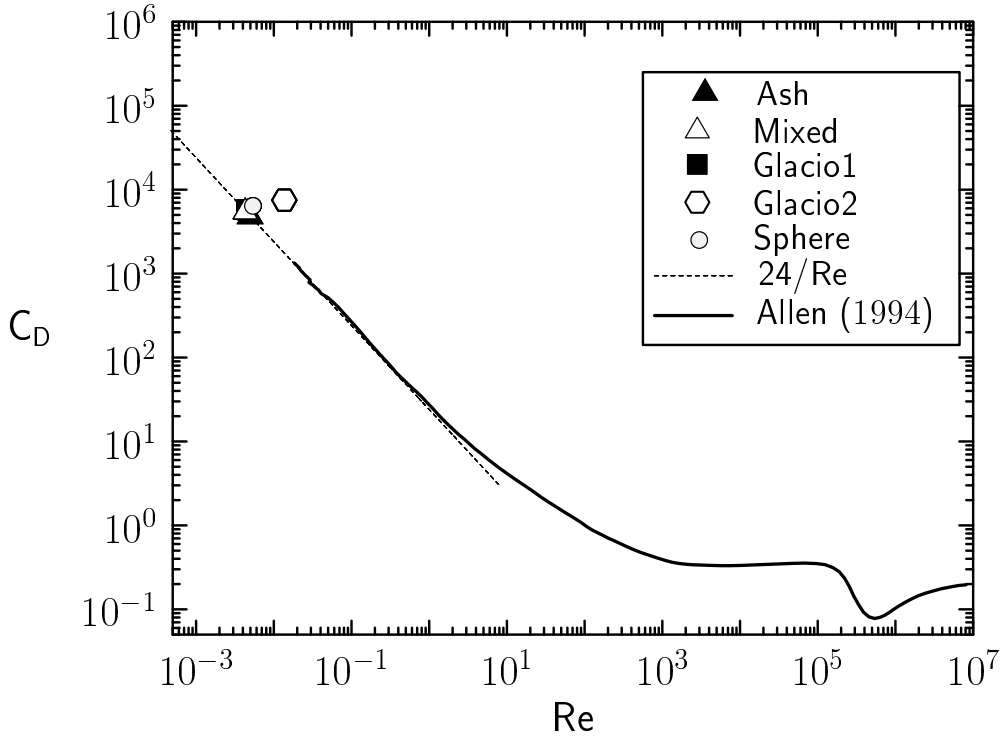

Figure 5.9: Estimates of the drag coefficient (C_D) based on median values of the particle diameter and vertical velocity.

5.3.4 Drag coefficient analysis

Many experimental studies have determined the drag coefficient (C_D) for irregularly-shaped particles of volcanic origin (Bagheri et al., 2015, 2013, 2016; Del Bello et al., 2017; Dietrich, 1982; Komar and Reimers, 1978; Loth, 2008; Riley, 2003; Walker et al., 1971), and non-spherical particles of simple geometry (e.g., spheres, disks, cubes, cylinders, spheroids: Allen, 1984; Jayaweera and Mason, 1965; McNown and Malaika, 1950; Pettyjohn and Christiansen, 1948; Stringham et al., 1969; Wilson and Huang, 1979; Wu et al., 2008) falling in still air. However, very few of these studies have evaluated C_D at very low Reynolds numbers ($Re \ll 1$). As a consequence, dust modellers generally assume that the particles in suspension are spherical and that the settling velocity is well approximated by Stoke's law

(Armienti et al., 1988; Brazier et al., 1982; Glaze and Self, 1991; Jarzemba et al., 1997; Johnson et al., 1996; Spark et al., 1992; Suzuki, 1983). Analysis of the measurements obtained in the present study will be used to independently evaluate C_D.

A particle of density (ρ_s) settling in the air of density (ρ_a) undergoes acceleration due to gravity (g), until its terminal settling velocity (v) is attained. At this point, the gravitational force ($F_G = mg$) is exactly balanced by the drag force (F_D) modelled by the quadratic stress law:

$$F_D = \frac{1}{2} C_D \rho_a A v^2, \tag{5.3}$$

where A is the projected area of the particle. Assuming that the median particle velocity measured at the bottom of the fall column well approximates v for the particle source, an estimate of C_D therefore can be obtained from the dimensionless index:

$$C_D = \frac{4}{3} \left(\frac{\rho_s - \rho_a}{\rho_a} \right) \frac{g d_{50}}{v_{50}^2}, \tag{5.4}$$

where d_{50} is taken to be a reasonable estimate of the median value of the particle size distribution. Particle density (ρ_s) values for the four Icelandic samples are extracted from the study of Chapter 2.

The Reynolds number, Re, for spherical and angular particles is given by:

$$R_e = \frac{v_i d_i}{\nu}, \tag{5.5}$$

where ν is the kinematic viscosity of air.

Similarly, median values for the vertical velocity and particle diameter were used to determine Re. While some studies have measured C_D for settling particles when $Re < 1$ (e.g., Wilson and Huang, 1979; Wu et al., 2008), suitable values for

this parameter have never been determined experimentally for aerosols where Re is up to two orders of magnitude lower.

The experimentally derived values for C_D for all samples, including the solid glass spheres, are remarkably similar in magnitude (Fig. 5.9): Ash (4.8×10^3), Mixed (5.3×10^3), Glacio1 (5.8×10^3), Spheres (6.4×10^3) and Glacio2 (7.5×10^3). This outcome provides experimental confirmation that the influence of the particle shape, which influences form drag, is relatively unimportant when viscous effects dominate at very low Re. A comparison between the values of C_D determined for the Icelandic dust samples, and the solid glass spheres, indicates very good agreement with an extension ($24/Re$) of the experimental results of Allen (1994).

5.3.5 Role of humidity

One final factor to consider is the relative humidity of the air column, which is expected to alter interparticle cohesion. In order to evaluate the magnitude of this effect, the temporally lumped data for the velocity components measured at varied relative humidities (20−30 %, 50−60 % and 70−80 %) were binned to create a series of cumulative frequency distributions (Fig. 5.10). The corresponding median velocities for all distributions are reported in Table 5.3.

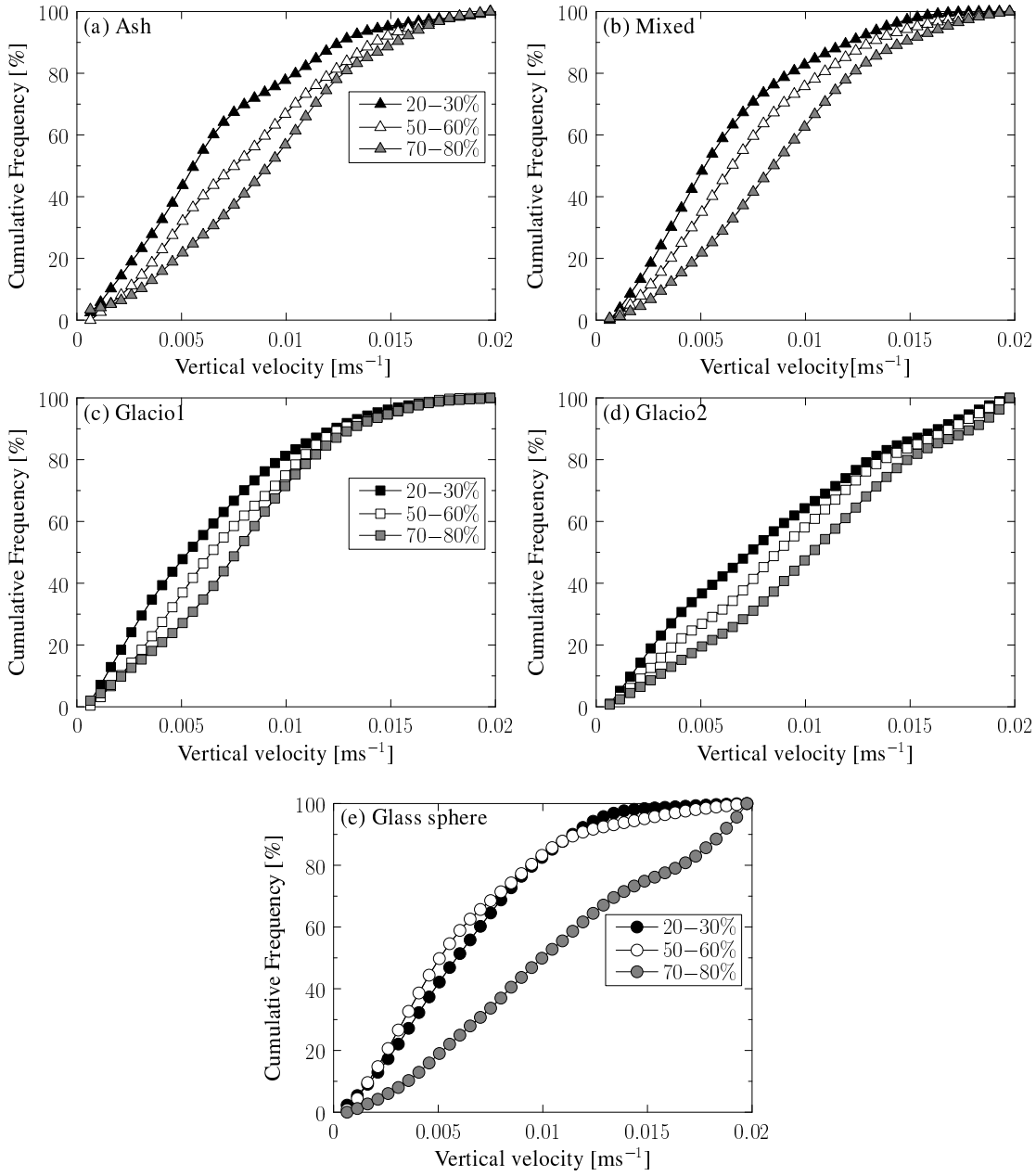

Figure 5.10: The effects of relative humidity on the vertical velocity component.

A systematic net increase in u_i (by a factor of 1.3 to 1.7) and v_i (by a factor of 1.6 to 2.6) is clearly apparent for all Icelandic samples over the full range of humidity investigated (Table 5.3). The greatest proportionate increase is observed

for the Ash particles. The glass spheres only demonstrate an increase in the vertical velocity component when RH exceeds 70%, while the horizontal drift component remains well below that for the Icelandic samples and does not respond consistently to the humidity changes. As confirmed by the BET measurements (Table 5.3), and those by Riley (2003), who also worked with varied sources of volcanic ash, highly porous, amorphous dust particles have very large specific surface areas relative to solid spheres of equivalent geometric diameter by as much as two orders of magnitude. As such, they may also adsorb greater amounts of water as shown by the gravimetric moisture content in Fig. 5.10.

Highly porous clay particles that are abundant in iron also are reported to adsorb substantial amounts of water relative to other dust components (Herich et al., 2009; Kumar et al., 2009; Schuttlefield et al., 2007), and to provide increased surface area for particle interactions (Kumar et al., 2009). Indeed, Icelandic dust particles are dominated by iron-rich minerals and amorphous glass (Arnalds et al., 2014, 2016). In the atmosphere, particle growth occurs when relative humidity increases (Pilinis et al., 1995, and references therein), so that the thin film of moisture tightly bound to each surface provides cohesion and thereby enhances aggregate growth during interparticle collision. While other factors may influence the likelihood of interparticle attraction and collision within a plume of particles descending within an air column (e.g., Brownian motion; electrostatic and Van Der Waal forces; volume fraction of suspended particles), they lie beyond the scope of this investigation. In the still air column, the additional mass associated with aggregate growth no doubt contributes toward increased gravitational force, relative to the opposing fluid drag, and thus settling velocity. Interestingly, Johnson et al. (1996) also discovered through lab experiments in water that higher settling velocities are associated with aggregates having increasingly greater void

space as compared to solid spheres.

The results in Table 5.3 clearly demonstrate that water adsorption increases the drift rate for the natural amorphous particles by a factor of approximately two over the full range in humidity investigated. This enhancement of the horizontal diffusion with increasing humidity could derive from Magnus effects (particle spin) arising from particle collisions. This hypothesis is supported by the work of Wu et al. (2008) and Wilson and Huang (1979) who demonstrate that the rotation of irregular particles is higher than those for spherical ones and increases with particle diameter. The lateral deflections are believed to be caused by the changing ratio between form and frictional resistance at different moments in time. If true, enhancement of aggregate formation at higher humidity should increase spin and drift.

Table 5.3: A summary of the physical properties and settling velocity components. The mean particle diameters before and after are obtained from the Horiba (Fig. 5.4).

Variables		Descriptions	Unit	Mixed	Ash	Glacio1	Glacio2	Spheres
		ρ_i	gcm^{-3}	1.95	1.77	1.76	2.32	n/a
Mean	**Particle Characteristics**	$\overline{\rho_s}$	gcm^{-3}	2.65	2.66	2.79	2.74	2.50
		$\overline{d}_i$ (Before)	µm	13	15	14	25	12.5
		$\overline{d}_i$ (After)	µm	14	16.5	14	27	13.5
		BET-SA	m^2g^{-1}	1.07	1.65	4.19	5.14	0.31
Median	**Aggregate Diameter** (d_{a50})	d_i (0 s)	µm	13	29	28	32	n/a
		d_i (3 min)	µm	9	10	10	13	n/a
		d_i (11 min)	µm	9	10	10	13	n/a
	Vertical velocity (v_{50})	RH (%)						
		$20-30$	ms^{-1}	0.0053	0.0056	0.0051	0.0075	0.006
		$50-60$	ms^{-1}	0.0065	0.0075	0.007	0.0086	0.005
		$70-80$	ms^{-1}	0.0085	0.0096	0.0077	0.001	0.0099
	Horizontal velocity (u_{50})	$20-30$	ms^{-1}	0.0013	0.0014	0.0012	0.0015	0.0009
		$50-60$	ms^{-1}	0.0023	0.0017	0.0015	0.0026	0.0015
		$70-80$	ms^{-1}	0.0029	0.0022	0.0023	0.0037	0.0012

$\overline{\rho}_s$-mean skeletal density, ρ_i-particle density

5.4 Conclusions

A unique feature of selected hlcc regions is that extremely active dust sources are interlinked with particles supplied from glacio-fluvial outwash systems, where new source areas are rapidly becoming exposed (Bullard et al., 2016; Gassó et al., 2018). Unlike most hlcc regions that are only linked to glaciofluvial systems, Iceland also has active volcanoes that supply and disperse the largest quantity of ash as compared to any other hlcc region, and so, Iceland is classified as the largest volcaniclastic desert within the Arctic and Europe.

Apart from recent collaborative efforts to measure and model high latitude dust emission, transport and deposition, a number of underlying physical mechanisms unique to cold, humid climates, and their geological environments are not well understood. The lack of emphasis on micro-scale characteristics supported by sophisticated equipment, design and analysis has contributed to these problems, thereby restricting the knowledge of hlcc dust processes to well-established studies focused on siliciclastic particles in dry, hot deserts (Bullard et al., 2016; Gassó et al., 2018). This experimental study identified several unique morphological properties that strongly influence the deposition rate of Icelandic volcaniclastic particles. The experimental results suggest that:

(i) In relatively dry conditions, the effects of the micro-scale characteristics (particle roughness, porosity and shape) appear to increase the horizontal velocity components relative to that of a solid glass sphere, but have no significant effects on the vertical velocities, although, the horizontal velocities are an order of magnitude lower than the vertical.

(ii) In increasingly humid conditions, the amount of moisture adsorbed by Icelandic particulates is strongly dependent on the micro-scale characteristics,

such as angularity, surface area, and porosity, which thereby enhance aggregation and lead to increased horizontal and vertical velocities.

Although further study is required, the results show that humidity certainly plays a role, and may be of considerable importance in cool, humid climates typical of high latitudes, but the settling velocities are strongly dependent on the particle micro-scale features. In hlcc regions, the atmosphere is humid and windy (Bullard et al., 2016; Bullard, 2013), therefore it is much more difficult for discrete particles to fall out individually. On much larger scales at high atmospheric altitudes, large suspended volumes of volcanic originated particles are able to form large aggregates more easily and very quickly, thus increasing their settling velocity and fallout. Therefore, it is critical for dust transport and dispersion models to take into consideration the effects of relative humidity on the settling velocity of particles that are especially porous, otherwise models will either over predict or under predict their settling rates.

Chapter 6

General Conclusions

"The important thing is to never stop questioning." Albert Einstein

6.1 Conclusions

This doctoral dissertation aims to improve understanding of the physics of Icelandic dust entrainment, emission and deposition in order to minimize the uncertainties and limitations in model predictions and thus lead to better recommendations and hazard assessments on climate, health, and the environment. The research strategy and structure for this thesis is reviewed first, followed by a consideration of the limitations of this study. A summary of the principal findings gathered from each of the four Ph.D. thesis papers is also provided, and finally the recommendations for future work considered. Icelandic dust environments provide an accessible and highly suitable analogue for similar present-day and historical settings so that the findings of this study are relevant to other high latitude dust regions of similar geomorphology and climatic conditions that experience dust storm events.

This dissertation describes a series of laboratory experiments used to investigate Icelandic dust processes and is divided into four core chapters (2 to 5) written as four manuscripts. Chapter 2 deals with the fundamental characterization of the Icelandic dust particles (e.g., ash and Glaciogenic dust $\leq 50\,\mu m$) using several cutting-edge technologies and techniques, which are typically used in material science and chemistry. Various techniques used to obtain replicate measurements of the particle properties allowed for the examination of the sample homogeneity. The results from these analyses provide a detailed description of the nano- and micro-scale properties of the Icelandic particles, which allow for the investigation of relationships between these properties. Chapter 3 outlines a wind-tunnel experiment in which the dust emission rate was measured to quantify the suspension of Icelandic dust particulates when subjected to a range of wind speed at constant temperature and humidity. The influence of wind gusting on the dust emission rate was also examined.

Chapter 4 investigates the ejection of Icelandic dust particles by the impact of a rain droplet through a series of controlled laboratory experiments carried out in the Trent Environmental Wind Tunnel (TEWT) within a shearing flow, as well as on top of a lab bench and within a stairwell in still air. This study investigated the influence of the droplet, particle, and crater morphologies on the dynamics of the splash structure that emerged from the test bed. An algorithm designed in Matlab was used to analyze images of the droplet and crater morphologies, as well as the splash structure, recorded using a high-speed PCO.Dimax™ camera. The associated PM_{10} concentration was sampled downwind of the impact area using conventional technology. Chapter 5 provides direct measurements of the terminal settling velocity of a particle $\leq 50\,\mu m$ in diameter in 2D (x - *horizontal* and z - *vertical*) within large suspended volume fractions of particles, using a

laser Doppler anemometer. The effects of the particle morphology and climate (relative humidities, $20-30$, $50-60$ and $70-80\,\%$) on the settling velocity were also investigated in this chapter.

6.2 Limitations of the study

Although this study is the first laboratory investigation of several Icelandic dust sources, considered to be the most emissive in Iceland, the limitations of this study are recognized as follows:

- Several state-of-the-art technologies and techniques were used to characterize the Icelandic dust particles, but there are limitations associated with each of these technologies. For instance, the mercury intrusion technique can be used to estimate the pore size distribution of the Icelandic dust particles, but it cannot distinguish between the sizes of the intraparticle (within particles) pores and interparticle (between particles) voids.

- The aerodynamic surface roughness of the boundary layer in the wind tunnel is several orders of magnitude less than those in the field, and so the effects of the surface roughness had to be removed by normalizing the friction velocity by its threshold velocity, which allowed for comparable dust emission measurements in the wind tunnel with field studies performed in hlcc regions.

- The quantity of water ejected within daughter droplets jetting away from the surface remains unknown because they were coated with particles and dispersed within the cross-section flow of the splash structure.

- To the author's knowledge, Chapter 5 presented the first application of the Laser Doppler anemometer (LDA) to measure the settling velocity of Ice-

landic dust particles. The LDA can make high-resolution measurements without perturbing the airflow, but the velocity components (x - *horizontal*, z - *vertical*) measured were restricted to particles that passed through its 0.04 m^3 optical measurement volume. The LDA also cannot independently measure particle diameter.

6.3 Key findings

The particle characterization performed in Chapter 2 has shown that ultrafine Icelandic dust particles contain pores and voids, as well as large amounts of amorphous glass, and a significant quantity of nanosize dustcoats. The results also show that increasing particle sphericity is associated with progressively smaller particle size. An abundance of amorphous glass increases the surface area and roughness of the particles, which contributes to high porosity that alters the particle skeletal density. The pore-size distribution of the Icelandic dust samples shows that the size of the pores increases with the particle size, supporting the suggestion that coarse particles (up to 50 μm in diameter: Gislason et al., 2011) can be transported over long distances when they have a high degree of porosity.

Several interlinking relationships between these properties of complex Icelandic particles (Chapter 2) and dust entrainment and deposition (Chapter 3 to 5) were found in other parts of this study that emphasize the importance of knowing the particle characteristics. For instance, the wind tunnel experiments in Chapter 3 show that the sediments containing a higher portion of coarse silt and sand (e.g., Control, Glacio2, Gacio3) appear to be the most emissive, as compared to the finer sediments with more PM_{10} but less

sand (e.g., Ash, Mixed, Glacio1). This result would appear to confirm that saltation plays a key role in dust emission, as suggested by the field work of Mockford (2017). A possible explanation for the high concentration of airborne particulates is that dustcoats are ejected from the surface and pores of the coarse particles, as well as their sharp edges during mechanical abrasion. Of the three samples containing $> 40\,\%$ clay, the sample containing the most fines with the largest BET surface area emitted the most particulates, suggesting that the particle surface area may enhance dust entrainment and dispersion above the bed surface. The Icelandic dust emission rates measured in the wind tunnel experiments for the coarse Glaciogenic samples are similar in magnitude to those measured in field studies within other high latitude regions with similar geomorphology and climate.

Wetting of a given surface is widely perceived to increase cohesion and thereby suppress the particle supply available for entrainment and transport by winds as discussed in Chapter 4. However, rain droplet impact may also initiate both saltation and aerosol ejection. In Iceland, for example, field workers report that dust emission sometimes coincides with the onset of a precipitation event (Ashwell and Hannell, 1960; Prospero et al., 2012). Such reports are confirmed by the water droplet experiments carried out in Chapter 4. These experiments demonstrate that the PM_{10} concentration sampled downwind of the impact area (up to $10^3\,\mu\,gm^{-3}$) is positively correlated with the water droplet velocity, impact angle, and wind speed at a low relative humidity ($< 30\,\%$). The strong wind shear at the bed surface acts to disperse many of the tiny particle aggregates and coated liquid droplets contained within the splash structure. Notably, the splash height of the particles decreases with the particle diameter, suggesting that

the particle weight influences the height of the emerging splash structure. Furthermore, the maximum particle splash height lies well above the range ($0.07 - 0.28$ cm) in aerodynamic surface roughness length for most Icelandic surfaces (Arnalds et al., 2001), so that dust dispersion within the turbulent shearing flow is favoured at low relative humidity ($< 30\,\%$).

The deposition of suspended dust particulates in the atmosphere is also dependent on the particle characteristics and regional climate. In Chapter 5, the results reveal that in relatively dry conditions, the effects of the micro-scale characteristics (e.g., increased particle roughness, porosity and angularity) appear to increase the horizontal velocity component relative to that of a solid glass sphere, but have no significant effect on the vertical component, which is approximately an order of magnitude higher than the horizontal. The particle size strongly influences the vertical velocity component. Under increasingly humid conditions, the amount of moisture adsorbed by Icelandic dust particulates appears to be strongly dependent on the micro-scale characteristics (e.g., angularity, surface area, and porosity), which thereby may enhance aggregation and led to increased fall velocities. Scanning electron micrographs of the aggregate deposits from the fall-column experiments, as well as moisture adsorption measurements, reveal that dust particulates with large surface area absorb more moisture on their surfaces and in their pores, as compared to those with low surface areas. During particle interactions, the moisture on their surfaces influences aggregate formation, thereby influencing the settling rate of the particles. These results imply that model schemes related to dry conditions might not adequately reflect the deposition rate of volcaniclastic dust particles at high relative humidities.

6.4 Future work considerations

This dissertation supports the suggestion that saltation plays a vital role in hlcc dust emission processes but at low relative humidity. Further wind-tunnel investigations are needed to examine the variation of the vertical dust flux at varying temperature and humidity, which may alter the effects of the particle characteristics. Dustcoats may have contributed to high airborne particulate concentrations during saltation, further experiments in which scanning electron micrographs of the particles are obtained before and after the wind tunnel experiments are needed to confirm this.

Icelandic regions experience poor air quality and high suspended particulate matter (PM) concentrations during periods of light rainfall and high-frequency wind speed (e.g., up to 6 ms^{-1}: Ashwell and Hannell, 1960; Prospero et al., 2012). This study provides a first step towards the understanding of the dynamics of the ejection phenomena and quantifies the amount of dust particulates ejected during wind-driven rain splash. However, further experiments are needed to understand the influence of multiple water droplets on the emerging splash structure and PM concentration recorded at varying wind speeds. The release of several water droplets during an experiment can also be extended to identify when dust emission is either sharply decreased or halts altogether during wind-driven rain splash.

Icelandic dust particles falling within a settling chamber do not fall independently but rather as particles that interact and form aggregates (Bagheri, 2014), which typically have large settling velocity (e.g., Brown et al., 2012). The collision and bonding of the particles to form aggregates are still not well understood. The aerodynamic features of these large aggregates are also highly complex and need to be studied in further detail. The lateral drifting of the Icelandic aggregates

was found to increase with relative humidity, as a consequence of their large size, but further experiments are needed to understand the implications of the particle deflection and its consequences for dust dispersion.

6.4.1 Final remarks

The retreat of glaciers and ice-cap masses in hlcc environments is expected to expose new dust particulate sources as the global mean temperature continues to rise (Cannone et al., 2008; Radic and Hock, 2011). Catastrophic volcanic eruptions in Iceland are also expected to eject up to 10^4 m^3 of unique, ultrafine particles into the atmosphere (Butwin et al., 2019) that will replenish depleted terrestrial landscapes with ash deposits. The sediments available for transport by aeolian dust processes influence the frequency and duration of dust storm events (Björnsson and Pálsson, 2008; Bullard et al., 2016; Bullard, 2013; Marshall et al., 2012; Solomon et al., 2007; Thorsteinsson et al., 2012). The key findings that emerge from this study should be considered in air quality that forecast suspended volcaniclastic particulates.

Appendix A

Instrument Description

Instrument Description

A.1 Trent Environmental Wind Tunnel (TEWT)

Trent Environmental Wind Tunnel has a measured cross-sectional height, H=74 m, width, W=71 m and working test-sectional length, L=13.5 m. When TEWT is in operation, the air flow that enters the wind tunnel is first directed through a compression bell followed by a honeycomb straightener. The honeycomb straightener consists of an array of cellular channels created from plastic straws stacked onto each other with their opening positioned perpendicular to the direction of the airflow. The primary function of the straightener is to reduce any external large-scale turbulence within the airflow before entering the working test section of the tunnel. The airflow is then directed over an array of evenly spaced staggered wooden dowels each has a diameter, d=2.0 cm, height, H_d=2.5 cm, and center to center distance, C=4.5 cm. The staggered pattern is used to ensure that no roughness element was directly behind another roughness element in the row ahead of it. These wooden dowels are used as roughness elements to create shear stress within the near surface flow. Immediately following this roughness region, is a straight long section of the tunnel which rapidly develops an artificial turbulent boundary layer (BL) flow to naturally move particles resting on the surface. This straight long section is also called the working test section sufficiently long to reach streamwise stability, conforming to equilibrium conditions. This sophisticated design is used to ensure that the dynamics of the sediments are not restricted by the dimensions of the tunnel.

A.2 Horiba Partica LA- 950 V2

The size distributions of the samples were analyzed using the Horiba Partica LA-950 V2 that uses Mie Scattering (laser diffraction) to measure the size of particles. The core principle of this laser diffraction technique works by measuring the angle of the scattered light for differently sized particles. This angle is dependent on the size of the particle measured where larger particles scatter at small angles and smaller particles scatter at wide angles. As a result, a pattern of the scattered light is formed on a screen, creating an intensity distribution of fringes: dark and light bonds for each sample. These intensity distributions are transformed into the size distribution of the sample.

A.3 Size definition classification system

Particle diameter (d) ranges from more than 2 mm to <0.1 μm and are divided into four categories (Fig. 9): clay (d<4 μm), silt (4 μm<d≤63 μm), sand (63 μm<d≤2000 μm) and gravel (2000 μm<d≤2 m). Clay- and silt-size particles make up what is called dust-size particles. This dissertation is strongly focused on particles within the dust size range with d≤63 μm, unless the range of diameters is otherwise stated. Icelandic dust particles transported over long distance is up to 63 μm in size whereas those originating from silicate are up to 20 μm in size (Gislason et al., 2011; Pye, 1987; Duce, 1995; Fig. 9).

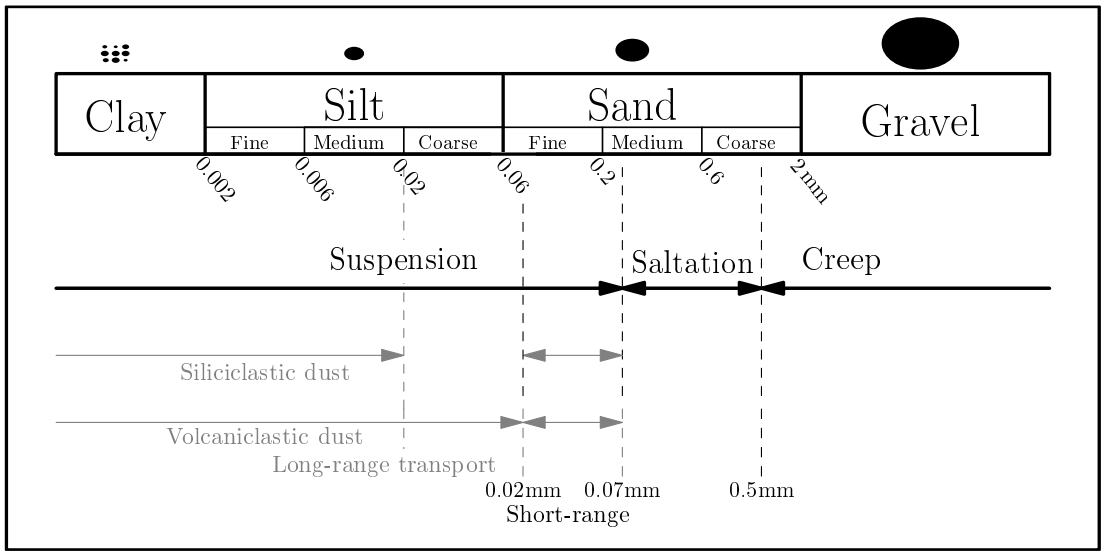

Figure A.1: Particle-size definition system

A.4 Micro-pitot tubes

Wind velocity profiles will be measured at two streamwise stations located upstream and downstream from the entrance of the working test section above the tunnel floor. These wind velocity profiles will be measured using stainless steel micropitot tubes with an outer diameter of 3 mm, and an inner diameter of 1 mm (McKenna-Neuman, 2003). Both tubes will be mounted onto a stepping motor that allow them to slide vertically. The vertical sliding of these tubes will be synchronized to sample wind velocity at precisely the same height for the same moment in time. Both micropitot tubes will be positioned along the same cross-wind location that is centered along the width of the wind tunnel roof. These tubes will be positioned sufficiently along the test section to ensure that the wind profiles are measured where the boundary layer is well-developed. To measure the horizontal wind velocity profiles at these stations, the micropitot tubes will traverse vertically upwards from its lowest sampling height, z=0.5 cm, through

the air flow and into the free stream to its highest sampling height, z=0.4 m, simultaneously.

To find the wind velocity profile, using the pressures at height measured by micropitot tubes, the Bernoulli equation is applied. The Bernoulli equation applied to an idealized fluid or air flow is given by

$$p + \frac{1}{2}\rho u^2 + \rho g h = \text{constant}, \tag{A.1}$$

where p is the pressure, the density, ρ, of the air/fluid is constant, u is the wind velocity, $g = 9.8\,\text{ms}^{-2}$ is the gravitational acceleration and h is the height/depth at which the measurements were taken.

The Bernoulli's equation can also be considered as the conservation of energy principle for a flow where the energy per unit volume before is equivalent to the energy per unit volume after:

$$P_1 + \frac{1}{2}\rho u_1^2 + \rho g h_1 = P_2 + \frac{1}{2}\rho u_2^2 + \rho g h_2 \tag{A.2}$$

where the energy terms are given as the hydrostatic pressure, P, the kinetic energy (energy of a moving object: fluid), $\frac{1}{2}\rho u^2$ and the potential energy (energy as a result of position), $\rho g h$, of the flow. The conservation of energy states that energy can not be created or destroyed, but it can be changed from one form to another such that the total amount of energy is constant.

Using Bernoulli's equation, the height, h_1 of the airflow with velocity, u_1 upstream of the wind-tunnel is equivalent to the height, h_2, at the stagnation point of the pitot tube (h_1=h_2). Hence, the conservation of energy principle given by

Equation (A.2) is reduced to

$$P_1 + \frac{1}{2}\rho u_1^2 = P_2 + \frac{1}{2}\rho u_2^2 \tag{A.3}$$

At the stagnation point, the flow velocity, u_2=0, hence, Equation (A.3) becomes

$$P_1 + \frac{1}{2}\rho u_1^2 = P_2 \tag{A.4}$$

where P_1=P_s is the static pressure measured, $\frac{1}{2}\rho u_1^2$ is the dynamic pressure, P_2=P_T, is the total pressure measured by the manometer (in the wind-tunnel calibrated pressure transducer). As a result, Equation A.4 can be rewritten as

$$u_1 = \sqrt{\frac{2(P_2 - P_1)}{\rho}}, \tag{A.5}$$

where $P_2 - P_1$=$P_T - P_s$ is the change or difference in pressure, Equation (A.5) forms the horizontal time-averaged velocity:

$$u_1 = \sqrt{\frac{2(P_T - P_s)}{\rho}} \Rightarrow u_1 = \sqrt{\frac{2(\Delta P)}{\rho}}. \tag{A.6}$$

A.5 DustTrak™

The DustTrak™ aerosol monitor operates by using an air pump to draw in a known volume of ambient air from the flow in a continuous stream and store to the selected log output while return to the screen a measured concentration value. From the principle of backscattering, the concentration of dust particles with $d \leq 10\mu m$ will be found from that known volume of air when illuminated by a laser light inside the DustTrak™. These DustTrak™ monitors will be

positioned along thes working test section of the tunnel. These DUSTTRAKS^{TM} aerosol monitors can also sample the total dust concentration as well as separate concentrations for $d \leq 2.5\mu$ m, $d \leq 10\mu$ m and respirables.

A.6 Laser Doppler Anemometry

The Laser Doppler Anemometry (LDA) is an optical technique used to measure velocity and turbulence distribution in 1D, 2D and 3D for free and internal flows. However, the Dantec^{TM} LDA that will be used in this study can only measure in 1D and 2D. Figure A.2 illustrates this 2D Dantec^{TM} LDA. Concept from which the LDA operate is of the doppler shift. Doppler shift is the frequency changes or variation of a wave for an observer moving relative to the source that produces the frequency. An example is an ambulance siren moving towards and away from an observer. These effects are also observed with light. Light reflected from a moving object will scatter and the scattered portion light frequency will shift by an amount proportional to the object's speed in this case particles. The Dantec^{TM} LDA has two visible and two non-visible laser beams of wavelength, λ=0.660 mm and λ=0.785 mm respectively. These laser beams intersect at a single point to form a 0.04 mm^3 volume measurement region. As sediments intersect the measurement volume, their fringe interferences are transformed into velocities: u and w. The Dantec^{TM} LDA is attached to a 2D traverse control that allows it to change positions in the x and y directions. The rate at which this LDA samples is dependent on some key parameters in the BSA software used to determine the performance of the LDA. The velocity and turbulence of the flow are measured with a Burst Spectrum Analysis (BSA)^{TM} desktop software.

Figure A.2: The Dantec^{TM} 2D Laser Doppler Anemometer

A.7 Canadian Standard Sieve Series

Selected Icelandic sediment size will be determined from dry sieving. A stack of successively-finer sieves called the Canadian Standard Sieve Series will be mounted on an electrically powered shaker/sieve called the Meinzer II sieve shaker. In the sieve container, sediments will be shaken until they present their smallest axis to fall through the holes of the sieve into a collection container of smaller diameter. This method of particle size selection creates a bias because particles not only of the selected size but also particles with smaller sizes will fall into the collection containers. Therefore, sieving favors the diameter of particles that are equal to and are less than the desired particle size and sieve holes. As a result, particles of only one specific dameter can not be collected.

A.8 Brunauer, Emmett & Teller System

The Brunauer, Emmett and Teller (BET) Gemini VII 2390 V1.02 (V1.02 a) surface area analyzer was used to measure and analyze the surface area of all the samples used in this study. The BET (Brunauer, Emmett, and Teller) method is commonly used on powders to obtain reliable surface area measurements (<10% error) and was used to determine the surface areas for bulk samples. This technique injects liquid nitrogen into a tube holding the sample and assumes that the gas is adsorbed onto the powder in multiple uniform layers (Brunauer, 1994). Pressure is decreased over time and the volume of gas for each pressure change is plotted to obtain an isotherm curve. This isotherm represents the point at which an equal amount of gas is being absorbed and released by the particles. In other words, the weight of the absorbed gas is plotted against the relative pressure, and the slope and intercept of the best fit line is calculated. The intercept of the isotherm provides the volume of gas absorbed onto the sample. Surface area can be calculated by knowing the gas molecule size and number of molecules in the measured volume of gas.

Appendix B

Analysis description

Analysis Description

B.1 Wind velocity profile: Aerodynamic Roughness & Friction Velocity

The horizontal wind speed will be computed from the difference between the total, E_d, and static, E_s, air pressures measured at each corresponding height above the tunnel surface over a time interval of 2 s. The differential pressures are obtained from a pressure transmitter (span 0−1" W.C.D., 0.25% accuracy), and then from Bernoulli's equation the wind velocity can be found. From the wind velocity profile, the general logarithmic empirical equation,

$$x = a\ln(y) + b, \tag{B.1}$$

is used to fit the dataset where the coefficients, a and b represent the slope and y-intercept of the exponential profile respectively. This empirical equation is used to fit the horizontal time-average velocity Equation 3.2 to experimental dataset. The laws of the wall equation formed from Equation (B.1) is given by:

$$\overline{u}(z) = \frac{u_\star}{\kappa_v}\ln(z) + c, \tag{B.2}$$

where κ_v=0.41 is the dimensionless Von Karman constant, $\overline{u}(z)$ is the velocity profile at height, z, c is a constant.

When the velocity, u goes to zero the empirical equation is reduced to the form,

$$0 = a\ln(z_o) + b \Rightarrow z_o = \exp\left(\frac{-b}{a}\right). \tag{B.3}$$

Using the laws of the wall, when the velocity goes to zero, the height, z is replaced by z_o. The aerodynamic roughness, z_o, is found when the wind speed following the log-law profile falls to zero ($\overline{u}(z_o)$=0) and the log-wind profile intercepts the graph (height equivalent to z_o on the y-axis). The aerodynamic surface roughness length, z_o, is found when the wind speed following the log-law profile falls to zero ($\overline{u}(z_o)$=0) and the log wind profile intercepts the graph at an height equivalent to z_o on the y-axis as shown in above equation B.3.

Following Equations B.1 and B.2, the friction velocity, $u_\star$ is given by

$$u_\star = \kappa_v a. \tag{B.4}$$

References

Ahn, S., S. H. Doerr, P. Douglas, R. Bryant, C. A. Hamlett, G. McHale, G. McHale, M. I. Newton, and N. J. Shirtcliffe (2012), Effects of hydrophobicity on splash erosion of model soil particles by a single water drop impact, Earth Surface Processes and Landforms, 38(11), 1225–1233, doi:10.1002/esp.3364.

Al-Durrah, M. M., and J. M. Bradford (1982), Parameters for describing soil detachment due to single waterdrop impact 1, J. Soil Sci. Soc. Am., 46(4), 836–840.

Alfano, F., C. Bonadonna, A. Volentik, C. Connor, S. Watt, D. Pyle, and L. Connor (2011), Tephra stratigraphy and eruptive volume of the May, 2008, Chaitén eruption, Chile, Bulletin of Volcanology, 73(5), 613–630, doi: 10.1007/s00445-010-0428-x.

Allen, J. (1994), Fundamental properties of fluids and their relation to sediment transport processes, 25–60 pp., Blackwell Scientific Publications.

Allen, J. R. L. (1984), Sedimentary structures: their character and physical basis, Elsevier Sci., 1, 183–188.

Armienti, P., G. Macedonio, and M. T. Pareschi (1988), A numerical model for simulation of tephra transport and deposition: Applications to May 18, 1980, Mount St. Helens eruption, J. Geophys. Res., 93(B3), 6463–6476, doi:10.1029/JB093iB06p06463.

Arnalds, Ó. (2005), Icelandic soils, Developments in Quaternary Sciences, 5, 309–318, doi:10.1016/S1571-0866(05)80015-6.

Arnalds, Ó. (2010), Dust sources and deposition of aeolian materials in Iceland, Icelandic Agricultural Sciences, 23, 3–21.

Arnalds, Ó., F. O. Gisladottir, and H. Sigurjonsson (2001), Sandy deserts of Iceland: an overview, Env. Science Policy., 47(3), 359–371, doi:10.1006/jare.2000.0680.

Arnalds, Ó., F. O. Gisladottir, and H. Sigurjonsson (2003), Soil erosion and land use policy in Iceland in relation to sheep grazing and government subsides, Env. Science Policy, 6, 105–113, doi:10.1016/S1462-9011(02)00115-6.

Arnalds, Ó., E. F. Thorarinsdottir, J. Thorsson, P. D. Waldhauserova, and A. M. Agustsdottir (2013), An extreme wind erosion event of the fresh Eyjafjallajökull 2010 volcanic ash, Scientific Reports, 3, 1257, doi:10.1038/srep01257.

Arnalds, Ó., H. Olafsson, and P. Dagsson-Waldhauserova (2014), Quantification of iron-rich volcanogenic dust emissions and deposition over the ocean from Icelandic dust sources, European Geoscience Union, 11, 5941–5967.

Arnalds, Ó., H. Olafsson, and P. Dagsson-Waldhauserova (2015), Quantification of iron-rich volcanogenic dust emissions and deposition over the ocean from Icelandic dust sources, Biogeosciences, 11, 6623–6632, doi:10.5194/bg-11-6623-2014.

Arnalds, Ó., P. Dagsson-Waldhauserova, and H. Olafsson (2016), The Icelandic volcanic aeolian environment: Processes and impacts: a review., Aeolian Research, 20, 176–195, doi:10.1016/j.aeolia.2016.01.004.

Ashwell, I. Y., and F. G. Hannell (1960), Wind and temperature variations at the edge of an ice cap, Meteorological Magazine, 89, 17–24.

Baddock, M. C., T. Mockford, J. E. Bullard, and T. Thorsteinsson (2017), Pathways of high-latitude dust in the North Atlantic, Earth and Planetary Science Letters, 457, 170–182.

Bagheri, G., C. Bonadonna, I. Manzella, and P. Vonlanthen (2015), On the characterization of size and shape of irregular particles., Powder Technology., 270, 141–153, doi:10.1016/j.powtec.2014.10.015.

Bagheri, G. H. (2014), Numerical and experimental investigation of particle terminal velocity and aggregation in volcanic plumes, University of Geneva, Ph.D. thesis, doi:10.13097/archive-ouverte/unige:77593.

Bagheri, G. H., C. Bonadonna, I. Manzella, P. Vonlanthen, and P. Hass (2013), Dedicated vertical wind tunnel for the study of sedimentation of non-spherical particles, Review of Scientific Iinstruments., 84(5), 054,501, doi:10.1063/1.4805019.

Bagheri, G. H., C. Bonadonna, I. Manzella, P. Vonlanthen, and P. Hass (2016), Aerodynamics of volcanic particles: Characterization of size, shape, and settling velocity., in Volcanic Ash: Hazard Observation., chap. 2, pp. 39–52, Elsevier Science & Technology.

Bagnold, R. A. (1935), The movement of desert sand, The Geographical Journal, 85(4), 342–365.

Bagnold, R. A. (1941), The physics of blown sand and desert dunes, Chapman & hall Ltd., London, UK.

Bagnold's, R. A. (1941), The physics of blown sand and desert dunes, Chapman & hall Ltd., London, UK.

Baratoux, D., N. Mangold, O. Arnalds, M. Bardintzeff, J., B. Platevoet, M. Gregorie, and P. Pinet (2011), Volcanic sands of Iceland-diverse origins of aeolian sand deposits revealed at Dyngjusandur and Lambahraun., Earth Surface Processes & Landforms., 36(13), 1789–1808, doi:10.1002/esp.2201.

Beard, K. V. (1976), Terminal velocity and shape of cloud and precipitation drops aloft, J. Atmosp. Sci., 33, 851–864.

Beczek, M., M. Ry?ak, A. Sochan, R. Mazur, C. Polakowski, and A. Bieganowski (2017), The differences in crown formation during the splash on the thin water layers formed on the saturated soil surface and model surface, PloS one, 12(7), e0181,974, doi:10.1371/journal.pone.0181974.

Behroozi, F. (2012), Determination of contact angle from the maximum height of enlarged drops on solid surfaces, American Journal of Physics, 80(4), 284–288, doi:10.1119/1.3678306.

Bergametti, G. (1998), Mineral aerosols: renewed interest for climate forcing and tropospheric chemistry studies, Int. Global Atm. Sc., 11, 13–17.

Bhattachan, A., L. Wang, M. F. Miller, K. J. Licht, and P. D'Odorico (2015), Antarctica's dry valleys: A potential source of soluble iron to the southern ocean?, Geophysical Research Letters, 6(42), 1912–1918.

Björnsson, H., and F. Pálsson (2008), Icelandic glaciers, Jökull, 58(58), 365–386.

Boxel, J. H. V. (1998), Numerical model for the fall speed of rain drops in a rainfall simulator, In Workshop on wind and water erosion, pp. 77–85.

Brazier, S., A. N. Davis, H. Sigurdsson, and R. S. J. Sparks (1982), Fall-out and deposition of volcanic ash during the 1979 explosive eruption of the Soufriere

of St. Vincent, J. Volcanol. Geotherm. Res., 14(3–4), 335–359, doi:10.1016/0377-0273(82)90069-5.

Brown, R. J., C. Bonadonna, and A. J. Durant (2012), A review of volcanic ash aggregation, Physics and Chemistry of the Earth, Parts A/B/C(45), 65–78, doi:10.1016/j.pce.2011.11.001.

Brunauer, S. (1994), The adsorption of gases and vapors, Physical Absorption, vol. 1, 25–60 pp., Princeton Univ. Press, Princeton, N. J.

Brunauer, S., P. H. Emmett, and E. Teller (1938), Adsorption of gases in multimolecular layers., J. Am. Chem. Soc., 60, 309–319, doi:10.1021/ja01269a023.

Bullard, J., et al. (2016), High-latitude dust in the earth system., Reviews of Geophysics., 54(2), 447—485, doi:10.1002/2016RG000518.

Bullard, J. E. (2013), Contemporary glaciogenic inputs to the dust cycle, Surface Processes and Landforms, 38(1), 71–89, doi:10.1002/esp.3315.

Bullard, J. E., and M. J. Austin (2011), Dust generation on a proglacial floodplain, West Greenland, Aeolian Research, 3(1), 43–54.

Bullard, J. E., M. Baddock, G. McTainsh, and j. Leys (2008), Sub-basin scale dust source geomorphology detected using MODIS, Geophysical Research Letters, 35(15).

Burat, F., O. Kangal, and G. Onal (2006), An alternative mineral in the glass and ceramic industry: Nepheline Syenite, Minerals engineering, 19(4), 370–371.

Butwin, M. K., S. von Löwis, M. A. Pfeffer, and T. Thorsteinsson (2019), The effects of volcanic eruptions on the frequency of particulate matter suspension events in Iceland, Journal of Aerosol Science, 128, 99–113.

Cannone, N., G. Diolaiuti, M. Guglielmin, and C. Smiraglia (2008), Accelerating climate change impacts on alpine glacier forefield ecosystems in the European Alps., Ecological Applications, 18(3), 637–648, doi:10.1890/07-1188.1.

Carlsen, H., et al. (2012), Health effects following the Eyjafjallajökull volcanic eruption: a cohort study., J. Hyd. Eng., 2(6), e001,851, doi:10.1136/bmjopen-2012-001851.

Chalmers, G. R., R. M. Bustin, and I. Power (2012), Characterization of gas shale pore systems by porosimetry, pycnometry, surface area, and field emission scanning electron microscopy/transmission electron microscopy image analyses: Examples from the barnett, woodford, haynesville, marcellus, and doig unitscharacterization of gas shale pore systems, AAPG bulletin, 96(9), 1099–1199, doi:10.1306/10171111052.

Chao, G. Y., D. C. Harris, A. W. Hounslow, J. A. Mandarino, and G. Perrault (1967), Minerals from the nepheline syenite, Mount Saint Hilaire, Quebec, The Canadian Mineralogist, 9(1), 109–123.

Chepil, W. S. (1959), The use of spheres to measure lift and drag on wind-eroded soil grains, Proceedings of the Soil Science Society of America, 23, 343–344.

Chepil, W. S. (1961), The use of spheres to measure lift and drag on wind-eroded soil grains, Soil Sci. Soc. Proc., 25, 334–335.

Chow, A. C., and E. E. Adams (2011), Prediction of drag coefficient and secondary motion of free-falling rigid cylindrical particles with and without curvature at moderate Reynolds number, J. Hyd. Eng., 137, 1406–1414, doi:10.1061/(ASCE)HY.1943-7900.0000437.

Christiansen, E. B., and D. H. Barker (1965), The effect of shape and density on the free settling of particles at high Reynolds numbers, AIChE Journal, 11, 145–151, doi:10.1002/aic.690110130.

Church, M. (1972), Baffin Island sandurs: a study of Arctic fluvial processes, Ottawa Department of Energy Mines and Resources.

Chuvochina, M. S., I. A. Alekhina, P. Normand, J. R. Petit, and S. A. Bulat (2011), Three events of saharan dust deposition on the Mont Blanc glacier associated with different snow-colonizing bacterial phylotypes, Microbiology, 80(1), 125–131, doi:10.1134/S0026261711010061.

Clift, R., J. R. Grace, and M. E. Weber (2005), Bubbles, drops, and particles, Dover Publications, Mineola, New York.

Cornelis, W. M., and D. Gabriels (2003), The effect of surface moisture on the entrainment of dune sand by wind: an evaluation of selected models, Sedimentology, 50(4), 771–790.

Cox, E. (1927), A method of assigning numerical and percentage values to the degrees of roundness of sand grains, J. Paleontol., 1, 179–183.

Crusius, J., A. W. Schroth, S. Gassò, C. M. Moy, R. C. Levy, and M. Gatica (2011), Glacial flour dust storms in the Gulf of Alaska: Hydrologic and meteorological controls and their importance as a source of bioavailable iron, Geophys. Res. Lett., 38, L06,602, doi:10.1029/2010g1046573.

Dagsson-Waldhauserova, P., O. Arnalds, and H. Olafsson (2013), Long-term frequency and characteristics of dust storm events in Northeast Iceland (1949−2011), Atmospheric environment, 77, 117–127.

Dagsson-Waldhauserova, P., et al. (2014), Physical properties of suspended dust during moist and low wind conditions in Iceland, Icel. Agric. Sci., 27, 25–39.

Dagsson-Waldhauserová, P., et al. (2015), Optical properties of Icelandic volcanic dust, EGU General Assembly 2014, pp. 176–195, doi:2014EGUGA..16.8640D.

Dagsson-Waldhauserová, P., H. Olafsson, and Ó. Arnalds (2017), Long-term dust aerosol production from natural sources in Iceland, Journal of the Air and Waste Management Association, 67(2), 173–181.

Davis, R. S. (1992), Equation for the determination of the density of moist air (1981/91), Metrologia, 29(1), 67.

De Lima, J. L. M. P. (1989), Raindrop splash anisotropy: slope, wind and overland flow velocity effects, Soil Technology, 2, 71–78.

Del Bello, E., J. Taddeucci, J. Merrison, S. Alois, J. Iversen, and P. Scarlato (2018), Experimental simulations of volcanic ash resuspension by wind under the effects of atmospheric humidity., Scientific reports, 8(1), 14,509, doi:10.1038/s41598-018-32807-2.

Del Bello, E. D., J. Taddeucci, M. D. M. Vitturi, P. Scarlato, D. Andronico, S. Scollo, U. Kueppers, and T. Ricci (2017), Effect of particle volume fraction on the settling velocity of volcanic ash particles: insights from joint experimental and numerical simulations, Scientific Reports, 7, 39,620, doi:10.1038/srep39620.

Delimelle, P., F. Villieras, and M. Pelletier (2005), Surface area, porosity and water adsorption properties of fine volcanic ash particles, Bull. Volcanol., 67, 160–169, doi:10.1007/s00445-004-0370-x.

Dietrich, W. E. (1982), Settling velocity of natural particles, Water Resources Research, 18(6), 1615–1626, doi:10.1029/WR018i006p01615.

Disrud, L. A., and a. E. L. S. L. Lyles (1969), How wind affects the size and shape of raindrops, Agric. Eng., 50(10), 617.

Drab, E., A. Jaffrezo, and J. L. Colin (2002), Mineral particles content in recent snow at Summit (Greenland, Atmos. Env.., 36, 5365–5376, doi:10.1016/S1352-2310(02)00470-3.

Drain, L. E. (1980), The laser doppler techniques, 250 pp., Wiley-Interscience, Chichester, Sussex, England and New York.

Duce, R. A. (1995), Sources, distributions, and fluxes of mineral aerosols and their relationship to climates, In Charlson, R.J., Heintzenberg, J. (Eds., pp. 43–72, doi:10.1136/bmjopen-2012-001851.

Duce, R. A., et al. (1991), The atmospheric input of trace species to the world ocean, Global biogeochemical cycles, 5(3), 193–259, doi:10.1029/91GB01778.

Durst, F., F. A. Melling, and H. J. Whitelaw (1976), Principles and Practice of Laser-Doppler Anemometry, Academic Press, London, doi:10.1017/S0022112077221604.

Einarsson, M. A. (1984), Climate of Iceland, World Survey of Climatology, 15(3), 673–697.

Ellison, W. D. (1944), Studies of raindrop erosion, Agricultural Engineering, 25, 131–136.

Ellison, W. D. (1947), Soil erosion studies, Agricultural Engineering, 28, 145–146 (7 parts), 197–201, 245–248;,297–300, 349–351, 407–408, 447–450.

Engelstaedter, S., I. Tegen, and R. Washington (2006), North African dust emis-

sions and transport, Earth-Science Reviews, 79(1-2), 73–100, doi:10.1016/j.earscirev.2006.06.004.

Epema, G. F., and H. T. Riezebos (1983), Fall velocity of waterdrops at different heights as a factor influencing erosivity of simulated rain, In Rainfall simulation runoff and soil erosion, 10(4), 1–17.

Erpul, G., L. D. Norton, and D. Gabriels (2003), The effect of wind on raindrop impact and rainsplash detachment, Transactions of the ASAE, 45, 51–62.

Erpul, G., D. Gabriels, W. Cornelis, H. Samray, and T. Guzelordu (2008), Sand detachment under rains with varying angle of incidence, Catena, 72(3–4), 413–422.

Erpul, G., D. Gabriels, W. Cornelis, H. Samray, and T. Guzelordu (2009), Sand transport under increased lateral jetting of raindrops induced by wind, Geomorphology, 104(3–4), 191–202.

Formenti, P., et al. (2011), Recent progress in understanding physical and chemical properties of African and Asian mineral dust., Atmospheric Chemistry and Physics., 11(6), 8231–8256, doi:10.5194/acp-11-8231-2011.

Gassó, S., and A. F. Stein (2007), Does dust from Patagonia reach the sub?Antarctic Atlantic Ocean, Geophysical Research Letters, 34(1).

Gassó, S., A. Stein, F. Marino, E. Castellano, R. Udisti, and J. Ceratto (2010), A combined observational and modeling approach to study modern dust transport from the Patagonia desert to East Antarctica, Atmospheric Chemistry and Physics, 10(17), 8287–8303, doi:10.5194/acp-10-8287-2010.

Gassó, S., T. Thorsteinsson, and C. McKenna-Neuman (2018), Assessing the many influences of high-latitude dust, Eos, 99, doi:10.1029/2018EO090315.

Gilbert, J. S., J. S. Lane, S. J. Sparks, R. S. J., and T. Koyaguchi (1991), Charge measurements on particle fallout from a volcanic plume, Nature, 349(6310), 598, doi:10.1038/349598a0.

Gillette, D. A. (1974), On the production of soil wind erosion aerosols having the potential for long range transport, J. des Recherches Atmospheriques, 8, 735–744.

Gillette, D. A. (1977), Fine particulate emissions due to wind erosion, Trans. ASAE, 20, 890–987.

Gillette, D. A. (1978), A wind tunnel simulation of the erosion of soil: effect of soil texture, sandblasting, wind speed and soil consolidation on dust production, Atmospheric Environment, 12, 1735–1743.

Gillette, D. A. (1981), Production of dust that may be carried great distances, Spec. Pap. Geol. Soc. Am., 186, 11–26.

Gillette, D. A., and R. Passi (1988), Modelling dust emission caused by wind erosion, J. Geophys. Res., 93(D11), 14,233–14,242.

Gillette, D. A., and T. R. Walker (1977), Characteristics of airborne particles produced by wind erosion on sandy soil, high plains of West Texas, Soil Sci., 123, 97–110.

Gillette, D. A., J. I. H. Blifford, and C. R. Fenster (1972), Measurements of aerosol size distributions and vertical fluxes of aerosols on land subject to wind erosion, J. App. Met., 11(6), 977–987.

Gillette, D. A., D. W. Fryear, T. E. Gill, T. Ley, T. A. Cahill, and E. A. Gearhart (1997), Relation of vertical flux of particles smaller than 10 μm to total aeolian horizontal mass flux at Owens Lake, J. Geophys. Res., 102, 26,009–26,015.

Gillies, J. A., and L. Berkofsky (2004), Eolian suspension above the saltation layer, the concentration profile, J. Sed. Res., 74(2), 176–183.

Gisladottir, F. O., Ó. Arnalds, and G. Gisladottir (2005), The effect of landscape and retreating glaciers on wind erosion in south Iceland. land degradation and development, Atmospheric Environment., 16(2), 177–187, doi: 10.1073/pnas.1015053108.

Gislason, S. R. (2008), Weathering in iceland, Jökull, 58, 387–408.

Gislason, S. R., T. Hassenkam, S. Nedel, N. Bovet, E. Eiriksdottir, H. Alfredsson, and B. Sigfusson (2011), Characterization of Eyjafjallajökull volcanic ash particles and a protocol for rapid risk assessment., Atmospheric Environment., 108(18), 7307–7312, doi:10.1073/pnas.1015053108.

Gittins, J. (1961), Nephelinization in the Haliburton-Bancroft district, Ontario, Canada, The Journal of Geology, 69(3), 291–308.

Glaze, L. S., and S. Self (1991), Ashfall dispersal for the 16 September 1986, eruption of Lascar, Chile, calculated by a turbulent diffusion model, Reviews of Geophy., 18(7), 1237–1240, doi:10.1029/91GL01501.

Gordon, M., and C. McKenna-Neuman (2009), A comparison of collisions of saltating grains with loose and consolidated silt surfaces, J. Geophys. Res.: Earth Surface, p. 114.F4.

Goudie, A. S., and N. J. Middleton (2001), Saharan dust storms: nature and consequences, Earth Sci. Rev.,, 56(1–4), 179–204.

Goudie, S. A., and J. N. Middleton (2006), Desert dust in the global system, Springer-Verlag, Germany, Heidelberg, doi:10.1007/3-540-32355-4.

Grainger, R. G., D. M. Peters, G. E. Thomas, A. J. A. Smith, R. Siddans, E. Carboni, and A. Dudhia (2013), Measuring volcanic plume and ash properties from space, Geological Society, London, Special Publications, 380(1), 293–320.

Greeley, P., and D. Iverson (1985), Wind as a Geological Process on Earth, Mars, Venus and Titan, Cambridge University Press, Cambridge.

Greenspan, L. (1977), Humidity fixed points of binary saturated aqueous solutions, J. Res. Nat. Bur. of Stand., 81(1), 89–96, doi:10.6028/jres.081a.011.

Grini, A., and C. S. Zender (1977), Roles of saltation, sandblasting, and wind speed variability on mineral dust aerosol size distribution during the Puerto Rican Dust Experiment (PRIDE), J. Geophys. Res.: Atmos., 109(D7).

Gunn, R., and G. D. Kinzer (1949), The terminal velocity of fall for water droplets in stagnant air, Journal of Meteorology, 6(4), 243–248, doi:10.1175/1520-0469(1949)006<0243:TTVOFF>2.0.CO;2.

Halliday, D., R. Resnick, and J. Walker (2006), Fundamentals of Physics, John Wiley & Sons:, Mississauga, Ontario.

Hamlette, C., S. Atherton, N. Shirtcliffe, G. McHale, S. Ahn, S. Doerr, R. Bryant, and M. I. Newton (2013), Transitions of water-drop impact behaviour on hydrophobic and hydrophilic particles, European Journal of soil science, 64(3), 324–333.

Harrison, R. G., and K. L. Aplin (2001), Atmospheric condensation nuclei formation and high-energy radiation, J. Atmos. Solar-Terres. Phys., 63(17), 1811–1819, doi:10.1016/S1364-6826(01)00059-1.

Haywood, J., and O. Boucher (2000), Estimates of the direct and indirect radiative

forcing due to tropospheric aerosols: A review, Reviews of Geophy., 38(4), 513–543, doi:10.1029/1999RG000078.

Heerden, W. M. V. (1964), Splash erosion as affected by the angle of incidence of raindrop impact, Unpublished Ph.D. thesis, Purdue University, Lafayette, Ind. USA.

Herich, H., T. Tritscher, A. Wiacek, M. Gysel, E. Weingartner, U. Lohmann, U. Baltensperger, and D. J. Cziczo (2009), Water uptake of clay and desert dust aerosol particles at sub-and supersaturated water vapor conditions, Physical Chemistry Chemical Physics, 11(36), 7804–7809, doi:10.1039/B901585J.

Hillier, S., and J. Marshall (1988), A rapid technique to make polished thin sections of sedimentary organic matter concentrates, J. Sed. Res., 58(4), 754–755.

Hope, A. S., J. B. Fleming, D. A. Stow, and E. Aguado (1991), Tussock tundra albedos on the north slope of alaska: effects of illumination, vegetation composition, and dust deposition, Journal of Applied Meteorology, 30(8), 11,200–1206.

Horwell, C. J. (2007), Grain size analysis of volcanic ash for the rapid assessment of respiratory health hazard., J. Env. Mon., 9, 1107–1115, doi:10.1039/b710583p.

Horwell, C. J., P. J. Baxter, S. E. Hillman, J. A. Calkins, D. E. Damby, . P. Delmelle, and J. S. L. Blond (2013), Physicochemical and toxicological profiling of ash from the 2010 and 2011 eruptions of Eyjafjallajökull and Grímsvötn volcanoes, Iceland using a rapid respiratory hazard assessment protocol., Env. Res., 127, 63–73, doi:10.1016/j.envres.2013.08.011.

Houser, C. A., and W. G. Nickling (2001), The emission and vertical flux of particulate matter $<10\,\mu m$ from a disturbed clay-crusted surface, Sedimentology, 48(2), 255–267.

Huang, C., J. M. Bradford, and J. M. Cushman (1983), A numerical study of raindrop impact phenomena. the elastic deformation case, Journal of the Soil Science Society of America, 47, 855–861, doi:10.2136/sssaj1983.03615995004700050003x.

IUPAC (1994), Physical chemistry division commission on colloid and surface chemistry, subcommittee on characterization of porous solids: Recommendations for the characterization of porous solids, Pure and Applied Chemistry, 66(8), 1739–1758.

Jarzemba, M. S., P. A. LaPlante, and K. J. Poor (1997), ASHPLUME Version 1.0-A Code for Contaminated Ash Dispersal and Deposition, Technical Description and User's Guide, Cent. for Nucl. Waste Regul. Anal.,, Southwest Res. Inst., San Antonio, Tex.

Jayaweera, K. O. L. K., and B. J. Mason (1965), The behaviour of freely falling cylinders and cones in a viscous, J. Fluid Mech., 22, 709, doi:10.1017/S002211206500109X.

Jena, S. K., N. Dhawan, D. S. Rao, P. K. Misra, B. K. Mishra, and B. Das (2014), Studies on extraction of potassium values from Nepheline Syenite, International Journal of Mineral Processing, 133, 13–22.

Johnson, B., et al. (2012), In situ observations of volcanic ash clouds from the FAAM aircraft during the eruption of Eyjafjallajökull in 2010., J. Geophys. Res.: Atmospheres., 117(D20), doi:10.1029/2011JD016760.

Johnson, C. P., X. Li, and B. E. Logan (1996), Settling velocities of fractal aggregates, Environmental Science and Technology, 30(6), 1911–1918, doi:10.1021/es950604g.

Joussaume, S. (1990), Three?dimensional simulations of the atmospheric cycle of desert dust particles using a general circulation model, Journal of Geophysical Research: Atmospheres, 95(D2), 1909–1941.

Katsuragi, H. (2011), Length and time scales of a liquid drop impact and penetration into a granular layer, J. Fluid Mech., 675, 552–573.

Kinnell, P. I. A. (2005), Raindrop?impact?induced erosion processes and prediction: a review, Hydrological Processes: An International Journal, 19(14), 2815–2844.

Kinnell, P. I. A., and L. M. Risse (1998), USLE-M: empirical modeling rainfall erosion through runoff and sediment concentration, Soil Science Society of America Journal, 62(6), 1667–1672, doi:10.2136/sssaj1998.03615995006200060026x.

Komar, P., and C. E. Reimers (1978), Grain shape effects on settling rates, J. Geol., 86(2), 193–209, doi:10.1086/649674.

Kumar, P., A. Nenes, and I. N. Sokolik (2009), Importance of adsorption for ccn activity and hygroscopic properties of mineral dust aerosol, J. Geol. Res. Letters, 36(24), doi:10.1029/2009GL040827.

Kylling, A., M. Kahnert, H. Lindqvist, and T. Nousiainen (2014), Volcanic ash infrared signature: porous non-spherical ash particle shapes compared to homogeneous spherical ash particles, Atmospheric Measurement Techniques 7, pp. 919–929.

Leadbetter, S. J., M. C. Hort, S. V. Löwis, W. K., and W. C. S. (2012), Modeling the resuspension of ash deposited during the eruption of Eyjafjallajökull in spring 2010, J. Geophy. Res., 117, D00U10, doi:10.1029/2011JD016802.

Legout, C., S. Leguédois, Y. L. Bissonnais, and O. M. Issa (2005), Splash distance and size distributions for various soils, Geoderma, 124, 279–292.

Li, B., and C. McKenna-Neuman (2012), Boundary-layer turbulence characteristics during aeolian saltation, Geophys. Res. Lett., 39(11), 1944–8007, doi: 10.1029/2012GL052234.

Liu, E. J., K. V. Cashman, and A. C. Rust (2015), Optimising shape analysis to quantify volcanic ash morphology, J. Geo. Res., 8, 14–30, doi:10.1016/j.grj. 2015.09.001.

Liu, X., Z. Dong, and X. Wang (2006), Wind tunnel modeling and measurements of the flux of wind-blown sand, J. Arid Env., 66(4), 657–672.

Loosmore, G. A., and J. R. Hunt (2000), Dust re-suspension without saltation, J. Geophys. Res., 105, 20,663–20,671.

Lopez, M. V. (1998), Wind erosion in agricultural soils: an example of limited supply of particles available for erosion, Catena, 33, 17–28.

Lopez, M. V., M. Sabre, R. Gracia, J. L. Arrue, and L. Gomes (1998), Tillage effects on soil surface conditions and dust emission by wind erosion in semi-arid aragon, (ne spain), Catena, 33, 17–28.

Loth, E. (2008), Drag of non-spherical solid particles of regular and irregular shape, Powder Technology, 182(3), 342–353, doi:10.1016/j.powtec.2007.06.001.

Macpherson, T., W. G. Nickling, J. A. Gillies, and V. Etyemezian (2008), Dust emission from undisturbed supply-limited desert surfaces, J. Geophys. Res., 113(F2), 1–16.

Maher, B. A., J. M. Prospero, D. Mackie, D. Gaiero, P. P. Hesse, and Y. Balkanski (2010), Global connections between aeolian dust, climate and ocean biogeochemistry at the present day and at the last glacial maximum, Earth-Science Reviews, 99(1–2), 61–97.

Mahowald, N. M., A. R. Baker, G. Bergametti, N. Brooks, R. A. Duce, T. D. Jikells, N. Kubilay, J. M. Propero, and I. Tegan (2005), Atmospheric global dust cycle and iron inputs to the ocean, Global Biogeochemical Cycles, 19(4), 133–165, doi:10.1029/2004GB002402.

Marshall, J. R., P. A. Bull, and R. M. Morgan (2012), Energy regimes for aeolian sand grain surface textures, Sedimentary Geology, 253, 17–24.

Marticorena, B., and G. Bergametti (1995), Modeling the atmospheric dust cycle: 1. Design of a soil?derived dust emission scheme, J. of Geophys. Res.: Atmos., 100(D8), 16,415–16,430.

Marx, S. K., B. S. Kamber, and H. A. McGowan (2005), Estimates of Australian dust flux into New Zealand: quantifying the eastern Australian dust plume pathway using trace element calibrated 210Pb as a monitor, Earth and Planetary Science Lette, 239(3–4), 336–351.

McGowan, H. A., and A. P. Sturman (1996), Interacting multi-scale wind systems within an alpine basin, Lake Tekapo, New Zealand, Meteorology and Atmospheric Physics, 58(1–4), 165–177.

McKenna-Neuman, C. (1993), A review of aeolian transport processes in cold environments, Progress in physical Geography, 17(2), 137–155.

McKenna-Neuman, C. (2003), Effects of temperature and humidity upon the entrainment of sedimentary particles by wind, Bound.-Lay. Meteorol., 108, 61–89.

McKenna-Neuman, C. (2009), Effects of temperature and humidity upon the entrainment of sedimentary particles by wind, Bound.-Lay. Meteorol., 108, 61–89.

McNown, J. S., and J. Malaika (1950), Effects of particle shape on settling velocity at low reynolds number, Eos Trans. AGU, 31(1), 74–82, doi:10.1029/TR031i001p00074.

Meinander, O. (2016), Effects of black carbon and icelandic dust on snow albedo, melt and density, Finnish Meteorological Institute, Ph.D. thesis.

Mihara, Y. (1952), Raindrops and soil erosion, Bulletin of the National Institute of Agricultural Sciences -Japan, Series A(1).

Mitchell, R. H., and R. G. Platt (1982), Mineralogy and petrology of nepheline syenites from the Coldwell alkaline complex, Ontario, Canada, Journal of Petrology, 23(2), 186–214.

Mockford, T. (2017), Sources, drivers and sedimentology of Icelandic dust events, Loughborough University, Ph.D. thesis.

Mockford, T., J. E. Bullard, and T. Thorsteinsson (2018), The dynamic effects of sediment availability on the relationship between wind speed and dust concentration, Earth Surface Processes and Landforms, 43(11), 2484–2492.

Morgan, R. P. C. (1978), Field studies of rainsplash erosion, Earth Surf. Process., 3, 295–299, doi:10.1002/esp.3290030308.

NASA (2014), Surface meteorology and solar energy (SSE), Release 6.0 Methodology Version 3.1.2.

Neuman, C. M. (2004), Effects of temperature and humidity upon the transport of sedimentary particles by wind, Sedimentology, 51(1), 1–17.

Neuman, C. M., and M. Maljaars (1997), Wind tunnel measurement of boundary-layer response to sediment transport, Boundary-Layer Meteorology, 84(1), 67–83.

Nickling, W. G. (1978), Aeolian sediment transport during dust storms: Slims River Valley, Yukon Territory, Can. J. Earth Sc., 15, 1069–1084.

Nickling, W. G., and J. A. Gillies (1989a), Emission of fine-grained particulates from desert soils, in paleoclimatology and paleometeorology: Modern and past patterns of global atmospheric transport, Kluwer Acad., pp. 133–165.

Nickling, W. G., and J. A. Gillies (1989b), Emission of fine-grained particulates from desert soils, in paleoclimatology and paleometeorology: Modern and past patterns of global atmospheric transport, Kluwer Acad., pp. 133–165.

Nickling, W. G., and J. A. Gillies (1993), Dust emission and transport in Mali, West Africa, Sedimentology, 40.5, 859–868.

Nickling, W. G., G. H. McTainsh, and J. F. Leys (1999), Dust emissions from the Channel Country of western Queensland, Australia., Z Geomorph N F, 116, 1–17.

Olsson, J., S. Stipp, K. Dalby, and S. Gislason (2013), Rapid release of metal salts and nutrients from the 2011 Grímsvötn, Iceland volcanic ash, Geochimica et Cosmochimica Acta., 123, 134–149, doi:10.1016/j.gca.2013.09.009.

Patterson, C. J. (1998), Laurentide glacial landscapes: The role of ice streams, Chem. Eng. Prog., 26(7), 643–646, doi:10.1130/0091-7613(1998)026<0643:LGLTRO>2.3.CO;2.

Pettyjohn, E. S., and E. B. Christiansen (1948), Effect of particle shape on free settling rates of isometric particles, Chem. Eng. Prog, 44(2), 157–172.

Pilinis, C., S. N. Pandis, and J. H. Seinfeld (1995), Sensitivity of direct climate forcing by atmospheric aerosols to aerosol size and composition, J. of Geophys. Res.: Atm., 100(D9), 18,739–18,754, doi:10.1029/95JD02119.

Prospero, M. J., J. E. Bullard, and R. Hogkins (2012), High latitude dust over the North Atlantic: inputs from icelandic proglacial dust storms, Science, 335, 1078–1082, doi:10.1126/science.1217447.

Pye, K. (1987), Copyright, Academic Press, doi:10.1016/B978-0-12-568690-7.50002-8.

Radic, V., and R. Hock (2011), Regionally differentiated contribution of mountain glaciers and ice caps to future sea-level rise, Nature Geoscience, pp. 91–94.

Ravi, S., T. M. Zobeck, T. M. Over, G. S. Okin, and P. A. O. L. O. D'ODORICO (2006), On the effect of moisture bonding forces in air-dry soils on threshold friction velocity of wind erosion, Sedimentology, 53(3), 597–609.

Reyssat, M., A. Pépin, F. Marty, Y. Chen, and D. Quéré (2006), Bouncing transitions on microtextured materials, EPL (Europhysics Letters), 74(2), 306.

Rice, M. A., B. B. Willets, and I. K. M^{c}Ewan (1995), An experiment study of multiple grain-size ejecta produced by collision of saltating grains with a flat bed, Sedimentorlogy, 42, 695–706.

Riezebos, H. T., and G. F. Epema (1985), Drop shape and erosivity part ii: Splash detachment, transport and erosivity indices, Earth Surface Processes and Landforms, 10(1), 69–74.

Riley, N. A. (1941), Projection sphericity., Journal of Sedimentary Research, 11, 94–95, doi:10.1306/D426910C-2B26.

Riley, N. A. (2003), Quantitative shape measurements of distal volcanic ash, J. of Geophy. Res., 108, 2504, doi:10.1029/2001JB000818.

Robock, A. (2000), Volcanic eruptions and climate, Geophys. Mono. Ser., 38(2), 191–219, doi:10.1029/1998RG000054.

Roney, J. A., and B. R. White (2006), Estimating fugitive dust emission rates using an environmental boundary layer wind tunnel, Atmos. Environ., 40, 7668–7685.

Rose, C. W. (1960), Soil detachment caused by rainfall, Soil Science, 89(1), 28–35, doi:1.

Ryan, B. J., and K. M. Poduska (2008), Roughness effects on contact angle measurements, American Journal of Physics, 76(11), 1074–1077.

Sanderson, R. S., C. McKenna-Neuman, and J. W. Boulton (2014), Windblown fugitive dust emission from smelter slag, Aeolian Research, 13(0), 19–29.

Saxton, K. E., L. Stetler, B. Lamb, C. Claiborn, and B. H. Lee (2000), Wind erosion and fugitive dust fluxes on agricultural lands in the Pacific Northwest, Transactions of the American Society of Agricultural Engineers, 43(3), 623–630.

Schumann, U. B., et al. (2011), Airborne observations of the Eyjafjallajökull volcano ash cloud over europe during air space closure in April and May 2010, Atmospheric Chemistry and Physics, doi:10.5194/acp-11-2245-2011.

Schuttlefield, J. D., D. Cox, and V. H. Grassian (2007), An investigation of water uptake on clays minerals using ATR-FTIR spectroscopy coupled with quartz crystal microbalance measurements, Aeolian Research, 112(D21), doi:10.1029/2007JD008973.

Shao, Y. (2000), Physics and Modelling of Wind Erosion, Dover, New York, USA.

Shao, Y. (2008), Physics and Modelling of Wind Erosion, vol 37 ed., Springer Science and Business Media, Berlin, Germany.

Shao, Y., M. R. Raupach, and P. A. Findlater (1993), The effect of saltation bombardment on the entrainment of dust by wind, J. Geophys. Res., 98(12), 12,719–12,726.

Shield, A. (1936), Application of similarity principles and turbulence research to bed-load movement. Mitteilungen der Preussischen Versuchsanstalt fur Wasserbau und Schifbau, Berlin. In : Ott, W.P. & van Uchelen, J.C. (translators), California Inst. Tech., W.M. Keck Lab. of Hydraulics and Water Resources, 13(167), 43.

Solomon, S., D. Qin, M. Manning, Z. Chen, M. Marquis, and K. A. et al. (2007), Contribution of working group i to the fourth assessment report of the Intergovernmental Panel on Climate Change.

Sorem, R. K. (1982), Volcanic ash clusters: tephra rafts and scavengers, Journal of Volcanology and Geothermal Research, 13(1–2), 63–71, doi:10.1306/D426910C-2B26.

Spark, R. S. J., M. I. Bursik, G. J. Ablay, R. M. E. Thomas, and S. N. Carey (1992), Sedimentation of tephra by volcanic plumes. Part 2: controls on thickness and grain-size variations of tephra fall deposits, Transactions of the American Society of Agricultural Engineers, 54(8), 685–695, doi:10.1007/bf00430779.

Stevenson, J., et al. (2012), Distal deposition of tephra from the Eyjafjallajökull 2010 summit eruption., J. of Geophy. Res.: Solid Earth, 117(B9), doi:10.1029/2011JB008904.

Stohl, A., et al. (2011), Determination of time-and height-resolved volcanic ash emissions and their use for quantitative ash dispersion modeling: the 2010 Eyjafjallajökull eruption, Atmospheric Chemistry and Physics, 11(9), 4333–4351, doi:10.5194/acp-11-4333-2011.

Stokes, G. G. (1951), On the effect of the internal friction of fluids on the motion of pendulums, Transactions of Cambridge Philosophical Society IX, 8–106, 3, 1–141, doi:10.1017/CBO9780511702266.002.

Stringham, G. E., D. B. Simons, and H. P. Guy (1969), The behavior of large particles falling in quiescent liquids, U.S. Geol. Surv. Prof. Pap., 562(C), 36, doi:10.3133/pp562C.

Suzuki, T. (1983), A theoretical model for dispersion of tephra, Arc volcanism: physics and tectonics, 95, 113.

Swindles, G., et al. (2017), Climatic control on icelandic volcanic activity during the mid-holocene., Geology, 46(1), 47–50, doi:10.1002/esp.1079.

Tedesco, M., M. Serreze, and X. Fettweis (2008), Diagnosing the extreme surface melt event 2011 over southwestern Greenland in 2007, the cryosphere, J. Geophys. Res., 3(2), 383–397, doi:10.5194/tcd-2-383-2008.

Tegen, I., and I. Fung (1994), Modeling of mineral dust in the atmosphere: sources, transport, and optical thickness, J. Geophys. Res., 99, 22,897–914.

Tegen, I., and A. Lacis (1996), Modeling of particle-size distribution and its influence on the radiative properties of mineral dust aerosol, J. Geophys. Res., 101(D14), 19,237–19,244, doi:10.1029/95JD03610.

Tennekes, H. (1973), The logarithmic wind profile, J. Atmos. Sc., 30, 234–238.

Terry, J. P. (1992), Rainsplash detachment and soil erosion in the Agueda Basin, Portugal: The effects of forest fire and land management changes, University College of Swansea, Ph.D. thesis.

Terry, J. P. (1998), A rainsplash component analysis to define mechanisms of soil detachment and transportation, Soil Research, 36(3), 525–542, doi:10.1002/esp.3290180605.

Thorsteinsson, T., G. Ísladóttir, J. Bullard, and G. McTainsh (2011), Dust storm contributions to airborne particulate matter in Reykjavík, Iceland, Atmospheric Environment, 45(32), 5924–5933, doi:10.1016/j.atmosenv.2011.05.023.

Thorsteinsson, T., T. Jóhannsson, A. Stohl, and N. I. Kristiansen (2012), High levels of particulate matter in Iceland due to direct ash emissions by the Eyjafjallajökull eruption and re-suspension of deposited ash, J. Geophys. Res.: Solid Earth, 117(B2).

Todd, M. C., et al. (2008), Quantifying uncertainty in estimates of mineral dust flux: An intercomparison of model performance over the Bodélé Depression, northern Chad, J. Geophys. Res.: Atmos., 113(D24).

Umback, C. R., and W. D. Lembke (1966), Effect of wind on falling water drops, Transactions of the ASAE, 9, 805–808.

Vieira, G., C. Mora, and M. Gouveia (2004), Oblique rainfall and contemporary geomorphological dynamics (Serra da Estrela, Portugal), Hydrological processes, 18(4), 807–824.

Waggoner, A. P., R. E. Weiss, N. C. Ahlquist, D. S. Covert, S. Will, and R. J. Charlson (1981), Optical characteristics of atmospheric aerosols, Atm. Env., 15(10–11), 1891–1909, doi:10.1016/0004-6981(81)90224-9.

Walker, G. P. L., L. Wilson, and E. L. G. Bowell (1971), Explosive volcanic eruptions-I: The rate of fall of pyroclasts, Geophys. J. R. Astron. Soc., 22(4), 377–383, doi:10.1111/j.1365-246X.1971.tb03607.x.

Webb, P., and C. Orr (1997), Analytical Methods in Fine Particle Technology, Micromeritics Instrument Corporation, Norcross, GA, there is no corresponding record for this reference.

White, B. R. (1996), Laboratory simulation of aeolian sand transport and physical modeling of flow around dunes, Annals of Arid Zone, 35(3), 187–213.

Wiegner, M., J. Gasteiger, S. GroSS, F. Schnell, V. Freudenthaler, and R. Forkel (2012), Characterization of the Eyjafjallajökulll ash-plume: Potential of lidar remote sensing, Physics and Chemistry of the Earth, Parts A/B/C(45), 76–86, doi:10.1016/j.pce.2011.01.006.

Willmarth, W. W., N. E. Hawk, and R. L. Harvey (1964), Steady and unsteady motions and wakes of freely falling disks, Physics of Fluids, 7(2), 197–208, doi: 10.1063/1.1711133.

Wilson, L., and T. Huang (1979), The influence of shape on the atmospheric settling velocity of volcanic ash particles, E. and Plan. Sci. Let., 44(2), 311–324, doi:10.1016/0012-821X(79)90179-1.

Wittmann, M., C. Zwaaftink, L. Schmidt, S. Gudmundsson, F. Pálsson, Ó. Arnalds, H. Björnsson, T. Thorsteinsson, and A. Stohl (2017), Impact of dust deposition on the albedo of Vatnajökull ice cap, Iceland, Cryosphere, 11, 741–754., doi:10.5194/tc-11-741-2017.

Worthington, A. M. (1908), A study of splashes, pearson ed., Longmans, Green & Co.

Wu, X., Q. Wang, Z. Luo, M. Fang, and K. Cen (2008), Experimental study of particle rotation characteristics with high-speed digital imaging system, Powder Technology, 181(1), 21–30, doi:10.1016/j.powtec.2007.04.007.

Xuan, J., I. N. Sokolik, J. Hao, F. Guo, H. Mao, and G. Yang (2004), Identification and characterization of sources of atmospheric mineral dust in East Asia, Atmos. Env., 38(36), 6239–6252.

Y. León, C. (1998), New perspectives in mercury porosimetry, Advances in colloid and interface science, 76, 341–372, doi:10.1016/S0001-8686(98)00052-9.

Yarin, A. L. (1984), Drop impact dynamics: Splashing, spreading, receding, bouncing, Annual Review of Fluid Mechanics, 38, 159–192.

Yilbas, B. S., H. Ali, A. Al-Sharafi, F. Al-Sulaiman, and C. Karatas (2018), Effect of environmental dust particles on laser textured yttria-stabilized zirconia surface in humid air ambient, Optics and Laser Technology, 101, 388–396, doi: 10.1016/S0001-8686(98)00052-9.

Young, R. A., and J. L. Wiersma (1973), The role of rainfall impact in soil detachment and transport, Water Resources Res., 9(6), 1629–1636.

Zobeck, T. M., and R. S. V. Pelt (2006), Wind-induced dust generation and transport mechanics on a bare agricultural field, J. Geophys. Res.: Atmospheres, 112(22), 13–678.

Zwaaftink, C. D. G., Ó. A. ans P. Dagsson-Waldhauserova, S. Eckhardt, J. M. Prospero, and A. Stohl (2017), Temporal and spatial variability of icelandic dust emissions and atmospheric transport, Atmospheric Chemistry and Physics, 17(17), 10,865–10,878.

Zwaaftink, C. G., H. Grythe, H. Skov, and A. Stohl (2016), Substantial contribution of northern high-latitude sources to mineral dust in the Arctic, J. Geophys. Res.: Atmospheres, 112(22), 13–678.